MECHANICAL CHARACTERIZATION OF MAMMALIAN BRAIN TISSUE AND ENERGY DISSIPATIVE POLYMERS

by

Bo Qing

Bachelor of Science, University of California, Berkeley, 2013

Submitted to the Department of Biological Engineering
in partial fulfillment of the requirements for the degree of

Doctor of Philosophy

at the

MASSACHUSETTS INSTITUTE OF TECHNOLOGY

June 2018

Signature redacted

Signature of Author..... .....
Department of Biological Engineering
May 21, 2018

Signature redacted

Certified by..... .....
Krystyn J. Van Vliet
Michael (1949) and Sonja Koerner Professor of Materials Science and Engineering and Biological Engineering
Thesis Supervisor

Signature redacted

Accepted by..... .....
Forest White
Professor of Biological Engineering
Graduate Program Chair

Mechanical Characterization of Mammalian Brain Tissue and Energy Dissipative Polymers

by

Bo Qing

Submitted to the Department of Biological Engineering
on May 25, 2018 in partial fulfillment of the
requirements for the degree of Doctor of Philosophy in
Biological Engineering

Abstract

The high incidence of traumatic brain injury due to adverse impact events ranging from head collisions to ballistic attacks has prompted significant interest in synthetic polymer gels capable of mimicking key mechanical properties of brain tissue. These so-called brain tissue simulants are valuable tools for developing protective strategies because they can serve as test media to evaluate new helmets or optimize robotic surgery techniques. However, the so-called "soft matter" employed to date for ballistic applications, such as ballistic gelatin and clay, are crude mechanical representations of brain tissue. Therefore, there remains a need for a class of tissue simulant materials that more accurately replicates the mechanical behavior of brain tissue under impact loading, specifically in terms of deformation resistance and impact energy dissipation.

This thesis focuses on design and synthesis of hierarchically structured gels, and mechanical characterization of these compliant gels for comparison with mammalian brain tissue. In particular, we use impact indentation to explore how the impact energy dissipation response varies as a function of species for brain tissue, or as a function of molecular composition and structure for synthetic gels. We find that a bilayered polydimethylsiloxane (PDMS) composite system enables the decoupling of the material's deformation resistance and energy dissipation characteristics, and can be tuned to fully match porcine brain tissue. However, given that the top PDMS layer is highly adhesive, we investigate whether adhesion plays a significant role in modulating the energy dissipation response, which has important implications in the utility of the tissue simulant material for ballistic applications. With a separate bilayered PDMS composite system, we decouple surface adhesion from bulk viscoelasticity, and quantify their individual contributions to impact energy dissipation. Through these experimental studies, in addition to a finite element computational analysis, we establish fundamental design principles and provide new insights regarding mechanisms that govern the extent of deformation and energy dissipation in compliant polymeric materials.

Finally, we extend the capabilities of our impact indentation technique by demonstrating a novel analytical approach to extract viscoelastic moduli and relaxation time constants directly from the measured impact deformation response, thus significantly broadening the utility of

impact indentation. With conventional characterization techniques such as shear rheology, several challenges arise when the material of interest has stiffness on the order of 1 kPa or lower, as is the case with brain tissue, largely due to difficulties detecting initial contact with the compliant sample surface. In contrast, impact indentation does not require contact detection *a priori*, and thus can potentially be utilized as a more accurate tool to characterize the viscoelastic properties of a wider range of soft matter for diverse biomedical or engineering applications, not limited to brain tissue simulants. This semi-analytical approach enables future studies to extract viscoelastic properties of brain tissue and tissue simulant polymers with increased accuracy and spatial resolution, in the context of traumatic brain injury, protection, and recovery.

Thesis Supervisor: Krystyn J. Van Vliet
Title: Michael (1949) and Sonja Koerner Professor of Materials Science and Engineering and Biological Engineering

Acknowledgements

First and foremost, I would like to acknowledge my thesis advisor, Prof. Krystyn J. Van Vliet. Her mentorship and unwavering support throughout my Ph.D. studies have been instrumental to my growth as a researcher and engineer. She has graciously provided feedback on almost a weekly basis, while allowing me the freedom to pursue ideas of my own and initiate new collaborations. Under her guidance, I have developed an array of new technical skills and also learned how to become a more effective communicator. Most of all, I would like to thank her for having my best interests in mind, despite the various other responsibilities that she had.

Next, I would like to thank my committee members, Prof. Alan Grodzinsky and Prof. Bradley Olsen. I am grateful to Prof. Grodzinsky, who was my committee chair, for providing valuable comments that were crucial to expanding the scope of my thesis work, specifically in terms of broadening the utility of a key characterization method that I employed heavily. I am grateful to Prof. Olsen, who was also a team member on a joint project, for providing helpful suggestions to all aspects of my research during the various meetings we had together.

My time in the Van Vliet Laboratory for Material Chemomechanics has been a great experience. It was highly motivating to have worked alongside such a bright, meticulous group of colleagues. I have benefited immensely from interactions with many former and current group members, including Dr. John Maloney, Dr. Anna Jagielska, Dr. Elizabeth Canovic, Dr. Frances Liu, Dr. Jessica Swallow, Frank McGrogan, Deena Rennerfeldt, Daniela Espinosa-Hoyos, and Yen-Ting Chi. I would like to give special thanks to Aleksandar Mijailovic and Kyle Geiser for working directly with me on various components of this thesis and challenging me to become a better researcher. I would not be where I am now without their help.

Most of the work conducted in this thesis was financially supported by the U.S. Army through the Institute for Soldier Nanotechnologies (ISN) under Contract W911NF-07-D-0004. I am fortunate to have been a part of a larger ISN interdisciplinary research team that included folks from Prof. Olsen's, Prof. Keith Nelson's, and Prof. Raul Radovitzky's group. I would like to especially thank Dr. Shengchang Tang (Olsen group), Dr. David Veysset (Nelson group), and Dr. Aurelie Jean (Radovitzky group) for all the collaborative work that we have done on this ISN project. I am also fortunate to have been awarded the National Defense Science and Engineering Graduate Fellowship during the beginning of my graduate career.

In addition to the ISN team, I had a number of other fantastic collaborators outside of the Van Vliet group. I am grateful to Dr. Liheng Cai and Prof. David Weitz (Harvard University) for being receptive to my collaboration request and working with me to elucidate the role of adhesion on mechanical energy dissipation. I am appreciative of Dr. Mustafa Sahin (Boston Children's Hospital) and Jennifer Haupt for supplying many brain tissue samples for me to characterize. I would like to thank Dr. Randy Mrozek and Dr. Joseph Lenhart (U.S. Army Research Laboratory) for their contributions in initiating the tissue simulant work and for synthesizing polymers that were key components of my research. I would also like to acknowledge Alan Schwartzman for training me to use the instrumented nanoindenter in the MIT NanoLab and helping me troubleshoot when problems arose. Although I never had the

chance to meet them in person, I am grateful to Dr. Jim Smith and Dr. Stephen Goodes (Micro Materials Ltd.) for their patience in addressing my questions and helping me implement new capabilities to the nanoindenter.

Outside of research, there are several people who I need to thank. I am grateful to my former roommates – Jaideep Dudani, Andrew Chen, Naveen Mehta, and Adrienne Rothschilds – for all the great memories and for making Cambridge a home away from home. Also, I would like to thank my soccer teammates and poker buddies; there are simply too many of you to name, but thanks to each for providing an outlet from research and for stimulating my competitive spirit. To my closest friends from back home, even though we have lived on opposite coasts for the past five years, thank you – Elaine, Mike, Nathan, Ben, Josh, Kenneth, Emily, and Bill – for always being able to make me laugh and for providing support whenever I needed it. I am truly proud of the lifelong relationships that we have built and look forward to all the future adventures that are in store for us.

Last, but not least, I would like to thank my family members. I am most grateful to my parents, Xinlin and Ping, for their unconditional love, unlimited support, and unwavering belief in me. I would not be the person I am today without the sacrifices that they have made to provide me with the best possible opportunities to succeed. Much thanks is also owed to my younger sister, Lisa, for pushing me to be the best version of myself. Despite our differences, I have always aspired to be a great role model to you just like how Mom and Dad were to me. Even though as a family, we rarely voice our love and appreciation for each other, you three are undoubtedly the most important, inspirational people in my life, and to them I dedicate this thesis.

Table of Contents

List of figures

List of tables

Chapter 1: Introduction

1.1 Motivation

Traumatic brain injury (TBI) caused by a focal impact to the head is a significant health problem affecting millions of individuals each year in the United States [1]. Athletes and soldiers are two subpopulations frequently exposed to adverse impact events ranging from head collisions to ballistic attacks and are thus highly susceptible to TBI. Although most of TBI cases (roughly 75%) may be considered minor or moderate, even these can lead to devastating and permanent consequences such as depression and cognitive defects [2,3]. To improve survivability, we must better understand the injury mechanisms and pathophysiology associated with TBI for treatment purposes, and must also focus on designing novel protective strategies that mitigate the risk of injury. Synthetic materials capable of accurately mimicking the mechanical deformation of brain tissue under such impact events are valuable tools because these mechanical brain surrogates, also termed tissue simulants, can serve as test media for assessing efficacy of new protective helmets, enabling the prediction of injury severity both experimentally and computationally [4-7]. However, the synthetic materials employed to date for ballistic testing applications in both civilian and defense contexts are extremely limited, and fail to recapitulate the mechanical deformation response of brain tissue. This shortcoming is due largely to challenges in robust gel design and insufficient methods to quantify tissue and surrogate response under high-rate impact loading. Thus, the primary aim of this thesis will be to examine quantitatively how the structure and composition of novel material systems affect the mechanical properties in order to ultimately establish fundamental design principles that enable the optimization of a tissue simulant gel to mechanically mimic brain tissue under concentrated impact loading. Note that while brain tissue simulant materials can also help optimize robotic surgery techniques and guide the design of brain implant devices to minimize the risk of injury [8-12], this thesis will mainly focus on conditions relevant to ballistic testing applications.

Aside from tissue simulant applications, the performance of biologically inspired materials used in other engineering applications can similarly either be limited by or enabled by the mechanical properties of the material. For example, in the tissue engineering field, replacements for bone and cartilage must be biocompatible and also require specific load-bearing capabilities

to function properly and remain biomechanically stable [13-19]. Accurate measurement of the mechanical properties is relevant not only for replacing or mimicking tissues, but also for elucidating the role of material mechanics in disease diagnosis or progression. Several distinct cell types have been demonstrated to exhibit sensitivity to both biochemical and mechanical cues [20-25]. Thus, investigation of physical factors such as tissue structure and mechanical properties during pathology has attracted increasing interest in the biological engineering community. Recent studies have revealed that a wide range of diseases – including cancer, atherosclerosis, asthma, Alzheimer's, multiple sclerosis, and encephalomyelitis – all exhibit abnormalities in cellular mechanotransduction that are correlated with changes in extracellular matrix structure and mechanics [26-31]. Better understanding of the precise mechanistic origins of these variations in stiffness during disease pathology may ultimately lead to new treatment targets or diagnostic markers. Unfortunately, several experimental challenges arise when the tissue of interest is of low stiffness and exhibits complex deformation rate-dependent behavior (e.g., brain tissue). Therefore, the latter portion of this thesis focuses on improving existing experimental and analytical methods to enable more accurate measurement of key mechanical properties for highly compliant materials including brain tissue and brain tissue simulants.

1.2 Brain structure and composition

Brain tissue is a highly heterogeneous and hierarchical material, with biological polymers arranged in convoluted structures at the nanoscale and microscale that impart specific function. Thus, the tissue exhibits mechanical behavior that is strongly dependent on strain rate (time-scales) and impact geometry (length scales) [32,33], making it challenging to design a simple, synthetic material that can mechanically mimic brain tissue with high fidelity. Here, we first review the structure and composition of brain, which directly give origin to its complex mechanical properties.

On the tissue level, mammalian brain is broadly comprised of an outer layer of gray matter, consisting of neuronal cell bodies, dendrites, and axons (mostly unmyelinated), and an inner core of white matter, consisting of oligodendrocytes, astrocytes, microglia, and tightly packed bundles of myelinated axons [34-38]. Myelin is a membranous, lipid-rich sheath that wraps around axons, acting as an insulating layer to enhance electric signal propagation [39]. The loss of

myelin sheaths is referred to as demyelination, and is a hallmark of lesions caused by traumatic injury and of numerous neurodegenerative or autoimmune diseases like multiple sclerosis [40]. While myelin has been extensively studied in the context of its electrical function, the mechanical importance of myelin has been recently recognized and requires further investigation [41,42].

Although one can macroscopically distinguish the gray and white matter of brain tissue through optical contrast correlated chiefly with myelin density, different regions of the brain contain different proportions of gray and white matter in addition to cerebral ventricles filled with cerebrospinal fluid. For example, the corpus callosum, which lies beneath the cerebral cortex and comprises highly aligned axons connecting the left and right cerebral hemispheres, is the largest white matter structure in the human brain and has been the subject of many research studies involving TBI and demyelinating diseases [43-48]. Additionally, the overall gray to white matter ratio in the brain varies significantly among mammalian species, as shown in Fig. 1-1, further complicating attempts to elucidate the relationship between brain microstructure and mechanical properties. Figure 1-1 also demonstrates that the geometry of brain tissue, or the degree of convolution in the outer cerebral cortex, can vary among species due to differences in brain folding during development [49,50]. Human and porcine brains are both gyrencephalic (highest degree of convolution) and contain roughly 40% gray and 60% white matter. In contrast, murine brains are lissencephalic (smooth; not convoluted) and are predominantly gray matter, containing only roughly 10% white matter [51-54].

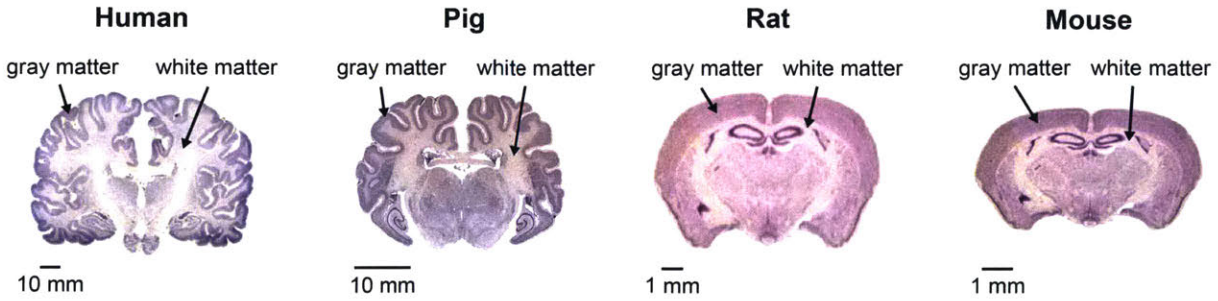

Figure 1-1 Histological stains of coronal brain sections from four adult mammalian species, adapted with permission from http://brainmuseum.org (supported by the United States National Science Foundation). Larger animals tend to have increased cortical folding and a higher proportion of white matter. Porcine brain is structurally similar to human brain, whereas murine brain exhibits significant differences.

On the cellular level, the brain is characterized by a complex network of two main cell types: neurons and glia. Neurons, which consist of a soma (cell body), dendrites, and an axon, are the basic functional units of the nervous system responsible for the synaptic signaling process. Glial cells, a term derived from the Greek word "glue," comprise the majority of brain cells and play important supportive roles, such as maintaining homeostasis, forming myelin, and providing physical and nutritional support for neurons [55-57]. Different types of glial cells include astrocytes, oligodendrocytes, and microglia. Previous mechanical studies on isolated individual cells revealed different viscoelastic behavior between different cells (e.g., neurons vs. astrocytes) and between different components of a single cell (e.g., cell body vs. cell processes), thus further demonstrating the heterogeneity of brain [58,59]. The intercellular architectural components of neural cells are similar to that of other mammalian cell types, with cytoskeletal networks comprising actin filaments, microtubules, or intermediate filaments giving rise to the cellular mechanics [60,61]. It is generally believed that the mechanical properties and organization of neurons and glial cells are the key parameters responsible for the mechanical compliance of brain tissue [59].

However, brain tissue also contains an extracellular matrix (ECM), which has garnered far less attention than the cellular components. Brain tissue's ECM occupies the space between neurons and glia, and is estimated to comprise 10-20% of the total brain volume [62]. Unlike the ECM of systemic tissues like cartilage, the ECM of brain has relatively small amounts of fibrous proteins (i.e., collagen and elastin) and adhesive proteins (i.e., fibronectin and laminin), but is rich in glycoproteins and proteoglycans [63,64]. The specific constituents and organization of brain tissue's ECM is illustrated in Fig. 1-2, with the ECM arranged into three principal compartments: a basement membrane, perineuronal nets, and a diffuse interstitial matrix. While the ECM is thought chiefly to provide topographical and biochemical cues to regulate cell behavior in brain tissue [59,65,66], there has been no direct experimental evidence to support such claims to our knowledge. Better understanding of the ECM functions and regulation in relation to the overall tissue mechanical behavior is needed. Modifications to the ECM structure in models of traumatic injury, neurodegenerative diseases, and natural aging may alter local mechanical properties. Whether any such mechanical differences can be detected robustly and whether this can lead to discovery of new therapeutic targets for clinical processes like remyelination remain open and important research questions.

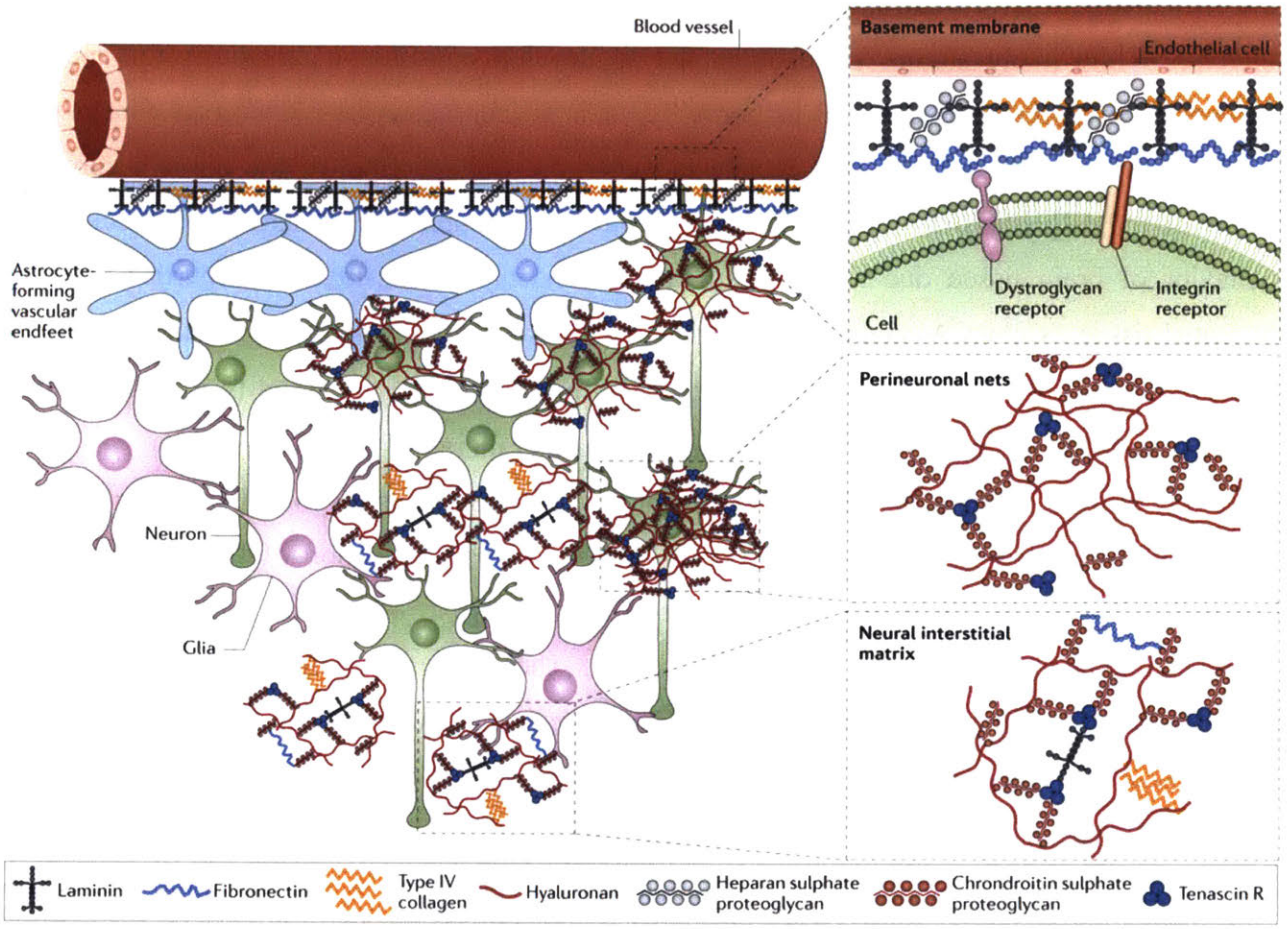

Figure 1-2 Structure and composition of the ECM in brain tissue. ECM is arranged into three main compartments: a basement membrane, perineuronal nets, and a diffuse interstitial matrix. Interactions among various ECM components and cellular components are shown. The pink glial cells may depict astrocytes, oligodendrocytes, or microglia. Image is taken from Lau et al. [64], reprinted with permission from *Nature Reviews Neuroscience*.

1.3 Mechanical behavior of brain tissue

1.3.2 Viscoelastic models

Better understanding of the relationship between brain microstructure and brain mechanical properties has important implications for several engineering applications, including the design of synthetic brain tissue simulants. However, accurate mechanical characterization of brain tissue is a challenging task, and there remains much more to be done to rigorously characterize this

complex material. Ideally, there would be a constitutive model that describes comprehensively the shear, compressive, and tensile response of brain tissue within the loading rate regime of interest. While many studies have attempted to develop constitutive equations for specific aspects of brain tissue mechanical response, there is no consensus on a universal constitutive model for brain tissue to date that is able to match the full spectrum of the tissue's complex behavior [67-69]. Various viscoelastic models have been applied to describe the mechanical behavior of brain tissue due to the strain rate-dependent and dissipative properties that the hydrated tissue exhibits. Models often idealize brain tissue to be incompressible (time invariant Poisson ratio $\upsilon = 0.5$), homogeneous, isotropic, and linear, but these are simplifying assumptions that may be true only at very small strains (~ 0.1%) and strain rates [70-76].

Here, we review the generalized Maxwell model, also known as the Wiechert model, which is commonly used to describe the viscous or time-dependent relaxation of linear viscoelastic materials [77-79]. As illustrated in Fig. 1-3, this model consists of a spring in parallel with N Maxwell elements (spring and dashpot in series). The springs, which represent the elastic component of the response, each have a stiffness k or an equivalent shear modulus G; the dashpots, which represent the viscous component of the response, each have a damping coefficient b or an equivalent viscosity η. The generalized Maxwell model takes into account that the material does not have a single relaxation time, but rather a distribution of relaxation times. The total number of Maxwell elements N corresponds to how many relaxation times are necessary to accurately represent the distribution. Note that if $N = 1$, the generalized Maxwell model reduces to the standard linear solid (SLS) model, which is also often used for simple approximations of the viscoelastic behavior of tissues and polymer gels. The parameters G_i and τ_i correspond to the spring stiffness and relaxation time associated to the i-th Maxwell element in Fig. 1-3. At infinite time, every dashpot will be fully relaxed, and every Maxwell element in the model will behave similarly to an open circuit, leading to an elastic response solely from the single spring described by G_∞. Thus, the equilibrium modulus G_∞ characterizes the material's modulus at very long timescales or low frequencies once the material is fully relaxed. In the other limiting condition (i.e., at very short timescales or high frequencies), all springs in parallel are deformed instantaneously; the response is governed by the instantaneous modulus G_0, which corresponds to the sum of stiffnesses for all individual springs. While G_0 may be the more relevant viscoelastic moduli for certain applications that involve high strain rate deformations,

such as ballistic testing, it is notably more difficult to characterize accurately through existing methods (compared to G_∞).

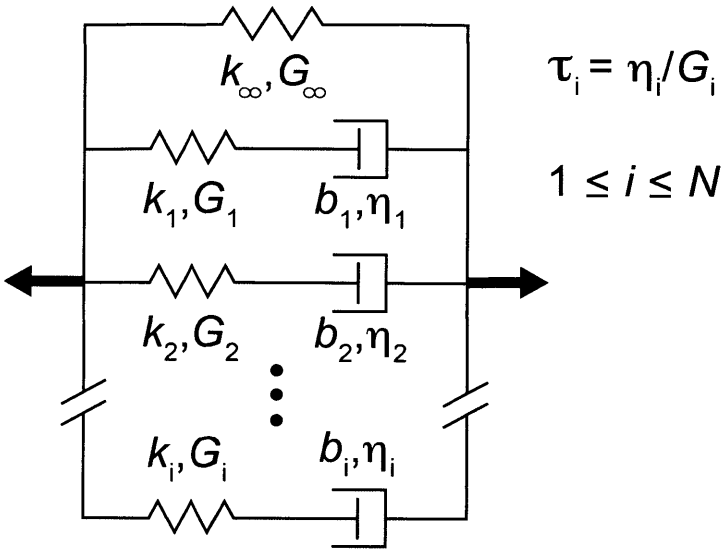

Figure 1-3 Schematic of the generalized Maxwell model, a common constitutive model of linear viscoelasticity, composed of a spring in series with N Maxwell elements. Each spring has a stiffness k that can be converted to a shear modulus G, and each dashpot has a damping coefficient b that can be converted to a viscosity η. This model has a distribution of N relaxation times τ. The relaxation function can be described by a Prony series.

Equation 1-1 expresses the shear relaxation function in the time domain through a Prony series:

$$G_R(t) = G_\infty + \sum_{i=1}^{N} G_i e^{-\frac{t}{\tau_i}}, \tag{1-1}$$

or

$$G_R(t) = G_0 - \sum_{i=1}^{N} G_i (1 - e^{-\frac{t}{\tau_i}}).$$

Certain experiments such as creep compliance and stress relaxation are conducted in the time domain. In contrast, other experimental approaches such as oscillatory shear rheology and dynamical mechanical analysis generate data in the frequency domain to obtain the frequency-dependent storage moduli G' and loss moduli G''. Equation 1-1 can be rewritten in the frequency

(s) domain through a Laplace transform, and expressed in terms of the real component corresponding to G' (Equation 1-2) and imaginary component corresponding to G'' (Equation 1-3) as follows:

$$G'(s) = G_\infty + \sum_{i=1}^{N} \frac{G_i s^2 \tau_i^2}{1+s^2\tau_i^2}, \tag{1-2}$$

$$G''(s) = \sum_{i=1}^{N} \frac{G_i s \tau_i}{1+s^2\tau_i^2}. \tag{1-3}$$

Although the generalized Maxwell model is useful for approximating the mechanical properties of viscoelastic materials at the extreme limiting conditions (i.e., very short or long timescales), there are several caveats with using linear viscoelastic models and Prony series to describe the behavior of brain tissue. First, a power-law relationship between measured moduli and applied frequency is observed when characterizing brain tissue. This corresponds physically to an infinite distribution of relaxation time constants, whereas the generalized Maxwell model uses a discrete number of time constants. Furthermore, brain tissue exhibits a very low linear viscoelastic strain limit on the order of 0.1 to 1%, which renders it non-linearly viscoelastic at most strains of practical interest and thus necessitates more complex non-linear constitutive models. Various non-linear models that combine the principles of viscoelasticity and also hyperelasticity have been developed and used in finite element simulations [68,69,78,80-82]. However, these non-linear models require extraordinary computational time and still are only suitable within a limited range of loading (or displacement) amplitude and loading (or displacement) rate.

Finally, we note terminology to indicate the relative elastic moduli of materials, when linear elastic or linear viscoelastic models are adopted as reasonable approximations of load-displacement or stress-strain responses. Materials and tissues of lower elastic modulus (Young's modulus E in uniaxial deformation or shear moduli G in shear deformation) are termed compliant, while materials of higher elastic modulus are termed stiff. These elastic parameters indicate a reversible response (instantaneous in linear elastic deformation responses and time-lagging in viscoelastic deformation responses). These opposing terms of compliant and stiff are distinct from descriptors of plastic or permanent deformation, described historically in material

mechanics by the property of hardness or yield stress. Materials with higher resistance to permanent deformation are termed hard or strong, and those of lower resistance to permanent deformation are termed soft or weak. By this definition, many biological tissues and polymers are mechanically resistant to permanent deformation and would be considered hard. While these are the accurate mechanical descriptors of elastic (reversible) and plastic (irreversible without input of additional energy) properties of materials, we recognize that the terms "soft matter" and "soft tissue" are prevalent and taken to mean materials and tissues that exhibit low elastic moduli or resistance to any deformation, as compared with engineered metals, ceramics, or polymers with elastic moduli on the order of 10s to 100s of GPa. Within this thesis, we refer to materials and tissues of relatively low elastic moduli as compliant, so brain tissue and its synthetic polymer simulants are both mechanically compliant and referred to colloquially as "soft matter."

1.3.3 Conventional characterization methods

Measurement of brain tissue mechanics has attracted increasing interest due to the prevalence of TBI and neurological diseases. Beginning in the 1960s, the vast majority of characterization methods have been *in vitro* tests on excised brain tissue samples. More recently, magnetic resonance elastography (MRE) has emerged as a promising method to investigate the mechanical properties of brain tissue *in vivo* [83-88]. However, because MRE has yet to be fully mapped out and better calibration standards are needed, this section will only summarize the traditional *in vitro* techniques. Most *in vitro* studies in the literature examined brain tissue in shear or compression using dynamic frequency sweep experiments or creep compliance and stress relaxation experiments. Additionally, contact-based indentation approaches have been used heavily to quantify the nanoscale and microscale mechanical properties of brain tissue. Brain tissue properties in tension, however, are not well characterized due largely to the challenges of gripping the tissue sample effectively [80,89].

Oscillatory shear rheology is a power, well-established technique used to characterize viscoelastic solids at the macro-length scale. For inhomogeneous materials like brain tissue, this technique will only give an average bulk measurement of the mechanical properties, which can be sufficient for certain engineering applications such as tissue simulants. Numerous groups have employed oscillatory shear rheology with a parallel plate geometry to measure G' and G'' of brain tissue at discrete frequencies. However, there is a wide discrepancy in the magnitudes of

G' and G" reported in the literature, as demonstrated by Fig. 1-4. In a subset of these studies, G' of brain tissue was found to be on the order of 10^2-10^3 Pa at low frequencies and 10^3-10^4 Pa at high frequencies (Fig. 1-4(A)); G" was found to be on the order of 10^1-10^2 Pa at low frequencies and 10^3-10^4 Pa at high frequencies (Fig. 1-4(B)) [90]. Both moduli were characterized by weak power-law behavior, as evident by the log-log plots.

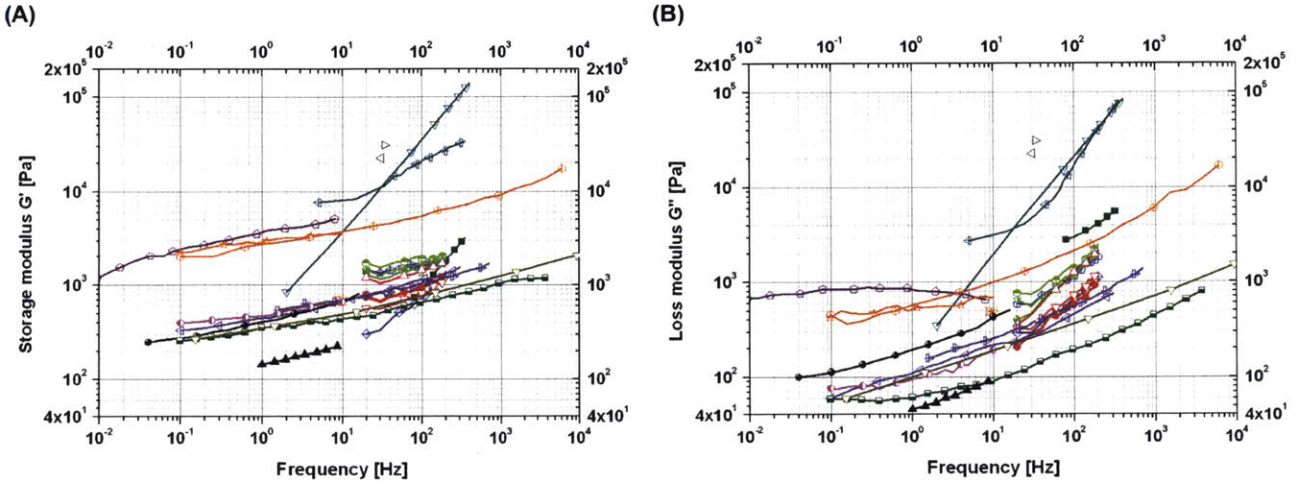

Figure 1-4 Compilation of oscillatory shear rheology results reported in the literature for brain tissue. (A) Shear storage moduli G' and (B) shear loss moduli G" measured at a range of oscillation frequencies. Each color represents data obtained by a distinct research group. Significant disparities are observed among measurements from different studies, with values in some cases differing by orders of magnitude. This large variation in reported data demonstrates the difficulties of accurate mechanical characterization of brain tissue. Figure is taken from Chatelin et al. [90], reprinted with permission from *Biorheology*.

Shear rheology measurements from different research groups varied in some cases by orders of magnitude, especially for G". The sources of this significant disparity in reported values have been difficult to pinpoint, but are often attributed to inconsistencies in protocol. For example, the animal species, animal age, post-mortem time, and experimental parameters (i.e., strain amplitude, temperature, and attachment methods) often varied from study to study. As mentioned earlier, brain tissue has a very low linear viscoelastic limit, and previous rheological experiments were very likely to have been conducted in the non-linear range, which would introduce substantial errors in the data analysis. More rigorous rheological testing protocols are

ultimately needed to reconcile the results present in the literature. Additionally, one inherent limitation of using oscillatory shear rheology to study highly compliant materials like brain tissue is that significant pre-stress/pre-strain in the sample cannot be avoided during the contact detection process. Premature compression of the sample will lead to an overestimation of the measured moduli that is directly dependent on the degree of pre-stress [30,91,92]. Finally, the high frequency or "instantaneous" response of brain tissue is challenging to measure with shear rheology due to instrument limitations, such as frame inertia upon reversal of shearing displacement [93-95]. For a typical rheometer, for frequencies on the order 10-100 Hz or greater, the instrument inertial effects will be too large compared to the measured signal from the relatively compliant brain tissue sample.

In contrast to macroscale oscillatory shear rheology, contact-based indentation enables measurement of local mechanical properties with spatial resolution on the order of nanometers to micrometers. Therefore, *in vitro* indentation experiments via an instrumented indenter or atomic force microscope (AFM) have gained popularity approach as a high-resolution, high-fidelity approach for investigating brain tissue mechanics, specifically for probing regions of gray and white matter individually [34,70,96-102]. Indentation experiments are typically used to estimate an effective Young's elastic modulus of a biological sample at low strains (~1%) [103-105], though the same instrument can also be leveraged to measure viscoelastic properties through creep compliance and stress relaxation experiments [106-108]. However, similar to rheological experiments, accurate measurement of the short timescale or "instantaneous" response is challenging because the experimentally applied load or indentation depth are not ideal step functions. Loads and indentation depths are instead applied over short timescales (< 1 sec), and these loading histories can affect the measured creep and relaxation responses, resulting in underestimated instantaneous moduli. Nonetheless, indentation is a powerful experimental method employed by many for the characterization of not only brain tissue mechanics but also of individual neural cells.

While the mechanical properties of brain at the tissue continuum level have been investigated for numerous decades, continuing advancements in testing methods and data analysis are required to reconcile the disparities found in the literature. Moreover, there is a need to quantify the mechanical behavior of brain tissue under more dynamic loading conditions compared to conventional indentation or rheology in order to predict the extent of deformation and energy

dissipation caused by impact events representative of collisions or ballistic assaults. A technique called impact indentation, adopted and further developed for polymers in the Van Vliet Laboratory for Material Chemomechanics, was previously employed to measure the mechanical response of other hydrated biological soft tissues, including heart and liver tissue, to concentrated impact loading that approached ballistic strain energy densities [109,110]. In this thesis, we aim to extend impact indentation to brain tissue to characterize its impact energy dissipation response and subsequently engineer novel synthetic tissue simulant gels that can be optimized to recapitulate the mechanical properties of brain tissue.

1.4 Current tissue simulant materials

1.4.1 Ballistic gelatin

Developing effective strategies to protect the brain from injury is of significant interest to the national defense, automobile, and contact sport industries. In ballistic testing applications, tissue simulant materials facilitate the evaluation of new protective equipment such as helmets by serving as a mechanical surrogate or test media. The U.S. Army has routinely used ballistic gelatin (Fig. 1-5(A)) as a simulant material for soft tissues mainly due to facile processing and cheap costs [111]. Ballistic gelatin is a thermoreversible hydrogel derived from denatured collagen and crosslinked polypeptide chains with an elastic modulus on the order of 100 kPa [112,113]. While ballistic gelatin is mechanically comparable to skeletal muscle tissue [114], it is approximately three orders of magnitude stiffer than brain tissue, and thus is a poor brain tissue simulant candidate. Another key shortcoming of ballistic gelatin is the lack of thermal stability as rheological experiments have found the storage modulus of ballistic gelatin to decrease drastically as a function of temperature [6]. Water evaporation will dramatically alter the mechanical properties of gelatin as well. Finally, naturally derived gelatin is polydisperse, meaning it can have a variable molecular weight distribution as a function of gel preparation conditions; this can result in inconsistent mechanical properties from batch to batch [115]. The ideal brain tissue simulant material should mimic the viscoelastic mechanical properties of brain tissue as closely as possible, should also exhibit structural stability in ambient air, and should be easily manufacturable.

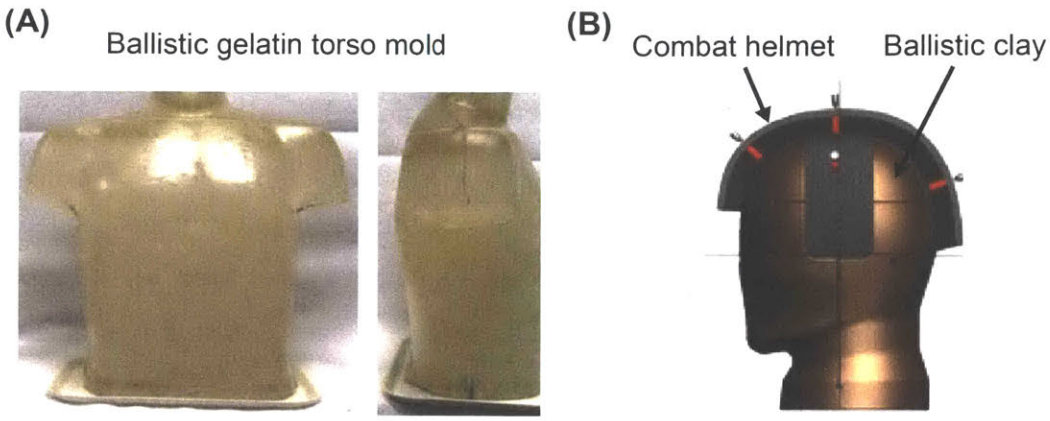

Figure 1-5 (A) Ballistic gelatin has been used as a standard test medium for over 50 years to evaluate the effects of ballistics and firearms on soft tissues. (B) Current U.S. Department of Defense test protocol for new combat helmets employs a headform packed with Roma Plastilina #1 ballistic clay. Helmet performance is assessed based on resistance to penetration and backface deformation. Both materials poorly represent the mechanical behavior of brain tissue.

1.4.2 Ballistic clay

Currently, the standard protocol used by the U.S. Department of Defense to assess newly developed combat helmets employs Roma Plastilina #1 (RP1) ballistic clay [116]. During ballistic testing, the helmet under evaluation is affixed to a headform packed with RP1 (Fig. 1-5(B)), and various projectiles will be fired into the helmet. RP1, which is an oil-based modeling clay, acts as a recording medium for assessing potential penetration through the helmet and measuring backface deformation [117,118]. However, RP1 is similar in stiffness to ballistic gelatin and is highly susceptible to plastic deformation [119,120]. In addition, it exhibits notable sensitivity to time, temperature, and handling procedure, which can all introduce undesirable testing variation [117,118]. Together, the limitations of ballistic gelatin and RP1 ballistic clay motivate the need to engineer novel brain tissue simulant materials with stable mechanical properties in ambient environments and the mechanical tunability to fully match the impact response of brain tissue.

1.4.3 Crosslinked polymer networks

A recent study of individual polydimethylsiloxane (PDMS) organogels as potential tissue simulant candidates revealed that they display a wide range of mechanical tunability and possess

exceptional structural stability [110]. As shown in Fig. 1-6, these organogels comprised a chemically crosslinked PDMS network, formed from vinyl-terminated PDMS and tetrafunctional silane crosslinkers, swollen in a non-reactive methyl-terminated PDMS solvent. The viscoelastic properties of such material could be systematically tuned by adjusting parameters including the concentration of chemical crosslinkers, molecular weight of polymer chains, and amount of solvent loading [121-123]. However, a significant limitation is that each of these parameters influences both the material's deformation resistance and energy dissipation characteristics during impact tests. As a result, independent modulation of each of these properties has not been achieved. While previous work demonstrated that this PDMS organogel could coincidentally be tuned to match murine heart tissue under concentrated impact loading, it failed to fully mimic the complex strain rate-dependent behavior of more compliant tissues such as liver and brain tissue.

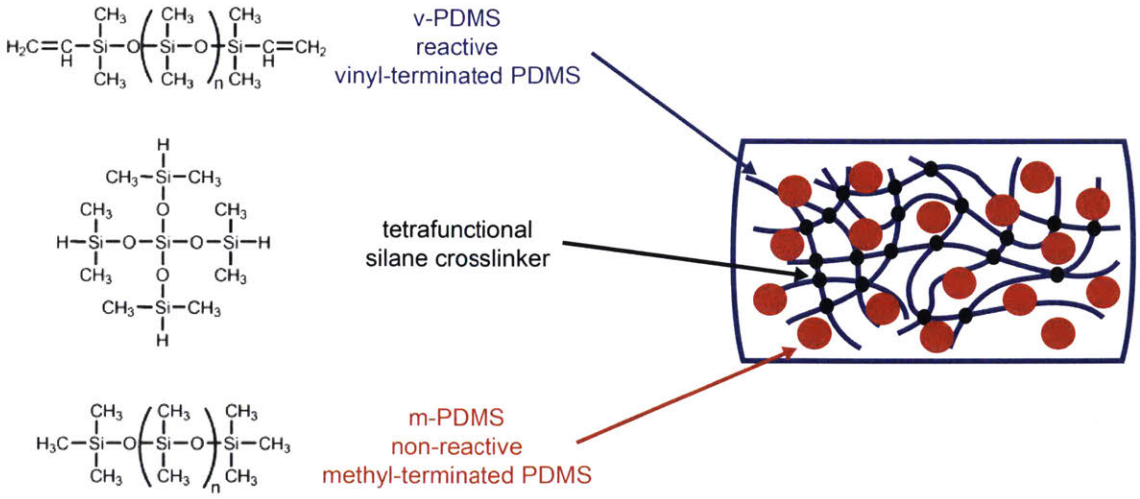

Figure 1-6 Schematic of a PDMS organogel synthesized by the U.S. Army Research Laboratory. Tunable parameters of this tissue simulant candidate include the stoichiometric ratio of vinyl to silane groups, molecular weight of the solvent, and the volume fraction of the solvent.

1.5 Thesis goals and organization

This thesis aims to (1) characterize the mechanical behavior of brain tissue from various animal models primarily in response to concentrated impact loading, and (2) engineer novel synthetic tissue simulant materials that can be optimized to mechanically mimic brain tissue with high fidelity. Through experimental studies in parallel with computational modeling, we seek to

establish fundamental design principles and gain new insights on the mechanisms governing the extent of deformation and energy dissipation. More broadly, this thesis develops new methodologies that avoid certain technical challenges of existing characterization techniques, and thus enable more accurate measurement of the viscoelastic mechanical properties of highly compliant materials. Figure 1-7 presents a graphical overview illustrating the scope of this thesis.

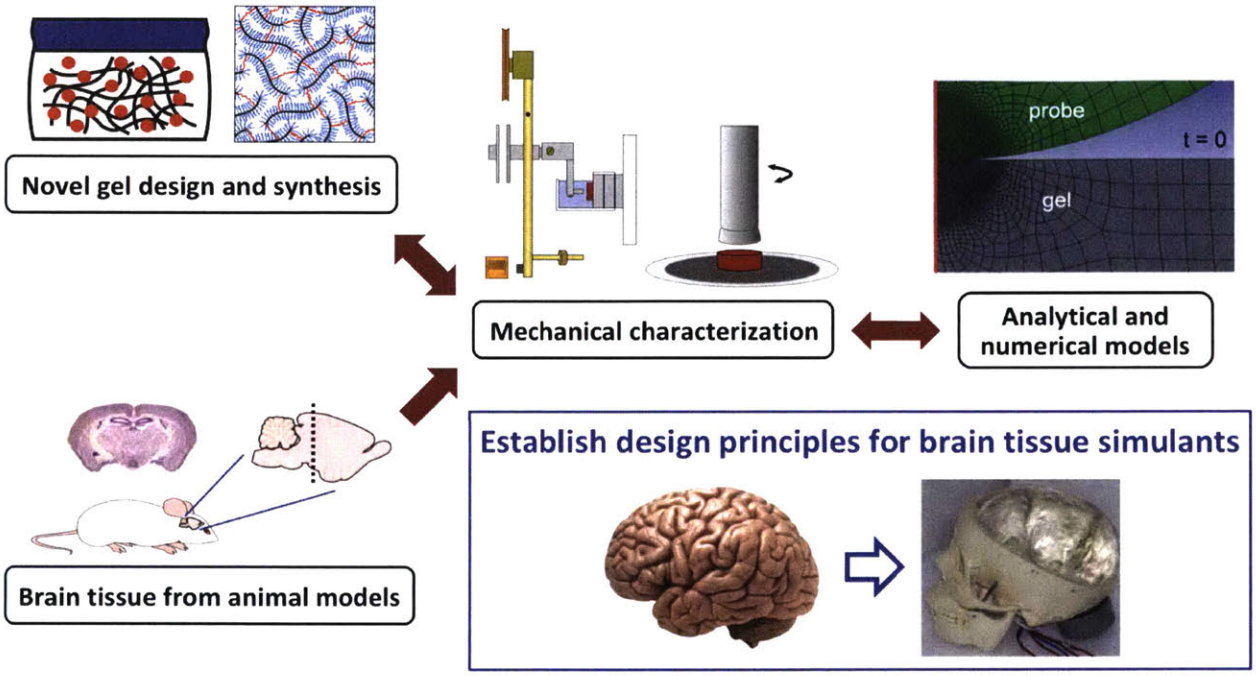

Figure 1-7 This thesis will detail the collection of brain tissues from various animal models, mechanical characterization of these tissues, synthesis and characterization of novel gels for comparison against brain tissue, and modeling approaches used to gain new insights on the mechanisms that govern the mechanical behavior of compliant materials, with the primary goal of establishing fundamental principles to inform the design of brain tissue simulants.

Chapter 1 introduced the motivation for this thesis research and included background on brain structure and composition at the tissue, cellular, and molecular level. A brief review on the efforts by others to characterize and model brain tissue mechanics was provided, highlighting the difficulties of quantifying the mechanical behavior of brain tissue accurately. Additionally, this chapter discussed the soft matter employed to date as soft tissue simulants, such as ballistic gelatin and ballistic clay, which are crude mechanical representations of brain tissue.

Chapter 2 describes the mechanical characterization of brain tissue obtained from various animal models, with a primary focus on measuring the response of brain tissue to concentrated mechanical impact events in fully hydrated conditions. This chapter first details the brain tissue procurement and sample preparation procedure for subsequent mechanical testing. Next, we discuss rigorously the methodology for the three characterization techniques – AFM-enabled indentation, oscillatory shear rheology, and impact indentation – that we employed to ensure sound comparisons among different brain tissue samples. This chapter concludes by comparing the measured impact response of healthy porcine and murine brain tissues, and demonstrating that species-to-species variation can be detected.

Chapter 3 presents an in depth study of the effects of demyelination, an important structural change observed during traumatic injury and neurological diseases, on the mechanical properties of brain tissue. We examine specifically a tuberous sclerosis (TSC) genetic mouse model of autism that has been shown previously to exhibit demyelination and abnormal axon morphology. This study compares the mechanical properties between TSC and healthy control brain tissue at multiple length- and time-scales of deformation using the three methods described in Chapter 2. Additionally, this chapter describes an immunohistochemical study, in which we fluorescently stain TSC and control brain tissue for fibronectin, a component of the ECM, to explore whether the structure and composition of the ECM is significantly altered in this disease model in ways that can potentially affect the brain tissue mechanics. We emphasize that the results presented in this chapter are reflective only of our TSC mouse model. Whether any mechanical differences can be detected in other animal models of autism or other disease models that also feature abnormal brain structure requires future investigation.

Chapter 4 examines two novel material systems as potential candidates for brain tissue simulants. Inspired by the hierarchical structure of actual biological tissues, we first study PDMS-based bilayered composite gels, which is a direct extension of the previous work on the PDMS organogels synthesized by the U.S. Army Research Laboratory. Using impact indentation, we investigate the enhanced tunability of the bilayer design to see whether we can leverage the key properties of each individual layer to optimize the impact response of the composite to match that of porcine brain tissue. In addition to examining this PDMS-based system, we also experimentally characterize the impact response of hierarchically structured protein-based hydrogels and compare to that of brain tissue. This chapter focuses on informing

the design of an environmentally stable and mechanically tunable tissue simulant gel that can accurately mimic the mechanical behavior of brain tissue under impact loading, specifically in terms of both the extent of deformation and energy dissipation.

Chapter 5 describes an in depth study of the role of surface adhesion on mechanical energy dissipation. Because the PDMS-based composites introduced in Chapter 4 are highly adhesive, we are interested in whether surface adhesion contributes significantly to the impact response that we measured or whether bulk viscous dissipation dominates. With a novel bilayered PDMS composite that is distinct from the one studied in Chapter 4, we demonstrate successful decoupling of surface adhesion and bulk viscoelasticity. We quantify the contributions from surface adhesion to the extent of energy dissipation relative to contributions from bulk viscous dissipation at various strain rates. To complement our experimental studies, we also develop a finite element model that implements adhesive contact and conduct parametric analysis studies. Together, the results from this chapter provide new insights on the underlying mechanisms of energy dissipation and their dependence on strain rate in compliant, adhesive polymer gels, which can inform the material design for diverse engineering applications, including ballistic testing and robotic surgery optimization.

Chapter 6 presents a new approach to analyze impact indentation data that enables direct measurement of viscoelastic mechanical properties of compliant materials. Previous impact indentation analyses were limited to quantifying empirical parameters, and thus significantly inhibited the practical utility of impact indentation. In this chapter, we first describe the theory behind this new analytical method. We then validate this method by quantitatively comparing the viscoelastic moduli and relaxation time constants measured via impact indentation to those measured via oscillatory shear rheology for various polymer gels and biological soft tissues. Throughout this chapter, we highlight the advantages of impact indentation over conventional techniques for very compliant materials like brain tissue that have been traditionally challenging to characterize mechanically with high accuracy and precision.

Finally, Chapter 7 concludes this thesis with a discussion of the most important findings of these studies and suggests several directions for future work in brain tissue mechanics and in design and characterization of synthetic simulant materials.

1.6 References

[1] J.D. Voss, J. Connolly, K.A. Schwab, and A.I. Scher, Update on the epidemiology of concussion/mild traumatic brain injury, *Current Pain and Headache Reports*, 2015, 19, 32.

[2] B. Roozenbeek, A.I. Maas, and D.K. Menon, Changing patterns in the epidemiology of traumatic brain injury, *Nature Reviews Neurology*, 2013, 9, 231-236.

[3] A.I. Maas, N. Stocchetti, and R. Bullock, Moderate and severe traumatic brain injury in adults, *Lancent Neurology*, 2008, 7, 728-741.

[4] M.L. Fackler, J.S. Surinchak, J.A. Malinowski, and R.E. Bowen, Bullet fragmentation: a major cause of tissue disruption, *Journal of Trauma-Injury Infection & Critical Care*, 1984, 24, 35.

[5] M.J. Thali, B.P. Kneubuehl, U. Zollinger, and R. Dirnhofer, The skin-skull-brain model: a new instrument for the study of gunshot effects, *Forensic Science International*, 2002, 125, 178-189.

[6] T.F. Juliano, A.M. Forster, P. Drzal, T. Weerasooriya, P. Moy, and M.R. VanLandingham, Multiscale mechanical characterization of biomimetic physical associating gels, *Journal of Materials Research*, 2006, 21, 2084-2092.

[7] J.C. Roberts, T.P. Harrigan, E.E. Ward, T.M. Taylor, M.S. Annett, and A.C. Merkle, Human head-neck computational model for assessing blast injury, *Journal of Biomechanics*, 2012, 45, 2899-2906.

[8] S. Misra, K.B. Reed, B.W. Schafer, K.T. Ramesh, and A. Okamura, Mechanics of flexible needles robotically steered through soft tissue, *The International Journal of Robotics Research*, 2010, 29, 1640-1660.

[9] N. Abolhassani, R. Patel, and M. Moallem, Needle insertion into soft tissue: a survey, *Medical Engineering and Physics*, 2007, 29, 413-431.

[10] N.V. Datla, B. Konh, M. Honarvar, T.K. Podder, A.P. Dicker, Y. Yu, and P. Hutapea, A model to predict deflection of bevel-tipped active needle advancing in soft tissue, *Medical Engineering and Physics*, 2014, 36, 285-293.

[11] P. Gomes, Reviewing the past, analysing the present, imagining the future, *Robotics and Computer-Integrated Manufacturing*, 2011, 27, 261-266.

[12] A.A. Sharp, A.M. Ortega, D. Restrepo, D. Curran-Everett, and K. Gall, In vivo penetration mechanics and mechanical properties of mouse brain tissue at micrometer scales, *IEEE Transactions on Biomedical Engineering*, 2009, 56, 45-53.

[13] R.E. Neuendorf, E. Saiz, A.P. Tomsia, and R.O. Ritchie, Adhesion between biodegradable polymers and hydroxyapatite: relevance to synthetic bone-like materials and tissue engineering scaffolds, *Acta Biomaterialia*, 2008, 4, 1288-1296.

[14] C. Correia, S. Bhumiratana, L.P. Yan, A.L. Oliveira, J.M. Gimble, D. Rockwood, D.L. Kaplan, R.A. Sousa, R.L. Reis, and G. Vunjak-Novakovic, Development of silk-based

scaffolds for tissue engineering of bone from human adipose-derived stem cells, *Acta Biomaterialia*, 2012, 8, 2483-2492.

[15] J.R. Porter, T.T. Ruckh, and K.C. Popat, Bone tissue engineering: a review in bone biomimetics and drug delivery strategies, *Biotechnology Progress*, 2009, 25, 1539-1560.

[16] S. Yang, K.F. Leong, Z. Du, and C.K. Chua, The design of scaffolds for use in tissue engineering. Part I. Traditional factors, *Tissue Engineering*, 2001, 7, 679-689.

[17] S.J Bryant and K.S. Anseth, Controlling the spatial distribution of ECM components in degradable PEG hydrogels for tissue engineering cartilage, *Journal of Biomedical Materials Research Part A*, 2003, 64, 70-79.

[18] W. Zhao, X. Jin, Y. Cong, Y. Liu, and J. Fu, Degradable natural polymer hydrogels for articular cartilage tissue engineering, *Journal of Chemical Technology and Biotechnology*, 2013, 88, 327-339.

[19] L. Zhang, S. Miramini, D.W. Smith, B.S. Gardiner, and A.J. Grodzinsky, Time evolution of deformation in a human cartilage under cyclic loading, *Annals of Biomedical Engineering*, 2015, 43, 1166-1177.

[20] D.E. Discher, P. Janmey, and Y.L. Wang, Tissue cells feel and respond to the stiffness of their substrate, *Science*, 2005, 310, 1139-1143.

[21] R.G. Wells, The role of matrix stiffness in regulating cell behavior, *Hepatology*, 2008, 47, 1394-1400.

[22] N.D. Leipzig and M.S. Schoichet, The effect of substrate stiffness on adult neural stem cell behavior, *Biomaterials*, 2009, 30, 6867-6878.

[23] Y. Sun, C.S. Chen, and J. Fu, Forcing stem cells to behave: a biophysical perspective of the cellular microenvironment, *Annual Review of Biophysics*, 2012, 41, 519-542.

[24] A.S. Zeiger, B. Hinton, and K.J. Van Vliet, Why the dish makes a difference: quantitative comparison of polystyrene culture surfaces, *Acta Biomaterialia*, 2013, 9, 7354-7361.

[25] A. Jagielska, A.L. Norman, G. Whyte, K.J. Van Vliet, J. Guck, and R.J.M. Franklin, Mechanical environment modulates biological properties of oligodendrocytes progenitor cells, *Stem Cells and Development*, 2012, 21, 2905-2914.

[26] D.E. Ingber, Mechanobiology and diseases of mechanotransduction, *Annals of Medicine*, 2003, 35, 564-577.

[27] A. Goriely, M.G. Geers, G.A. Holzapfel, J. Jayamohan, A. Jerusalem, S. Sivaloganathan, W. Squier, J.A. van Dommelen, S. Waters, and E. Kuhl, Mechanics of the brain: perspectives, challenges, and opportunities, *Biomechanics and Modeling in Mechanobiology*, 2015, 14, 931-965.

[28] M.C. Murphy, J. Huston, C.R. Jack, K.J. Glaser, A. Manduca, J.P Felmlee, and R.L. Ehman, Decreased brain stiffness in Alzheimer's disease determined by magnetic resonance elastography, *Journal of Magnetic Resonance Imaging*, 2012, 34, 494-498.

[29] J. Wuerfel, F. Paul, B. Beierbach, U. Hamhaber, D. Klatt, S. Papazoglou, F. Zipp, P. Martus, J. Braun, and I. Sack, MR-elastography reveals degradation of tissue integrity in multiple sclerosis, *NeuroImage*, 2010, 49, 2520-2525.

[30] K. Pogoda, L. Chin, P.C. Georges, F.J Byfield, R. Bucki, R. Kim, M. Weaver, R.G. Wells, C. Marcinkiewicz, and P.A. Janmey, Compression stiffening of brain and its effect of mechanosensing by glioma cells, *New Journal of Physics*, 2014, 16, 75002.

[31] K. Riek, J.M. Millward, I. Hamann, S. Mueller, C.F. Pfueller, F. Paul, J. Braun, C. Infante-Duarte, and I. Sack, Magnetic resonance elastography reveals altered brain viscoelasticity in experimental autoimmune encephalomyelitis, *NeuroImage: Clinical*, 2012, 1, 81-90.

[32] S. Nicolle, P. Vezin, and J.F. Palierne, A strain-hardening bi-power law for the nonlinear behaviour of biological soft tissue, *Journal of Biomechanics*, 2010, 43, 927-932.

[33] A.A. Zadpoor, Nanomechanical characterization of heterogeneous and hierarchical biomaterials and tissues using nanoindentation: the role of finite mixture models, *Materials Science and Engineering: C*, 2015, 48, 150-157.

[34] S. Budday, R. Nay, R. de Rooij, P. Steinmann, T. Wyrobek, T.C. Ovaert, and E. Kuhl, Mechanical properties of gray and white matter brain tissue by indentation, *Journal of the Mechanical Behavior of Biomedical Materials*, 2015, 46, 318-330.

[35] Q. Wen and D.B. Chklovskii, Segregation of the brain into gray and white matter: a design minimizing conduction delays, *PLoS Computational Biology*, 2005, 1, e78.

[36] J.S. O'Brien and E.L. Sampson, Lipid composition of the normal human brain: gray matter, white matter, and myelin, *Journal of Lipid Research*, 1965, 6, 537-544.

[37] J.N. Giedd, J. Blumenthal, N.O. Jeffries, F.X. Castellanos, H. Liu, A. Zijdenbos, T. Paus, A.C. Evans, and J.L. Rapoport, Brain development during childhood and adolescence: a longitudinal MRI study, *Nature Neuroscience*, 1999, 2, 861-863.

[38] Y. Ge, R.I. Grossman, J.S. Babb, M.L. Rabin, L.J. Mannon, and D.L. Kolson, Age-related total gray matter and white matter changes in normal adult brain. Part I: volumetric MR imaging analysis, *American Journal of Neuroradiology*, 2002, 23, 1327-1333.

[39] P. Morell and R.H. Quarles, Myelin formation, structure and biochemistry, G.J. Siegel, B.W. Agranoof, R.W. Albers, S.K. Fisher, M.D. Uhler (Eds.), *Basic Neurochemistry: Molecular, Cellular and Medical Aspects* (6^{th} ed.), Lippincott-Raven, Philadelphia, 2003, 69-94.

[40] C.F. Lucchinetti, W. Bruck, J.E. Parisi, B. Scheithauer, M. Rodriguez, and H. Lassman, Heterogeneity of multiple sclerosis lesions: implication for the pathogenesis of demyelination, *Annals of Neurology*, 2001, 47, 707-717.

[41] J. Weickenmeier, R. de Rooij, S. Budday, P. Steinmann, T.C. Ovaert, and E. Kuhl, Brain stiffness increases with myelin content, *Acta Biomaterialia*, 2016, 42, 265-272.

[42] J. Weickenmeier, R. de Rooij, S. Budday, P. Steinmann, T.C. Ovaert, and E. Kuhl, The mechanical importance of myelination in the central nervous system, *Journal of the Mechanical Behavior of Biomedical Materials*, 2017, 76, 119-124.

[43] E. Luders, P.M. Thompson, and A.W. Toga, The development of the corpus callosum in the healthy human brain, *The Journal of Neuroscience*, 2010, 30, 10985-10990.

[44] F. Aboitiz, A.B. Scheibel, R.S. Fisher, and E. Zaidel, Fiber composition of the human corpus callosum, *Brain Research*, 1992, 598, 143-153.

[45] D.B. Mendelsohn, H.S. Levin, H. Harward, and D. Bruce, Corpus callosum lesions after closed head injury in children: MRI, clinical features and outcomes, *Neuroradiology*, 1992, 34, 384-388.

[46] E.A. Wilde, Z. Chu, E.D. Bigler, J.V. Hunter, M.A. Fearing, G. Hanten, M.R. Newsome, R.S. Scheibel, X. Li, and H.S. Levin, Diffusion tensor imaging in the corpus callosum in children after moderate to severe traumatic brain injury, *Journal of Neurotrauma*, 2006, 23, 1412-1426.

[47] N. Evangelou, D. Konz, M.M. Esiri, S. Smith, J. Palace, and P.M. Matthews, Regional axonal loss in the corpus callosum correlates with cerebral white matter lesion volume and distribution in multiple sclerosis, *Brain*, 2000, 123, 1845-1849.

[48] R.O. Barnard and M. Triggs, Corpus callosum in multiple sclerosis, *Journal of Neurology, Neurosurgery & Psychiatry*, 1974, 37, 1259-1264.

[49] D.P. Richman, R.M. Stewart, J. Hutchinson, and V.S. Caviness Jr., Mechanical model of brain convolutional development, *Science*, 1975, 189, 18-21.

[50] T. Tallinen, J.Y. Chung, F. Rousseau, N. Girard, J. Lefevre, and L. Mahadevan, On the growth and form of cortical convolutions, *Nature Physics*, 2016, 12, 588-593.

[51] S. Herculano-Houzel, The human brain in numbers: a linearly scaled-up primate brain, *Frontiers in Human Neuroscience*, 2009, 3, 31.

[52] D.W. Howells, M.J. Porritt, S.S.J. Rewell, V. O'Collins, E.S. Sena, H.B. van der Worp, R.J. Traystman, and M.R. Macleod, Different strokes for different folks: the rich diversity of animal models for focal cerebral ischemia, *Journal of Cerebral Blood Flow & Metabolism*, 2010, 30, 1412-1431.

[53] E.C. Bush and J.M. Allman, The scaling of white matter to gray matter in cerebellum and neocortex, *Brain, Behavior and Evolution*, 2003, 61, 1-5.

[54] P. Sauleau, E. Lapouble, D. Val-Laillet, and C.H. Malbert, The pig model in brain imaging and neurosurgery, *Animal*, 2009, 3, 1338-1351.

[55] B. Pakkenberg and H.J.G. Gundersen, Total number of neurons and glial cells in human brain nuclei estimated by the disector and the fractionator, *Journal of Microscopy*, 1988, 150, 1-20.

[56] K.R. Jessen and R. Mirsky, Glial cells in the enteric nervous system contain glial fibrillary acidic protein, *Nature*, 1980, 286, 736-737.

[57] G.G. Somjen, Nervenkitt: notes on the history and concept of neuroglia, *Glia*, 1988, 1, 2-9.

[58] Y.B. Lu, K. Franze, G. Seifert, C. Steinhauser, F. Kirchhoff, H. Wolburg, J. Guck, P. Janmey, E. Wei, J. Kas, and A. Reichenbach, Viscoelastic properties of individual glial cells and neurons in the CNS, *Proceedings of the National Academy of Sciences of the United States of America*, 2006, 103, 17759-17764.

[59] K. Franze, P.A. Janmey, and J. Guck, Mechanics in neuronal development and repair, *Annual Review of Biomedical Engineering*, 2013, 15, 227-251.

[60] C. Nicholson and E. Sykova, Extracellular space structure revealed by diffusion analysis, *Trends in Neurosciences*, 1998, 21, 207-215.

[61] L.L. Kirkpatrick and S.T. Brady, Cytoskeleton of neurons and glia. In: G.J. Siegel, B.W. Arganoff, R.W. Albers, et al., editors, *Basic Neurochemistry: Molecular, Cellular, and Medical Aspects*, 6th edition, Philadelphia: Lippincott-Raven, 1999, Chapter 8.

[62] J. Howard, *Mechanics of Motor Proteins and the Cytoskeleton*, Sinaeur Associates, Inc., Sunderland, Massachusetts, 2001.

[63] E.R. Burnside and E.J. Bradbury, Review: manipulating the extracellular matrix and its role in brain and spinal cord plasticity and repair, *Neuropathology and Applied Neurobiology*, 2014, 40, 26-59.

[64] L.W. Lau, R. Cua, M.B. Keough, S. Haylock-Jacobs, and V.W. Yong, Pathophysiology of the brain extracellular matrix: a new target for remyelination, *Nature Reviews Neuroscience*, 2013, 14, 722-729.

[65] J. van Horssen, C.D. Dijkstra, and H.E. de Vries, The extracellular matrix in multiple sclerosis pathology, *Journal of Neurochemistry*, 2007, 103, 1293-1301.

[66] D. Bonneh-Barkay and C.A. Wiley, Brain extracellular matrix in neurodegeneration, *Brain Pathology*, 2009, 19, 573-585.

[67] J.A. van Dommelen, M. Hrapko, and G.W. Peters, Mechanical properties of brain tissue: characterization and constitutive modelling, *Mechanosensitivity of the Nervous System*, 2009, 2, 249-279.

[68] T.P. Prevost, A. Balakrishnan, S. Suresh, and S. Socrate, Biomechanics of brain tissue, *Acta Biomaterialia*, 2011, 7, 83-95.

[69] M. Hrapko, J.A. van Dommelen, G.W. Peters, and J.S. Wismans, The mechanical behavior of brain tissue: large strain response and constitutive modelling, *Biorheology*, 2006, 43, 623-636.

[70] A. Samadi-dooki, G.Z. Voyiadjis, and R.W. Stout, A combined experimental, modeling, and computational approach to interpret the viscoelastic response of white matter brain tissue during indentation, *Journal of the Mechanical Behavior of Biomedical Materials*, 2018, 77, 24-33.

[71] P.A. Janmey, P.C. Georges, and S. Hvidt, Basic rheology for biologists, *Methods in Cell Biology*, 2007, 83, 3-27.

[72] S. Nicolle, M. Lounis, R. Willinger, and J.F. Palierne, Shear linear behavior of brain tissue over a large frequency range, *Biorheology*, 2005, 42, 209-223.

[73] L.E. Bilston, Z. Liu, and N. Phan-Thien, Linear viscoelastic properties of bovine brain tissue in shear, *Biorheology*, 1997, 34, 377-385.

[74] K. Miller, *Biomechanics of the Brain*, Springer, New York, 2011.

[75] J.S. Ruan, T. Khalil, and A.I. King, Dynamic response of the human head to impact by three-dimensional finite element analysis, *Journal of Biomechanical Engineering*, 1994, 116, 44-50.

[76] L. Zhang, K.H. Yang, and A.I. King, Comparison of brain responses between frontal and lateral impacts by finite element modeling, *Journal of Neurotrauma*, 2001, 18, 21-30.

[77] C.E. Jamison, R.D. Marangoni, and A.A. Glaser, Viscoelastic properties of soft tissue by discrete model characterization, *Journal of Engineering for Industry*, 1968, 90, 239-247.

[78] Y.C. Fung, *Biomechanics: Mechanical Properties of Living Tissues*, 2nd edition, Springer, New York, 2013.

[79] D. Gutierrez-Lemini, *Engineering viscoelasticity*, Springer, New York, 2013.

[80] K. Miller and K. Chinzei, Mechanical properties of brain tissue in tension, *Journal of Biomechanics*, 2002, 35, 483-490.

[81] F. Shen, T.E. Tay, J.Z. Li, S. Nigen, P.V.S. Lee, and H.K. Chan, Modified Bilston nonlinear viscoelastic model for finite element head injury studies, *Journal of Biomechanical Engineering*, 2006, 128, 797-801.

[82] L.E. Bilston, Z. Liu, and N. Phan-Thien, Large strain behavior of brain tissue in shear: some experimental data and differential constitutive model, *Biorheology*, 2001, 38, 335-345.

[83] G. Low, S.A. Kruse, and D.J. Lomas, General review of magnetic resonance elastography, *World Journal of Radiology*, 2016, 8, 59-72.

[84] R. Muthupillai, D. Lomas, P. Rossman, J.F. Greenleaf, A. Manduca, and R.L. Ehman, Magnetic resonance elastography by direct visualization of propagating acoustic strain waves, *Science*, 1995, 269, 1854-1857.

[85] P.J. McCracken, A. Manduca, J.P. Felmlee, and R.L. Ehman, Mechanical transient-based magnetic resonance elastography, *Magnetic Resonance in Medicine*, 2005, 53, 628-639.

[86] I. Sack, B. Beierbach, U. Hamhaber, D. Klatt, and J. Braun, Non-invasive measurement of brain viscoelasticity using magnetic resonance elastography, *NMR in Biomedicine*, 2008, 21, 265-271.

[87] M.A. Green, L.E. Bilston, and R. Sinkus, In vivo brain viscoelastic mechanical properties measured by magnetic resonance elastography, *NMR in Biomedicine*, 2008, 21, 755-764.

[88] J. Vappou, E. Breton, P. Choquet, C. Goetz, R. Willinger, and A. Constantinesco, Magnetic resonance elastography compared with rotational rheometry for in vitro brain tissue viscoelasticity measurement, *Magnetic Resonance Materials in Physics, Biology and Medicine*, 2007, 20, 273-278.

[89] F. Velardi, F. Fraternali, and M. Angelillo, Anisotropic constitutive equations and experimental tensile behavior of brain tissue, *Biomechanics and Modeling in Mechanobiology*, 2006, 5, 53-61.

[90] S. Chatelin, A. Constantinesco, and R. Willinger, Fifty years of brain tissue mechanical testing: from in vitro to in vivo investigations, *Biorheology*, 2010, 47, 255-276.

[91] M. Ayyildiz, S. Cinoglu, and C. Basdogan, Effect of normal compression on the shear modulus of soft tissue in rheological measurements, *Journal of the Mechanical Behavior of Biomedical Materials*, 2015, 49, 235-243.

[92] G. Mattei, A. Tirella, G. Gallone, and A. Ahluwalia, Viscoelastic characterisation of pig liver in unconfined compression, *Journal of Biomechanics*, 2014, 47, 2641-2646.

[93] K.B. Arbogast, K.L. Thibault, B.S. Pinheiro, K.I. Winey, and S.S. Margulies, A high-frequency shear device for testing soft biological tissues, *Journal of Biomechanics*, 1997, 30, 757-759.

[94] A. Jaishankar, V. Sharma, and G.H. McKinley, Interfacial viscoelasticity, yielding and creep ringing of globular protein-surfactant mixtures, *Soft Matter*, 2011, 7, 7623-7634.

[95] R.H. Ewoldt, M.T. Johnston, and L.M. Caretta, Experimental challenges of shear rheology: how to avoid bad data, in S. Spagnolie (ed.), *Complex Fluids in Biological Systems*, Springer, New York, 2015, 207-241.

[96] J.A. van Dommelen, T.P.J. van der Sande, M. Hrapko, and G.W. Peters, Mechanical properties of brain tissue by indentation: interregional variation, *Journal of the Mechanical Behavior of Biomedical Materials*, 2010, 3, 158-166.

[97] B.S. Elkin, A. Ilankova, and B. Morrison, Dynamic, regional mechanical properties of the porcine brain: indentation in the coronal plane, *Journal of Biomechanical Engineering*, 2011, 133, 071009.

[98] A.F. Christ, K. Franze, H. Gautier, P. Moshayedi, J. Fawcett, R.J. Franklin, R.T. Karadottir, and J. Guck, Mechanical difference between white and gray matter in the rat cerebellum measured by scanning force microscopy, *Journal of Biomechanics*, 2010, 43, 2986-2992.

[99] Y. Feng, R.J. Okamoto, R. Namani, G.M. Genin, and P.V. Bayly, Measurements of mechanical anisotropy in brain tissue and implications for transversely isotropic material models of white matter, *Journal of the Mechanical Behavior of Biomedical Materials*, 2013, 23, 117-132.

[100] A. Gefen, N. Gefen, Q. Zhu, R. Raghupathi, and S.S. Margulies, Age-dependent changes in material properties of the brain and braincase of the rat, *Journal of Neurotrauma*, 2003, 20, 1163-1177.

[101] T.P. Prevost, G. Jin, M.A. de Moya, H.B. Alam, S. Suresh, and S. Socrate, Dynamic mechanical response of brain tissue in indentation in vivo, in situ and in vitro, *Acta Biomaterialia*, 2011, 7, 4090-4101.

[102] J.D. Finan, S.N. Sundaresh, B.S. Elkin, G.M. McKhann II, and B. Morrison III, Regional mechanical properties of human brain tissue for computational models of traumatic brain injury, *Acta Biomaterialia*, 2017, 55, 333-339.

[103] G. Thomas, N.A. Burnham, T.A. Camesano, and Q. Wen, Measuring the mechanical properties of living cells using atomic force microscopy. *Journal of Visualized Experiments*, 2013, 76, e50497.

[104] F. Liu and D.J. Tschumperlin, Micro-mechanical characterization of lung tissue using atomic microscopy. *Journal of Visualized Experiments*, 2011, 54, e2911.

[105] A. Peaucelle, AFM-based mapping of the elastic properties of cell walls: at tissue, cellular, and subcellular resolutions. *Journal of Visualized Experiments*, 2014, 89, e51317.

[106] S. Moreno-Flores, R. Benitez, M.D. Vivanco, and J.L. Toca-Herrera, Stress relaxation and creep on living cells with the atomic force microscope: a means to calculate elastic moduli and viscosities of cell components, *Nanotechnology*, 2010, 21, 445101.

[107] N. Desprat, A. Richert, J. Simeon, and A. Asnacios, Creep function of a single living cell, *Biophysical Journal*, 2005, 88, 2224-2233.

[108] H. Lu, B. Wang, J. Ma, G. Huang, and H. Viswanathan, Measurement of creep compliance of solid polymers by nanoindentation, *Mechanics Time-Dependent Materials*, 2003, 7, 189-207.

[109] Z.I. Kalcioglu, M. Qu, K.E. Strawhecker, T. Shazly, E. Edelman, M.R. VanLandingham, J.F. Smith, and K.J. Van Vliet, Dynamic impact indentation of hydrated biological tissues and tissue surrogate gels, *Philosophical Magazine*, 2011, 91, 1339-1355.

[110] Z.I. Kalcioglu, R.A. Mrozek, R. Mahmoodian, M.R. VanLandingham, J.L. Lenhart, and K.J. Van Vliet, Tunable mechanical behavior of synthetic organogels as biofidelic tissue simulants, *Journal of Biomechanics*, 2013, 46, 1583-1591.

[111] N.C. Nicholas and J.R. Welsch, *Ballistic Gelatin*, Institute for Non-Lethal Defense Technologies Report, Penn State Applied Research Laboratory, Happy Valley, PA, 2004.

[112] J.J. Amato, L.J. Billy, R.P. Gruber, N.S. Lawson, and N.M. Rich, Vascular injuries. An experimental study of high and low velocity missile wounds, *JAMA Surgery*, 1970, 101, 167-174.

[113] M.L. Frackler, Wound ballistics. A review of common misconceptions, *JAMA*, 1988, 259, 2730-2736.

[114] Y. Yoshikawa, T. Yasuike, A. Yagi, and T. Yamada, Transverse elasticity of myofibrils of rabbit skeletal muscle studied by atomic force microscopy, *Biochemical and Biophysical Research Communications*, 1999, 256, 13-19.

[115] M.L. Frackler, J.S. Surinchak, J.A. Malinowski, and R.E. Bowen, Bullet fragmentation: a major cause of tissue disruption, *Journal of Trauma Injury Infection and Critical Care*, 1984, 24, 35.

[116] Review of Department of Defense Test Protocols for Combat Helmets, Chapter 4: Combat Helmet Testing, Washington DC: National Academies Press, 2014.

[117] J.E. Seppala, Y. Heo, P.E. Stutzman, J.R. Sieber, C.R. Snyder, K.D. Rice, and G.A. Holmes, Characterization of clay composite ballistic witness materials, *Journal of Materials Science*, 2015, 50, 7048-7057.

[118] T.D. Edwards, E.D. Bain, S.T. Cole, R.M. Freeney, V.A. Halls, J. Ivancik, J.L. Lenhart, E. Napadensky, J.H. Yu, J.Q. Zheng, and R.A. Mrozek, Mechanical properties of silicone based composites as a temperature insensitive ballistic backing material for quantifying back face deformation, *Forensic Science International*, 2018, 285, 1-12.

[119] F.A. Andrade, H.A. Al-Qureshi, and D. Hotza, Measuring the plasticity of clays: a review, *Applied Clay Science*, 2011, 51, 1-7.

[120] C. Hernandez, M.F. Buchely, and A. Maranon, Dynamic characterization of Roma Plastilina No. 1 from drop test and inverse analysis, *International Journal of Mechanical Sciences*, 2015, 100, 158-168.

[121] S.K. Patel, S. Malone, C. Cohen, J.R. Gillmor, and R.H. Colby, Elastic modulus and equilibrium swelling of poly(dimethylsiloxane) networks, *Macromolecules*, 1992, 25, 5241-5251.

[122] L.E. Roth, D.A. Vega, E.M. Valles, and M.A. Villar, Viscoelastic properties of networks with low concentration of pendant chains, *Polymer*, 2004, 45, 5923-5931.

[123] R.A. Mrozek, P.J. Cole, K.J. Otim, K.R. Shull, and J.L. Lenhart, Influence of solvent size on the mechanical properties and rheology of polydimethylsiloxane-based polymeric gels, *Polymer*, 2011, 52, 3422-3430.

Chapter 2: Characterization of brain tissue mechanical properties

2.1 Introduction

To design novel protection strategies that mitigate traumatic brain injuries, it is essential to first characterize the behavior of brain tissue under various external mechanical loads. Measurement of the deformation and energy dissipation metrics of brain tissue will provide a target response for the development of synthetic simulant materials intended to mechanically mimic brain tissue. Additionally, detailed understanding of brain tissue mechanics is needed to deduce better constitutive models, which will ultimately enable the prediction of brain injury severity computationally. However, accurate mechanical characterization of brain tissue remains a challenge largely because brain is one of the most compliant organs in the body and exhibits heterogeneous, hierarchical structure that gives rise complex mechanical behavior [1-7]. Although the mechanical properties of brain tissue have been studied for many years, the reported moduli in the literature may vary by several orders of magnitude and are thus difficult to reconcile [8]. This variation has been attributed to several inconsistencies in experimental protocols, namely the species or age of the specimens (human, porcine, bovine, or murine; infant or adult), regions tested within the brain tissue (white or gray matter), loading configurations (tension, compression, shear, or indentation), loading histories (cyclic, impact, creep, or stress relaxation), and test regime (small or large strains; low or high strain rates) [8,9]. Therefore, part of this thesis aims to systematically investigate the multiscale mechanical properties of brain tissue obtained from various sources through using multiple *in vitro* characterization methods.

This chapter first presents details on the procurement of various brain tissues and preparation of these tissue samples for subsequent mechanical testing (Section 2.2). Next, Section 2.3 introduces the three characterization techniques – AFM-enabled indentation, oscillatory shear rheology, and impact indentation – that were employed to measure the mechanical properties of brain tissue at multiple length- and time-scales of deformation. Note that this chapter primarily focuses on adapting the impact indentation method to characterize how brain tissue responds to concentrated mechanical impacts, which will be important in the future design of brain tissue simulant materials for ballistic testing applications. Section 2.4 examines and compares the impact response of brain tissue obtained from three different healthy animal models to examine

potential species-to-species variation. The methods and analyses described here will be further utilized in all subsequent chapters.

Much of the methodology discussed in this chapter was published in *Journal of Visualized Experiments* and *Journal of Biomechanical Engineering* as the result of a collaboration between the Van Vliet Laboratory for Material Chemomechanics at MIT and the laboratory of Dr. Mustafa Sahin at Boston Children's Hospital and Harvard Medical School [10,11]. Elyza Kelly and Daria Turner (Sahin group) handled the breeding of mouse populations and acquisition of mouse brain tissues according to approved protocols. Dr. Elizabeth Canovic (Van Vliet group), with the assistance of Dr. Anna Jagielska and Dr. Matt Whitfield (Van Vliet group), conducted the AFM-enabled indentation experiments and developed analysis codes to quantify elastic and viscoelastic mechanical properties. Aleksandar Mijailovic (Van Vliet group) assisted with the acquisition of pig brain tissue and conducted a significant portion of the rheological experiments. The impact indentation studies described in Section 2.4 were published in *Molecular Systems Design & Engineering* [12].

2.2 Brain tissue procurement and preparation

Whole brains were harvested from three rodent models (healthy adult rat, healthy infant mouse, and diseased infant mouse) and one porcine model (healthy adult pig). The only animal disease model investigated in this work was a genetic mouse model of tuberous sclerosis/autism spectrum disorder (TSC/ASD). More details regarding this TSC/ASD mouse model will be discussed in Chapter 3. A total of three rat brains, fifty-one mouse brains, and eight pig brains were collected from the Division of Comparative Medicine at MIT, Boston Children's Hospital, and a local stockyard in Massachusetts, respectively. All experiments that involved animals followed the University IACUC protocol and NIH guidelines for the care and use of laboratory animals.

After excision, whole brains were sectioned in preparation for mechanical characterization. Each characterization technique that was employed required specific sample geometries and thus distinct slicing procedures. For AFM-enabled indentation, the cerebellum was first removed from the brain using a razor blade. The brain was then mounted in a vibratome so that 350 μm thick coronal sections can be cut. Further details regarding the vibratome settings that enabled

such thin brain tissue sections to be sliced can be found in Appendix A. For oscillatory shear rheology, mouse brains were sliced into 1 mm thick coronal sections with the vibratome, while pig brains were sliced into 6 mm thick sections. Because pig brain is significantly larger in size compared to mouse brain, a larger diameter measurement plate was used to probe the pig brain tissue, allowing for thicker samples that were more straightforward to slice. For impact indentation, whole brains were sliced into several sections of 6 mm thickness along both the coronal and sagittal plane. Dual razor blades were used with careful lateral motions to achieve brain tissue sections with flat and parallel surfaces. Examples of the different mounted tissue samples after slicing and immediately prior to mechanical characterization are shown in Fig. 2-1.

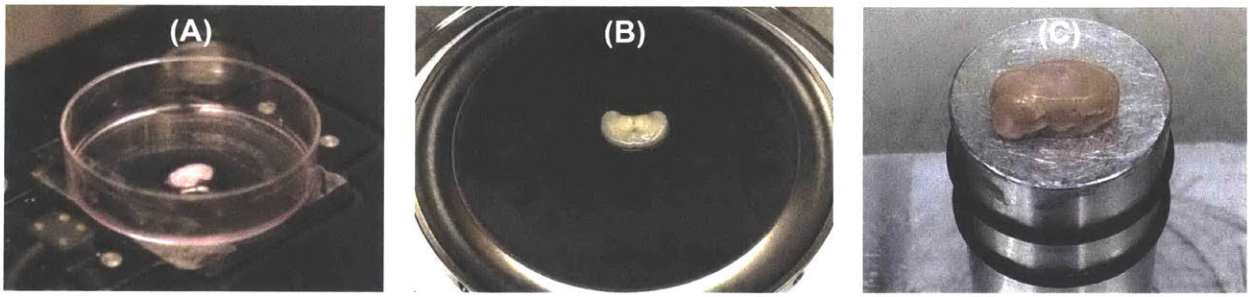

Figure 2-1 Representative images of mouse brain tissue slices prepared for mechanical testing. (A) 350 μm thick coronal slice mounted in a Petri dish using Cell-Tak (Corning®) for AFM-enabled indentation. (B) 1 mm thick coronal slice placed on the bottom measurement plate of the rheometer. (C) 6 mm thick brain tissue sliced along the sagittal plane and adhered to the impact indentation sample post using a thin layer of low-viscosity cyanoacrylate adhesive (Loctite® 4013). Photos were taken before the tissue samples were immersed in medium.

If necessary, tissue samples were immediately stored in Hibernate®-A, a CO_2-independent nutrient medium for adult neural tissue, on ice. All subsequent characterization experiments were conducted with the tissues immersed in the same medium, as the mechanical properties of tissue depend strongly on their hydration state [13,14]. Measurements were taken at either room temperature or physiological temperature (37°C). The total post-mortem time elapsed between animal death and mechanical characterization of the prepared brain tissue slices varied between 3 and 48 h. Over this duration, the brain slices maintained their structural integrity, and the measured mechanical properties did not vary detectably.

2.3 Characterization techniques

This section describes three experimental techniques that we employed to characterize the multiscale mechanical properties of brain tissue *in vitro*. Details of the data analysis and the unique limitations of each method will be discussed.

2.3.1 AFM-enabled indentation

2.3.1.1 Methods

All AFM-enabled indentation experiments on brain tissue were conducted on an MFP-3D atomic force microscope (Asylum Research) using a silicon-nitride cantilever with a nominal spring constant of 0.03 N/m and an attached 20 μm diameter borosilicate bead (Novascan). Note that this was the lowest cantilever stiffness commercially available for that probe geometry. Measurements were conducted on tissue fully immersed in Hibernate®-A media, and temperature was maintained at 37°C using the stage-mounted heater. A schematic of the AFM experimental setup is illustrated in Fig. 2-2.

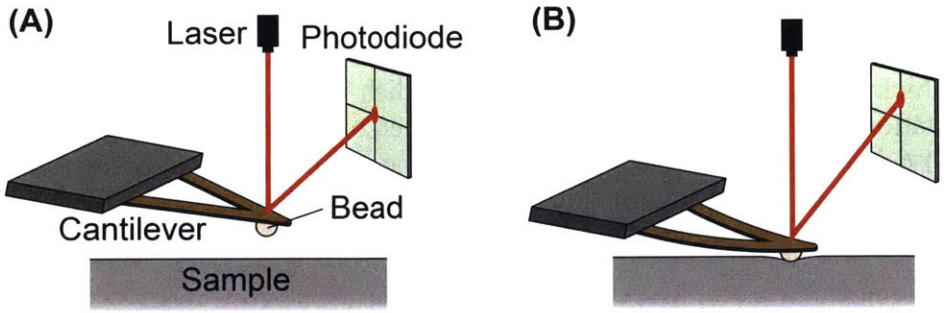

Figure 2-2 (A) AFM-enabled indentation is conducted using a flexible cantilever of specified spring constant comparable to sample stiffness and with a spherical bead of nano- to microscale radius attached to the free-end. (B) During indentation, cantilever deflection is measured using a laser reflected off the end of the cantilever and onto a photodiode. From [10].

AFM-enabled indentation is used typically to measure the effective Young's elastic modulus E of a sample [15-17]. For each tissue sample, force vs. depth responses (F-δ) were obtained. Samples were indented nominally to a depth of 4 μm at an indentation velocity of 4 μm/s, which were maximum depths and velocities similar to those in previous AFM mechanical studies on brain tissue [18]. From the F-δ response, the contact point was determined using an algorithm

described by Lin et al. [19]. An example of a typical F-δ response obtained via AFM-enabled indentation on murine brain tissue is shown in Fig. 2-3. Elastic modulus E was calculated according to the model derived by Oliver and Pharr for an incompressible material indented with a spherical probe of radius R = 10 μm [20-22]. Herbert et al. previously detailed the application of the Oliver-Pharr model for a spherical indenter [22]. This model, which analyzes the unloading response, was chosen over the more frequently used Hertzian analysis to account for inelastic deformation of the sample, as demonstrated by the hysteresis between the approach and retract curves from the F-δ responses (Fig. 2-3).

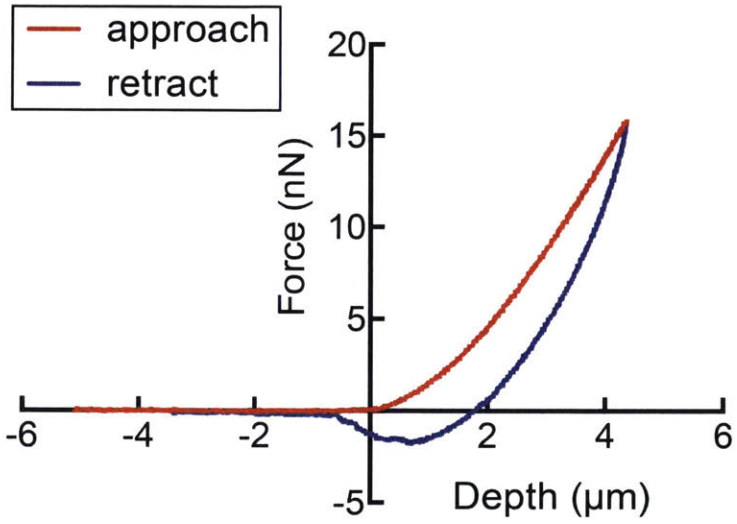

Figure 2-3 Typical force-depth response measured using AFM-enabled indentation for healthy murine brain tissue. Red represents the loading response, while blue represents the unloading response. Due to the hysteresis observed upon unloading, the Oliver-Pharr method, which analyzes the unloading response to determine mechanical properties, was used to calculate the effective Young's elastic modulus. From [11].

Additionally, the same AFM can be used to measure viscoelastic (time- or rate-dependent) properties of brain tissue through creep compliance or stress relaxation experiments [23-27]. In creep compliance experiments, the tissue was indented to a set force, and deformation was measured over time as it increased to obtain indentation depth vs. time responses (δ-t) (Fig. 2-4(A)). Idealizing the tissue as incompressible, creep compliance $J_C(t)$ was calculated from the solution derived by Lee and Radok [28]:

$$J_C(t) = \frac{16\sqrt{R}}{3F_0}\delta^{3/2}(t). \quad (2\text{-}1)$$

The maximum applied force F_0 was nominally 5 nN, though the exact applied force had to be determined by the product of the calculated cantilever stiffness and deflection. The time required to ramp to this set force was approximately 0.5 s. $J_C(t)$ was fit to a standard linear solid spring-dashpot model (spring in parallel with a Maxwell element) to obtain the long-term equilibrium shear modulus G_∞, short-term instantaneous shear modulus G_0, and creep relaxation time τ_c:

$$J_C(t) = \frac{1}{G_\infty} - \left(\frac{G_0 - G_\infty}{G_0 G_\infty}\right) e^{-\frac{t}{\tau_C}}. \tag{2-2}$$

In stress relaxation experiments, the tissue was indented to a specified cantilever base displacement corresponding to a maximum measured indentation depth, and force was measured as it decreased or relaxed over time. Force vs. time responses (F-t) were obtained with a nominal indentation depth δ_0 = 3 μm (Fig. 2-4(B)). The time needed to reach this set displacement was approximately 0.2 s. Shear relaxation modulus $G_R(t)$ was calculated using the solution derived by Lee and Radok [28]:

$$G_R(t) = \frac{3}{16\sqrt{R}\delta_0^{3/2}} F(t). \tag{2-3}$$

$G_R(t)$ was also fit to the standard linear solid model to obtain viscoelastic moduli and the relaxation time τ_r:

$$G_R(t) = G_\infty + (G_0 - G_\infty) e^{-\frac{t}{\tau_r}}. \tag{2-4}$$

The creep relaxation time τ_c can be related to the relaxation time τ_r by:

$$\tau_r = \frac{G_\infty}{G_0} \tau_c. \tag{2-5}$$

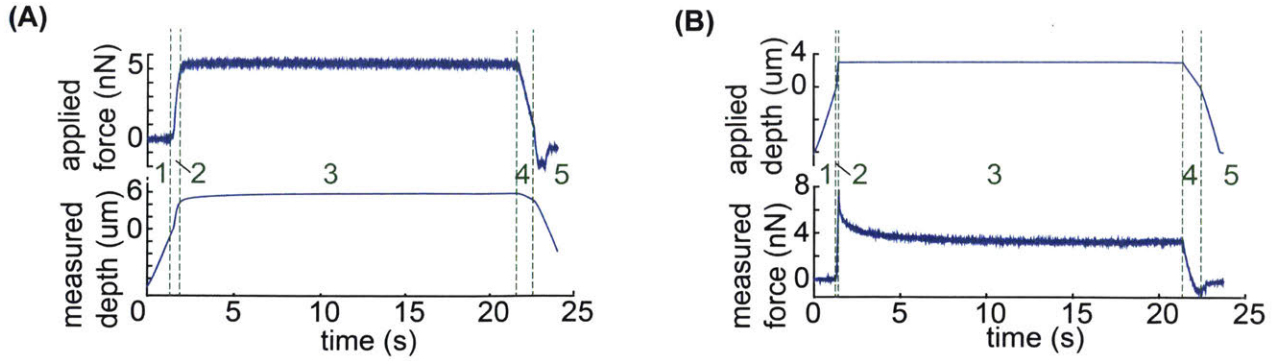

Figure 2-4 (A) Creep compliance measures the changing indentation depth of the cantilever with a constant applied force. (B) Stress relaxation measures the force as it decays with respect to time when a constant indentation depth is applied. Both (A) and (B) have been divided into five regions (green text): (1) approach of the AFM probe to the sample surface, (2) contact with sample and ramp up to a setpoint indentation depth or force, (3) maintenance of the setpoint indentation depth or force, (4) ramp down, and (5) retraction of the AFM probe from the sample surface. From [10].

By only assuming that the material is linear viscoelastic and isotropic, Lakes et al. have demonstrated that the shear relaxation function $G(t)$ and Young's relaxation function $E(t)$ may be related in the frequency domain by:

$$\bar{E}(s) = 2\bar{G}(s)(1 + s\bar{\nu}(s)), \tag{2-6}$$

where $\bar{E}(s)$, $\bar{G}(s)$, and $\bar{\nu}(s)$ are the Laplace transformed Young's relaxation function, shear relaxation function, and Poisson's ratio, respectively; s is complex frequency [29]. If $\bar{\nu}(s)$ is assumed to be constant ν and incompressible ($\nu = 0.5$), as is assumed frequently for hydrated biological soft tissues [30,31], Equation 2-6 may be rewritten in the time domain as:

$$E(t) = 2G(t)(1 + \nu) = 3G(t)\,, \tag{2-7}$$

It follows that the equilibrium Young's modulus E_∞ and instantaneous Young's modulus E_0 are:

$$E_\infty = 3G_\infty, \tag{2-8}$$

$$E_0 = 3G_0. \tag{2-9}$$

2.3.1.2 Discussion

AFM-enabled indentation is a technique with high spatial resolution (nanometer to micrometer length scales), enabling measurement of mechanical properties of anatomically distinct areas of the brain, such as the white and gray matter regions of the corpus callosum and cortex, respectively, or of individual neurites grown in cell culture. While there are other techniques for measuring microscale mechanical properties of biological specimens, including magnetic twisting cytometry, optical tweezers, and microrheology, these techniques have not been successfully used on tissue samples due in part to the relatively strong scattering of light within semi-opaque tissues. However, AFM-enabled indentation also confers unique limitations, especially if probing highly compliant, anisotropic, nonlinear, and viscoelastic materials such as brain tissue.

One key limitation of using AFM cantilevers to extract unknown moduli of new samples is that the stiffness or spring constant of the cantilever should ideally match the contact stiffness of the probed sample [32]. Measurement accuracy in calculated moduli is thus facilitated by choice of cantilever stiffness, but this becomes an issue for samples as compliant as brain tissue. Additionally, spherical probes with large diameter are preferred when characterizing brain tissue in order to apply lower strains such that assumptions of the material constitutive behavior are more accurate [33,34]. Larger probe geometries, however, are more difficult for cantilevers with low spring constants to support due in part to the weight of the large colloidal spherical probes. The cantilever stiffness used in our studies (0.03 N/m) and other AFM-indentation studies in the literature is considerably high compared to the contact stiffness of brain tissue, but more compliant cantilevers are unavailable commercially for our required probe geometries. Hence, the internal resistance of the cantilever/instrument is the dominant contributor providing resistance to deformation rather than the resistance of the tissue sample, which would ultimately affect the accuracy of estimated moduli computed from the unloading stiffness.

When conducting creep compliance or stress relaxation experiments to estimate viscoelastic mechanical properties, it is important to note that the experimentally applied load and indentation depth are not ideal (instantaneous) step functions. Loads and indentation depths are applied over short timescales (<1 sec), and these loading histories can affect the measured creep and relaxation responses [25,35]. Specifically, assuming an applied step indentation results in slight underestimation of the relaxation modulus, while assuming an applied step load results in slight

overestimation of the creep compliance. This limitation also holds true for creep compliance and stress relaxation experiments conducted with techniques other than AFM-enabled indentation, although the instrument timescale resolution may differ. The discrepancies between the actual and calculated mechanical properties will decrease as the ramp rates of the applied loads and indentation increase. Ultimately, these non-ideal step functions of applied load or displacement will lead to inaccuracies in the measured short timescale or "instantaneous" behavior but will not influence the long timescale or equilibrium behavior of the material.

Like with all characterization techniques, the data analysis of AFM-enabled indentation requires assumptions of the material constitutive behavior (e.g., linear elastic, linear viscoelastic, or elastically isotropic), sample geometry (e.g., semi-infinite half-plane), and material microstructure (e.g., homogeneous) that may potentially affect the accuracy of the magnitudes of extracted mechanical properties. Despite the limitations of these assumptions and the limitations of the instrumentation, AFM-enabled indentation remains a valuable technique for probing the elastic and viscoelastic response of brain tissue, and specifically for facilitating the comparison of mechanical properties between sample groups that are known to exhibit distinct structural or functional differences. All experimental parameters should be designed to enable sound, systematic comparison to address the question at hand.

2.3.2 Oscillatory shear rheology

2.3.2.1 Methods

Rheological experiments were conducted using a parallel plate rheometer (MCR 501, Anton-Paar) at 25°C with a plate diameter of 10 mm or 25 mm and a torque limit of 0.5 μN-m. Sandpaper (320 grit, McMaster Carr) was adhered to the top and bottom rheometer plates to minimize slip between the plates and brain tissue. Contact between the top measurement plate and brain tissue was determined to have occurred when the force transducer maintained a normal force of 0.01 N after a relaxation period of 5 min. After contact, the tissue was hydrated using Hibernate®-A media, and a thermal hood was placed over the sample to minimize evaporation. As illustrated in Fig. 2-5, a harmonic angular strain (and corresponding shear strain) is applied at known amplitudes and frequencies, and the reactional torque (and corresponding shear stress) is measured.

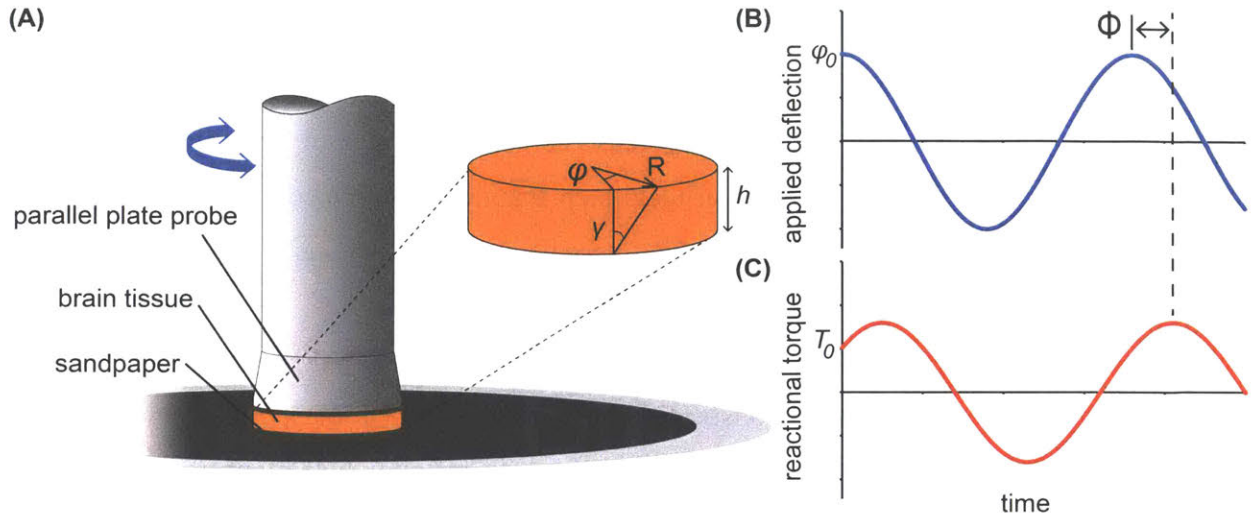

Figure 2-5 (A) Schematic of parallel plate rheometer setup for characterization of brain tissue and definitions related to applied oscillatory shear strain. (B) Representative applied strain (or deflection) and (C) resulting stress (or torque) as a function of time. Shear storage modulus G' and shear loss modulus G'' are calculated via the strain amplitude φ_0, torque amplitude T_0, phase lag Φ, probe and sample radius R, and sample height h. From [10].

Amplitude sweeps were conducted at 1 and 10 rad/s, and the linear viscoelastic limit was measured to be approximately 1-3% shear strain. Frequency sweeps were performed at 1% shear strain in the frequency range of 0.1 to 40 rad/s. Shear storage moduli G' and loss moduli G'' were calculated as a function of frequency via software within the Anton-Paar instrument using the radius of the plate R, height of the sample L, amplitude of the applied angular displacement ϕ_0, measured torque T_0, and phase lag φ:

$$G' = \frac{2L}{\pi R^4}\frac{T_0}{\phi_0}\cos\varphi, \tag{2-10}$$

$$G'' = \frac{2L}{\pi R^4}\frac{T_0}{\phi_0}\sin\varphi. \tag{2-11}$$

The measured G' and G'' at different frequencies can be converted to a Prony series:

$$G'(\omega) = G_\infty + \sum_{j=1}^{N}\frac{G_j\omega^2\tau_j^2}{1+\omega^2\tau_j^2}, \tag{2-12}$$

$$G''(\omega) = \sum_{j=1}^{N}\frac{G_j\omega\tau_j}{1+\omega^2\tau_j^2}, \tag{2-13}$$

where ω is frequency, N is the number of Maxwell elements, and G_j and τ_j are the elastic components and relaxation times associated with the Maxwell elements, such that:

$$G_0 = G_\infty + \sum_{j=1}^{N} G_j. \tag{2-14}$$

A constrained nonlinear least squares optimization scheme in MATLAB was used to determine the number of Maxwell elements (Section 1.3.2) needed to produce a good fit to the rheological data. G_∞ and G_0 can be converted to E_∞ and E_0 as mentioned previously in Section 2.3.1.1.

2.3.2.2 Discussion

Oscillatory shear rheology measures the frequency-dependent mechanical properties of viscoelastic materials on the macroscale level or based on the deformation of entire brain tissue sections. The shear moduli components, G' and G'', can be obtained in frequency ranges typically spanning 0.001-0.1 rad/sec to 10-100 rad/sec, depending on the instrument, probe geometry, and sample [31]. For accurate measurement, an amplitude sweep should be performed prior to a frequency sweep to determine the linear viscoelastic range of the material; this is the range of strain for which G' and G'' remain constant [36,37]. The shear strain chosen for the frequency sweep should be as high as possible within the linear viscoelastic range (typically 1-2% shear strain) such that sufficient torque is achieved during measurement. The torque during measurements should always be in the allowable range provided by the manufacturer to ensure a sufficient signal to noise ratio.

Additionally, the measurement probe – typically a parallel plate for brain tissue mechanical studies – should be as large in diameter as possible to maximize the torque, but must overlay with the sample completely [31]. This creates potential problems when examining brain tissue from certain animal models, such as mouse, due to the small size of sectioned mouse brain (diameter < 10 mm). In preparing the sample, the tissue should be sliced as flat as possible to minimize stress gradients during contact detection. When contact is made between the top plate and sample, the tissue should not have any water droplets on it to minimize slip at that interface. However, the tissue also must not be dried out prior to or during characterization as this will degrade the tissue structure and ultimately affect the measured mechanical properties [13,14]. The tissue should be fully hydrated with the appropriate media immediately after contact

between both plates. Adhesive, waterproof sandpaper may also be attached to the plates to minimize slip [38].

Although many studies of viscoelastic materials traditionally employ oscillatory shear rheology, one significant limitation of this technique is the inability to accurately detect initial contact with the sample surface of highly compliant materials like brain tissue. Accurate contact detection becomes extremely challenging for materials of very low stiffness (< 10 kPa), due in part to limited signal-to-noise sensitivity of commercial force transducers and to the inertia and finite compliance of the instrument load frame. Axial compression has been shown to alter the magnitude of G' of soft tissue, including brain and liver tissue [39-42]. Since rheology samples are typically thin (~1 to 5 mm), small changes in height (100s of μm) may produce large compressive strains (e.g., ~10%), and therefore significant changes in the measured shear modulus. Moreover, as the sample is viscoelastic, the material will undergo stress relaxation due to axial compression [38], which may affect measurements. Therefore, repeated measurements should be performed at similar operating axial strains, and the sample should be allowed to relax (e.g., 5-10 min) prior to characterization. Despite the errors associated with pre-strain or pre-stress, slight axial compression in rheology is actually necessary to minimize slip. Unfortunately, for brain tissue, it is very difficult to precisely control the amount of sample compression prior to the initiation of the experiment.

Shear rheology is also constrained by a maximum measurable frequency due to instrument limitations, such as frame inertia upon reversal of shearing displacement, making the high frequency or "instantaneous" response challenging to measure. While time-temperature superposition may be used to widen the accessible frequency or timescale and thus approach the high frequency or short timescale response [43], this method is limited in measuring high frequency response (i.e., low temperatures) of hydrated biological tissues since they will freeze at low temperatures. Additional limitations of macroscale shear rheology include stringent constraints for the sample geometry and lack of spatial resolution, which can be important when investigating heterogeneous, hierarchically structured materials like brain tissues. Nonetheless, oscillatory shear rheology provides another tool to study the viscoelastic mechanical properties of brain tissue at discrete frequencies or time-scales of deformation and at larger length scales compared to AFM-enabled indentation.

2.3.3 Impact indentation

2.3.3.1 Methods

To characterize and compare the dynamic response of brain tissues and polymer gels under spatially concentrated impact loading, impact indentation experiments were conducted using a pendulum-based instrumented indenter (Micro Materials Ltd., NanoTest Vantage). The experimental configuration is illustrated in Fig. 2-6(A), highlighting the ability to conduct impact tests in fully hydrated conditions [44]. Full details on transforming the default experimental setup to the configuration required for impact indentation on highly compliant materials is described in Appendix B. Electromagnetic interactions between a conductive coil at the top of the pendulum and a stationary magnetic plate behind the coil (not shown) apply the load, causing the pendulum to move about a frictionless pivot. The parallel plate capacitor measures indenter displacement as the pendulum moves. Activating the solenoid causes the pendulum to swing back and maintain its position. After the electromagnetic coil current increases to the desired amount, deactivating the solenoid releases the "loaded" pendulum such that the probe swings into the tissue sample at an impact velocity that increases with increasing electromagnetic coil current (stored energy).

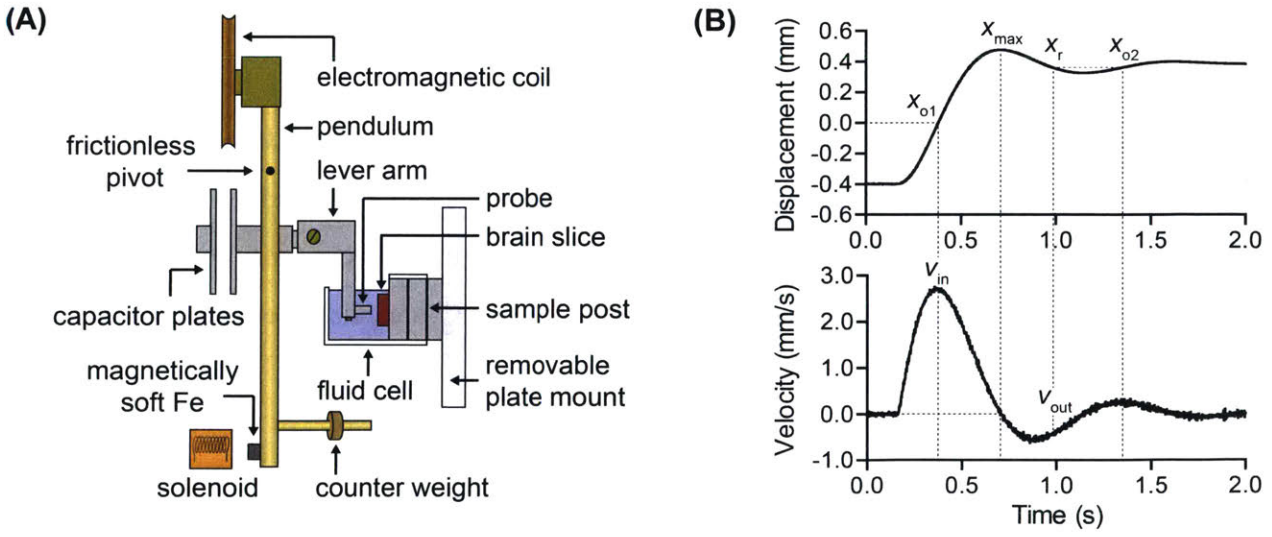

Figure 2-6 (A) Schematic of pendulum-based instrumented indenter used to conduct impact indentation experiments on brain tissues and simulant gel candidates in fully immersed environments. (B) Representative probe displacement profile as a function of time collected from a mouse brain slice and the corresponding velocity profile. Raw data can be analyzed to extract impact energy dissipation response parameters including maximum penetration depth x_{max}, energy dissipation capacity K, and dissipation quality factor Q. From [10,12].

During the impact process, probe displacement is recorded over time and can be described by a damped harmonic oscillation. An example of the raw displacement profile obtained for a mouse brain tissue slice is illustrated in Fig. 2-6(B). With this raw displacement profile and the corresponding velocity profile, we can compute key impact energy dissipation response parameters such as the maximum penetration depth x_{max}, energy dissipation capacity K, and dissipation quality factor Q using customized MATLAB scripts [45,46]. To quantify x_{max}, we must first determine the impact velocity $v_{in,}$ which is the maximum probe velocity immediately prior to contact and thus defines the contact position x_0. After setting the displacement profile relative to the contact position, we calculate x_{max} as the deformation at which the probe velocity first decreases to zero. The calculation of K is less straightforward because we need to account for the inherent damping of the pendulum itself [47,48]. We define K as the energy dissipated by the sample E_d^s normalized by the sum of dissipated and restored sample energies ($E_d^s + E_r^s$) in the first impact cycle:

$$K = \frac{E_d^s}{E_d^s + E_r^s} \tag{2-15}$$

The total energy of the system is calculated as:

$$E_t^{system} = \frac{1}{2}mv_{in}^2 = E_r^s + E_r^p + E_d^s + E_d^p \tag{2-16}$$

where m is the effective pendulum mass, E_r^p is the energy restored by the pendulum at its minimum rebound velocity v_{out}, and E_d^p is the energy dissipated by the pendulum. Note that the subscripts r and d denote restored and dissipated energies, respectively, and the superscripts s and p denote the sample and pendulum, respectively. E_r^p and E_d^p are calculated as follows:

$$E_r^p = \frac{1}{2}k_p(x_{max} - x_r)^2 \tag{2-17}$$

$$E_d^p = \int_{x_0}^{x_{max}} b_p \frac{\partial x}{\partial t} dx + \int_{x_{max}}^{x_r} b_p \frac{\partial x}{\partial t} dx \tag{2-18}$$

where k_p is the rotational stiffness of the pendulum, b_p is the pendulum damping coefficient, and x_r is the displacement at v_{out}. Lastly, we can relate the total recovered energy at v_{out} to the sum of E_r^s and E_r^p:

$$\frac{1}{2}mv_{\text{out}}^2 = E_{\text{r}}^{\text{s}} + E_{\text{r}}^{\text{p}} \tag{2-19}$$

Equations 2-16 through 2-19 can be combined and substituted into Equation 2-15 to formally calculate K as follows:

$$K = \frac{\frac{1}{2}m(v_{\text{in}}^2 - v_{\text{out}}^2) - \int_{x_0}^{x_{\max}} b_p \frac{\partial x}{\partial t} dx - \int_{x_{\max}}^{x_{\text{r}}} b_{\text{p}} \frac{\partial x}{\partial t} dx}{\frac{1}{2}mv_{\text{in}}^2 - \frac{1}{2}k_{\text{p}}(x_{\max} - x_{\text{r}})^2 - \int_{x_0}^{x_{\max}} b_p \frac{\partial x}{\partial t} dx - \int_{x_{\max}}^{x_{\text{r}}} b_{\text{p}} \frac{\partial x}{\partial t} dx} \tag{2-20}$$

To determine the third energy dissipation parameter Q, which is directly related to how quickly the sample dissipates the impact energy, we fit an exponential decay function to the peaks of the probe displacement as a function of time profile. The dimensionless quantity Q is defined as the product between π and the number of impact cycles required for the oscillation amplitude to decay by a factor of e. Therefore, a larger magnitude of Q corresponds to a lower energy dissipation rate.

For all impact indentation experiments on brain tissue, a stainless steel cylindrical flat punch probe with a radius of 1 mm was employed. This probe connected to a lever arm attached to the pendulum (Fig. 2-6(A)), which allowed for lowering of the probe into the fluid cell. Each tissue sample was adhered to the aluminum sample post also within the fluid cell by using a thin layer of low-viscosity cyanoacrylate adhesive (Loctite® 4013). In this configuration, loading occurred in the horizontal direction, normal to the vertically mounted sample. During mechanical testing, brain tissue was immersed in Hibernate®-A media to preserve tissue integrity. Separate experiments were conducted previously in air and in media to confirm that the presence of fluid caused negligible damping; this verified that testing in media did not influence the measured energy dissipation properties [45]. Applied impact velocities ranged from 2 to 6 mm/s, which corresponded to large strain energy densities approaching ballistic conditions (~1 kJ/m^3) due to the relatively small physical dimensions of the probe (see Appendix C).

2.3.3.2 Discussion

In contrast to the quasistatic AFM-enabled indentation at nanoNewton (nN)-scale forces and μm-scale depths, impact indentation applies a concentrated dynamic load of mN-scale forces and measures the specimen's deformation response to depths approaching the mm-scale. Impact indentation can accommodate probe radii ranging from μm to mm, and thus, this technique can

probe local mechanical properties of heterogeneous materials, similar to AFM-enabled indentation. The results of these experiments provide information about how brain tissue deforms and dissipates mechanical energy in response to traumatic injury. Penetration depth measures the deformation resistance, which strongly correlates with the tissue's effective Young's elastic modulus. Stiffer tissues exhibit smaller penetration depths for a given impact velocity and impact energy. Energy dissipation capacity is a unitless measure of the extent to which the tissue dissipates the impact energy during the first impact cycle. Dissipation quality factor measures how many cycles occur before the oscillations from impact are damped significantly, and thus relates directly to the rate of energy dissipation, though this is not expressed in units of time. These three impact response parameters can be quantified at different impact velocities, providing a means to study the mechanical properties of the tissue at varying strains and strain rates.

When using impact indentation to test materials as compliant and fragile as brain tissue, important considerations must be taken into account. First, the maximum measurable depth into the material is approximately 1 mm, a limitation set by the length scales of the instrument itself; any further pendulum displacement will be physically halted by the collision between the electromagnetic coil located at the top of the pendulum and the stationary magnetic plate. For brain tissue, this limits the highest impact velocity that can be successfully applied to approximately 6 mm/s. Second, it can potentially become difficult for the instrument to detect contact between the probe and tissue surface. As the sample stage travels toward the probe, contact is detected when the pendulum is pushed back by the moving sample. However, for highly compliant samples, the pendulum may not be deflected detectably while the probe penetrates into the sample. To address this problem, we can increase the speed at which the sample stage moves such that there will be a greater momentum during contact to drive the pendulum back. The sample should also be as flat as possible, to further minimize any errors in detecting the proper contact point. Before the pendulum is ready to swing forward and impact the tissue, enough time should be allowed for the tissue to restore and relax to its initial condition prior to any accidental deformation. Additionally, the impact load is not a true impulse load, in that the electromagnetic current at the pendulum top continues to supply a driving force for penetration after the first impact event. Thus, impact indentation can be thought of essentially as a creep test superimposed with an impact test. For viscoelastic materials like brain tissue,

significant creep may occur, especially at the higher loading conditions, which potentially complicates the analysis of energy dissipation characteristics such as the dissipation quality factor Q by obscuring the amplitudes of the damped oscillation.

Finally, a significant limitation of the impact data analysis described in Section 2.3.3.1 is that x_{max}, K, and Q are all empirical parameters and not material properties (e.g., E, G', or other moduli). Therefore, comparisons between impact indentation and rheological results have been constrained solely to qualitative observations (e.g., x_{max} increases with decreasing G' or K increases with increasing G''). Since oscillatory shear rheology is a well-established technique employed vastly by the scientific community, the ability to quantitatively predict the impact response from rheological data would enable very rapid identification of potential brain tissue simulant materials that have been characterized previously by rheology. Furthermore, if impact indentation can accurately measure viscoelastic mechanical properties rather than empirical parameters with minimal physical meaning, this technique, which holds many advantages over conventional indentation-based or rheological approaches for highly compliant materials, can be applied much more broadly to investigate important research questions related to biomechanics and not limited to brain tissue simulants. The previous limitation of the impact indentation analysis has since been addressed and will be discussed in detail in Chapter 6.

2.4 Impact response of healthy brain tissue from different animal models

To design polymers as mechanically biofidelic brain tissue simulants, we first studied the impact response of animal brain tissue under loading conditions relevant to mechanical insult and injury. Additionally, because numerous animal models of traumatic brain injury exist, each with its own strengths and weaknesses [49,50], we hypothesized that we would detect species-to-species variation in terms of the three impact energy dissipation parameters of interest. We conducted impact indentation experiments on brain slices obtained from three different animal models: infant mice, adult rats, and adult pigs. Figure 2-7(A-C) shows the measured x_{max}, K, and Q, respectively, for each species at impact velocities between 2 and 6 mm/s. Because brain is highly compliant (low elastic moduli as compared with other biological organs such as heart or bone), impact velocities greater than 6 mm/s tended to penetrate the sample so deeply that the pendulum motion was impeded physically by the electromagnetic coil contacting with the stationary

magnetic plate. Although the velocities investigated here are on the order of only mm/s, the corresponding impact strain energy densities, which range from 0.5 kJ/m^3 to 3.5 kJ/m^3 due to the small size of the probe, are comparable to ballistic strain energy densities [51].

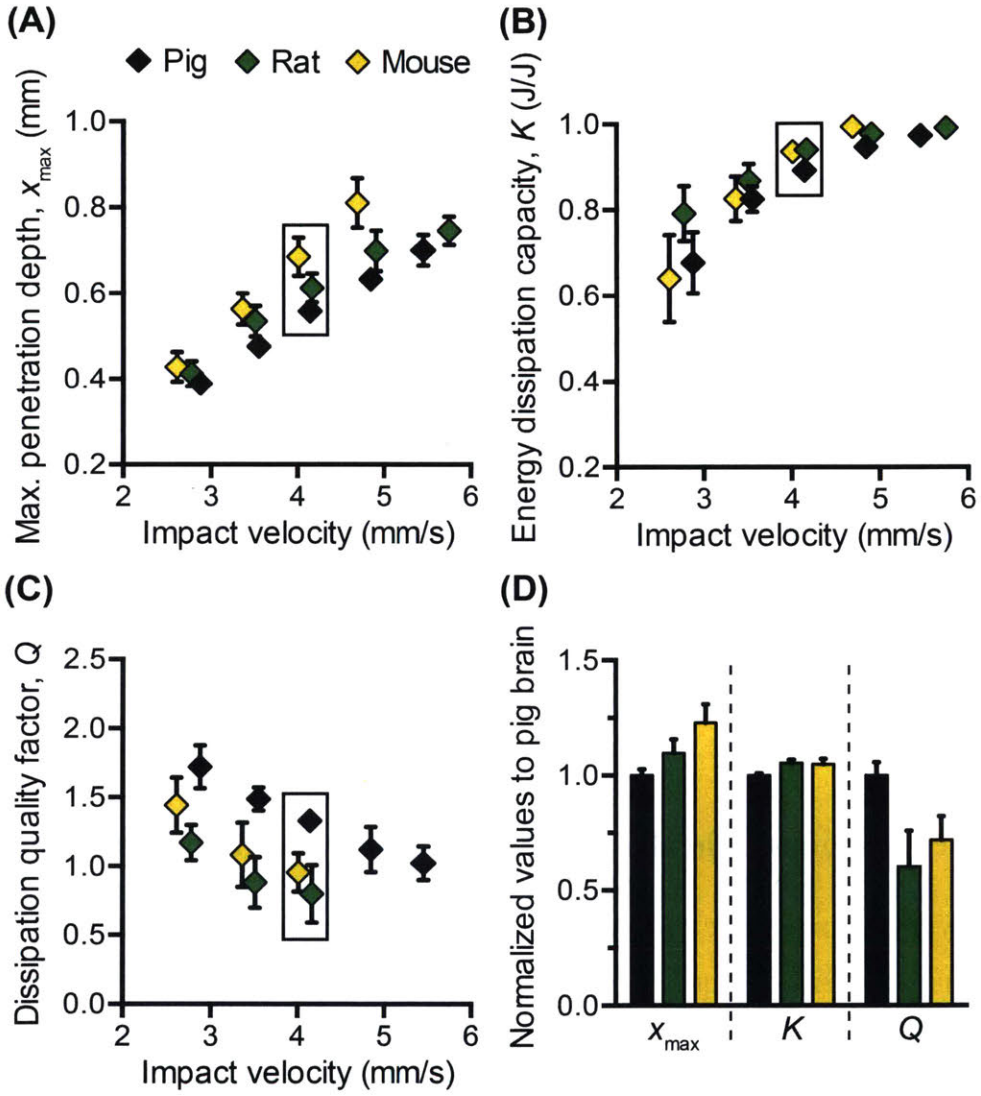

Figure 2-7 Impact response of brain tissues harvested from pigs, rats, and mice at a range of impact velocities: (A) maximum penetration depth, (B) energy dissipation capacity, and (C) dissipation quality factor. (D) To emphasize the variations observed among the different species, the values corresponding to the boxed data points in (A), (B), and (C) at an impact velocity of approximately 4 mm/s were normalized to that of pig brain. A one-way ANOVA confirmed a statistical difference among the three species (p-values < 0.0001) for all three energy dissipation metrics. Data are represented as mean ± standard deviation (n = 7–27 replicate measurements per data point specified by a given tissue and impact velocity). From [12].

We observed all brain tissues to exhibit the following trends: as the impact velocity increased, the probe penetrated into the sample further, the sample dissipated more energy and this energy was dissipated at a quicker rate. Compared to previous impact loading studies on other soft tissues, brain tissue was similar to liver tissue in terms of deformation resistance and was much more dissipative than either liver or heart tissue [46]. All experiments on tissues were conducted in aqueous fluid at 25°C because at the time, the impact indentation setup did not allow for testing at constant, elevated temperatures. Previous studies of brain tissue macroscale rheology have noted decreased stiffness (specifically, shear storage modulus) at physiological temperature (37°C) as compared to the ambient room temperature of interest here [52], and such increased compliance may potentially and slightly reduce x_{max} and increase K. After the completion of these experiments, we have successfully extended the impact indentation instrumentation to enable characterization of such tissues at 37°C (see Appendix D).

Additionally, we identified detectable differences in the magnitude of all three impact response parameters when comparing brain tissue from different species. Impact velocities were not necessarily identical because impact velocity is a parameter that is controlled in open loop format. The control parameter is the electromagnetic coil current (related directly to a pre-load on the cocked pendulum) and the magnitude of the corresponding velocity may vary slightly due to the pendulum swing distance calibration conducted for each set of experiments. Since the different brain tissue samples were collected periodically over an extended period of time, the experimental setup was reconfigured and recalibrated several times, which led to slightly different impact velocities for the same requested driving force. To highlight the species-to-species variation, we normalized the magnitudes of each impact response parameter to that of porcine brain and conducted one-way ANOVA (see Appendix E). Figure 2-7(D) shows normalized data that correspond to an impact velocity of approximately 4 mm/s (boxed data points in Fig. 2-7(A-C)). A statistically significant distinction was identified among the three species for x_{max}, K, and Q (p-values < 0.001) at this impact velocity, and also at the other impact velocities considered (not shown). These variations in mechanical properties among species were anticipated, due to species-dependent differences in structure and composition.

Histological staining of coronal brain sections in Fig. 2-8 indicates several key differentiating features such as brain size, degree of convolution in the outer cerebral cortex, and the ratio of white to gray matter. Of the three species considered herein, porcine brain is the most similar to

human brain, as both are gyrencephalic (highest degree of convolution) and consist of roughly 60% white and 40% gray matter [53,54]. In contrast, rodent brains are lissencephalic (not convoluted) and contain only roughly 10% white matter [55]. Several studies have reported the stiffness of white matter to be greater and the stress relaxation times to be longer, as compared to gray matter from the same species [56-58]. Our observations are consistent with those findings, in that porcine brain was more resistant to deformation (lower x_{max}) and dissipated energy more slowly (higher Q) than both types of rodent brains. These data do not resolve why the impact response of rat and mouse brains differs, but we note that the animal ages for each cohort also differed and may reflect differences in the maturity of the brain structure and composition (rats aged 6 to 18 months, and mice aged 3 weeks). However, this hypothesis cannot be addressed by the current data due to undersampling (i.e., relatively low number of brains obtained for each age cohort). Additionally, we note that the relatively smaller dimensions of mouse brain tissue constrained the measurement positions near the sample center to be within 1 to 2 mm from the tissue perimeter. As this distance is similar to the probe contact radius, it is possible that the closer proximity of those measurements to the sample edge could have contributed to increased penetration depths in mouse brain tissue (as compared with larger tissue samples from porcine brain that were located at least 10 mm from sample perimeters).

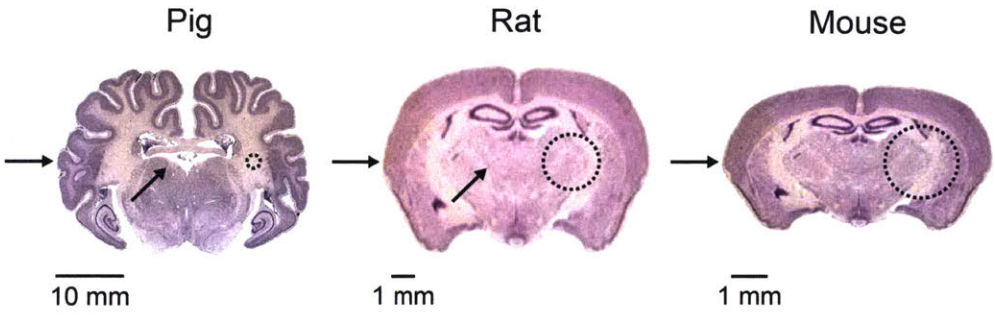

Figure 2-8 Histological stains of coronal brain sections from the three species adapted with permission from http://brainmuseum.org (supported by the United States National Science Foundation), illustrating significant differences in structure, size, and composition. The arrows indicate the direction of impact during experiments, and the dashed circles indicate the probe contact area at scale. From [12].

From Fig. 2-7(D), we also observed that the impact response parameters varied to different degrees among species. For example, at an impact velocity of 4 mm/s, the mean penetration depth x_{max} of mouse brain was 23% greater than that of pig brain (with a 95% confidence interval of this difference ranging from 19 to 27%), whereas the mean impact dissipation capacity K of mouse brain was only 5% greater than that of pig brain (with a 95% confidence interval of this difference ranging from 4 to 6%). This contrast could be problematic when developing mechanically biofidelic tissue simulant materials that are capable of mimicking multiple animal models, because the primary limitation of existing materials is the strong coupling between deformation resistance and energy dissipation. If the material is well-matched to the penetration depth exhibited by the target soft tissue, but not well-matched to the targeted magnitude of K, further tuning to approximate the brain tissue K would be at the expense of a change in x_{max}. As a result, the implications of the differences among species are twofold: first, they highlight the importance of selecting an appropriate animal model for brain injury because differences in anatomy and structure translate to a difference in mechanical behavior; second, they prompt the need for a highly tunable materials system to afford such variation in and decoupling of these metrics.

2.5 Conclusions

Together, the methods described in this chapter enable the mechanical characterization of brain tissue in fully hydrated conditions at the micro-, meso-, and macro- length scales, and at different rates and loading configurations. The methods presented herein can be used on a number of highly compliant materials, including both biological soft tissues and engineered polymeric gels. Impact indentation experiments, specifically, provided a means to characterize the mechanical response of brain tissues under spatially and temporally concentrated impact loading through empirical quantification of the deformation resistance, energy dissipation capacity, and energy dissipation rate. Brain tissues from all three animal models studied were highly susceptible to deformation and highly dissipative when compared to other soft tissues such as heart and liver tissue. Additionally, we observed slight but detectable species-to-species variation in all three impact response metrics, which may be attributed to the structural and compositional differences among mouse, rat, and pig brains. With a stronger understanding of the multiscale viscoelastic

properties of brain tissue, we can establish better design criteria for synthetic materials intended to accurately mimic the mechanical response of the brain. Ultimately, these tissue simulant materials can facilitate prediction of traumatic brain injury and development of novel protective strategies. We note that this chapter included only impact indentation studies on brain tissue obtained from healthy animal models. Before we present the materials systems that we investigated as potential candidates to match brain tissue response in Chapter 4, in Chapter 3, we first summarize our detailed study to examine whether the structural changes observed in a mouse disease model of autism (i.e., demyelination) would translate to detectable differences in mechanical properties using the three characterization methods presented herein. As mentioned in Section 1.2, demyelination or reduced myelin content is also a common characteristic associated with traumatic brain injuries.

2.6 References

[1] N.D. Leipzig and M.S. Shoichet, The effect of substrate stiffness of adult neural stem cell behavior, *Biomaterials*, 2009, 30, 6867-6878.

[2] M. Hrapko, J.A. van Dommelen, G.W. Peters, and J.S. Wismans, The mechanical behavior of brain tissue: large strain response and constitutive modelling, *Biorheology*, 2006, 43, 623-636.

[3] L.E. Bilston, Z. Liu, and N. Phan-Thien, Linear viscoelastic properties of bovine brain tissue in shear, *Biorheology*, 1997, 34, 377-385.

[4] S. Budday, C. Raybaud, and E. Kuhl, A mechanical model predicts morphological abnormalities in the developing human brain, *Scientific Reports*, 2014, 4, 5644.

[5] C. Zhou, L. Zemanova, G. Zamora-Lopez, C.C. Hilgetag, and J. Kurths, Structure-function relationship in complex brain networks expressed by hierarchical synchronization, *New Journal of Physics*, 2007, 9, 178.

[6] S. Budday, G. Sommer, C. Birkl, C. Langkammer, J. Haybaeck, J. Kohnert, M. Bauer, F. Paulsen, P. Steinmann, E. Kuhl, and G.A. Holzapfel, Mechanical characterization of human brain tissue, *Acta Biomaterialia*, 2017, 48, 319-340.

[7] S. Nicolle, M. Lounis, and R. Willinger, Shear properties of brain tissue over a frequency range relevant for automotive impact situations: new experimental results, *Stapp Car Crash Journal*, 2004, 48, 239-258.

[8] S. Chatelin, A. Constantinesco, and R. Willinger, Fifty years of brain tissue mechanical testing: from in vitro to in vivo investigations, *Biorheology*, 2010, 47, 255-276.

[9] T.P. Prevost, A. Balakrishnan, S. Suresh, and S. Socrate, Biomechanics of brain tissue, *Acta Biomaterialia*, 2011, 7, 83-95.

[10] E.P. Canovic, B. Qing, A.S. Mijailovic, A. Jagielska, M.J. Whitfield, E. Kelly, D. Turner, M. Sahin, and K.J. Van Vliet, Characterizing multiscale mechanical properties of brain tissue using atomic force microscopy, impact indentation, and rheometry, *Journal of Visualized Experiments*, 2016, 115, e54201.

[11] B. Qing, E.P. Canovic, A.S. Mijailovic, A. Jagielska, M.J. Whitfield, A.L. Lowe, E. Kelly, D. Turner, M. Sahin, and K.J. Van Vliet, Probing mechanical properties of brain in a tuberous sclerosis model of autism, *Journal of Biomechanical Engineering*, 2018, in review.

[12] B. Qing and K.J. Van Vliet, Hierarchical design of synthetic gel composites optimized to mimic the impact energy dissipation response of brain tissue, *Molecular Systems Design & Engineering*, 2016, 1, 290-300.

[13] D.M. Ebenstein and L.A. Pruitt, Nanoindentation of soft hydrated materials for application to vascular tissues, *Journal of Biomedical Materials Research Part A*, 2004, 69, 222-232.

[14] S. Nicolle and J.F. Palierne, Dehydration effect on the mechanical behavior of biological soft tissues: observations on kidney tissues, *Journal of the Mechanical Behavior of Biomedical Materials*, 2010, 3, 630-635.

[15] G. Thomas, N.A. Burnham, T.A. Camesano, and Q. Wen, Measuring the mechanical properties of living cells using atomic force microscopy. *Journal of Visualized Experiments*, 2013, 76, e50497.

[16] F. Liu and D.J. Tschumperlin, Micro-mechanical characterization of lung tissue using atomic microscopy. *Journal of Visualized Experiments*, 2011, 54, e2911.

[17] A. Peaucelle, AFM-based mapping of the elastic properties of cell walls: at tissue, cellular, and subcellular resolutions. *Journal of Visualized Experiments*, 2014, 89, e51317.

[18] E. Moeendarbary, I.P. Weber, G.K. Sheridan, D.E. Koser, S. Soleman, B. Haenzi, E.J. Bradbury, J. Fawcett, and K. Franze, The soft mechanical signature of glial scars in the central nervous system, *Nature Communications*, 2017, 8, 14787.

[19] D.C. Lin, E.K. Dimitriadis, and F. Horkay, Robust strategies for automated AFM force curve analysis-II: adhesion-influenced indentation of soft, elastic materials, *Journal of Biomechanical Engineering*, 2007, 129, 904-912.

[20] W.C. Oliver and G.M. Pharr, An improved technique for determining hardness and elastic modulus using load and displacement sensing indentation experiments, *Journal of Materials Research*, 1992, 7, 1564-1583.

[21] W.C. Oliver and G.M. Pharr, Measurement of hardness and elastic modulus by instrumented indentation: advances in understanding and refinements to methodology, *Journal of Materials Research*, 2004, 19, 3-20.

[22] E. Herbert, G.M. Pharr, W.C. Oliver, B.N. Lucas, and J.L. Hay, On the measurement of stress-strain curves by spherical indentation, *Thin Solid Films*, 2001, 398-399, 331-335.

[23] S. Moreno-Flores, R. Benitez, M.D. Vivanco, and J.L. Toca-Herrera, Stress relaxation and creep on living cells with the atomic force microscope: a means to calculate elastic moduli and viscosities of cell components, *Nanotechnology*, 2010, 21, 445101.

[24] N. Desprat, A. Richert, J. Simeon, and A. Asnacios, Creep function of a single living cell, *Biophysical Journal*, 2005, 88, 2224-2233.

[25] H. Lu, B. Wang, J. Ma, G. Huang, and H. Viswanathan, Measurement of creep compliance of solid polymers by nanoindentation, *Mechanics Time-Dependent Materials*, 2003, 7, 189-207.

[26] L. Cheng, X. Xia, L.E. Scriven, and W.W. Gerberich, Spherical-tip indentation of viscoelastic material, *Mechanics of Materials*, 2005, 37, 213-226.

[27] S. Moreno-Flores, R. Benitez, M.D. Vivanco, and J.L. Toca-Herrera, Stress relaxation microscopy: imaging local stress in cells, *Journal of Biomechanics*, 2010, 43, 349-354.

[28] E.H. Lee and J.R.M. Radok, The contact problem for viscoelastic bodies, *Journal of Applied Mechanics*, 1960, 27, 438-444.

[29] R.S. Lakes and A. Wineman, On Poisson's ratio in linearly viscoelastic solids, *Journal of Elasticity*, 2006, 85, 45-63.

[30] A. Samadi-dooki, G.Z. Voyiadjis, and R.W. Stout, A combined experimental, modeling, and computational approach to interpret the viscoelastic response of white matter brain tissue during indentation, *Journal of the Mechanical Behavior of Biomedical Materials*, 2018, 77, 24-33.

[31] P.A. Janmey, P.C. Georges, and S. Hvidt, Basic rheology for biologists, *Methods in Cell Biology*, 2007, 83, 3-27.

[32] M. Oyen, Handbook of Nanoindentation, New York: Pan Stanford, 2010.

[33] S. Nicolle, M. Lounis, and R. Willinger, Shear properties of brain tissue over a frequency range relevant for automotive impact situations: new experimental results, *Stapp Car Crash Journal*, 2004, 48, 239-258.

[34] Y. Feng, R.J. Okamoto, R. Namani, G.M. Genin, and P.V. Bayly, Measurements of mechanical anisotropy in brain tissue and implications for transversely isotropic material models of white matter, *Journal of the Mechanical Behavior of Biomedical Materials*, 2013, 23, 117-132.

[35] P. Du, H. Lu, and X. Zhang, Measuring the Young's relaxation modulus of PDMS using stress relaxation nanoindentation, *Symposium DD – Microelectromechanical Systems – Materials and Devices III*, 2009, 1222.

[36] D.W. Brands, P.H. Bovendeerd, G.W. Peters, J.S. Wismans, M.H. Paas, and J.L. van Bree, Comparison of the dynamic behavior of brain tissue and two model materials, *43rd Stapp Car Crash Conference Proceedings*, 1999, 313-320.

[37] S. Tang, M.J. Glassman, S. Li, S. Socrate, and B.D. Olsen, Oxidatively responsive chain extension to entangle engineered protein hydrogels, *Macromolecules*, 2014, 47, 791-799.

[38] M. Hrapko, J.A. van Dommelen, G.W. Peters, and J.S. Wismans, Characterization of the mechanical behaviour of brain tissue in compression and shear, *Biorheology*, 2008, 45, 663-676.

[39] M. Ayyildiz, S. Cinoglu, and C. Basdogan, Effects of normal compression on the shear modulus of soft tissues in rheological measurements, *Journal of the Mechanical Behavior of Biomedical Materials*, 2015, 49, 235-243.

[40] K. Tan, S. Cheng, L. Juge, and L.E. Bilston, Characterising soft tissues under large amplitude oscillatory shear and combined loading, *Journal of Biomechanics*, 2017, 46, 1060-1066.

[41] K. Pogoda, L. Chin, P.C. Georges, F.J Byfield, R. Bucki, R. Kim, M. Weaver, R.G. Wells, C. Marcinkiewicz, and P.A. Janmey, Compression stiffening of brain and its effect of mechanosensing by glioma cells, *New Journal of Physics*, 2014, 16, 75002.

[42] G. Mattei, A. Tirella, G. Gallone, and A. Ahluwalia, Viscoelastic characterisation of pig liver in unconfined compression, *Journal of Biomechanics*, 2014, 47, 2641-2646.

[43] F. Shen, T.E. Tay, J.Z. Li, S. Nigen, P.V.S. Lee, and H.K. Chan, Modified Bilston nonlinear viscoelastic model for finite element head injury studies, *Journal of Biomechanical Engineering*, 2006, 128, 797-801.

[44] G. Constantinides, C.A. Tweedie, M. McFarland, J.F. Smith, and K.J. Van Vliet, Probing mechanical properties of fully hydrated gels and biological tissues, *Journal of Biomechanics*, 2008, 41, 3285-3289.

[45] Z.I. Kalcioglu, M. Qu, K.E. Strawhecker, T. Shazly, E. Edelman, M.R. VanLandingham, J.F. Smith, and K.J. Van Vliet, Dynamic impact indentation of hydrated biological tissues and tissue surrogate gels, *Philosophical Magazine*, 2011, 91, 1339-1355.

[46] Z.I. Kalcioglu, R.A. Mrozek, R. Mahmoodian, M.R. VanLandingham, J.L. Lenhart, and K.J. Van Vliet, Tunable mechanical behavior of synthetic organogels as biofidelic tissue simulants, *Journal of Biomechanics*, 2013, 46, 1583-1591.

[47] G. Constantinides, C.A. Tweedie, D.M. Holbrook, P. Barragan, J.F. Smith, and K.J. Van Vliet, Quantifying deformation and energy dissipation of polymeric surfaces under localized impact, *Materials Science and Engineering: A*, 2008, 489, 403-412.

[48] G. Constantinides, C.A. Tweedie, N. Savva, J.F. Smith, and K.J. Van Vliet, Quantitative impact testing of energy dissipation at surfaces, *Experimental Mechanics*, 2009, 49, 511-522.

[49] Y. Xiong, A. Mahmood, and M. Chopp, Animal models of traumatic brain injury, *Nature Reviews Neuroscience*, 2013, 14, 128-142.

[50] D.M. Morales, N. Marklund, D. Lebold, H.J. Thompson, A. Pitkanen, W.L. Maxwell, L. Longhi, H. Laurer, M. Maegele, E. Neugebauer, D.I. Graham, N. Stocchetti, and T.K. McIntosh, Experimental models of traumatic brain injury: do we really need to build a better mousetrap?, *Neuroscience*, 2005, 136, 971-989.

[51] J.G. Snedeker, M. Barbezat, P. Niederer, F.R. Schmidlin, and M. Farshad, Strain energy density as a rupture criterion for the kidney: impact tests on porcine organs, finite element simulation, and a baseline comparison between human and porcine tissues, *Journal of Biomechanics*, 2005, 38, 993-1001.

[52] M. Hrapko, J.A. van Dommelen, G.W. Peters, and J.S. Wismans, The influence of test conditions on characterization of the mechanical properties of brain tissue, *Journal of Biomechanical Engineering*, 2008, 130, 031003-031013.

[53] S. Herculano-Houzel, The human brain in numbers: a linearly scaled-up primate brain, *Frontiers in Human Neuroscience*, 2009, 3, 31.

[54] D.W. Howells, M.J. Porritt, S.S.J. Rewell, V. O'Collins, E.S. Sena, H.B. van der Worp, R.J. Traystman, and M.R. Macleod, Different strokes for different folks: the rich diversity of animal models for focal cerebral ischemia, *Journal of Cerebral Blood Flow & Metabolism*, 2010, 30, 1412-1431.

[55] E.C. Bush and J.M. Allman, The scaling of white matter to gray matter in cerebellum and neocortex, *Brain, Behavior and Evolution*, 2003, 61, 1-5.

[56] S. Budday, R. Nay, R. de Rooij, P. Steinmann, T. Wyrobek, T.C. Ovaert, and E. Kuhl, Mechanical properties of gray and white matter brain tissue by indentation, *Journal of the Mechanical Behavior of Biomedical Materials*, 2015, 46, 318-330.

[57] J.A. van Dommelen, T.P.J. van der Sande, M. Hrapko, and G.W. Peters, Mechanical properties of brain tissue by indentation: interregional variation, *Journal of the Mechanical Behavior of Biomedical Materials*, 2010, 3, 158-166.

[58] F. Pervin and W.W. Chen, Dynamic mechanical response of bovine gray matter and white matter brain tissues under compression, *Journal of Biomechanics*, 2009, 42, 731-735.

Chapter 3: Effects of demyelination on mechanical properties of brain tissue

3.1 Introduction

The previous chapter described three experimental techniques that can be used to characterize the mechanical properties of brain tissue *in vitro*, and specifically demonstrated the application of one technique, impact indentation, to identify differences in impact energy dissipation response among brain tissues from different species. The observed species-to-species variation suggested that differences in brain structure and composition could potentially translate to differences in mechanical properties, which would have several important implications. First, in the context of traumatic brain injury, white matter tracts, which are particularly susceptible to damage from impact-acceleration forces, often contain lesions post-injury that feature significant morphological changes to axons, including swelling, disconnections, bulb formation, and most notably, demyelination [1-3]. Therefore, understanding the consequences of demyelination on the mechanical properties of brain tissue is essential to developing accurate physical models of brain lesions. Several applications, such as robotic surgery and brain implant devices, will typically require operation on injured brain tissue, rather than their healthy counterpart. If there are indeed mechanical differences between the two, it may be necessary to develop tissue simulant materials that can be tuned to mimic the appropriate type of brain tissue.

Demyelination is also a hallmark in many debilitating neurological diseases, such as multiple sclerosis and autism spectrum disorders. Recently, there has been increasing evidence suggesting that the mechanical environment of brain plays a key role in disease, with several independent studies reporting changes in brain stiffness for different pathological conditions [4-7]. However, the precise mechanistic origin of these variations in stiffness is not yet clearly understood. One hypothesis is that myelin, in addition to improving the electrical function of axons, also provides structural support and mechanical stiffness to brain tissue [8,9]. Thus, to test this hypothesis, the relationship between myelin content and brain tissue stiffness must first be investigated thoroughly. If true, the mechanical properties of brain tissue can be used as a clinical biomarker to quantify the onset of disease progression in demyelinating disorders.

In this chapter, we explore whether cellular-level structural changes (i.e., demyelination) translate to changes in brain mechanics by using a tuberous sclerosis mouse model of autism spectrum disorder. Section 3.2 provides background on the mouse model that we employed. Section 3.3 compares the measured mechanical properties of brain tissue from healthy control and diseased cohorts at the micro-, meso-, and macro-length scale using the characterization techniques detailed in Chapter 2. Section 3.4 examines whether the extracellular matrix differed detectably in the tuberous sclerosis mouse model, since the composition and organization of the extracellular matrix could also theoretically affect brain tissue mechanics. Finally, Section 3.5 discusses our results in the context of previously reported studies in the literature, while highlighting the caveats of our findings and important considerations for future work.

The work presented in this chapter was published in *Journal of Biomechanical Engineering* as the result of a collaboration between the Van Vliet Laboratory for Material Chemomechanics at MIT and the laboratory of Dr. Mustafa Sahin at Boston Children's Hospital and Harvard Medical School [10]. Elyza Kelly and Daria Turner (Sahin group) handled the breeding of two mouse populations and acquisition of brain tissues in accordance with approved protocols. Dr. Elizabeth Canovic (Van Vliet group) conducted AFM-enabled indentation experiments on brain tissue slices and individual neurites grown in cell culture. Aleksandar Mijailovic (Van Vliet group) conducted a significant portion of the rheological experiments. Alexis Lowe (Van Vliet group) assisted with imaging the brain tissue slices that were immunohistochemically stained for extracellular matrix components.

3.2 Tuberous sclerosis mouse model of autism spectrum disorder

Tuberous sclerosis complex (TSC) is a multi-system disease that includes multiple neurological symptoms. Approximately 50% of TSC patients also present autism spectrum disorders (ASD) [11,12]. Because of this co-occurrence, mice with TSC are used as animal models for autism research studies [13]. TSC is caused by mutations in the *TSC*1 and *TSC*2 genes and the resulting loss of function of the encoded proteins, hamartin (TSC1) and tuberin (TSC2), which play critical roles in protein synthesis and cell growth control [11]. Using *Tsc*1/2 gene-deficient mouse models, researchers have identified defects in axonal formation, guidance and myelination. Specifically, they have shown that loss of TSC function leads to neurons with

abnormal axon morphology, hypomyelination, and hyperactivation of the mTOR pathway resulting in increased protein synthesis and cell growth [14-17]. Hypomyelination, characterized by reduced amounts of myelin ensheathing neuronal axons, is especially apparent in the corpus callosum and the radiating fibers extending into the cerebral cortex [14]. Fluorescent staining images demonstrating reduced myelin content in brain slices from TSC mouse is shown in Fig. 3-1. Similar defects in axonal organization and hypomyelination have also been found in TSC patients using diffusion tensor imaging [18-20]. While previous work has focused on the genetic and biochemical parameters contributing to the neurological symptoms in TSC/ASD patients, the physical factors that may affect brain pathology have not yet been investigated thoroughly, and represent an appealing new area of exploration for therapeutic and diagnostic applications in TSC/ASD and other neurological disorders affecting brain structure.

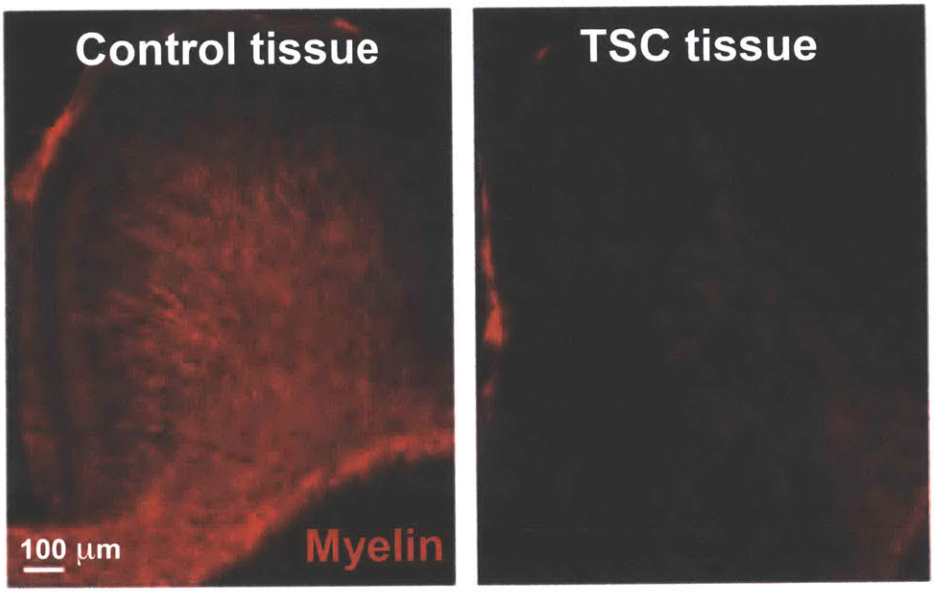

Figure 3-1 Immunohistological staining of brain tissue slices for expression of myelin basic protein (red) revealed reduced myelin content in TSC mouse compared to control mouse. Images were adapted from Meikle et al. [14], reprinted with permission from *Journal of Neuroscience*.

As described previously by Meikle et al. [14], mouse experiments were conducted in a mixed strain background (129S4/SvJae, C57BL/6, and CBA) but have been maintained as an inbred population in our colony for longer than 7 years. Mice bearing the *SynI-cre* allele were a generous gift from Jamey Marth (University of California, San Diego, La Jolla, CA) [21]. Mice were generated through breeding between *Tsc1cc* females and either *Tsc1w_SynI-cre_* or

*Tsc1w_SynI-cre_* males or between *Tsc1cc* males and *Tsc1cwSynI-cre_* females. We use *c*, *w*, and _ to denote the conditional (floxed), wild-type, and null alleles of *Tsc1*, respectively; the formal name of the *c* allele is *Tsc1tm1Djk*. Mice were anesthetized at post-natal day 21 using ketamine (AnaSed Injections).

3.3 Experimental results

3.3.1 Microscale mechanical properties

Using AFM-enabled indentation, we probed microscale volumes comparable to cell sizes, and characterized the mechanical properties of brain tissues from healthy control mice and TSC mice as shown in Fig. 3-2. Of the various methods we employed, only AFM provided enough spatial resolution to enable local measurements of white matter-rich regions, such as the corpus callosum (Fig. 3-2(A)). We were interested primarily in the corpus callosum because this region contains the highest concentration of myelinated axons. To determine whether the mechanical properties of control brain tissue differed statistically from that of TSC brain tissue, a series of Mann-Whitney tests were conducted for each measured parameter. Our criteria for significance was $p < 0.01$. The Mann-Whitney rank-based test is a nonparametric test applied to independent samples and does not require the assumption of normal distributions (see Appendix E).

Since we sought to identify any mechanical changes caused by the TSC mutation, we first idealized brain tissue as a linear elastic material, and used the Oliver-Pharr analysis to quantify the Young's elastic moduli E for each tissue sample. Although this assumption of brain tissue deforming linear elastically is an idealization and imperfect assumption for the strains applied in this study [22,23], this enabling simplification facilitated comparison between the effective E of the control and TSC cohorts, and specifically the identification of any detectable and statistically significant differences between those cohorts. We measured the mean E to be 381 Pa for control white matter and 348 Pa for TSC white matter (Fig. 3-2(B)). However, we identified no statistically significant differences between the elastic moduli of control and TSC brain tissue.

Next, we idealized brain tissue as a linear viscoelastic material to explore for potential differences in time-dependent behavior. To characterize microscale viscoelastic properties, we conducted creep compliance and stress relaxation experiments. From the creep and stress

relaxation response, we calculated the equilibrium modulus E_∞ (Fig. 3-2(C)), instantaneous modulus E_0 (Fig. 3-2(D)), and relaxation time τ_r (Fig. 3-2(E)) by assuming a standard linear solid model. The fits matched well to our creep compliance and stress relaxation response, with R^2 values exceeding 0.93 and 0.85, respectively. Note that the measured values of E_0 and τ are not as accurate as the values of E_∞ because ideal instantaneous steps of applied load or displacement cannot be achieved experimentally, and thus short timescale information is lost during the ramp period. Nonetheless, we can still compare the relative values of these properties between the two cohorts since the same loading conditions were maintained. We did not observe statistically significant differences in any of these viscoelastic properties between control and TSC brain tissue. Comparing the creep compliance to the stress relaxation results, we found E_∞ and E_0 were similar in magnitudes. However, the relaxation time constants measured via stress relaxation were higher than those measured via creep likely because the ramp time to achieve a "step" was longer in creep than in stress relaxation, providing the material more time to relax.

We also considered whether the mechanical stiffness of individual neurites could differ for TSC cohorts. Detectable differences in axon stiffness, for example, could serve as a mechanical cue to the oligodendrocytes that engage and myelinate the axons, as those glial progenitor cells have been shown to exhibit mechanosensitive migration and differentiation *in vitro* [24]. To consider this possibility, we transfected neurons with the TSC vector and its empty vector control, and measured the elastic moduli of neurites from each cohort. We first used optical microscopy to select the neurite that appeared the most elongated per cell body. These neurites were assumed to be axons and were characterized via AFM-enabled indentation (Fig. 3-3).

The data in Fig. 3-3 are presented as stiffness normalized by the mean of the unmodified control cohort because the μm-scale diameter of the neurons conflated accurate measurement of the axon stiffness. However, qualitative comparison among these three groups of cells is sound, as the axon diameter was imaged and measured for each measurement and the relative deformation was maintained comparable among groups. While the *Tsc1* knockout axons were observed to be more compliant than the control or unmodified axons, there were no statistically significant differences between the stiffness of the *Tsc1* knockout axons and the stiffness of the axons from cells transfected with only the empty vector control. Thus, we cannot conclude that the control axons are stiffer, as the detectable changes in mechanical properties may also or instead be attributable to the transfection procedures.

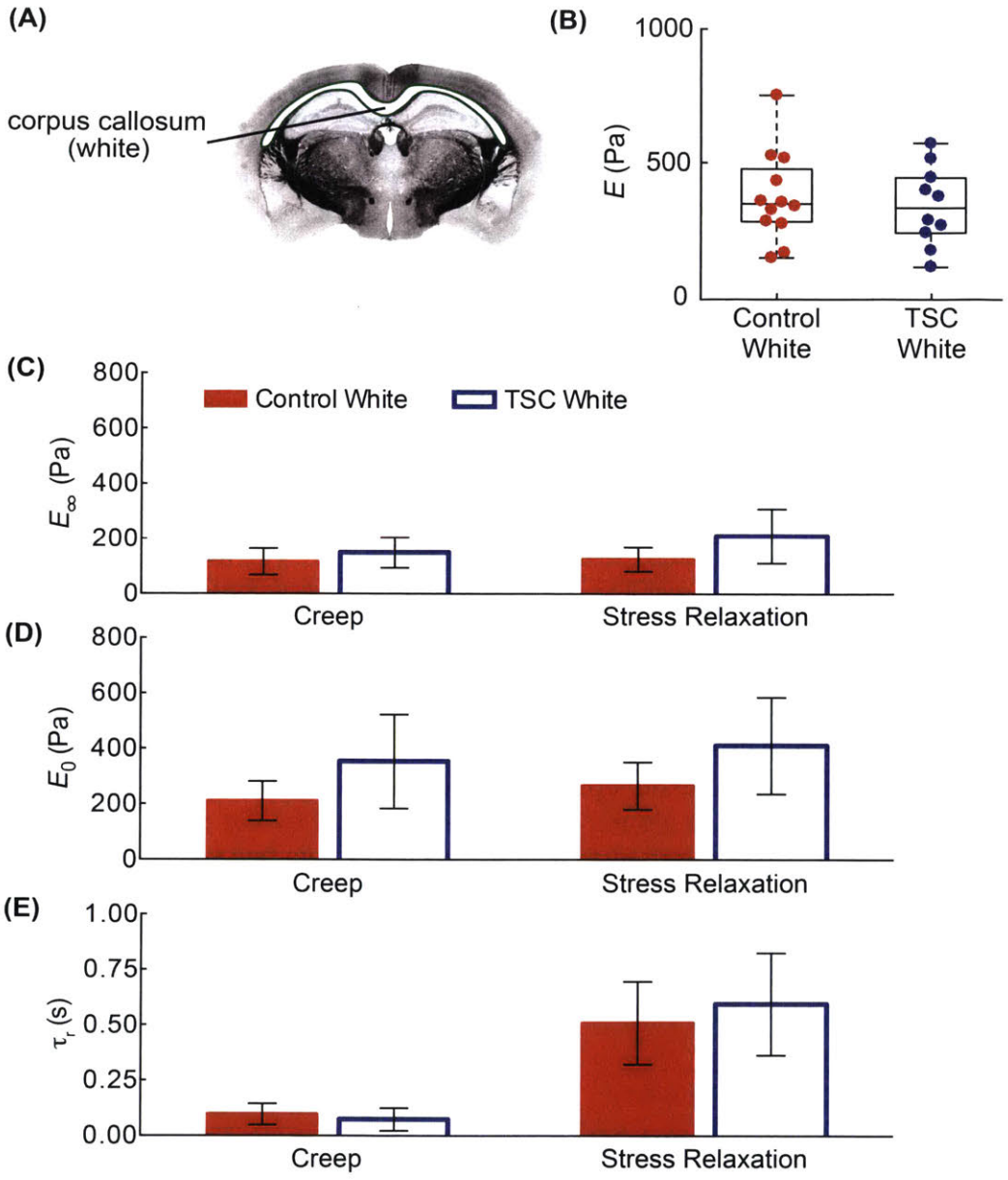

Figure 3-2 Mechanical properties at the micrometer length scale measured using AFM-enabled indentation in the white matter of healthy control and TSC mice. (A) Schematic of a coronal section of mouse brain indicating the location of the corpus callosum (outlined in green). (B) The Young's elastic modulus E of TSC brain tissue is not significantly different than that of control tissue. (C) Equilibrium modulus E_∞, (D) instantaneous modulus E_0, and (E) relaxation time τ_r obtained from fitting creep (left) and stress relaxation (right) data with a standard linear solid model. Data are represented as mean ± standard deviation (n > 10 measurements per animal; each data point in Fig. 1B represents an animal; in Fig. 1C-E, 4 control and 3 TSC animals were characterized for creep and stress relaxation experiments). From [10].

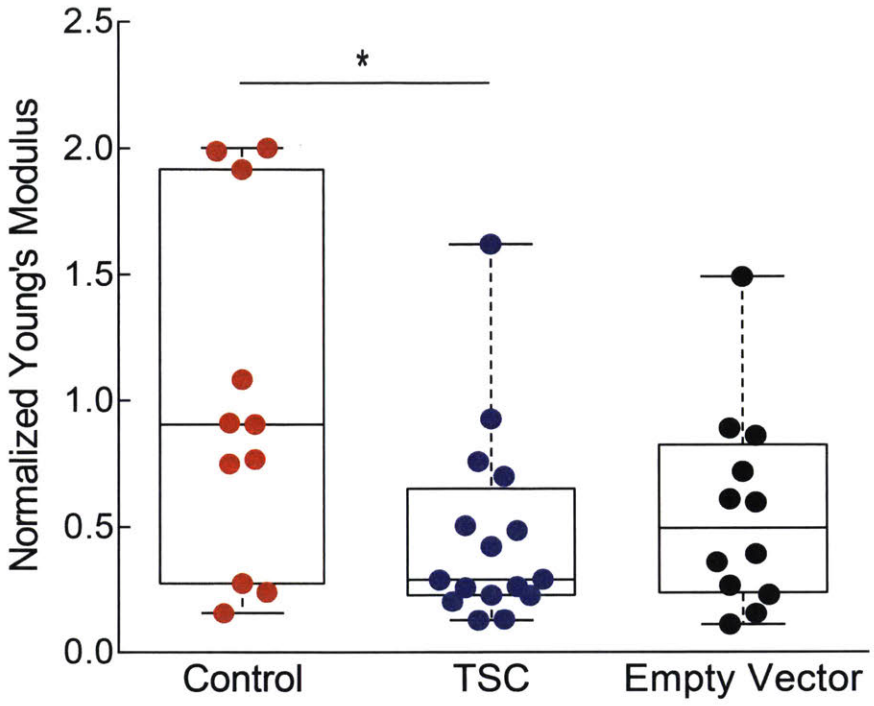

Figure 3-3 Elastic moduli of axons (specifically, the longest neurites of imaged neurons) from neurons transfected with TSC are lower than that of untransfected control neurons (unpaired t-test, $p < 0.02$), but statistically similar to that of axons from cells transfected with the empty vector *GL3*. Thus, differences in axon stiffness cannot be attributed unambiguously to the *Tsc1* knockout. Data are represented as Young's moduli normalized by the mean of the control cell group because the maximum depth used to acquire sufficient data had the potential to introduce the finite thickness effect of stiffness contributed by the underlying TCPS substrate. Note that $n > 10$ measurements were acquired per neuron; 11 control neurons, 16 TSC neurons, and 12 GL3 neurons were characterized. From [10], with AFM-enabled indentation data acquired and analyzed by E. Canovic.

3.3.2 Mesoscale mechanical properties

At the mesoscale or intermediate deformation length scales, we conducted impact indentation using a 1 mm radius cylindrical flat punch probe, quantifying the tissue's energy dissipation response to loading representative of adverse impact events that can cause traumatic injuries. The measured maximum penetration depth x_{max} (Fig. 3-4(A)), unitless energy dissipation capacity K (Fig. 3-4(B)), and unitless dissipation quality factor Q (Fig. 3-4(C)) are shown as a function of impact velocity, allowing investigation of these deformation rate-dependent properties of brain tissue. A larger magnitude of x_{max}, K, and Q corresponds to a lower resistance to deformation, a

greater extent of impact energy dissipation during the first impact cycle, and a lower energy dissipation rate, respectively. All three parameters depended on impact velocity: x_{max} and K increased, while Q decreased with increasing impact velocity. These trends are consistent with those reported previously by impact loading studies on other soft tissues obtained from heart and liver [25,26]. When comparing the control and TSC brains, we observed no statistically significant differences for each of the impact response parameters considered, within the ranges of loading conditions studied here. For example, at the lowest impact velocity, control brain tissue exhibited x_{max} of 0.428 ± 0.035 (mean ± standard deviation), K of 0.640 ± 0.101, and Q of 1.443 ± 0.202, while TSC brain tissue exhibited an x_{max} of 0.378 ± 0.072, K of 0.701 ± 0.137, and Q of 1.571 ± 0.160.

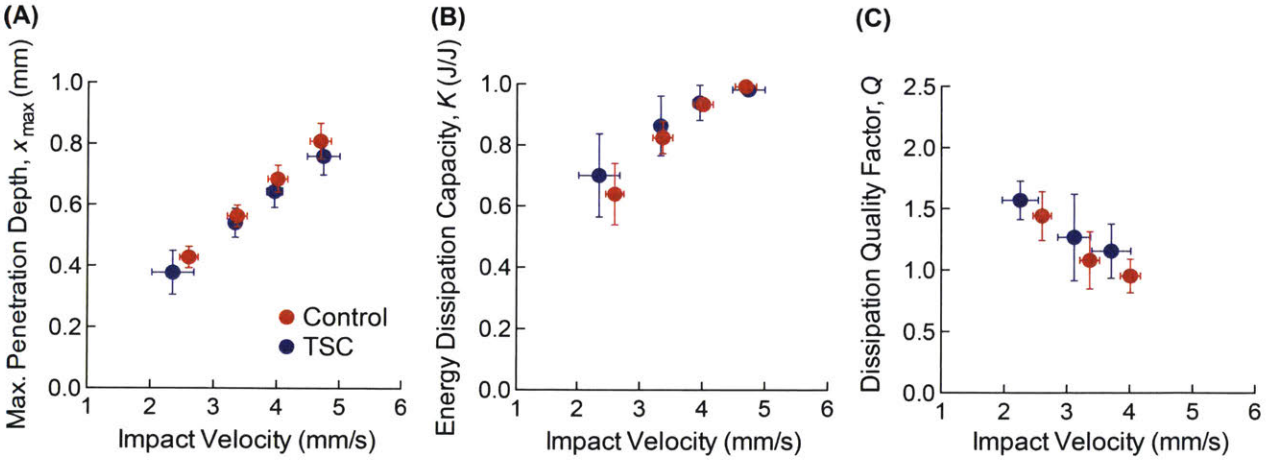

Figure 3-4 Impact energy dissipation response metrics of control (red) and TSC (blue) mouse brain tissue. (A) Maximum penetration depth x_{max}, (B) energy dissipation capacity K, and (C) dissipation quality factor Q obtained at different impact velocities show no statistical difference between control and TSC brain tissue. Data are represented as mean ± standard deviation (n > 3 measurements per animal; 6 control and 4 TSC animals were characterized). From [10].

3.3.3 Macroscale mechanical properties

At the macroscale or deformation of entire brain tissue sections, we used oscillatory shear rheology to quantify the frequency-dependent shear storage modulus G' and loss modulus G'' of the tissue. Figure 3-5 shows G' and G'' for frequencies ranging from 0.1 rad/s to 40 rad/s. We measured the mean G' to range from 141 Pa (at 0.1 rad/s) to 576 Pa (at 40 rad/s), and mean G'' to

range from 27 Pa (at 0.1 rad/s) to 109 Pa (at 40 rad/s) for the control tissues. For the TSC tissues, we found the mean G' to range from 132 Pa (at 0.1 rad/s) to 530 Pa (at 40 rad/s) and mean G'' to range from 28 Pa (at 0.1 rad/s) to 118 Pa (at 40 rad/s). The magnitudes of G' and G'' of all brain tissues increased monotonically with increasing oscillation frequency within the ranges studied herein. While the magnitude and trend of G' and G'' agree well with previous studies in healthy murine and porcine brain tissue that examined a similar frequency range [23,27,28], we identified no significant differences in these macroscale, dynamic shear moduli as a function of disease state (i.e., control vs. TSC). These findings are consistent with our results at the micro- and meso-length scales.

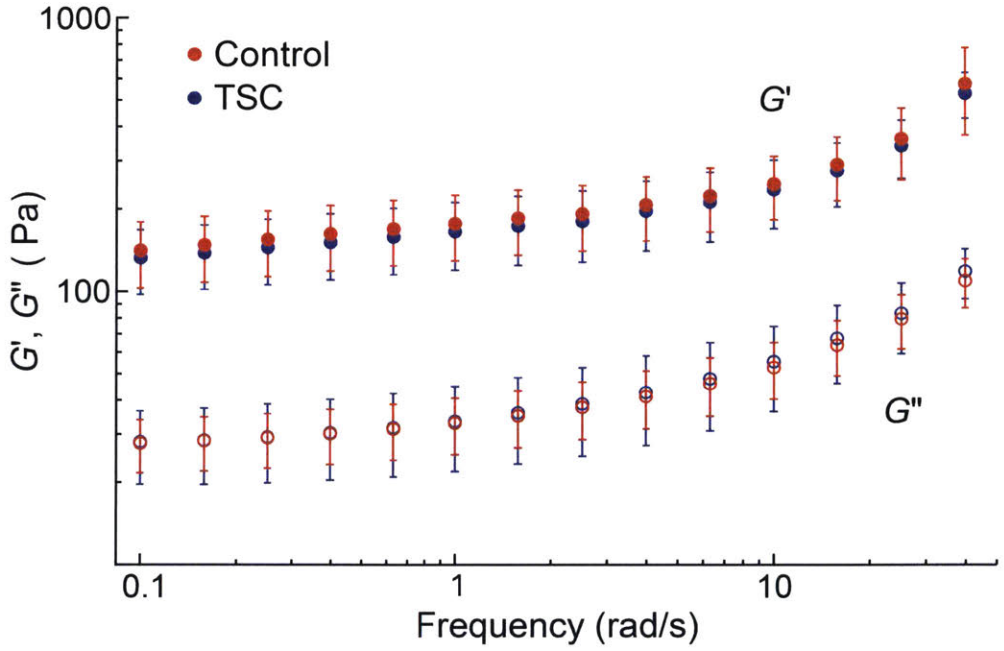

Figure 3-5 Shear storage moduli G' (filled symbols) and loss moduli G'' (open symbols) of control (red) and TSC (blue) brain tissue at a range of frequencies. Both G' and G'' show no statistical difference between control and TSC brain tissue for all frequencies measured here. Data are represented as mean ± standard deviation (n = 7 control and 5 TSC mouse brains). From [10].

3.4 Histological staining to compare ECM of control and TSC brain tissue

Given that we identified no statistically significant differences in tissue mechanical properties between healthy control and TSC mouse brain, we sought to explore whether the extracellular matrix (ECM) was also similar in these tissues. Using fluorescent immunohistochemistry, we stained brain tissues from both cohorts for fibronectin, a component of the ECM, because increased fibronectin expression in the brain has been associated with demyelination diseases and changes in tissue stiffness [29-31]. Additionally, changes in fibronectin expression by cultured fibroblasts from skin lesions of patients with TSC have also been observed [32].

Immunohistochemical fluorescent staining was conducted on mouse brains that were first sectioned into coronal slices. Next, the sections were fixed using paraformaldehyde and mounted onto glass slides. After washing in 150 mM NaCl phosphate-buffered saline (PBS), slides containing the fixed brain sections were incubated in blocking buffer (0.5% Triton^{TM} X-100 and 10% goat serum in PBS) for 30 min. Image-iT® FX signal enhancer was used to cover the slices for 30 min to mitigate nonspecific fluorescence. Sections were incubated with a rabbit polyclonal antibody to fibronectin (Millipore, AB2033) diluted 1:100 in blocking buffer overnight at 4°C. After washing in PBS, sections were incubated with secondary antibody (Alexa Fluor® 594-conjugated goat anti-rabbit) diluted 1:500 and with Hoescht® 33342 diluted 1:10000 in PBS for 2 h. Sections were washed again in PBS and after drying, and slides were mounted and visualized with a fluorescent microscope (Olympus IX51 equipped with Haramatsu Orca ER CCD camera). Using ImageJ, the entire area within each brain slice was selected as the region of interest for quantification of fibronectin expression. For each slice, the mean fluorescence intensity was calculated by first dividing the integrated density value by the area of the region of interest and then subtracting the mean intensity of background readings.

Figures 3-6(A) and 3-6(B) show representative images of the fibronectin stain (red) for control and TSC brain slices, respectively. The expression level of fibronectin was low for brain tissue, as expected from previous immunohistochemical reports [29]. Figure 3-6(C) compares quantitatively mean fluorescence intensity. We observed no significant difference in signal intensity between control and TSC slices, but noted higher standard deviation of the intensity for the TSC group. The similar degree of fibronectin expression between the two groups is consistent with our statistically indistinguishable mechanical characterization results between these two cohorts of control and TSC mice.

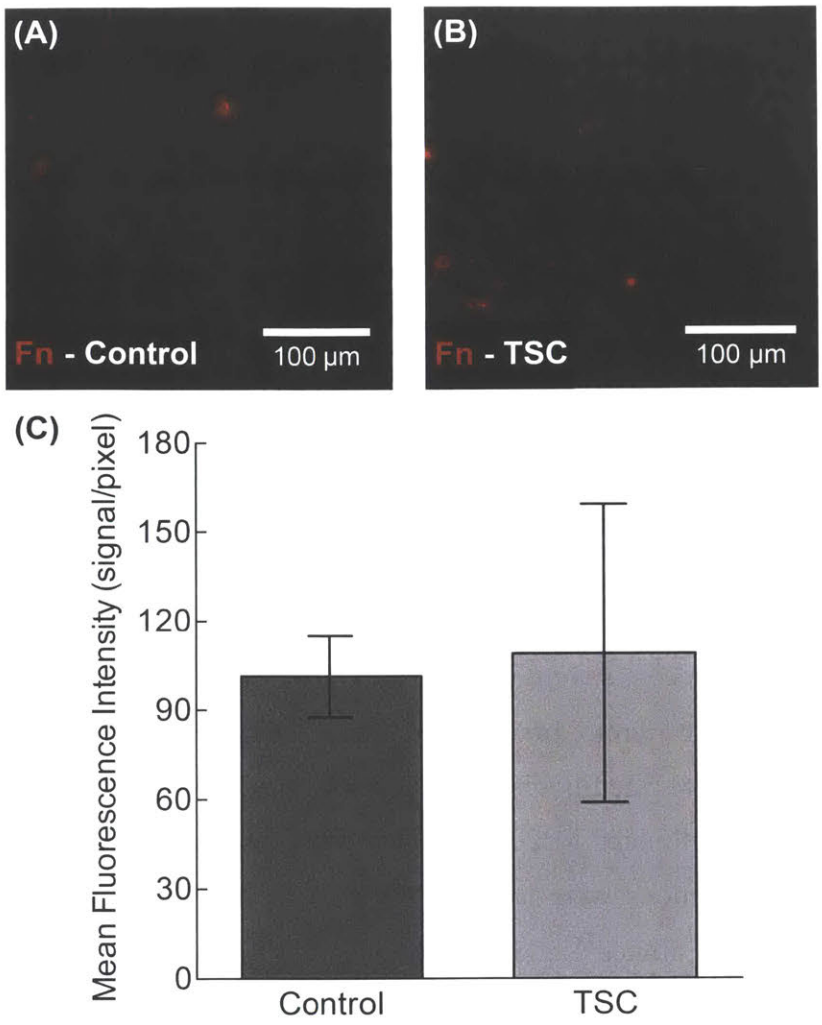

Figure 3-6 Representative images of (A) control and (B) TSC coronal brain slices analyzed for the expression of fibronectin protein (Fn) using fluorescent immunohistochemistry. (C) Mean fluorescence intensity shows no statistical difference between control and TSC slices. Data are represented as mean ± standard deviation (n = 4 control and 5 TSC slices). From [10].

3.5 Discussion

3.5.1 Effects of brain structure on tissue mechanical properties

The goal of our study was to identify any detectable and statistically significant differences in mechanical response between control and TSC brain tissue – under the simplifying assumptions and limitations of several methods distinguished by different deformation length and time scales – given that the TSC/ASD condition is associated with optically detectable changes in tissue structural features such as demyelination that have been correlated with changes in animal

functional behavior. The most striking evidence for demyelination altering properties correlated with tissue mechanics is from a recent study by Schregel et al. These authors showed that chemically induced demyelination in mouse brain was associated with a reduction in signals generally correlated with mouse brain tissue stiffness as measured by magnetic resonance elastography (MRE) [31]. Moreover, they showed that the mechanical changes were reversible, as remyelination led to a restoration of MRE signals correlated with stiffness. However, the copper-chelator cuprizone that was used to induce demyelination in that study also resulted in a number of other changes in brain physiology. These induced changes included degradation of ECM density and homogeneity, upregulation of glycosaminoglycans and fibronectin, increased glial cell populations, and increased beta-amyloid precursor protein in axons. It is unclear which of those parameters contributed to the decrease in the complex shear modulus inferred from MRE. Thus, although chemically induced demyelination led to detectable changes in a mechanical parameter, that study did not intend to show or claim that a different demyelinating condition such as TSC would result in similar structural or mechanical changes. Even more recently, Weickenmeier et al. used nanoindentation experiments in combination with histological staining to examine the relationship between brain stiffness and myelin content in pre-natal and post-natal bovine brains. Those authors found that white matter stiffness and myelin content exhibited a strong Pearson correlation coefficient above 0.90, as both significantly increased upon tissue maturation in the brains that they studied [8,9].

In the present study, we explored whether a similar relationship between tissue stiffness and tissue structure could be identified in our genetic mouse model of TSC/ASD. We characterized the mechanical properties over a range of length scales, spanning the microscale via AFM-enabled indentation, mesoscale via impact indentation, and macroscale via oscillatory shear rheology. Table 3-1 summarizes our key results, providing a comprehensive list of moduli as determined by the various approaches we employed. The magnitudes of these measured moduli were dependent on the technique used and the corresponding assumptions. Indeed, each approach included assumptions regarding material constitutive laws and contact mechanics that relate to the accuracy of a reported mechanical property, but these practical constraints were maintained constant between the control and TSC cohorts to enable comparisons. A series of Mann-Whitney tests were conducted for each parameter to compare the two tissue groups (significance at $p < 0.01$). Table 3-1 also lists the p values. Together, these results demonstrate

that despite exploring multiple length and time scales, we found no statistically significant differences when comparing healthy control and TSC brain tissue. Ultimately, the lack of detectable differences over a broad array of methods and scales suggests that the structural changes associated with this genetic defect do not correspond to significant changes in the brain mechanical properties quantified herein.

Table 3-1 Moduli of healthy control and TSC brain tissue calculated using various techniques and assumptions. Data are represented as mean ± standard deviation ($n > 30$ measurements for AFM-related experiments; $n > 5$ measurements for shear rheology experiments). For each property, p-value corresponds to Mann-Whitney comparisons between control and TSC cohorts, with statistical significance threshold of $p < 0.01$. From [10].

Moduli	Characterization method	Control brain tissue	TSC brain tissue	p value
Young's modulus E (Pa); elastic assumption	AFM-enabled indentation	381 ± 166	348 ±148	0.125
Equilibrium modulus E_∞ (Pa); viscoelastic assumption	Creep via AFM	116 ± 48	150 ± 56	0.083
	Stress relaxation via AFM	125 ± 43	210 ± 98	0.058
	Oscillatory shear rheology	339 ± 100	306 ± 77	0.551
Instantaneous modulus E_0 (Pa); viscoelastic assumption	Creep via AFM	211 ± 71	353 ± 170	0.036
	Stress relaxation via AFM	265 ± 85	410 ± 175	0.074
	Oscillatory shear rheology	1064 ± 265	1057 ± 320	0.967

One of the most notable differences in TSC brain structure is the significant reduction of myelinated axons. Since white matter contains the highest concentration of axons, we hypothesized that the corpus callosum would exhibit the most pronounced differences in mechanical properties. Murine brain contains only roughly 10% white matter, such that the

corpus callosum constitutes a very low percentage of the total sample volume [33]. Thus, AFM-enabled indentation was the only technique of those considered herein that could distinguish reliably between white and gray matter and measure to detect potential differences in local elastic and viscoelastic properties. However, as shown in Fig. 3-2, we found that the effective Young's elastic modulus E and the viscoelastic mechanical properties (E_∞, E_0, and τ_r) of white matter in TSC brain tissue did not differ significantly from that of white matter in our healthy control group. In this study, we considered only coronal brain sections using AFM-enabled indentation; other section orientations (in particular sagittal) require future exploration as they may exhibit different mechanical properties due to the structure and alignment of white matter tracts [34-37].

Additionally, we did not discount the possibility that mechanical differences could be identified at larger length scales, because there is also pronounced demyelination in the murine TSC cortex [14] and potentially other structural differences associated with cellular and ECM organization. Therefore, we conducted spatially concentrated impact loading (impact indentation) and oscillatory shear rheology experiments on whole brain slices. For impact indentation, we observed no detectable differences in maximum penetration depth, energy dissipation capacity, and energy dissipation rate for all impact velocities examined here (Fig. 3-4). Similarly, for rheology, we found no measurable differences in the magnitude and trend of dynamic shear moduli as a function of frequency (Fig. 3-5), suggesting that both stiffness and viscous energy dissipation are similar between TSC and healthy brain tissue. Together, these results suggest that the differences in TSC axon structure, connectivity, and degree of myelination are not sufficient to elicit detectable changes in the mechanical properties that we measured.

To further understand how brain structure may affect mechanical properties, we also examined the ECM of our healthy control and TSC brain tissue. Although we were aware of the differences in axon structure and myelination levels, it was not established whether the composition and organization of the ECM were also detectably altered in this TSC model. Because brain tissue lacks the typical proportion of fibrillar collagen present in other tissues, it is generally believed that the mechanical properties and organization of neurons and glia are the key parameters responsible for the mechanical compliance of brain tissue [38]. The ECM is thought chiefly to provide topographical and biochemical cues to regulate cell behavior [31,38-

41]. However, to our knowledge there has been no direct experimental evidence to support such claims. In our study, we quantified the expression levels of fibronectin and found no significant alterations in TSC compared to control (Fig. 3-6). The similar amount of fibronectin expression is consistent with the hypothesis that the ECM in TSC brain remains similar to that of healthy cohorts, but future work is needed to quantify the levels and organization of other ECM constituents, including laminin, collagen IV, and various chondroitin sulphate proteoglycans. If the ECM is the same in TSC compared to control brain tissue, this structural similarity of the matrix can potentially explain the lack of differences in the tissue mechanical properties that we measured.

While there were no detectable differences between TSC and healthy brain tissue mechanics by the above analyses, our mechanical measurements on mouse brain tissue generally agree well with existing data for healthy brain tissue. Due to the difficulties associated with characterizing compliant materials and brain tissue's complex mechanical behavior caused by its non-linear, viscoelastic, poroelastic, and anisotropic properties, previously reported measurements of linear viscoelastic moduli and elastic moduli have varied by orders of magnitude [42]. Our findings for the elastic moduli of mouse brain are consistent with previous work that have reported E to be on the order of hundreds of Pascals [43,44]. Furthermore, our shear rheology data exhibit similar magnitudes and trends compared to many previous studies reported for various animals, including mice, with weak power laws in G' and G'' as a function of oscillation frequency and a shear relaxation modulus on the order of hundreds of Pascals [28,36,42].

3.5.2 Limitations of characterization methods and mouse model

Each mechanical characterization method utilized herein confers unique limitations and advantages, especially if probing highly compliant, anisotropic, nonlinear, and viscoelastic materials such as brain tissue. Strictly, each method includes assumptions of the material constitutive behavior (e.g., linear elastic or elastically isotropic), sample geometry (e.g., semi-infinite half-plane), and material microstructure (e.g., homogeneous). Additionally, each method employs instrumentation that varies in the instrument control loops for closed feedback control of applied load, applied displacement, or neither. More detailed discussion on the limitations and challenges associated with the techniques we employed can be found in Chapter 2, Section 2.3. For each deformation length scale and method, we recognized these limitations and

simplifications that would affect the accuracy of the magnitude of extracted mechanical properties, and thus designed our experiments to enable systematic comparisons of a given property between two sample groups: brain tissue obtained from control and TSC cohorts. In fact, Table 3-1 illustrates that the magnitude of a given property can vary with measurement approach; such differences are attributed reasonably to each method's deviation from all assumptions employed in data analysis and potentially to actual differences at different length scales and deformation rates. However, we emphasize that our goal herein was to consider detectable and significant differences in any one property, measured in the same way and under the same conditions, between murine brain tissue with and without this TSC genetic mutation associated with ASD.

The various limitations for each characterization method, along with the inherent interregional and sample-to-sample variation of brain tissue, can contribute to the standard deviation of properties reported in Section 3-3, as one consideration of measurement precision. This variation can potentially obfuscate resolution of any differences in mechanical properties between control and TSC brain tissue. However, the number of replicate measurements, replicate samples, and independent experiments for each approach provides confidence that these mechanical properties do not differ among mouse brain tissue obtained from the control and TSC cohorts. While this finding is clear for this animal model, our findings do not demonstrate nor do we suggest that brain tissue of humans exhibiting ASD are mechanically indistinguishable from brain tissue of those who do not exhibit such characteristics. One key feature of human brain, not shared by murine brain, is that it undergoes gyrification. Previous studies have associated abnormalities in brain folding with autism [45-47], and thus that distinction remains a topic of important future consideration that can draw on the approaches and findings discussed herein. We also note that the age of our mice prior to sacrifice was 21 days, and it is possible that the mechanical properties of white matter in TSC and control brains will vary differently with developmental age. However, as is observed with this mouse model, the TSC cohort did not survive consistently beyond 21 days such that we could not consider differences at later developmental stages.

3.6 Conclusions

Despite structural changes of the cellular components in our TSC/ASD mouse brain model, such as hypomyelination and disorganization of axons, we found that tissue mechanical properties were unaffected at every length- and time-scale explored. Stiffness of neuronal axons transfected with *Tsc1* knockout was also unaffected in ways that could be correlated with this mutation. We found the expression levels of fibronectin in TSC and control brain tissue to be similar, which is consistent with the lack of mechanical differences observed. Our results indicate that cell-level changes in myelination and neuronal organization do not manifest in detectable mechanical changes for this particular murine model of ASD. This investigation of the mechanical characteristics of the brain has broadened our understanding of causes and markers of TSC/ASD, while raising questions about whether any mechanical differences can be detected in other animal models of ASD or other disease models that also feature abnormal brain structure. Additionally, future work can leverage these methods to characterize the mechanical properties of brain tissue after exposure to traumatic injury to investigate whether the reduced myelin content associated with injured brain lesions will translate to significant mechanical differences. For subsequent studies, more sophisticated animal models, such as porcine or bovine models, would be preferable to murine models because any potential differences are expected to be more pronounced and more likely to be detectable if the white matter composition is more prevalent and the brain undergoes gyrification similar to human brain. Having studied the mechanical behavior of brain tissue from various species and disease models, Chapter 4 describes our efforts in developing and characterizing new synthetic polymeric gels for comparison against brain tissue. Our goal in those studies is to establish fundamental principles to inform the design of engineered brain tissue simulants.

3.7 References

[1] R.C. Armstrong, A.J. Mierzwa, C.M. Marion, and G.M. Sullivan, White matter involvement after TBI: clues to axon and myelin repair capacity, *Experimental Neurology*, 2016, 275, 328-333.

[2] R.A. Hurley, J.C. McGowan, K. Arfanakis, and K.H. Taber, Traumatic axonal injury: novel insights into evolution and identification, *Journal of Neuropsychiatry & Clinical Neurosciences*, 2004, 16, 1-7.

[3] D.M. Morales, N. Marklund, D. Lebold, H.J. Thompson, A. Pitkanen, W.L. Maxwell, L. Longhi, H. Laurer, M. Maegele, E. Neugebauer, D.I. Graham, N. Stocchetti, and T.K. McIntosh, Experimental models of traumatic brain injury: do we really need to build a better mousetrap?, *Neuroscience*, 2005, 136, 971-989.

[4] A. Goriely, M.G. Geers, G.A. Holzapfel, J. Jayamohan, A. Jerusalem, S. Sivaloganathan, W. Squier, J.A. van Dommelen, S. Waters, and E. Kuhl, Mechanics of the brain: perspectives, challenges, and opportunities, *Biomechanics and Modeling in Mechanobiology*, 2015, 14, 931-965.

[5] M.C. Murphy, J. Huston, C.R. Jack, K.J. Glaser, A. Manduca, J.P Felmlee, and R.L. Ehman, Decreased brain stiffness in Alzheimer's disease determined by magnetic resonance elastography, *Journal of Magnetic Resonance Imaging*, 2012, 34, 494-498.

[6] J. Wuerfel, F. Paul, B. Beierbach, U. Hamhaber, D. Klatt, S. Papazoglou, F. Zipp, P. Martus, J. Braun, and I. Sack, MR-elastography reveals degradation of tissue integrity in multiple sclerosis, *NeuroImage*, 2010, 49, 2520-2525.

[7] K. Riek, J.M. Millward, I. Hamann, S. Mueller, C.F. Pfueller, F. Paul, J. Braun, C. Infante-Duarte, and I. Sack, Magnetic resonance elastography reveals altered brain viscoelasticity in experimental autoimmune encephalomyelitis, *NeuroImage: Clinical*, 2012, 1, 81-90.

[8] J. Weickenmeier, R. de Rooij, S. Budday, P. Steinmann, T.C. Ovaert, and E. Kuhl, Brain stiffness increases with myelin content, *Acta Biomaterialia*, 2016, 42, 265-272.

[9] J. Weickenmeier, R. de Rooij, S. Budday, P. Steinmann, T.C. Ovaert, and E. Kuhl, The mechanical importance of myelination in the central nervous system, *Journal of the Mechanical Behavior of Biomedical Materials*, 2017, 76, 119-124.

[10] B. Qing, E.P. Canovic, A.S. Mijailovic, A. Jagielska, M.J. Whitfield, A.L. Lowe, E. Kelly, D. Turner, M. Sahin, and K.J. Van Vliet, Probing mechanical properties of brain in a tuberous sclerosis model of autism, *Journal of Biomechanical Engineering*, 2018, in review.

[11] P. Curatolo, R. Bombardieri, and S. Jozwiak, Tuberous sclerosis, *Lancet*, 2008, 372, 657-668.

[12] S.S. Jeste, M. Sahin, P. Bolton, G.B. Ploubidis, and A. Humphrey, Characterization of autism in young children with tuberous sclerosis complex, *Journal of Child Neurology*, 2008, 23, 520-525.

[13] P. Tsai and M. Sahin, Mechanisms of neurocognitive dysfunction and therapeutic considerations in tuberous sclerosis complex, *Current Opinion in Neurology*, 2011, 24, 106-113.

[14] L. Meikle, D.M. Talos, H. Onda, K. Pollizzi, A. Rotenberg, M. Sahin, F.E. Jensen, and D.J. Kwiatkowski, A mouse model of tuberous sclerosis: neuronal loss of Tsc1 causes dysplatisc and ectopic neruons, reduced myelination, seizure activity, and limited survival, *The Journal of Neuroscience*, 2007, 27, 5546-5558.

[15] L. Meikle, K. Pollizzi, A. Egnor, I. Kramvis, H. Lane, M. Sahin, and D.J. Kwiatkowski, Response of a neuronal model of tuberous sclerosis to mammalian target of rapamycin (mTOR) inhibitors: effects of mTORC1 and Akt signaling lead to improved survival and function, *The Journal of Neuroscience*, 2008, 28, 5422-5432.

[16] Y. Choi, A. Di Nardo, I. Kramvis, L. Meikle, D.J. Kwiatkowski, M. Sahin, and X. He, Tuberous sclerosis complex proteins control axon formation, *Genes & Development*, 2008, 22, 2485-2495.

[17] D. Nie, A. Di Nardo, J.M. Han, H. Baharanyi, I. Kramvis, T. Huynh, S. Dabora, S. Codeluppi, P. Pandolfi, E. Pasquale, and M. Sahin, Tsc2-Rheb signaling regulates EphA-mediated axon guidance, *Nature Neuroscience*, 2010, 13, 163-172.

[18] W.W. Lewis, M. Sahin, B. Scherrer, J.M. Peters, R.O. Suarez, V.K. Vogel-Farley, S.S. Jeste, M.C. Gregas, S.P. Prabhu, C.A. Nelson, and S.K. Warfield, Impaired language pathways in tuberous sclerosis complex patients with autism spectrum disorders, *Cerebral Cortex*, 2013, 23, 1526-1532.

[19] J.M. Peters, M. Sahin, V.K. Vogel-Farley, S.S. Jeste, C.A. Nelson, M.C. Gregas, S.P. Prabhu, B. Scherrer, and S.K. Warfield, Loss of white matter microstructural integrity is associated with adverse neurological outcome in tuberous sclerosis complex, *Academic Radiology*, 2012, 19, 17-25.

[20] J.M. Tillema, J.L. Leach, D.A. Krueger, and D.N. Franz, Everolimus alters white matter diffusion in tuberous sclerosis complex, *Neurology*, 2012, 78, 526-531.

[21] Y. Zhu, M.I. Romero, P. Ghosh, Z. Ye, P. Charnay, E.J. Rushing, J.D. Marth, and L.F. Parada, Ablation of NF1 function in neurons induces abnormal development of cerebral cortex and reactive gliosis in the brain, *Genes & Development*, 2001, 15, 859-876.

[22] S. Nicolle, M. Lounis, and R. Willinger, Shear properties of brain tissue over a frequency range relevant for automatic impact situations: new experimental results, *Stapp Car Crash Journal*, 2004, 48, 239-258.

[23] M. Hrapko, J.A. van Dommelen, G.W. Peters, and J.S. Wismans, The mechanical behaviour of brain tissue: large strain response and constitutive modelling, *Biorheology*, 2006, 43, 623-636.

[24] A. Jagielska, A.L. Norman, G. Whyte, K.J. Van Vliet, J. Guck, and R.J. Franklin, Mechanical microenvironment modulates biological properties of oligodendrocytes progenitor cells, *Stem Cells and Development*, 2012, 21, 2905-2914.

[25] Z.I. Kalcioglu, M. Qu, K.E. Strawhecker, T. Shazly, E. Edelman, M.R. VanLandingham, J.F. Smith, and K.J. Van Vliet, Dynamic impact indentation of hydrated biological tissues and tissue surrogate gels, *Philosophical Magazine*, 2011, 91, 1339-1355.

[26] Z.I. Kalcioglu, R.A. Mrozek, R. Mahmoodian, M.R. VanLandingham, J.L. Lenhart, and K.J. Van Vliet, Tunable mechanical behavior of synthetic organogels as biofidelic tissue simulants, *Journal of Biomechanics*, 2013, 46, 1583-1591.

[27] F. Shen, T.E. Tay, J.Z. Li, S. Nigen, P.V. Lee, and H.K. Chan, Modified Bilston nonlinear viscoelastic model for finite element head injury studies, *Journal of Biomechanical Engineering – Transactions of the ASME*, 2006, 128, 797-801.

[28] K. Pogoda, L. Chin, P.C. Georges, F.J. Byfield, R. Bucki, R. Kim, M. Weaver, R.G. Wells, C. Marcinkiewicz, and P.A. Janmey, Compression stiffening of brain and its effect on mechanosensing by glioma cells, *New Journal of Physics*, 2014, 16, 075002.

[29] J.M. Stoffels, J.C. de Jonge, M. Stancic, A. Nomden, M.E. van Strien, D. Ma, Z. Siskova, O. Maier, C. Ffrench-Constant, R.J. Franklin, D. Hoekstra, C. Zhao, and W. Baron, Fibronectin aggregation in multiple sclerosis lesions impairs remyelination, *Brain*, 2013, 136, 116-131.

[30] R. Milner, S.J. Crocker, S. Hung, X. Wang, R.F. Frausto, and G.J. del Zoppor, Fibronectin- and vitronectin-induced microglial activation and matrix metalloproteinase-9 expression is mediated by integrins alpha5beta1 and alphavbeta5, *Journal of Immunology*, 2007, 178, 8158-8167.

[31] K. Schregel, E. Wuerfel, P. Garteiser, I. Gemeinhardt, T. Prozorovski, O. Aktas, H. Merz, D. Petersen, J. Wuerfel, and R. Sinkus, Demyelination reduces brain parenchymal stiffness quantified by magnetic resonance elastography, *Proceedings of the National Academy of Sciences of the United States of America*, 2012, 109, 6650-6655.

[32] H. Uysal and F.W. Hemming, Changes in the expression and distribution of fibronectin, laminin and tenascin by cultured fibroblasts from skin lesions of patients with tuberous sclerosis, *British Journal of Dermatology*, 1999, 141, 658-666.

[33] E.C. Bush and J.M. Allman, The scaling of white matter to gray matter in cerebellum and neocortex, *Brain, Behavior and Evolution*, 2003, 61, 1-5.

[34] J.D. Finan, E.M. Pearson, and B. Morrison III, Viscoelastic properties of the rat brain in the horizontal plane, *IRCOBI Conference*, 2012.

[35] N. Yoganandan, F.A. Pintar, B.D. Stemper, M.B. Schlick, M. Philippens, and J. Wismans, Biomechanics of human occupants in simulated rear crashes: documentation of neck injuries and comparison of injury criteria, *Stapp Car Crash Journal*, 2000, 44, 189-204.

[36] M. Hrapko, J.A. van Dommelen, G.W. Peters, and J.S. Wismans, Characterization of the mechanical behaviour of brain tissue in compression and shear, *Biorheology*, 2008, 45, 663-676.

[37] Y. Feng, R.J. Okamoto, R. Namani, G.M. Genin, and P.V. Bayly, Measurements of mechanical anisotropy in brain tissue and implications for transversely isotropic material

models of white matter, *Journal of Mechanical Behavior of Biomedical Materials*, 2013, 23, 117-132.

[38] K. Franze, P.A. Janmey, and J. Guck, Mechanics in neuronal development and repair, *Annual Review of Biomedical Engineering*, 2013, 15, 227-251.

[39] J. van Horssen, C.D. Dijkstra, and H.E. de Vries, The extracellular matrix in multiple sclerosis pathology, *Journal of Neurochemistry*, 2007, 103, 1293-1301.

[40] D. Bonneh-Barkay and C.A. Wiley, Brain extracellular matrix in neurodegeneration, *Brain Pathology*, 2009, 19, 573-585.

[41] A. Dityatev, C.I. Seidenbecher, and M. Schachner, Compartmentalization from the outside: the extracellular matrix and functional microdomains in the brain, *Trends in Neurosciences*, 2010, 33, 503-512.

[42] S. Chatelin, A. Constantinesco, and R. Willinger, Fifty years of brain tissue mechanical testing: from in vitro to in vivo investigations, *Biorheology*, 2010, 47, 255-276.

[43] J.A. van Dommelen, T.P. van der Sander, M. Hrapko, and G.W. Peters, Mechanical properties of brain tissue by indentation: interregional variation, *Journal of the Mechanical Behavior of Biomedical Materials*, 2010, 3, 158-166.

[44] B.S. Elkin, A. Ilankovan, and B. Morrison, Age-dependent regional mechanical properties of the rat hippocampus and cortex, *Journal of Biomechanical Engineering*, 2010, 132, 011010.

[45] A.Y. Hardan, R.J. Jou, M.S. Keshavan, R. Varma, and N.J Minshew, Increased frontal cortical folding in autism: a preliminary MRI study, *Pyschiatric Research*, 2004, 131, 263-268.

[46] C.W. Nordahl, D. Dierker, I. Mostafavi, C.M. Schumann, S.M. Rivera, D.G. Amaral, and D.C. Van Essen, Cortical folding abnormalities in autism revealed by surface-based morphometry, *Journal of Neuroscience*, 2007, 27, 11725-11735.

[47] S. Budday, P. Steinmann, and E. Kuhl, Physical biology of human brain development, *Frontiers in Cellular Neuroscience*, 2015, 9, 257.

Chapter 4: Hierarchically structured gels as potential brain tissue simulants

4.1 Introduction

The primary aim of this thesis is to engineer synthetic polymer gels that accurately mimic key mechanical properties of brain tissue. These mechanical surrogates, which we call brain tissue simulants, can be valuable tools for evaluating protective equipment and understanding injury mechanisms, for example in response to concentrated mechanical impact events [1-3]. The previous two chapters focused on the mechanical characterization of brain tissue using multiple techniques that differ in loading configurations, loading histories, deformation length scales, and deformation timescales. Of those techniques, impact indentation applies loading conditions that are most representative of ballistic testing conditions. Therefore, in this chapter, we seek to design a materials system that can be tuned to fully match the impact response of brain tissue as measured by impact indentation, specifically in terms of deformation resistance, energy dissipation capacity, and energy dissipation rate.

A recent study of individual polydimethylsiloxane (PDMS) organogels as potential tissue simulant candidates indicated a wide range of mechanical tunability, but failed to fully reflect the complex rate-dependent behavior of brain tissue [4]. The elastic and viscoelastic properties of such PDMS organogels can be tuned systematically by adjusting parameters such as the concentration of chemical crosslinkers, molecular weight of polymer chains, and amount of solvent loading [5-7]. However, a significant limitation of those organogels was that each of those composition parameters influenced both the deformation resistance and energy dissipation characteristics of the impacted material. As a result, independent modulation of each of these properties had not been achieved by prior studies [4]. To address this problem, we here extended that monolithic system to create a simple bilayered composite, by bonding a highly compliant PDMS elastomer (CY52-276 Dow Corning®) layer with a PDMS organogel layer. Our objective was to introduce hierarchical structure into the synthetic material, chiefly to decouple these impact dissipation characteristics but also noting that biological tissues naturally exhibit complex hierarchical structures that influence their mechanical properties at different time and length scales [8-10]. We chose to build on the existing PDMS organogels because this polymer is

environmentally stable in air, easily manufactured, and cost effective – all of which are important features of a practical brain tissue simulant material for applications including ballistic testing and robotic surgery optimization [2,11].

Our studies on this PDMS-based hierarchical system were predicated on previous computational work initiated by Dr. Roza Mahmoodian (Van Vliet group). Dr. Mahmoodian developed a multiscale finite element model of impact indentation, and was the first to investigate bilayered gel systems as potential candidates for soft tissue simulants [12]. She used the finite element model to produce higher fidelity designs for simultaneous capturing of energy dissipation and impact resistance metrics via a layered arrangement that took advantage of already available and easily synthesized materials with different dissipative properties as a means for decoupling the two design metrics. This approach enabled control over tissue simulant material design at two scales: at the component level (solvent and crosslinked polymer chains) for each individual gel, and at the layer level. The main advantage of this bilayered composite system is that it could achieve a target performance with great flexibility and tunability, by leveraging the key properties of each involved component. Appendix F presents a manuscript [12] in preparation that describes these computational studies as well as the experimental validation of those predictions that was conducted by the thesis author.

In this chapter, we aimed to further validate those computational predictions and demonstrate experimentally that PDMS-based bilayered composites can indeed be optimized to fully match the impact response of brain tissue – the most mechanically compliant tissue comprising biological organs (Section 4.2). The work presented in Section 4.2 was published in *Molecular Systems Design & Engineering* [13]. We synthesized variations of the bilayered PDMS composite and conducted impact indentation experiments to explore whether and how the layer stiffness and thickness affected the impact response metrics over a range of impact velocities. With this understanding of how the properties of each layer modulate the material's overall impact response, we designed and optimized a bilayered composite to fully match the impact energy dissipation response of porcine brain tissue.

Although we demonstrated successfully that the PDMS composites could be tuned to match porcine brain tissue under the range of conditions studied here, there are potential disadvantages of using a PDMS-based materials system, such as the high surface adhesion that these compliant gels exhibit, which could limit its effectiveness in certain applications. For example, in ballistic

testing applications, if surface adhesion is the dominating energy dissipation mechanism that allowed the PDMS composite to behave like brain tissue, the impact energy dissipation response of the composite may differ once a protective helmet is introduced and the projectile no longer directly contacts the gel. Thus, as part of a collaboration with Prof. Bradley Olsen's group at MIT, we also explored hierarchically structured protein-based hydrogels as an alternative candidate for brain tissue simulants (Section 4.3). Dr. Shengchang Tang (Olsen group) designed and synthesized these physically associating protein-based hydrogels that incorporated coiled-coil associations and topological entanglement. The thesis author conducted impact indentation experiments to characterize and compare the impact energy dissipation response to that of brain tissue.

4.2 PDMS-based bilayered composites

4.2.1 Materials synthesis

The bilayered polymer composite consisted of a viscoelastic PDMS organogel beneath a more compliant PDMS elastomer. An illustration of the composite is shown in Fig. 4-1. The PDMS organogel was a chemically crosslinked PDMS network (formed from vinyl-terminated PDMS and tetrafunctional silane crosslinkers) swollen in a non-reactive methyl-terminated PDMS solvent. Full processing details for the organogel, developed by Mrozek and Lenhart et al. at the U.S. Army Research Laboratory (ARL), have been reported earlier [7]. Each polymer composite in the present study included a organogel layer of 5 mm thickness and the same composition: 60 vol% 1.1 kg/mol solvent with 2.25:1 silane:vinyl stoichiometry. The silicone rubber that served as the top layer was a commercial grade of PDMS called CY 52-276 (Dow Corning®). Similar to the more commonly known Sylgard® 184, CY 52-276 is a two-component silicone kit comprising a prepolymer base (Part A) and a catalyst (Part B), which allows for facile variation of elastomer stiffness based on the relative amount of each component in the mixture. However, CY 52-276 produced fully cured elastomers with a lower shear elastic modulus G of ~ 1 kPa that we confirmed using macroscale oscillatory shear rheology and was necessary for mimicking brain tissue compliance; Sylgard® 184 is considerably stiffer at concentrations required for full polymerization. The thickness of the compliant top silicone layer was controlled by the volume

of mixture that was prepared, and these samples were cured at 80°C overnight. Because the top and bottom layer were both PDMS-based materials, oxygen plasma treatment of each layer enabled complete bonding. It has been shown previously that oxidation at the surface of PDMS layers creates covalent siloxane bonds from exposed silanol groups [14,15]. Immediately after exposure to oxygen plasma (for 30 s at 30 W), the two layers were pressed together to form a bilayered polymer composite.

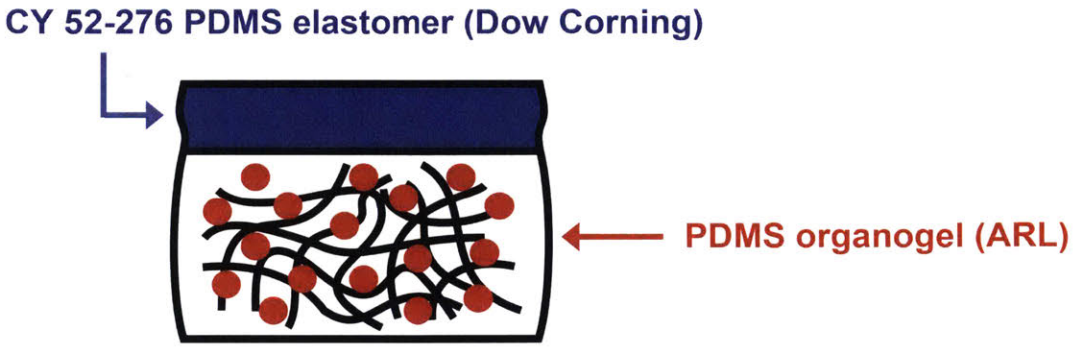

Figure 4-1 Bilayered PDMS-based composite as potential brain tissue simulant gel. Bottom layer comprises a 5 mm thick viscoelastic PDMS organogel originally synthesized at Army Research Laboratory (ARL) by Mrozek et al. The organogel is a chemically crosslinked PDMS network (shown in black), which is formed from vinyl-terminated PDMS and tetrafunctional silane crosslinkers, swollen in a non-reactive methyl-terminated PDMS solvent (represented as red circles). Top layer comprises of a PDMS elastomer called CY 52-276 of tunable thickness and stiffness, and commercially available from Dow Corning.

4.2.2 Enhanced tunability of bilayered composite design

Motivated by the need to decouple energy dissipation capacity and deformation resistance in synthetic polymers, and by the inherent hierarchical structure of many biological tissues, we sought to investigate whether a simple bilayer composite could provide the necessary tunability to match the impact response of brain tissue with respect to all three impact energy dissipation metrics. As in all composites, the goal was to leverage key properties of different materials to optimize overall performance. Using a previously characterized PDMS organogel [4] as a starting point, which did not reflect the energy dissipation characteristics of brain tissue, we added a more compliant PDMS elastomer (CY 52-276 Dow Corning®) as a top layer (Fig. 4-1).

One advantage of multiple layers is the introduction of two new tunable parameters: the thickness and the stiffness of the top layer. Although we could also adjust the mechanical properties of the PDMS organogel, we chose to maintain one molecular composition of the bottom layer for all composites and focused on how the addition of the top layer modulated the overall deformation resistance and energy dissipation characteristics of the composite. Additionally, the thickness of bottom PDMS organogel was maintained at 5 mm for all bilayered composites, which was sufficiently thick to eliminate any contributions from the finite thickness effect for the ranges of deformation studied here.

4.2.2.1 Effects of varying top layer stiffness

We first considered the effects of varying the stiffness of the top layer, while maintaining the layer thickness constant. Figure 4-2(A-C) shows the measured impact response for three bilayered composites at a range of impact velocities. The shear storage modulus G', which we use to quantify stiffness, of the CY 52-276 layer of bilayer 1, 2, and 3 was 4.75 kPa, 1 kPa, and 0.85 kPa, respectively; the top layer thickness t was 2.6 mm and the overall sample thickness was approximately 8 mm. As expected, a bilayered composite with a stiffer top layer exhibited lower x_{max} (Fig. 4-2(A)). Additionally, K decreased and Q increased with increasing stiffness of the top layer (Fig. 4-2(B and C)). Note that for the sample with the lowest top layer stiffness (bilayer 3), we could only quantify Q at the lowest applied impact velocity because at higher impact velocities, the impact energy dissipated so quickly that we could not reliably fit an exponential decay function to the damped oscillations.

These results reflect the fact that elastic and viscous properties are typically coupled in bulk viscoelastic materials. Increasing the crosslinking density of the PDMS top layer leads to higher storage moduli but also lower loss moduli. The loss moduli or energy dissipative properties of PDMS are primarily driven by the amount and relative molecular weight distribution of network imperfections, which are mostly dangling chains that can entangle [16]. Chain entanglement also drives the adhesiveness of PDMS, and thus increasing the stiffness of the PDMS top layer will result in lower surface adhesion [16,17]. This effect was especially pronounced for the silicone formulations studied here. During the impact event, the rebound velocity v_{out} is expected to decrease if more adhesive forces inhibit the pendulum from retracting; Equation 2-20 implies that K will then effectively increase. Because more energy is dissipated during the first impact

cycle, the overall energy dissipation rate will also increase, corresponding to a lower Q value. Although we reduced molecular interactions between the probe and sample surface by conducting experiments in PBS containing 3% Pluronic® F108, surface adhesion is likely still a non-negligible mechanism of energy dissipation in these material systems. Whether surface adhesion or viscous dissipation in the bulk material is the dominating mechanism of energy dissipation under these loading conditions and strain rates will be explored in the subsequent chapter.

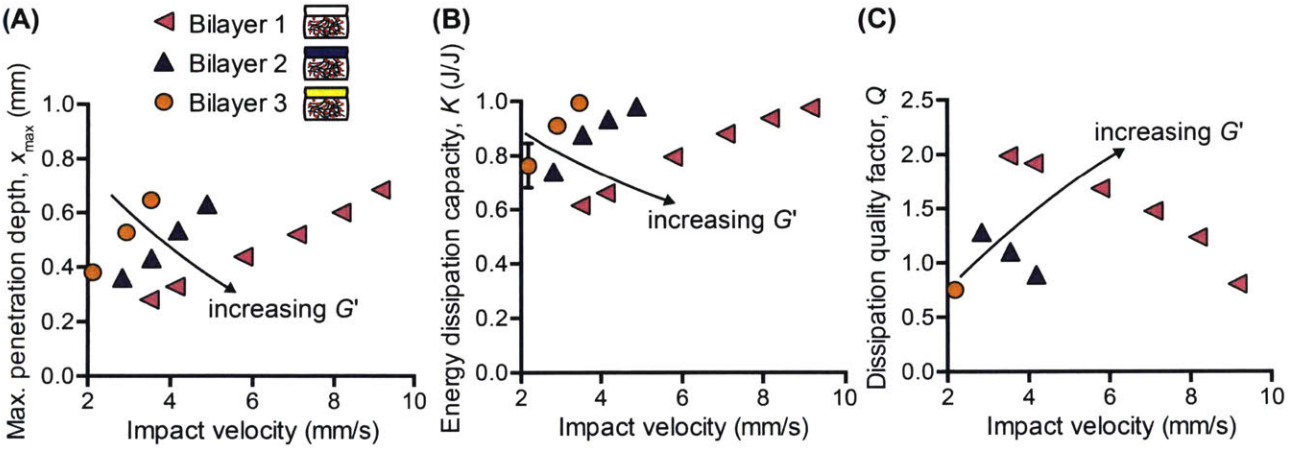

Figure 4-2 Mechanical tunability of bilayered composite gels. All bilayers included the same 5 mm thick bottom PMDS organogel layer of 60 vol% 1.1 kg/mol solvent with 2.25:1 silane:vinyl stoichiometry. Bilayer 1, 2, and 3 consisted of a top PDMS layer of 2.6 mm thickness and varied stiffness (4.75 kPa, 1 kPa, and 0.85 kPa, respectively). (A) Maximum penetration depth, (B) energy dissipation capacity, and (C) dissipation quality factor as a function of impact velocity. Bilayers with a stiffer top layer were more resistant to deformation, dissipated less impact energy, and dissipated energy faster. Data are represented as mean ± standard deviation, and error bars may appear smaller than data symbols (n = 3–4 measurements per data point). From [13].

4.2.2.2 Effects of varying top layer thickness

Next, we maintained G' of the CY 52-276 layer constant at 1 kPa and explored the effects of varying only the top layer thickness. Bilayer 2, 4, and 5 consisted of a 2.6 mm, 0.9mm, and 0.7 mm thick top layer, respectively. Tuning the thickness of the top layer, within the range studied here, negligibly affected the deformation resistance of the composite (Fig. 4-3(A)). Interestingly, the measured x_{max} of these three composites was also identical to that of the CY 52-276 PDMS

material itself (Fig. 4-5(A)). Note that this monolithic CY 52-276 sample also had a G' of 1 kPa but was made thicker (5 mm) to minimize contributions from the finite thickness effect [18-21]. This indicates that the deformation resistance of the bilayered composite is governed strongly by the stiffness of the top layer, when the top layer is more compliant than the bottom layer. To support this conclusion, we also conducted impact indentation experiments on a thin CY 52-276 monolayer (0.9 mm thick) adhered directly to the aluminum sample post. We found x_{max} to be the same magnitude for the thin monolayer and thick monolayer at impact velocities under 4 mm/s, and observed a finite thickness effect only at the higher impact velocities, as shown in Fig. 4-4. The contributions from the underlying aluminum substrate were sufficiently small (considerably less than the differences in x_{max} between bilayer 1 and 2 in Fig. 4-2(A)) that it is understandable that the viscoelastic PDMS organogel substrate of kPa stiffness did not detectably influence the composite's overall resistance to deformation under the loading conditions investigated here.

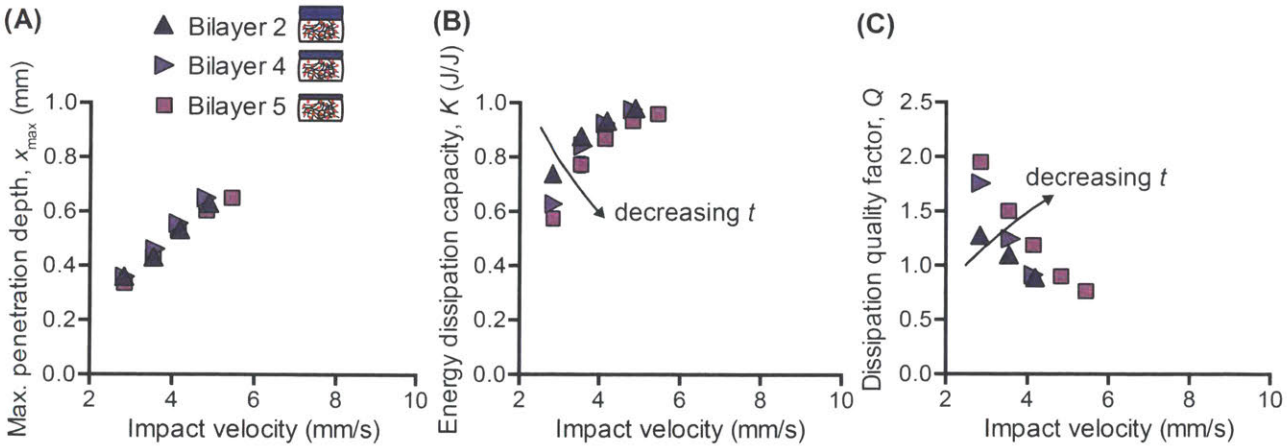

Figure 4-3 Mechanical tunability of bilayered composite gels. All bilayers included the same 5 mm thick bottom PMDS organogel layer of 60 vol% 1.1 kg/mol solvent with 2.25:1 silane:vinyl stoichiometry. Bilayer 2, 4, and 5 consisted of a top layer of 1 kPa stiffness and varied thickness (2.6 mm, 0.9 mm, and 0.7 mm, respectively). (A) Maximum penetration depth, (B) energy dissipation capacity, and (C) dissipation quality factor as a function of impact velocity. Bilayers with a thicker top layer exhibited a slightly higher energy dissipation capacity and a slightly lower dissipation quality factor. Maximum penetration depth was not affected detectably when only the top layer thickness was varied over the range considered. Data are represented as mean ± standard deviation, and error bars appear smaller than data symbols (n = 3–4 measurements per data point). From [13].

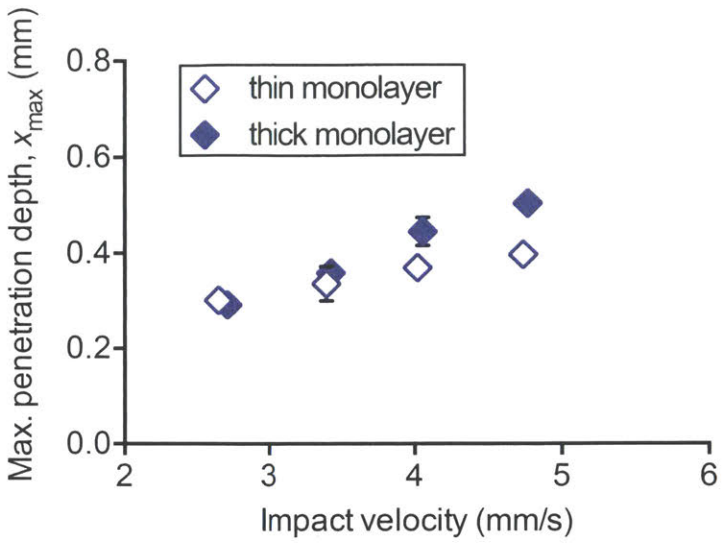

Figure 4-4 Impact indentation experiments were conducted on a thinner CY 52-276 monolayer (thickness of 0.9 mm) and a thicker CY 52-276 monolayer (thickness of 5 mm). The maximum penetration depths of the two samples were indistinguishable at impact velocities less than 4 mm/s. Contributions from the underlying stiff aluminum sample post were only observed at impact velocities greater than 4 mm/s. Data are represented as mean ± standard deviation, and error bars may appear smaller than data symbols (n = 3 measurements per data point).

Separately, varying only the thickness of the top layer, while maintaining its composition and thus mechanical properties constant, detectably altered the energy dissipation characteristics of the composite (Fig. 4-3(B and C)). As the thickness decreased, K decreased and Q increased – trends that were particularly evident at the lower impact velocities. Bilayer 5, which included the thinnest top layer among these samples, responded most similarly to the monolithic PDMS organogel, suggesting that the bottom PDMS organogel layer dominated the composite's overall energy dissipation response. When comparing Fig. 4-2 with Fig. 4-3, the differences among bilayers 2, 4, and 5 were not as pronounced as those among bilayers 1, 2, and 3. Therefore, these data demonstrate the means to first coarsely tune the composite system (by adjusting the stiffness of the top layer) and then finely tune (by adjusting the thickness of the top layer) toward an overall targeted energy dissipation response. Also, because x_{max} is independent of top layer thickness whereas K and Q are not, we were able to decouple the composite's deformation resistance from its energy dissipation characteristics – an important feature that was lacking in previous polymer simulant materials. However, we note that the extent to which we could decouple x_{max} from K and Q was still bound by the properties of each individual layer. For

example, with the bilayered composites studied here, it would not be straightforward to achieve a magnitude of x_{max} exceeding that of the PDMS organogel and also a magnitude of K less than that of the PDMS organogel. Nonetheless, for compliant biological tissues such as brain tissue, which exhibit both substantial deformation and high energy dissipation capacity, the tunability accessible within this system is sufficient.

4.2.3 Optimization to match impact response of porcine brain tissue

With the improved tunability of this bilayered PDMS composite, we next considered whether the impact response of adult porcine (pig) brain could be replicated over a range of loading conditions. Porcine brain was chosen as the target in this study because it was the closest representation of human brain that is readily accessible for replicate experiments, such that adverse tissue preservation steps (such as freezing that can alter tissue structure) are not required [22]. The first objective of our optimization process was to identify a composition of CY 52-276 PDMS with mechanical stiffness that resulted in the same deformation resistance as porcine brain. We iteratively characterized the storage modulus G' (at 1 Hz) of this polymer for different prepolymer:initiator-catalyst ratios, and measured the corresponding x_{max} via impact indentation. If deformation resistance was too low compared to that of brain tissue, we synthesized a more compliant CY 52-276 by increasing the volume fraction of prepolymer, and vice versa. These steps were iterated to establish the composition and stiffness required to achieve the target penetration depth over the range of velocities of interest.

For adult porcine brain tissue, a CY 52-276 layer with G' = 1 kPa (6:5 prepolymer to initiator-catalyst v/v) was needed. The next objective of our optimization process was to tune the thickness of the CY 52-276 layer such that the bilayered composite exhibited the same K and Q as porcine brain over a range of impact velocities. Recall that varying the thickness of the top layer incurred negligible effects on x_{max}, so if we met our second objective, this composite would be expected to fully recapitulate all three energy dissipation metrics. Following the trends in Fig. 4-3(B and C), we used a thinner CY 52-276 layer to decrease K and increase Q, and iteratively identified that a top layer thickness of 0.7 mm and stiffness of 1 kPa reflected the deformation resistance, energy dissipation capacity, and energy dissipation rate of porcine brain tissue over a range of impact velocities.

Figure 4-5 illustrates that neither of the individual components of this bilayer exhibited all of these impact energy dissipation properties, such that the bilayer provided a unique composite response. The PDMS organogel failed to replicate any of the three metrics of porcine brain. Although the CY 52-276 PDMS monolayer exhibited the same deformation resistance as porcine brain (Fig. 4-5(A)), its energy dissipation characteristics were noticeably different (Fig. 4-5(B and C)). When we combined these two materials in a simple bilayer, x_{max} was similar to that of the monolithic CY 52-276, but both K and Q were modified to intermediary values that reflected those of porcine brain.

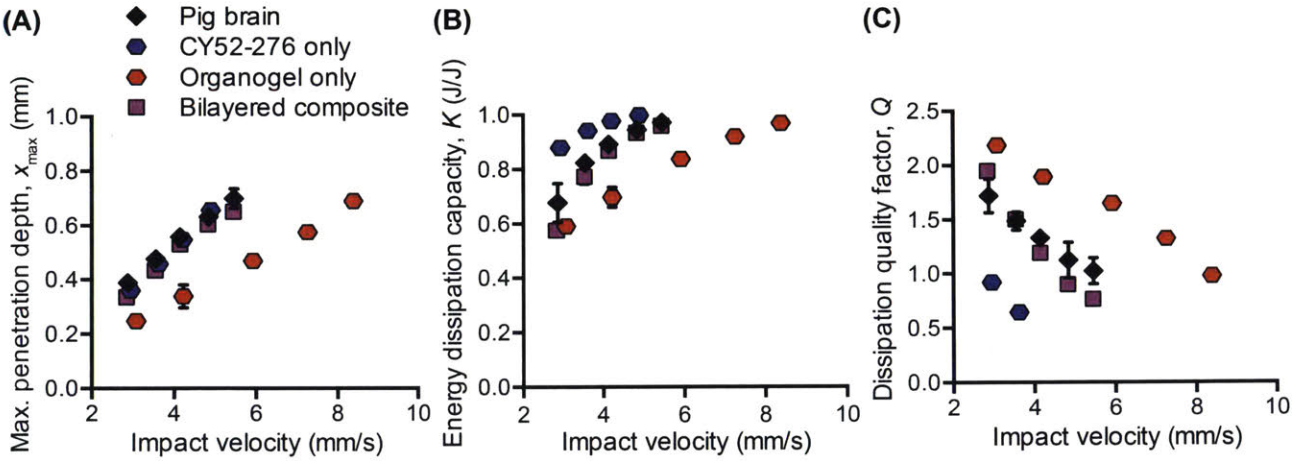

Figure 4-5 Comparison of the impact response of a bilayered composite to that of the individual layer components and the target porcine brain tissue: (A) maximum penetration depth, (B) energy dissipation capacity, and (C) dissipation quality factor as a function of impact velocity. The composition of the bilayered composite corresponds to that of bilayer 5 from Fig. 4-3. This composite gel reasonably approximated the impact response of porcine brain tissue for all three impact response metrics, whereas the individual layers alone did not. Data are represented as mean ± standard deviation, and error bars may appear smaller than data symbols (n = 3–4 measurements per data point). From [13].

Figure 4-5 demonstrates clearly our primary design objective of a simple composite that serves as a mechanical surrogate for porcine brain tissue under concentrated impact loading. However, we also note that this mechanical impact response indicated mechanisms of energy dissipation that motivated further study, which will be presented subsequently in Chapter 5. Upon closer examination of the impact velocity- dependence in Fig. 4-5, we found the bilayered

composite to behave similarly to the bottom organogel at the lowest impact velocity in terms of K and Q. However, as the impact velocity increased, the energy dissipation response of the composite deviated from that of the organogel and approached that of the CY 52-276. One might have initially predicted the opposite trend, because higher impact velocities translate to greater penetration depths (very close to the total thickness of the top layer when applying the highest impact velocity), which should lead to a greater contribution from the underlying organogel to the composite's overall impact energy dissipation response. Therefore, We posited that adhesion between the impacting probe and top layer strongly modulated impact energy dissipation, despite the fact that these experiments on the PDMS bilayers were conducted in saline that included a surfactant to reduce probe-sample adhesion. Impact indentation experiments on brain tissues intentionally did not include this surfactant. Greater penetration depths also imply a greater contact area between the probe and sample surface when interfacial wetting occurs between the probe and impacted polymer, thus promoting adhesive interactions that would increase K and decrease Q [23,24].

Although the bilayered composite mechanically mimicked porcine brain during these impact indentation experiments, and thus met our primary goal of tunability and parameter decoupling, we note that in the wider context of certain tissue surrogate applications (e.g., assessment of a new protective helmet subjected to ballistic tests), the simulant material may not directly come into contact with the fired projectiles. In those cases and applications, the adhesive nature of the CY 52-276 surface would no longer contribute significantly to impact energy dissipation. Finally, we note that soft tissues may also exhibit stickiness [25-27], and the extent of probe-tissue adhesion depends on the molecular composition of the tissue, the impacting probe, and the surrounding medium. Future work in this area could include using computational modeling to distinguish the relative contributions of surface adhesion affecting the impact energy dissipation response.

4.3 Protein-based hydrogels

As an alternative to the PDMS-based composites, protein-polymer hydrogels designed and synthesized by the Olsen group at MIT were also investigated as potential brain tissue simulant candidates. Protein engineering enables the opportunity to mimic specific chemical and structural

elements present in biological tissues using natural proteins within synthetic hydrogel systems. Unlike the bilayered PDMS composites, these hydrogels are homogeneous on the macroscale but exhibit hierarchical structure on the microscale. Thus, these hydrogels will potentially be easier to scale up compared to the bilayer design such that the material can be packed or molded into a headform for helmet evaluation. Here, we aimed to explore the range of mechanical tunability of this new material system and determine whether these hydrogels could ultimately mimic the impact energy dissipation response of brain tissue as measured by impact indentation experiments.

4.3.1 Materials

The hierarchically structured protein-polymer hydrogels are comprised of coiled-coil associations and topological chain entanglement, as shown in Fig. 4-6. Tang and Glassman et al. have described previously the details regarding the protein synthesis and purification procedure [28-30]. These double physical network gels are redox-responsive, and in the fully reduced state Cys-P_4-Cys (or P_4 for short), the protein consists of four coiled-coil domains (P) separated by flexible polyelectrolyte blocks (C_{10}) with cysteine residues near the N- and C-termini. Upon oxidation using thiol coupling chemistry, the cysteine end groups form disulfide bonds, which will extend the chain length and lead to a higher molecular weight product *o*-Cys-P_4-Cys that now undergoes topological entanglement. Together, the coiled-coils and topological entanglement provide distinct length and time scales of deformation, which potentially allows us, for example, to modulate the mechanical response at low strain rates while leaving the response at high strain rates largely unaffected.

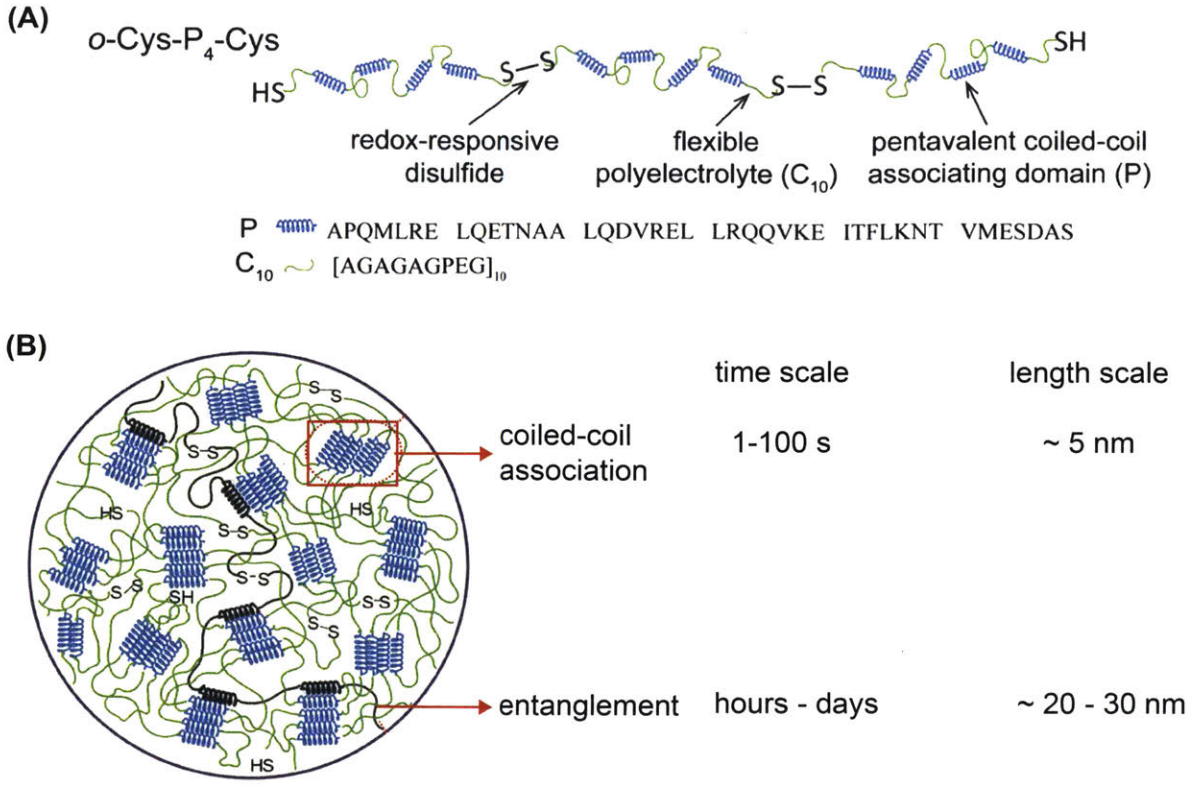

Figure 4-6 (A) Molecular design of oxidatively responsive chain extension and amino acid composition of protein blocks. (B) Illustration of networks combining coiled-coil associations and topological entanglement in protein hydrogels. Reprinted with permission from Tang et al. [28]. Copyright 2014 American Chemical Society.

The effects of the extent of oxidation, thiol coupling chemistry, and molecular architecture (e.g., branched vs. linear chains) on the macroscale mechanical properties have been thoroughly characterized previously via shear rheology and uniaxial loading by the Olsen group [28-31]. To complement these studies, impact indentation experiments were employed to investigate the mechanical behavior of the protein-based hydrogels under concentrated impact loading. We were particularly interested in finding which synthesis conditions maximized the gel's impact energy dissipation capacity given that we had already found brain tissue to be highly dissipative. To prepare the protein-based hydrogels for impact indentation, they were hydrated in phosphate buffer and packed into a hollow cylindrical mold of 15 mm diameter and 5 mm height using clamps and flat Teflon sheets. After storage overnight at 4°C, the sample was removed from the mold and adhered to the impact indentation sample post using a thin layer of cyanoacrylate

adhesive (Loctite® 4013). During mechanical characterization with the impact indentation setup, the sample was fully immersed in mineral oil to minimize water evaporation such that the hydration state was maintained [32].

4.3.2 Impact indentation experiments

4.3.2.1 Results

The protein-based hydrogel in its non-extended, reduced state (P_4) and fully extended, oxidized state (*o*-Cys-P_4-Cys) were characterized using impact indentation. The impact energy dissipation response of both samples is shown in Fig. 4-7. The impact energy dissipation response of adult pig brain tissue is also included in Fig. 4-7 to illustrate that many modifications to the protein hydrogel need to be made before it can match brain tissue. The P_4 gel exhibited higher x_{max} magnitudes than the *o*-Cys-P_4-Cys gel across all impact velocities (Fig. 4-7(A)), which was expected since physical chain entanglement should lead to a stiffer hydrogel. This was also consistent with previous rheological measurements as the shear storage modulus *G'* was higher for *o*-Cys-P_4-Cys across all frequencies [28]. However, both protein-based hydrogels exhibited significantly lower penetration depths than the brain tissue. When comparing the energy dissipation metrics *K* and *Q*, the relative differences between the P_4 and the *o*-Cys-P_4-Cys gel became less clear, though they both clearly displayed the same trend as the applied impact velocity increased. Compared to brain tissue, not only were the protein-based hydrogels much less dissipative (smaller *K* and larger *Q*), but also the energy dissipation characteristics of the hydrogels were non-monotonic with respect to impact velocity, which was especially evident for *Q* since there was a clear peak at approximately 7 mm/s (Fig. 4-7(B and C)). We hypothesized that this non-monotonic behavior was directly reflective of the frequency-dependent loss modulus *G"* measured by shear rheology, which also exhibited non-monotonic behavior with respect to frequency. The parameters *K*, *Q*, and *G"* are all related to the viscous damping behavior of the material.

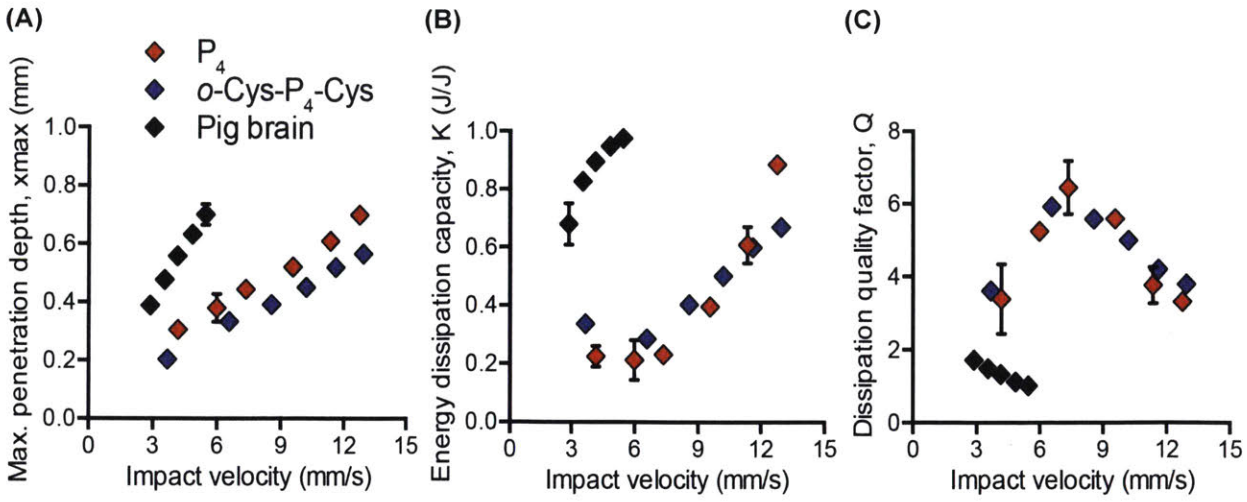

Figure 4-7 Comparison of the impact energy dissipation response of two protein-based hydrogels (P_4 and *o*-Cys-P_4-Cys) and adult pig brain: (A) maximum penetration depth, (B) energy dissipation capacity, and (C) dissipation quality factor as a function of impact velocity. The x_{max} of P_4 was consistently greater than that of *o*-Cys-P_4-Cys, while the differences in K and Q were less clear. Pig brain exhibited a significantly higher x_{max}, higher K, and lower Q than both hydrogels. Data are represented as mean ± standard deviation, and error bars may appear smaller than data symbols (n = 3−4 measurements per data point).

4.3.2.2 Discussion

The protein-based hydrogels that have been characterized via impact indentation to date were unable to recapitulate the impact energy dissipation response of pig brain tissue (or any other brain tissue). The next steps would be to systematically alter the nanoscale architectural features of these gels and investigate the corresponding changes in impact response in terms of x_{max}, K, and Q. From Fig. 4-7, to better mimic brain tissue, the stiffness of the gels must be decreased and the viscous dissipation of the gels must be increased. One approach to synthesize a more compliant version of the gel is to lower the protein concentration. The protein-based hydrogel samples in Fig. 4-7 were all hydrated in phosphate buffer to a final concentration of 20 vol%. By decreasing the concentration to 10%, for example, the gel's shear modulus will approach 1 kPa when measured by macroscale oscillatory shear rheology, which is in the stiffness range required to match brain tissue as demonstrated earlier by the bilayered PDMS composite system. Another approach of tuning the gel mechanics is to apply different thiol coupling chemistries to extend the protein-polymer chains [29]. Only samples that have been extended using disulfide bridging

have been characterized via impact indentation. Alternative coupling strategies that are available include thiol-maleimide, thiol-bromomaleimide, and thiol-ene [29,33-35]. The differences in chemistries' reactivity and side reactions ultimately provide variations in molecular weight and entanglement distribution, which will subsequently alter the stiffness of the gel as well as its rate-dependent energy dissipation response. Additionally, using trifunctional coupling agents to introduce branching architecture can also affect the gel mechanics. Other approaches include designing block copolymers with different protein composition or mutating the amino acid sequence of specific protein domains [31]. In summary, there are numerous methods to modify the structure and chemistry of these engineered protein-based hydrogels, and how each modification affects their mechanical response under concentrated impact loading remains to be studied.

However, there are certain limitations associated with this material system that make these protein-based hydrogels challenging to characterize precisely with impact indentation. The experimental setup of impact indentation requires the sample to be mounted vertically with only one surface adhered to the sample post. Because these gels, especially in their non-extended, reduced state, behave like fluids at long timescales, the free edge begins to flow and heavily sag due to gravitational forces as time progresses, thus limiting the characterization time and reduces the number of measurements that can be made per sample. The non-extended P_4 gels are also highly susceptible to fracture, such that contact with the flat punch probe may ruin the sample and result in inaccurate data. Currently, we cannot image the immersed sample at high resolution while mounted within the instrument, which makes it difficult to identify when and if the gel has fractured.

Additionally, for applications such as ballistic testing and robotic surgery optimization, the ideal tissue simulant material should not only replicate the viscoelastic mechanical properties of brain tissue but also exhibit structural stability in ambient air. Hydrogel systems thus have operational constraints since the water solvent can easily evaporate and change the material's hydration state. Instead, the solvent can be composed of low volatility organic molecules to form an organogel, such as the PDMS organogel layer of our PDMS composite, which are much more stable in ambient environment [7]. The stark differences in impact response between the protein-based hydrogels and brain tissue (Fig. 4-7) coupled with the limitations described above ultimately discouraged further impact indentation experiments on this hydrogel system.

4.4 Conclusions

A primary aim of this thesis was to characterize the dynamic impact response of various brain tissues, and to identify a simple, manufacturable polymer system capable of generating the same response with material stability in room-temperature air. Impact indentation experiments provided a means to quantify the deformation resistance, energy dissipation capacity, and energy dissipation rate of tissues and simulant gels in fully hydrated conditions. As discussed in Chapter 2, we observed slight but detectable species-to-species variation in all three impact response metrics, which may be attributed to the structural and compositional differences among mouse, rat, and pig brains. Motivated by previous computational design by Dr. Mahmoodian, we fabricated PDMS-based bilayered composites, and demonstrated experimentally that such an approach leverages the key properties of each component to facilitate the independent tuning of deformation resistance and energy dissipation. We deliberately chose to limit the number of composite layers to two because tissue surrogate applications ideally use materials that are simple, cost effective, and easily manufactured at large scales. Additional layers or compositionally graded soft matter could certainly be introduced for situations that require even more tunability than our current system, though not required and beyond the scope of the present focus on mammalian brain tissue. With only two layers, we showed that we could optimize the impact response of the composite gel to successfully match that of porcine brain tissue by independently modulating the stiffness and thickness of the more compliant top layer. Hierarchically structured protein-based hydrogels were also explored as an alternative tissue simulant candidate, but the impact response of these hydrogels differed significantly from that of brain tissue. In summary, these findings provide the design principles required to synthesize a physical surrogate of brain tissue for use in material modeling or in testing of protective strategies, by enabling accurate predictions of mechanical deformation of brain tissue under concentrated impact loading. In the next chapter, we seek to address one potential limitation of our PDMS-based composite system, namely to identify whether the extreme adhesivity of the top CY 52-276 PDMS layer contributed to the mechanical energy dissipation response that we measured using impact indentation.

4.5 References

[1] M.J. Thali, B.P. Kneubuehl, U. Zollinger, and R. Dirnhofer, The skin-skull-brain model: a new instrument for the study of gunshot effects, *Forensic Science International*, 2002, 125, 178-189.

[2] T.F. Juliano, A.M. Forster, P. Drzal, T. Weerasooriya, P. Moy, and M.R. VanLandingham, Multiscale mechanical characterization of biomimetic physical associating gels, *Journal of Materials Research*, 2006, 21, 2084-2092.

[3] J.C. Roberts, T.P. Harrigan, E.E. Ward, T.M. Taylor, M.S. Annett, and A.C. Merkle, Human head-neck computational model for assessing blast injury, *Journal of Biomechanics*, 2012, 45, 2899-2906.

[4] Z.I. Kalcioglu, R.A. Mrozek, R. Mahmoodian, M.R. VanLandingham, J.L. Lenhart, and K.J. Van Vliet, Tunable mechanical behavior of synthetic organogels as biofidelic tissue simulants, *Journal of Biomechanics*, 2013, 46, 1583-1591.

[5] S.K. Patel, S. Malone, C. Cohen, J.R. Gillmor, and R.H. Colby, Elastic modulus and equilibrium swelling of poly(dimethylsiloxane) networks, *Macromolecules*, 1992, 25, 5241-5251.

[6] L.E. Roth, D.A. Vega, E.M. Valles, and M.A. Villar, Viscoelastic properties of networks with low concentration of pendant chains, *Polymer*, 2004, 45, 5923-5931.

[7] R.A. Mrozek, P.J. Cole, K.J. Otim, K.R. Shull, and J.L. Lenhart, Influence of solvent size on the mechanical properties and rheology of polydimethylsiloxane-based polymeric gels, *Polymer*, 2011, 52, 3422-3430.

[8] S. Nicolle, P. Vezin, and J.F. Palierne, A strain-hardening bi-power law for the nonlinear behaviour of biological soft tissue, *Journal of Biomechanics*, 2010, 43, 927-932.

[9] A. Gautieri, S. Vesentini, A. Redaelli, and M.J. Buehler, Hierarchical structure and nanomechanics of collagen microfibrils from the atomistic scale up, *Nano Letters*, 2011, 11, 757-766.

[10] A.A. Zadpoor, Nanomechanical characterization of heterogeneous and hierarchical biomaterials and tissues using nanoindentation: the role of finite mixture models, *Materials Science and Engineering: C*, 2015, 48, 150-157.

[11] D.C. Duffy, O.J.A. Schueller, S.C. Brittain, and G.M. Whitesides, Rapid prototyping of microfluidic switches in poly(dimethyl siloxane) and their actuation by electro-osmotic flow, *Journal of Micromechanics and Microengineering*, 1999, 9, 211-217.

[12] R. Mahmoodian, B. Qing, A. Adityan, and K.J. Van Vliet, Multiscale computational design of synthetic gels as simulants of soft-tissue impact response, *Journal of Biomechanics*, in preparation.

[13] B. Qing and K.J. Van Vliet, Hierarchical design of synthetic gel composites optimized to mimic the impact energy dissipation response of brain tissue, *Molecular Systems Design & Engineering*, 2016, 1, 290-300.

[14] D.C. Duffy, J.C. McDonald, O.J.A Scheuller, and G.M. Whitesides, Rapid prototyping of microfluidic systems in poly(dimethylsiloxane), *Analytic Chemistry*, 1998, 70, 4974-4984.

[15] M.A. Eddings, M.A. Johnson, and B.K. Gales, Determining the optimal PDMS-PDMS bonding technique for microfluidic devices, *Journal of Micromechanics and Microengineering*, 2008, 18, 067001.

[16] L. Cai, T.E. Kodger, R.E. Guerra, A.F. Pegoraro, M. Rubinstein, and D.A. Weitz, Soft poly(dimethylsiloxane) elastomers from architecture-driven entanglement free design, *Advanced Materials*, 2015, 27, 5132-5140.

[17] J. Chen, K.E. Wright, and M.A. Birch, Nanoscale viscoelastic properties and adhesion of polydimethylsiloxane for tissue engineering, *Acta Mechanica Sinica*, 2014, 30, 2-6.

[18] J.A.C. Santos, L.M. Rebelo, A.C. Araujo, E.B. Barros, and J.S. de Sousa, Thickness-corrected model for nanoindentation of thin films with conical indenters, *Soft Matter*, 2012, 8, 4441.

[19] R. Long, M.S. Hall, M. Wu, and C. Hui, Effects of gel thickness on microscopic indentation measurements of gel modulus, *Biophysical Journal*, 2011, 101, 643-650.

[20] V. Gonda, J. den Toonder, J. Beijer, G.Q. Zhang, and L.J. Ernst, Finite thickness influence on spherical and conical indentation of viscoelastic thin polymer film, *Journal of Electronic Packaging*, 2005, 127, 33-37.

[21] N.E. Waters, The indentation of thin rubber sheets by cylindrical indentors, *British Journal of Applied Physics*, 1965, 16, 1387.

[22] P. Sauleau, E. Lapouble, D. Val-Laillet, and C.H. Malbert, The pig model in brain imaging and neurosurgery, *Animal*, 2009, 3, 1138-1151.

[23] A.R. Savkoor and G.A.D. Briggs, The effects of tangential force on the contact of elastic solids in adhesion, *Proceedings of the Royal Society of London, Series A*, 1977, 356, 103-114.

[24] K.E. Jensen, R. Sarfati, R.W. Style, R. Boltyanskiy, A. Chakrabarti, M.K. Chaudhury, and E.R. Dufresne, Wetting and phase separation in soft adhesion, *Proceedings of the National Academy of Sciences of the United States of America*, 2015, 112, 14490-14494.

[25] T. Lecuit and P.F. Lenne, Cell surface mechanics and the control of cell shape, tissue patterns and morphogenesis, *Nature Reviews Molecular Cell Biology*, 2007, 8, 633-644.

[26] S. Budday, R. Nay, R. de Rooij, P. Steinmann, T. Wyrobek, T.C. Ovaert, and E. Kuhl, Mechanical properties of gray and white matter brain tissue by indentation, *Journal of the Mechanical Behavior of Biomedical Materials*, 2015, 46, 318-330.

[27] A.A. Sharp, A.M. Ortega, D. Restrepo, D. Curran-Everett, and K. Gall, In vivo penetration mechanics and mechanical properties of mouse brain tissue at micrometer scales, *IEEE Transactions on Biomedical Engineering*, 2009, 56, 45-53.

[28] S. Tang, M.J. Glassman, S. Li, S. Socrate, and B.D. Olsen, Oxidatively responsive chain extension to entangle engineered protein hydrogels, *Macromolecules*, 2014, 47, 791-799.

[29] S. Tang and B.D. Olsen, Controlling topological entanglement in engineered protein hydrogels with a variety of thiol coupling chemistries, *Frontiers in Chemistry*, 2014, 2, 1-11.

[30] M.J. Glassman, J. Chan, and B.D. Olsen, Reinforcement of shear thinning protein hydrogels by responsive block copolymer self-assembly, *Advanced Functional Materials*, 2013, 23, 1182-1193.

[31] M.J. Glassman and B.D. Olsen, End block design modulates the assembly and mechanics of thermoresponsive, dual-associative protein hydrogels, *Macromolecules*, 2015, 48, 1832-1842.

[32] E. Berthier, J. Warrick, H. Yu, and D.J. Beebe, Managing evaporation for more robust microscale assays Part 1. Volume loss in high throughput assays, *Lab on a Chip*, 2008, 6, 852-859.

[33] S.S. Ghosh, P.M. Kao, A.W. McCue, and H.L. Chappelle, Use of maleimide-thiol coupling chemistry for efficient syntheses of oligonucleotide-enzyme conjugate hybridization probes, *Bioconjugate Chemistry*, 1990, 1, 71-76.

[34] A. Dondoni, The emergence of thiol-ene coupling as a click process for materials and bioorganic chemistry, *Angewandte Chemie International Edition*, 2008, 47, 8995-8997.

[35] J. Xu, L. Tao, C. Boyer, A.B. Lowe, and T.P. Davis, Combining thio-bromo "click" chemistry and RAFT polymerization: a powerful tool for preparing functionalized multiblock and hyperbranched polymers, *Macromolecules*, 2010, 43, 20-24.

Chapter 5: Role of surface adhesion on mechanical energy dissipation

5.1 Introduction

As discussed in the previous chapter, although the bilayered PDMS composites could be tuned to match the impact response of porcine brain tissue under the range of loading conditions investigated, we were concerned that extreme adhesivity of the top CY 52-276 layer (referred to hereafter as CY PDMS) strongly contributed to the significant energy dissipation by these gel composites. In ballistic testing applications, adhesive contact between the tissue simulant gel and projectiles will be purposely circumvented by the presence of the skull (mineralized bone tissue) and/or protective helmet under evaluation. Consequently, the impact energy dissipation response that we measured during impact indentation may not reflect the material's true capacity to dissipate energy under ballistic testing conditions.

Although the mechanisms of energy dissipation in polymers have been explored extensively, those studies focus primarily on properties characteristic of the bulk viscoelastic material, such as network defects, physical entanglements, and solvent interactions [1-4]. However, during situations in which the compliant polymer comes into contact with another material, the surface properties, such as the adhesivity of the polymer, can also influence the energy dissipation response [5-7]. Here, we define adhesivity or adhesion as the capacity for the material free surface to join or bond strongly to a contacting material; this can be quantified most typically by the force required to separate those contacting surfaces [6,7]. For example, when a solid ball impacts an adhesive, viscoelastic polymer gel, the kinetic energy of the ball is partially lost through bulk viscous dissipation; as the gel deforms and then springs the ball back, adhesive contact will lead to tensile loading and additional deformation of the gel upon retraction. This additional deformation means impact energy is further lost through viscous dissipation and conversion to elastic strain energy. If the ball manages to separate from the adhesive surface, the fracture of interfacial bonds will also contribute to energy dissipation.

While both surface and bulk properties are known to affect the energy dissipation response, it remains difficult to distinguish their individual contributions and identify whether surface adhesion or bulk viscous dissipation dominates under a given loading condition. The key

limitation is that surface and bulk properties are intrinsically coupled in monolithic systems [8]. For example, silicone gels such as PDMS are formed typically by crosslinking linear polymer chains. Lowering the crosslink density will not only decrease the stiffness, but also lead to large amounts of unreacted molecules and entangled chains that will significantly increase both the adhesive surface energy and viscous dissipation of the material [9-11]. Therefore, a more viscous gel of this type will naturally be more adhesive. To elucidate how surface adhesion and bulk viscoelasticity individually contribute to energy dissipation in compliant gels, methods to independently modulate the adhesivity without affecting the bulk viscoelastic properties, or vice versa, are needed. Simple approaches like using a Teflon-coated probe or covering the gel with a different nonadhesive material pose their own issues. When conventional and commercially available PDMS formulations such as Sylgard® 184 or CY 52-276 are synthesized to be on the order of 1 kPa in stiffness, the adhesivity is so extreme such that the PDMS will still stick to Teflon probes. Placing a non-adhesive cover like plastic wrap atop the gel to eliminate adhesive contributions is problematic because of the material mismatch. Although plastic wrap is thin (<100 μm thickness), the elastic moduli of commonly used plastics are many orders of magnitude greater than that of the compliant gels of interest [12,13], and thus, other factors such as the material deformation will not be consistent during mechanical characterization.

This chapter presents a novel approach to experimentally decouple the effects caused by surface and bulk properties. Recently, Cai et al. demonstrated that PDMS could exhibit much lower surface adhesion than expected for commercial formulations, while maintaining exceptionally low and controllable equilibrium shear moduli down to the order of 1 kPa, by crosslinking bottlebrush chains rather than linear polymer chains [9]. The bottlebrush molecular architecture reduced formation of chain entanglements and minimized the amount of uncrosslinked moeities, which significantly reduced adhesion and viscous dissipation compared to conventional PDMS networks. Here, we developed a bilayered composite polymer, in which a thick PDMS substrate that is highly adhesive and viscous is covered with a thin layer of PDMS that is similar in stiffness and incorporates the bottlebrush architecture (Section 5.2). With this hierarchical design, we independently controlled the surface adhesion and bulk viscoelastic properties. By coating the substrate with a very thin layer of bottlebrush PDMS, we significantly lowered the adhesive surface energy, while maintaining the bulk viscoelastic properties constant, and thus isolated the effects caused by the presence of adhesion. Additionally, by systematically

increasing the thickness of the top layer, we maintained constant the adhesive surface energy but vary the effective bulk properties of the composite polymer. Using an instrumented indenter, we characterized the energy dissipation response of our system at both high and low strain rates (Section 5.3). Two distinct regimes for energy dissipation were identified: at strain rates greater than 1/sec, surface adhesion had negligible effects on energy dissipation; whereas at strain rates less than 0.01/sec, increased surface adhesion significantly increased energy dissipation (Section 5.4). We verified our experimental findings through finite element numerical simulations, and further demonstrated that surface adhesion plays a diminishing role in energy dissipation relative to bulk viscoelastic contributions as strain rate increases (Section 5.5).

The work described in this chapter was part of a collaboration between the Van Vliet Laboratory for Material Chemomechanics at MIT and the laboratory of Prof. David Weitz at Harvard University. Dr. Li-Heng Cai (Weitz group), along with Samuel Lienemann (Weitz group), synthesized the bottlebrush PDMS and assisted with the experimental design. Kyle Geiser (Van Vliet group) helped to construct the finite element model that incorporated adhesive contact. A manuscript for this work is currently in preparation for submission to *Soft Matter* [14].

5.2 Materials

5.2.1 Bottlebrush PDMS

For conventional linear PDMS polymers, the entanglement molecular weight is approximately 10^4 g/mol [10]. Unlike a linear polymer, a bottlebrush molecule is comprised of a long linear backbone with many relatively short linear side chains chemically attached [15]. The entanglement molecular weight for such a bottlebrush polymer easily exceeds 10^7 g/mol, which is multiple orders of magnitude greater than that of linear polymers. As a result, using bottlebrush polymers instead of linear polymers eliminates entanglements in a polymer melt. An elastomer formed by crosslinking such a bottlebrush polymer melt will contain chemical crosslinks but no entanglements, and thus minimizes the adhesion and viscous dissipation of the elastomer.

Bottlebrush PDMS polymers, which we refer to hereafter as BB PDMS, are synthesized through hydrosilylation, which proceeds by the addition of silicone hydride to unsaturated vinyl

groups [16]. A multifunctional linear PDMS copolymer, trimethylsiloxy terminated vinylmethyl-siloxane-dimethylsiloxane, acts as the backbone of bottlebrush molecules; this copolymer carriers approximately 300 methyl-vinyl siloxane units, which allows for multiple hydrosilylation reactions per chain [9]. To form a bottlebrush molecule, many monofunctional linear PDMS polymers, monohydride terminated polydimethylsiloxane, each with one terminal hydride group, are grafted to the backbone, acting as side chains. To simultaneously crosslink the bottlebrush molecules to form a network, difunctional linear PDMS polymers, dihydride terminated polydimethylsiloxane, are used as chemical crosslinks. Note that half of the units in the backbone are dimethylsiloxane groups, which favorably interact with other PDMS units on both the side chains and crosslinking chains to enable miscibility.

5.2.2 Novel bilayered PDMS composite to decouple surface and bulk properties

The bottom layer of our bilayered polymer composite consisted of a commercial silicone CY PDMS, while the top BB PDMS layer contained the bottlebrush molecular architecture, as shown in Fig. 5-1. To facilitate synthesis of the composite samples, we used customized molds created by laser cutting polyacrylate plastic sheets. The mold was a hollow cylinder with inner diameter of 20 mm and height of 5 mm, and one of its two ends was sealed with a thin polyacrylate sheet. This dimension allowed the mold to fit the geometry of our instrumented indenter for subsequent mechanical characterization. We used a two-step process to synthesize a bilayered PDMS composite: first, crosslink the CY PDMS substrate and then coat it with a layer of BB PDMS. To do so, we weighed a certain amount of CY PDMS to ensure its thickness of 4 mm in the mold, desiccated the sample for about 15 min to remove gas bubbles, and then incubated it at 80°C overnight to fully crosslink the gel. Using a similar procedure, we coated the CY PDMS with a layer of BB PDMS with prescribed thickness, except that we incubated the sample for 48 hours to ensure that the BB PDMS was fully crosslinked. Additionally, we prepared monolithic bulk controls of both CY and BB PDMS from the same respective batches used to generate the bilayers. The dynamic mechanical properties of CY and BB PDMS were characterized separately via oscillatory shear rheology to verify that the equilibrium shear moduli G_∞ of the PDMS comprising the different layers were approximately equal (~5 kPa).

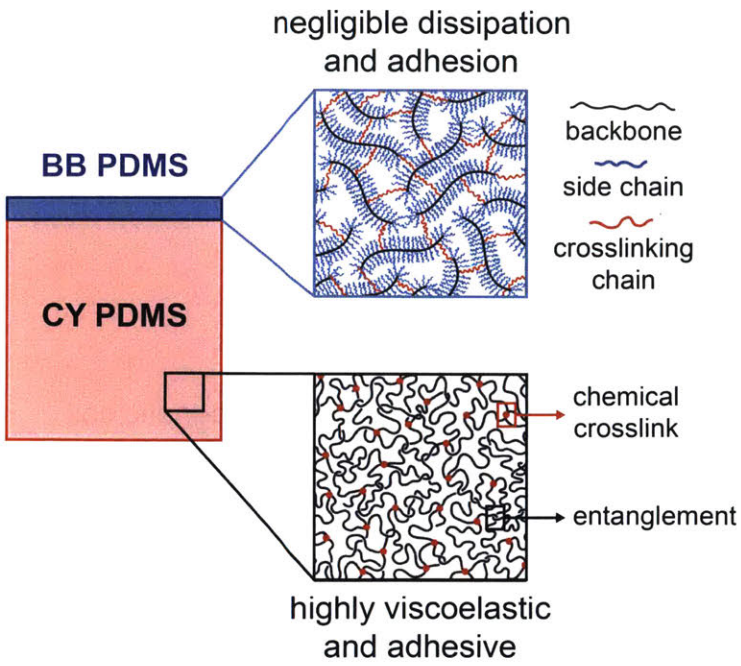

Figure 5-1 Hierarchical bilayer design, in which a thick CY PDMS substrate (highly viscoelastic and adhesive) is coated with a layer of BB PDMS (negligible dissipation and adhesion compared to CY PDMS). Varying the thickness of the top BB PDMS from micrometers to millimeters will modulate the composite's overall or volume-homogenized viscoelastic properties while maintaining constant surface properties. From [14].

5.3 Experimental methods to quantify mechanical energy dissipation

5.3.1 High strain rate impact indentation

To examine the energy dissipation response of PDMS composites and monolithic controls at high strain rates, we conducted impact indentation experiments [17-22] using a commercially available pendulum-based instrumented indenter (Micro Materials Ltd.) as described in the previous chapters. We used a stainless steel spherical probe with a radius of 2 mm to characterize all materials. Figure 5-2 shows a schematic of the instrument configuration. Load is applied through electromagnetic interactions between a conductive coil at the top of the pendulum and a stationary magnetic plate behind the coil (not shown). The parallel plate capacitor measures probe displacement as the pendulum moves about its pivot. To achieve impact loading, activating the bottom solenoid causes the pendulum to swing towards it and maintain its position.

After the electromagnetic coil current reaches the desired amount, deactivating the solenoid releases the "loaded" pendulum such that the probe swings into the sample at an impact velocity that increases with increasing electromagnetic coil current. Impact velocities investigated here ranged from 3 to 7 mm/s. Effective strain rates were on the order of 1 to 10/s depending on the applied impact velocity.

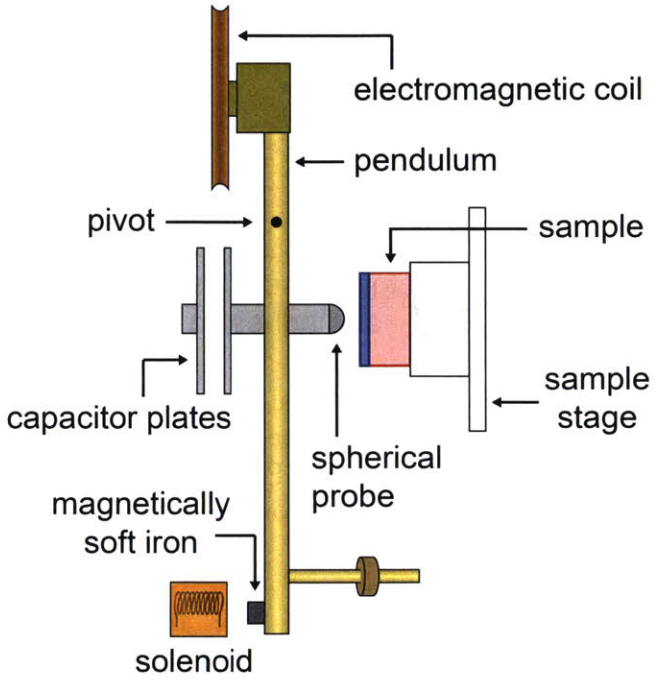

Figure 5-2 Schematic of pendulum-based instrumented nanoindenter (not drawn to scale) used to characterize mechanical energy dissipation. Solenoid setup at the bottom of the pendulum enables impact loading at strain rates greater than 1/s. The load-controlled instrument can also conduct quasistatic indentations at fixed loading and unloading rates, corresponding to strain rates less than 0.01/s, to measure load-depth hysteresis until the probe fully separates from the sample surface. From [14].

5.3.2 Low strain rate quasistatic indentation

Using the same instrument and spherical probe (Fig. 5-2), we also quantified the energy dissipation response at significantly lower strain rates by conducting quasistatic indentation experiments. With the probe starting in contact with the sample, we ramped the applied load at a constant rate of 0.05 mN/s until a depth of 200 μm was reached. Following a 60 s dwell period at

the maximum load to account for viscoelastic creep [23-27], unloading occurred at the same constant rate of 0.05 mN/sec until the probe fully separated from the sample surface. Effective strain rates at these loading and unloading rates were on the order of 0.001/s or approximately three orders of magnitude lower than those during impact indentation.

5.4 Experimental results and discussion

5.4.1 Comparison of bilayered composites to monolithic controls at high strain rates

We employed impact indentation to characterize the energy dissipation response of our materials under impact loading. For these high strain rate studies, we tested a total of six samples: the monolithic BB control, monolithic CY control, and four bilayered composite gels, each with the same CY substrate but a BB top layer of different thickness ranging from 100 μm to 1700 μm. As the probe impacted and indented into the sample, the instrument recorded the resulting probe displacement as a function of time. An example of a displacement profile and corresponding velocity profile obtained from impacting the BB control is shown in Fig. 5-3(A). This measured response can be described by a damped harmonic oscillation, which enables several approaches to quantify energy dissipation metrics [17,18,2128]. In this study, we synthesized CY PDMS at low crosslink densities to produce very compliant ($G_\infty \sim 5$ kPa) and viscous gels, such that almost all the impact energy was lost within two impact cycles. Thus, for all samples, we chose to only analyze the first impact cycle and identify the impact velocity v_{in} and rebound velocity v_{out} as indicated in Fig. 5-3(A). The total impact energy and total recovered energy are related directly to v_{in} and v_{out}, respectively, and energy dissipation can then be quantified as the ratio of v_{out} to v_{in}. A smaller ratio will indicate more energy is dissipated. Note that this velocity ratio is a straightforward metric to calculate, and is related to the energy of dissipation ($mv_{out}^2/2$) and energy of impact ($mv_{in}^2/2$); however, it is not equivalent to K because that term also accounts for energy dissipation of the pendulum instrument itself.

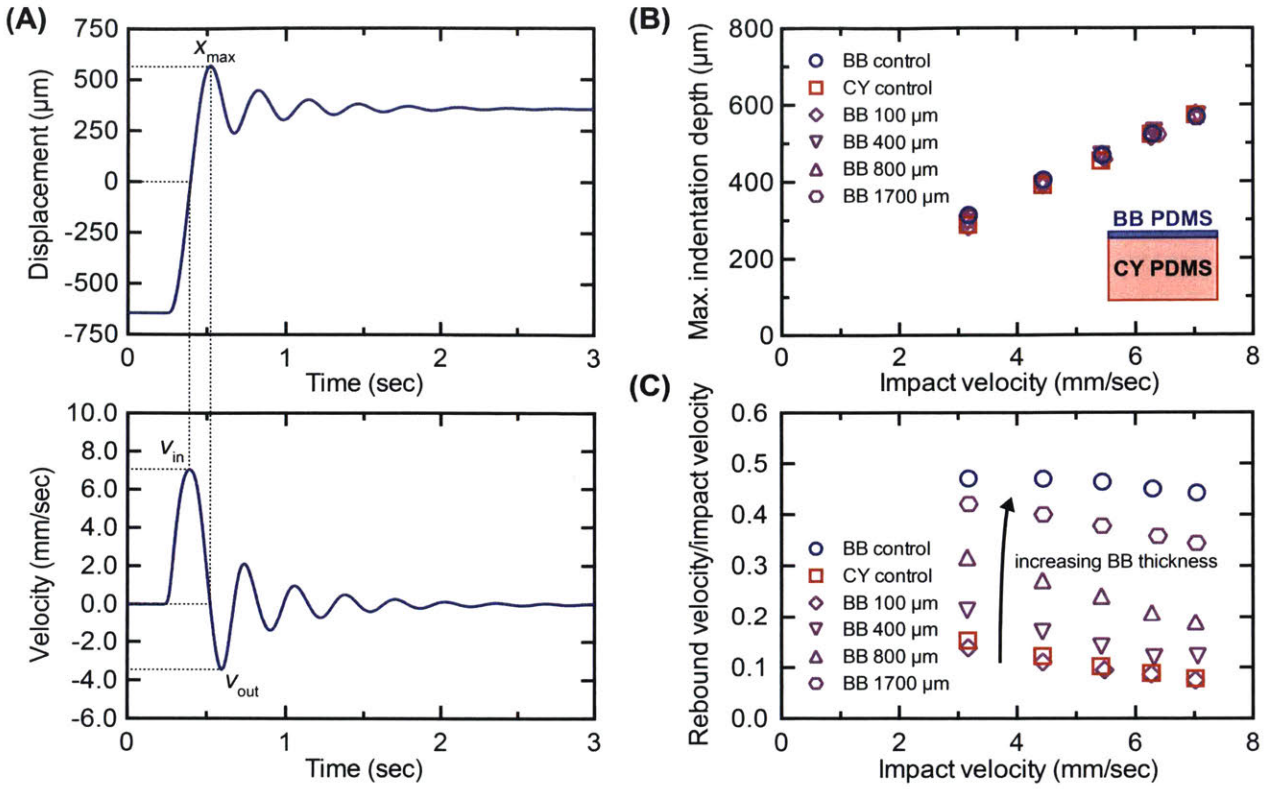

Figure 5-3 (A) Example of a displacement profile and corresponding velocity profile measured via impact indentation for the BB PDMS bulk sample (BB control). The two curves can be analyzed to quantify the deformation resistance and energy dissipation response of the sample. (B) Maximum indentation depth and (C) ratio of rebound velocity to impact velocity are compared among the BB control, CY control, and four bilayered composite gels at multiple impact velocities. All composite gels comprised the BB PDMS of varying thickness from 100 μm to 1700 μm, as indicated, adhered atop the CY PDMS substrate. Error bars (not shown) were on the order of or appeared smaller than the data symbol size (n = 3 replicate measurements per data point). From [14].

Before examining the energy dissipation response, we first checked if deformation was maintained comparable among all samples under each loading condition. We designed BB and CY PDMS layers to be as close in stiffness as possible ($G_\infty \sim 5$ kPa for both) so that the deformation zones in the bilayered composites and monolithic controls would be similar. Larger deformations in a viscoelastic material would lead to increased energy dissipation [1,29,30]. From Fig. 5-3(B), which plots the maximum indentation depth x_{max} as a function of applied impact velocity, we observed that the maximum deformation after initial impact of every sample was similar for the range of impact velocities studied here. As the impact velocity increased from

~3 to 7 mm/s, the maximum indentation depth increased from ~300 to 575 μm, which was a trend that we expected. Because all samples exhibited similar length and time scales of deformation at a given impact velocity, we confirmed that the strain rates should also be comparable among these samples. Although the true strain rate for each impact indentation experiment is time dependent and not constant, we used the contact radius, probe radius, maximum indentation depth, and time it takes to reach the maximum indentation depth to estimate an effective strain rate [31-33], which was on the order of 1 to 10/s depending on the applied impact velocity. This experimental apparatus did not afford higher strain rates on such compliant polymers, because impact velocities greater than 7 mm/s would indent such samples so deeply that the pendulum motion would be impeded physically by the electromagnetic coil colliding into the stationary magnetic plate (see Fig. 5-2). We also could not reliably test impact velocities smaller than 3 mm/s because then the electromagnetic coil load would be insufficient to accelerate the pendulum towards the sample due to the opposing gravitational torque and intrinsic rotational friction of the pendulum.

Next, we revisited the main objective of these impact indentation experiments, which was to determine precisely how much impact energy is dissipated due to the presence of surface adhesion relative to the amount dissipated through viscous mechanisms in the bulk material. Figure 5-3(C) shows the ratio of rebound velocity to impact velocity measured for each sample over the range of applied impact velocities. Note that although BB PDMS should exhibit negligible dissipation, the BB control still experienced a significant reduction in velocity upon impact (i.e., $v_{out}/v_{in} < 1$) because the pendulum naturally dissipated energy, as well; this intrinsic damping is well understood and calibrated [18]. However, any contributions from the intrinsic damping of the pendulum were consistent from sample to sample, and thus comparisons of v_{out}/v_{in} among the different samples remain sound. Compared to the BB bulk sample or BB control, the CY control dissipated significantly more energy, which resulted in rebound velocities that were approximately 70 to 80% lower (Fig. 5-3(C)). Subsequently, when we compared the CY control to the bilayered composite gel with the thinnest BB top layer in Fig. 5-3(C), any detectable differences in energy dissipation were assumed to be attributable to removing surface adhesion because the length scales of the deformation field were many factors greater than the top layer thickness of 100 μm such that this layer was not expected to significantly perturb the amount of viscous dissipation from the bulk material. Interestingly, we

found that v_{out}/v_{in} of this bilayered composite gel with the 100 μm BB layer thickness was indistinguishable from that of the CY control for every impact velocity investigated here, suggesting that effects from surface adhesion on energy dissipation are negligible under these loading rates.

From Fig. 5-3(C), we also observed that as the BB top layer became thicker, the composite gel exhibited higher rebound velocities and the energy dissipation response shifted increasingly towards that of the BB control, further supporting that bulk viscoelasticity is the dominant energy dissipation mechanism. This trend was expected because we modulated the bulk response of the composite gel while fixing the adhesive surface energy when we systematically varied the top layer thickness. An increase in BB layer thickness from 100 to 400 μm was sufficient to elicit a significant change in the measured rebound velocities. The composite gel with the thickest BB layer still dissipated more impact energy than the BB control, which demonstrates that the deformation field was extending below the sample surface beyond 1700 μm to allow the underlying CY substrate to contribute to the energy dissipation. Additionally, as the applied impact velocity increased from ~3 to 7 mm/s, v_{out}/v_{in} slightly decreased for each sample but to varying degrees (Fig. 5-3(C)). Generally, the energy dissipation response of bilayered composite gels skewed towards that of the CY control as impact velocity increased, with the exception of the composite with the 100 μm layer, which behaved the same as the CY control for all impact velocities. We concluded that this trend was consistent with the previous observation that higher impact velocities led to higher indentation depths (Fig. 5-3(B)), and subsequently, larger deformations led to increased contributions to the composite's energy dissipation response by the viscous CY substrate.

Together, these results demonstrate that although the presence of surface adhesion can provide additional avenues to dissipate mechanical impact energy, these contributions to the total energy dissipation response are vastly insignificant compared to viscous dissipation in the bulk material for the experimental conditions investigated here. The relative roles of surface adhesion and bulk viscoelasticity on energy dissipation in gels, however, should depend on several factors including strain rate, since viscoelastic materials exhibit rate-dependent behavior [1,34-36]. Thus, while we found that surface adhesivity negligibly affected impact energy dissipation at strain rates on the order of 1 to 10/s, we explored next whether the same conclusions would hold true if we characterized our material system at much lower strain rates.

5.4.2 Comparison of bilayered composites to monolithic controls at low strain rates

To achieve strain rates on the order of 0.001 to 0.01/s, or roughly three orders of magnitude smaller than those for impact indentation, we conducted quasistatic load-controlled indentations on the monolithic controls and bilayered composite gels. During these indentations, the extent of hysteresis related directly to the amount of energy that is dissipated or not recoverable over the measured timescales of deformation [37-41]. From the measured load-depth hysteresis response, we quantified the dissipated work of indentation W_d and recovered work of indentation W_r as the green and orange shaded areas indicated, respectively, in Fig. 5-4(A). We indented each sample to a maximum depth of 200 μm, but because the stiffness of the CY and BB PDMS were similar yet not identical, the maximum applied load differed for each sample. Thus, to enable sound comparison of the energy dissipation response among the samples, we normalized W_d to the total work of indentation W_t. This ratio, which we called the dissipated work ratio, describes how much of the total work inputted into the system to indent the viscoelastic polymer is dissipated upon unloading back to zero load (42-44). A larger dissipated work ratio indicates dissipation of more mechanical energy.

For these low strain rate studies, we characterized six composite gels, each with the same CY substrate but a BB top layer coating of different thickness. Here, we investigated BB layers as thin as 50 μm, compared to 100 μm thickness used in impact indentation, because the indentation depths were twofold lower than those incurred in those higher strain rate studies. We assumed that a 50 μm BB layer would be sufficient to remove the effects of surface adhesion without altering the extent of viscous dissipation from the CY substrate. Recall that BB PDMS is significantly less viscous than CY PDMS, and thus should contribute negligibly to the energy dissipation response [9]. Ideally, we would decrease the top layer thickness even further to ensure that we solely isolate the contributions from adhesion, but 50 μm was the thinnest we could reliably synthesize while still maintaining uniform surface coverage and surface roughness. Figure 5-4(B) illustrates the measured dissipated work ratio as a function of the BB top layer thickness, with the results for the CY control and BB control shown as red and blue dashed lines, respectively. On average, the highly adhesive and viscous CY control dissipated 38% of the total work of indentation (dissipated work ratio W_d/W_t of 0.38), while the BB control only dissipated 4% of the total work of indentation (dissipated work ratio W_d/W_t of 0.04). When we compared the composite gel with the 50 μm BB layer to the CY control, we detected a

difference in the energy dissipation response as the dissipated work ratio decreased to 0.26 for the composite gel. This finding vastly differed from our impact indentation findings, in which even adding the BB layer of 100 μm had negligible effects (Fig. 5-4(C)), thus demonstrating that the relative roles of surface adhesion and bulk viscoelasticity on energy dissipation indeed exhibit a rate dependency. At low strain rates (less than 0.01/s), reducing adhesion led to a decrease in dissipated work. The exact magnitude or extent of this decrease, however, is only characteristic of our material system, including the specific composition and synthesis protocols for these PDMS layers. Thus, we focused on the observed qualitative trends that depend on the relative adhesivity and mechanical properties of each layer, as illustrated by this specific composite system.

Next, when comparing the composite gel with the 50 μm BB layer to the BB bulk or control in Fig. 5-4(B), we observed that the composite gel dissipated more of the total work of indentation. Since the composite gel exhibits the same surface properties as the BB control, these differences in the energy dissipation response can be attributed solely to the differences in viscoelastic properties between the CY substrate and the BB control. As the BB layer thickness increased, the effective bulk response became more similar to that of the BB bulk control, and as expected, the dissipated work ratio of the composite gel decreased. Upon closer examination of the thickness dependence in Fig. 5-4(B), we observed a sudden drop in the dissipated work ratio between 200 and 400 μm. For example, as the BB layer thickness varied from 50 to 200 μm, the dissipated work ratio only decreased from 0.26 to 0.23, whereas the sample with the 400 μm BB layer exhibited a drastically lower dissipated work ratio of 0.08. Interestingly, the position of this sudden drop occurred after 200 μm, which happened to be the maximum indentation depth. This suggests that the top layer begins to vastly dominate the overall energy dissipation response of the composite gel once the top layer thickness exceeds the indentation depth. Future work can involve utilizing computational models to simulate indentations on our bilayered viscoelastic material system and explore the complex stress fields and deformation zones as the top layer thickness or indentation depth varies.

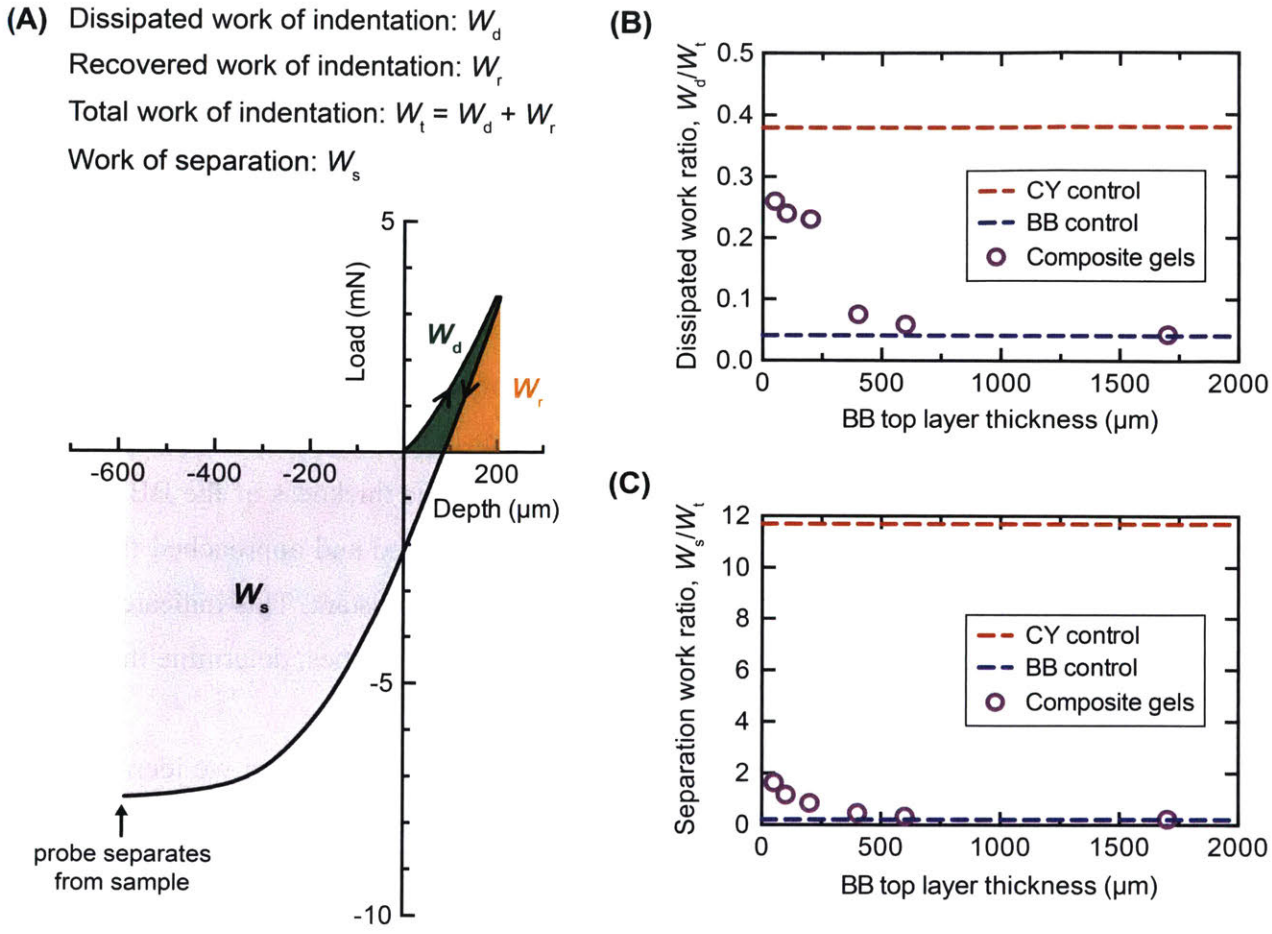

Figure 5-4 (A) Example of a load-depth hysteresis curve measured via quasistatic indentation for the CY bulk or control. (B) Dissipated work of indentation normalized to total work and (C) work of separation normalized to total work are plotted as a function of BB top layer thickness for the bilayered composite gels (circles). The values for the CY control and BB control are represented as dashed lines (red and blue, respectively). All samples were indented to a maximum depth of 200 μm. Error bars for the composite gels (not shown) were on the order of or appeared smaller than the data symbol size (n = 3 replicate measurements per data point). From [14].

In addition to examining the extent of energy dissipation from the indentation process, we also investigated how much work was required to fully separate the probe and sample, which can be quantified as the work of separation W_s or the gray shaded area in Fig. 5-4(A). During these quasistatic indentations, unloading continues (past zero load) until the spherical probe fully separates from the sample. Since our indenter is a load-controlled instrument, the probe does not return to zero load after separation. Figure 5-4(C) shows the separation work ratio (work of

separation normalized to total work of indentation) as a function of the BB top layer thickness, with the results for the CY control and BB control shown as red and blue dashed lines, respectively. The qualitative trends that we observed for the separation work ratio were identical to those observed for the dissipated work ratio. As expected, the adhesive CY control exhibited a much higher separation work ratio than the BB control. Upon adding a 50 μm BB layer atop the CY substrate, the adhesive interactions between the probe and sample decreased and consequently, the separation work ratio decreased significantly (Fig. 5-4(C)). The relative magnitude of this decrease was greater than the decrease observed for the dissipated work ratio in Fig. 5-4(B), which suggests that surface adhesion contributes more to energy dissipation during the separation process than the indentation process. As the thickness of the BB top layer increased, the separation work ratio of the composite gel decreased and approached that of the BB control even though the adhesivity of the top layer remained constant. This indicates that the bulk viscoelastic properties, in addition to the surface adhesive properties, determine the amount of work needed to fully separate the probe from the sample.

Through these impact indentation and quasistatic indentation experiments, we identified two distinct regimes for energy dissipation in our PDMS-based material system. At strain rates greater than 1/s, surface adhesion negligibly affected energy dissipation. In contrast, at strain rates less than 0.01/s, increased surface adhesivity significantly increased energy dissipation. We quantified the extent of energy dissipation during both the indentation and separation process at low strain rates via quasistatic indentation. However, for the high strain rate impact indentation experiments, the probe never retracts beyond the original surface plane of the undeformed sample during the entire impact process. Thus, the energy dissipation response we measured using impact indentation is more comparable to the dissipated work ratio we measured using quasistatic indentation. Nonetheless, we found experimentally that the mechanisms of energy dissipation exhibit an important dependence on strain rate, and more specifically, the relative effects of surface adhesion on energy dissipation diminish with increasing strain rate, as compared to bulk viscoelastic contributions.

5.5 Computational finite element simulations

5.5.1 Indentation model with adhesion implemented

To complement our experimental approach of using a bilayer system to decouple the effects of surface adhesion and bulk viscoelasticity on energy dissipation, we constructed a two-dimensional axisymmetric finite element model (FEM) in ANSYS® software version 17.2 to simulate experimental loading and geometry. Images of our axisymmetric finite element model of a spherical probe indenting a gel with adhesive contact implemented are illustrated in Fig. 5-5. The spherical probe (radius R = 2 mm) was modeled as structural steel, meaning that the probe was essentially rigid compared to the compliant sample. The probe size in our model was the same as the probe size we used for the impact indentation and quasistatic indentation experiments. Two rectangular sections, each with a width of 5 mm, were combined to generate the composite gel. Nodes at the layer interface were tied in directions, meaning no slip between layers. For our parametric analysis study, a bilayer model was not required because the surface and bulk material properties can be independently varied computationally. Both sections could be assigned identical material properties based on a linear viscoelastic Prony series obtained from fitting our experimental shear rheological data of CY PDMS (see Section 2.3.2.1). A mesh was constructed via a multizone method, allowing the mesh coarseness to increase as the distance from the contact point increased. A fixed support boundary condition was applied to the bottom edge of the sample to restrict normal or lateral displacement and simulate a rigid sample support.

The indentation process was simulated based on an input displacement profile, and the resulting reaction forces were outputted to generate the load-depth hysteresis response. Displacement-controlled loading and unloading rates ranged from 0.5 to 16 μm/s; note that FEM simulations are routinely implemented as displacement-controlled, while typical instrumented indentation experiments including ours are load-controlled. A dwell period of 10 s at the maximum indentation depth of 80 μm allowed for viscoelastic relaxation of the material before unloading occurred. Adhesion was implemented by assigning a fracture energy based debonding condition used for cohesive zone modeling. This method assumed that the probe surface and sample surface in contact separate via the propagation of a crack at the interface under Mode I fracture. Two parameters were needed: a maximum normal contact stress $\sigma_{max,adh}$ and a critical

fracture energy for normal separation. While both parameters played a role, varying the first parameter more effectively modulated the adhesivity of the surface because debonding between nodes can only occur once the maximum normal contact stress (or surface traction) is reached. For this study, we examined a range of $\sigma_{max,adh}$ from 0 Pa (no adhesion; frictionless contact) to 25 kPa ("maximal" adhesivity; no change in contact area throughout entire unloading process) in our model.

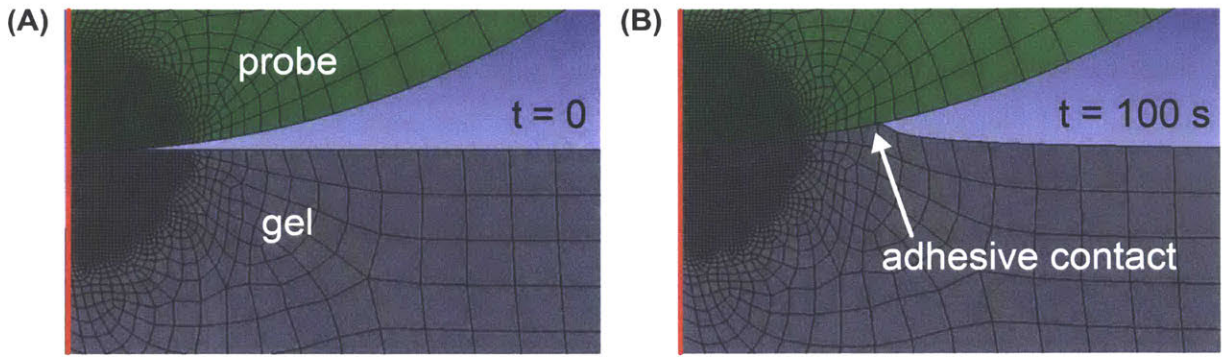

Figure 5-5 Axisymmetric finite element model of a spherical probe of 2 mm radius indenting a gel with adhesion implemented. (A) Image corresponding to the time point immediately before loading begins. (B) Image corresponding to a time point during the unloading process, illustrating adhesive contact between the probe and gel as the probe moves away. From [14].

5.5.2 Parametric analysis on monolithic samples with bulk properties constant

5.5.2.1 Effects of varying adhesiveness on indentation hysteresis

We simulated each indentation to a maximum depth of 80 μm based on an input displacement profile, and we generated the load-depth hysteresis response from the resulting reaction forces,. Figure 5-6 shows the load-depth hysteresis responses obtained at a constant probe displacement rate of 8 μm/s and different degrees of surface adhesion. The strain rates corresponding to this probe displacement rate were calculated to be similar to the strain rates from our quasistatic indentation experiments using a first order approximation. The adhesive strength, which was determined by $\sigma_{max,adh}$, ranged from 0 Pa, corresponding to the control case of no adhesion, to 25 kPa, corresponding to the upper adhesive limit in which every node in contact never separated throughout unloading.

From Fig. 5-6, we observed that the non-adhesive control exhibited hysteresis during the simulated indentation process. Here, the amount of hysteresis, which relates directly to energy dissipation and can be quantified as the dissipated work ratio, must be caused strictly by the viscoelastic properties input for the bulk material. We also note that for this non-adhesive control, the load and depth simultaneously returned to zero, and as expected, no pull-off force was detected upon full separation of the probe from the sample surface. After implementation of non-zero surface tractions to simulate adhesion in our model and systematical increase of the surface traction, we found that the dissipated work ratio increased with increasing $\sigma_{max,adh}$. This trend is evident by examining the area between the loading and unloading curves in the first quadrant of Fig. 5-6. Additionally, the pull-off force required to fully separate the probe and sample, and consequently the separation work ratio, also increased with increasing surface traction, which demonstrated that the $\sigma_{max,adh}$ parameter in our model did indeed modulate the degree of adhesivity. When $\sigma_{max,adh}$ was set to 25 kPa, load became linearly dependent on depth throughout the unloading portion, a behavior generally indicative of a cylindrical flat punch probe geometry under these indentation conditions [45,46]. In this case, our spherical probe essentially acted as a flat punch probe because the surface was so adhesive such that the area in adhesive contact did not decrease, but rather remained constant upon unloading. Even after the probe retracted 100 μm past the original surface plane of the undeformed sample, not a single node in contact separated. From these trends, we concluded that the presence of adhesion led to an increased dissipated work ratio under a probe displacement rate of 8 μm/s, and that the extent of this increase in energy dissipation was directly proportional to the magnitude of the surface traction that we assigned in our model.

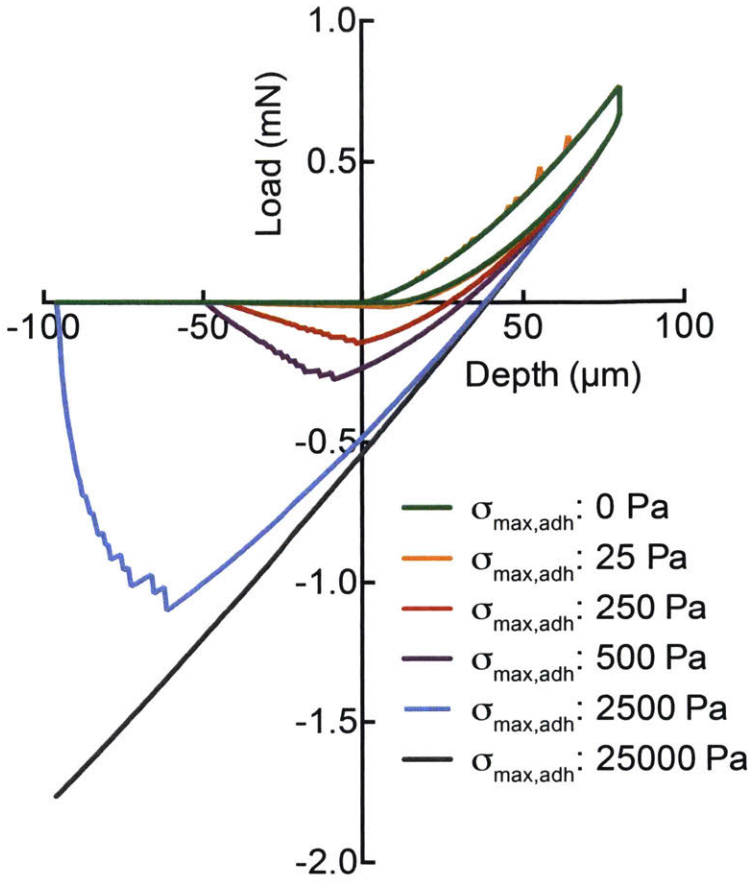

Figure 5-6 Load-depth hysteresis responses simulated at a probe displacement rate of 8 μm/s and at various degrees of adhesive strength ($\sigma_{max,adh}$ ranging from 0 to 25 kPa). Bulk viscoelastic properties were maintained constant for each simulation and were based on a Prony series obtained from fitting rheological data of CY PDMS. Effective strain rates were comparable to those from the quasistatic indentation experiments. As the adhesivity increased, the extent of indentation hysteresis increased and the pull-off force required to fully separate the probe and sample increased. At $\sigma_{max,adh}$ = 25000 Pa, no nodes in contact separated. From [14].

5.5.2.2 Effects of varying probe displacement rate

Next, we explored whether the adhesive contributions to energy dissipation exhibited a rate dependency in our model, similar to what we observed experimentally. Therefore, we simulated the indentations at other constant probe displacement rates ranging from 0.5 to 16 μm/s. Figure 5-7(A) shows the dissipated work ratio as a function of probe displacement rate, and juxtaposes the non-adhesive control with only one highly adhesive condition ($\sigma_{max,adh}$ = 2.5 kPa) for simplicity. Recall that the dissipated work ratio describes how much of the total work input into

the system to indent the viscoelastic sample is dissipated upon unloading back to zero load. The open symbols in Fig. 5-7(A) represent the fraction of total energy inputted into the system that was lost solely through viscous dissipation in the bulk material, and the closed symbols differ only in that the simulations incorporated adhesive contact. As a result, the increase in energy dissipation due to the addition of adhesion can be visualized by examining the difference between the filled and open symbols in Fig. 5-7(A). When we investigated the effects of probe displacement rate, we observed multiple important trends. First, as the rate increased, the dissipated work ratio for both the non-adhesive and adhesive condition increased, indicating that more energy dissipation occurred at higher rates for our viscoelastic system. Second, the difference in the dissipated work ratio between the non-adhesive and adhesive condition notably decreased with increasing rate.

Furthermore, taking this difference in the dissipated work ratio and dividing by the dissipated work ratio of the adhesive condition will quantify explicitly the percentage of total dissipated work that surface adhesion contributed towards, which we plotted for each probe displacement rate in Fig. 5-7(B). At the lowest simulated probe displacement rate of 0.5 μm/s, approximately 70% of the total dissipated work was lost due to the presence of adhesion. In contrast, at the highest simulated probe displacement rate of 16 μm/s, adhesion contributed to approximately 22% of the total dissipated work. The results from the parametric analysis shown in Fig. 5-7 clearly illustrate that the relative effects of surface adhesion on mechanical energy dissipation diminish with increasing rate, a trend that is consistent with our previous experimental observations.

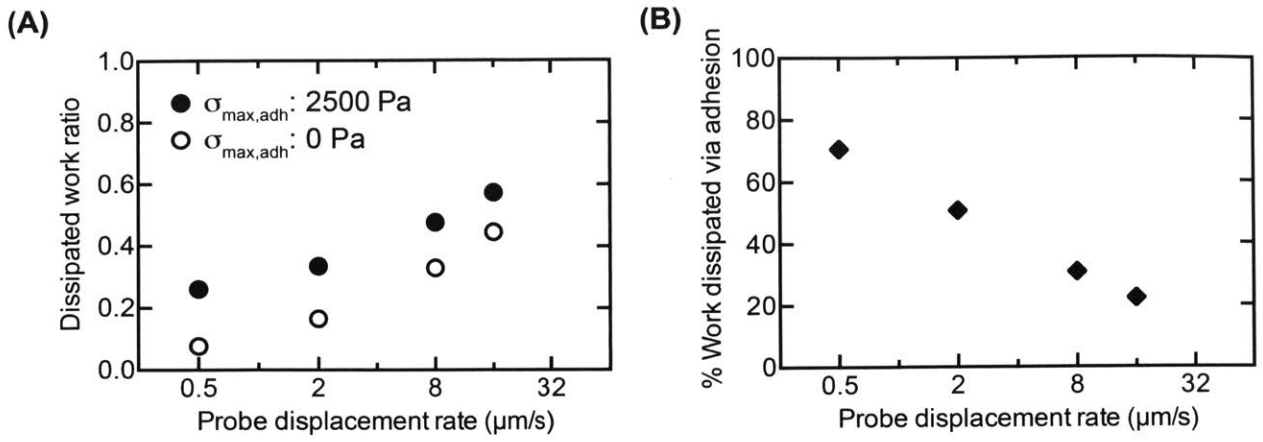

Figure 5-7 (A) Dissipated work of indentation normalized to total work, as a function of probe displacement rate. Comparison of highly adhesive surface (filled circles) to a non-adhesive control surface (open circles). (E) Quantification of the contributions from adhesion to the total dissipated work during indentation. As probe displacement rate increases, a smaller percentage of the total work is dissipated through adhesive interactions. From [14].

Since the total extent of energy dissipation still increased as indentation displacement rate increased (Fig. 5-7(A)), despite the diminishing contributions from adhesion, we can infer that the contributions of viscous dissipation in the bulk material also greatly increased. Therefore, the deformation rate dependence of energy dissipation appears to be driven predominantly by the bulk viscoelastic properties rather than surface adhesive properties of the impacted material system. We concluded that the bulk viscoelastic contributions to energy dissipation exhibit a significantly stronger dependence on strain rate than do adhesive contributions. During impact events, as more of the impact energy has been dissipated through viscous mechanisms in the bulk material, there is less recovered deformation upon rebound, which will subsequently decrease any additional dissipation through adhesive mechanisms. Table 5-1 provides additional data from our computational parametric analysis, which consider the full range of adhesivity ($\sigma_{max,adh}$) that we simulated. Another approach to effectively increase the adhesive contributions to energy dissipation, other than modulating $\sigma_{max,adh}$, is to increase the radius of the probe. A larger probe radius will lead to a larger area in adhesive contact, thus accentuating any effects caused by adhesion. Future work may include simulations using different probe radii and also different bulk viscoelastic properties of the impacted material systems.

Table 5-1 Computational parametric analysis to examine energy dissipation while varying probe displacement rate *dh/dt* and adhesive strength $\sigma_{max,adh}$. The third column is the dissipated work ratio. The fourth column is the difference in dissipated work ratio relative to the nonadhesive control. The last column is the fraction of total work dissipated due to the presence of adhesion.

$\frac{dh}{dt}$ (μm/s)	$\sigma_{max,adh}$ (Pa)	$\frac{W_d}{W_t}$	$\Delta\frac{W_d}{W_t}$	$\frac{\Delta W_d/W_t}{W_d/W_t}$
0.5	0	0.077	0	0
	25	0.092	0.015	0.163
	250	0.165	0.088	0.533
	500	0.203	0.126	0.621
	2500	0.261	0.184	0.705
	25000	0.264	0.187	0.708
2	0	0.166	0	0
	25	0.179	0.013	0.073
	250	0.246	0.08	0.325
	500	0.281	0.115	0.409
	2500	0.336	0.17	0.506
	25000	0.339	0.173	0.51
8	0	0.33	0	0
	25	0.346	0.016	0.046
	250	0.403	0.073	0.181
	500	0.433	0.103	0.238
	2500	0.477	0.147	0.308
	25000	0.48	0.15	0.313
16	0	0.446	0	0
	25	0.456	0.01	0.022
	250	0.506	0.06	0.119
	500	0.533	0.087	0.163
	2500	0.574	0.128	0.223
	25000	0.577	0.131	0.227

5.5.3 Extension of model to incorporate bilayers

In Section 5.5.2, we demonstrated how to systematically vary the surface properties of a material while maintaining the properties of the bulk material constant, as a means to computationally decouple the effects of surface adhesion and bulk viscous dissipation. The qualitative findings and trends observed from these parametric studies strongly supported our experimental results that surface adhesion only contributed detectably to energy dissipation at low strain rates (less than 0.01/s). To further validate our experimental work, we adapted the finite element model to incorporate a bilayered sample similar to that of our experimental material design, and investigated varying the top layer thickness and comparing to monolithic controls. For the bilayers, the top Gel A layer and bottom Gel B layer (Fig. 5-8(A)) were assigned bulk material properties based on a linear viscoelastic Prony series obtained from fitting experimental rheological data of BB PDMS and CY PDMS, respectively, and the maximum normal contact stress $\sigma_{max,adh}$ (related to adhesive strength) was assigned to be 50 Pa. For the Gel A and Gel B monolithic controls, $\sigma_{max,adh}$ were assigned to be 50 Pa and 2500 Pa, respectively. Note that we selected these $\sigma_{max,adh}$ values because they resulted in pull-off forces comparable to those observed experimentally for BB PDMS and CY PDMS. These traction stresses correspond to interfacial adhesion energies of approximately 0.5 mJ/m^2 and 80 mJ/m^2, respectively. We computationally varied the thickness of the Gel A layer from 50 μm to 1500 μm, which was a similar range compared to the bilayered PDMS gels that were synthesized and characterized via indentation. With this bilayer finite element model, we simulated indentations to a maximum depth of 80 μm at a constant probe displacement rate of 2 μm/s and examined the effects of varying the thickness of Gel A on the extent of hysteresis or amount of dissipated mechanical energy.

Overall, we found that the results from the simulations (Fig. 5-8(B)) matched strongly to the results from our quasistatic indentation experiments (Fig. 5-4(B)). Although the model applies displacement-controlled indentation (whereas the instrumented indenter is load-controlled), the effective strain rates during the simulations were comparable to those during the quasistatic indentations based on a first order approximation. The model predicted a significant decrease (~40%) in the dissipated work ratio for the bilayer with the thinnest top layer compared to the Gel B control. Assuming that the 50 μm top layer negligibly affects the bulk viscous response, this difference in dissipated work ratio can be attributed to adhesive contributions. When we

increased the top layer thickness, the dissipated work ratio of the bilayer decreased and approached that of the Gel A control, as expected. While the qualitative trends were well matched in these computational and experimental studies, we did not expect nor did we observe the same magnitudes of dissipated work for the various samples tested. The slight quantitative differences are attributed reasonably to various factors, including discrepancies in the input parameters for the material properties (e.g., Prony series idealization of the material constitutive law) and assumptions of the model (e.g., perfect normal traction at the contacting adhesive surfaces).

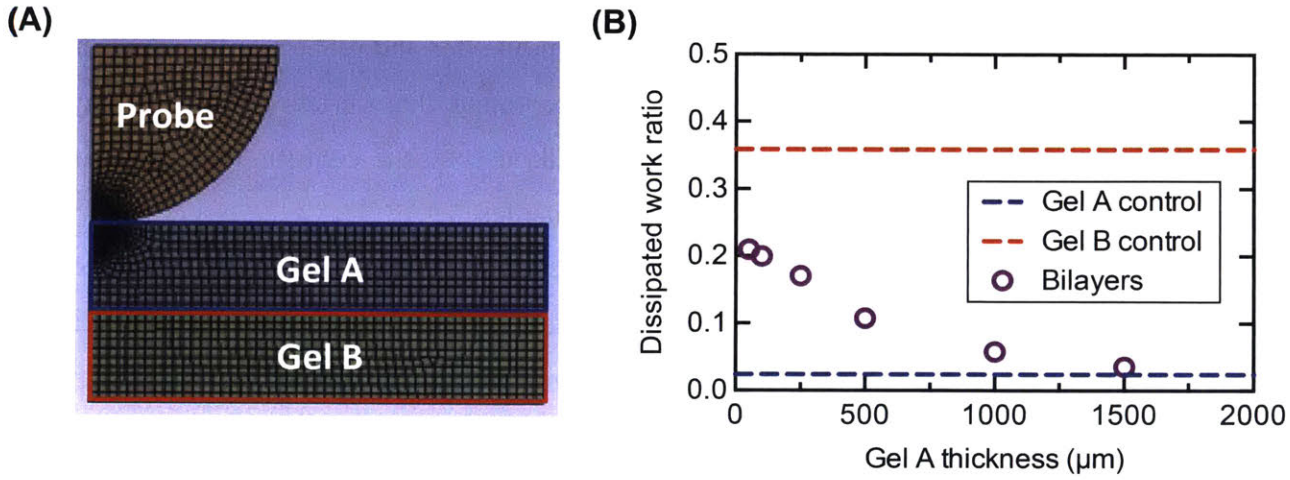

Figure 5-8 (A) Image of axisymmetric finite element model of a spherical probe of 2 mm radius indenting a bilayer sample (Gel A atop Gel B) with adhesion implemented. (B) Dissipated work ratio (dissipated work of indentation normalized to total work) plotted as a function of top Gel A layer thickness. Values for the bilayer samples are represented as circles, whereas the values for the monolithic or bulk Gel A control and Gel B control are represented as dashed lines (red and blue, respectively). Gel A represents a top layer of fixed adhesivity via a surface traction of 50 Pa, and varied thickness. All samples were indented to a maximum depth of 80 μm.

5.6 Conclusions

Our main goal in this chapter was to elucidate the role of surface adhesion on mechanical energy dissipation in compliant, adhesive polymer gels. We specifically sought to compare the amount of energy dissipated via surface adhesion and via bulk viscous mechanisms under various loading conditions and strain rates. To accomplish this experimentally, we engineered a PDMS-

based bilayered composite gel that enabled independent control of the material's surface and bulk properties through modulating the thickness of the top layer. Impact indentation and quasistatic indentation experiments provided a means to quantify the energy dissipation response of gels at high and low rates of loading, respectively. We observed that the relative contributions from surface adhesion and bulk viscoelastic properties to the extent of energy dissipation exhibited an important dependence on strain rate. At strain rates greater than 1/s, viscous dissipation in the bulk material vastly dominated and surface adhesion negligibly contributed to energy dissipation. However, at strain rates less than 0.01/s, increased surface adhesion significantly increased energy dissipation. To validate these experimental findings, we constructed a finite element model with adhesive contact implemented, and investigated the effects of independently varying the material's surface properties and probe displacement rate. In summary, our computational parametric analysis also found that surface adhesion played a diminishing role in energy dissipation compared to bulk viscoelastic contributions as strain rate increased, thus strongly supporting our experimental findings.

In the context of brain tissue characterization and brain tissue simulant design, we have now shown that the extreme adhesivity characteristic of the bilayered PDMS composites studied in Chapter 4 as potential brain tissue simulants does not affect the impact energy dissipation response that was measured via impact indentation. Ballistic testing application applies even greater strain rates compared to those that we investigated, which means that surface adhesion should contribute even less to mechanical energy dissipation compared to bulk viscoelastic properties. This alleviates our previous concern that the bilayered PDMS composites (CY PDMS of prescribed stiffness and thickness atop PDMS organogel) would exhibit different impact responses once adhesive contact has been eliminated by the presence of a synthetic skull and/or helmet under evaluation. Ultimately, the studies presented in this chapter provide new insights on the energy dissipation mechanisms in compliant, adhesive polymer gels that are considered key candidate materials for diverse engineering applications ranging from protective cushions for soft robotics to mechanical simulants for soft tissues. Additionally, we have now demonstrated on two separate occasions that a hierarchical bilayer design can enable decoupling of key properties – surface adhesion decoupled from bulk viscoelastic properties, and deformation resistance decoupled from energy dissipation characteristics – that are otherwise difficult to control independently in monolithic systems.

5.7 References

[1] X. Zhao, Multi-scale multi-mechanism design of tough hydrogels: building dissipation into stretchy networks, *Soft Matter*, 2014, 10, 672-687.

[2] Q. Chen, L. Zhu, H. Chen, H. Yan, L. Huang, J. Yang, and J. Zheng, A novel strategy for fully physically linked double network hydrogels with tough, fatigue resistant, and self-healing properties, *Advanced Functional Materials*, 2015, 25, 1598-1607.

[3] S. Abdurrahmanoglu, V. Can, and O. Okay, Design of high-toughness polyacrylamide hydrogels by hydrophobic modification, *Polymer*, 2009, 50, 5449-5455.

[4] R.A. Mrozek, P.J. Cole, K.J. Otim, K.R. Shull, and J.L. Lenhart, Influence of solvent size on the mechanical properties and rheology of polydimethylsiloxane-based polymeric gels, *Polymer*, 2011, 52, 3422-3430.

[5] A.R.C. Baljon and M.O. Robbins, Energy dissipation during rupture of adhesive bonds, *Science*, 1996, 271, 482-484.

[6] K.R. Shull, Contact mechanics and the adhesion of soft solids, *Materials Science and Engineering: R: Reports*, 2002, 36, 1-45.

[7] A.J. Crosby and K.R. Shull, Deformation and failure modes of adhesively bonded elastic layers, *Journal of Applied Physics*, 2000, 88, 2956.

[8] J.L. Lenhart and P.J. Cole, Adhesion properties of lightly crosslinked solvent-swollen polymer gels, *The Journal of Adhesion*, 2006, 82, 945-971.

[9] L. Cai, T.E. Kodger, R.E. Guerra, A.F. Pegoraro, M. Rubinstein, and D.A. Weitz, Soft poly(dimethylsiloxane) elastomers from architecture-driven entanglement free design, *Advanced Materials*, 2015, 27, 5132-5140.

[10] J.E. Mark, *Physical Properties of Polymer Handbook*, Springer, New York, 2006.

[11] M. Rubinstein and R.H. Colby, *Polymer Physics*, Oxford University Press, Oxford, UK, 2003.

[12] R.H. Carey, E.F. Schulz, and G.J. Dienes, Mechanical properties of polyethylene, *Industrial & Engineering Chemistry*, 1950, 42, 842-847.

[13] J. Lange and Y. Wyser, Recent innovations in barrier technologies for plastic packaging – a review, *Packaging Technology and Science*, 2003, 16, 149-158.

[14] B. Qing, L. Cai, K.T. Geiser, S. Lienemann, D.A. Weitz, and K.J. Van Vliet, Decoupling the contributions from surface adhesion and bulk viscoelastic properties to energy dissipation in compliant polymer gels, *Soft Matter*, in preparation.

[15] M.A. Brook, *Organosilicon Chemistry: Synthetic Applications in Organic, Organometallic, Materials, and Polymer Chemistry*, Wiley, New York, 1999.

[16] L. Leibler, Theory of microphase separation in block copolymers, *Macromolecules*, 1980, 13, 1602-1617.

[17] B. Qing and K.J. Van Vliet, Hierarchical design of synthetic gel composites optimized to mimic the impact energy dissipation response of brain tissue, *Molecular Systems Design & Engineering*, 2016, 1, 290-300.

[18] Z.I. Kalcioglu, M. Qu, K.E. Strawhecker, T. Shazly, E. Edelman, M.R. VanLandingham, J.F. Smith, and K.J. Van Vliet, Dynamic impact indentation of hydrated biological tissues and tissue surrogate gels, *Philosophical Magazine*, 2011, 91, 1339-1355.

[19] Z.I. Kalcioglu, R.A. Mrozek, R. Mahmoodian, M.R. VanLandingham, J.L. Lenhart, and K.J. Van Vliet, Tunable mechanical behavior of synthetic organogels as biofidelic tissue simulants, *Journal of Biomechanics*, 2013, 46, 1583-1591.

[20] G. Constantinides, C.A. Tweedie, D.M. Holbrook, P. Barragan, J.F. Smith, and K.J. Van Vliet, Quantifying deformation and energy dissipation of polymeric surfaces under localized impact, *Materials Science and Engineering: A*, 2008, 489, 403-412.

[21] G. Constantinides, C.A. Tweedie, N. Savva, J.F. Smith, and K.J. Van Vliet, Quantitative impact testing of energy dissipation at surfaces, *Experimental Mechanics*, 2009, 49, 511-522.

[22] E.P. Canovic, B. Qing, A.S. Mijailovic, A. Jagielska, M.J. Whitfield, E. Kelly, D. Turner, M. Sahin, and K.J. Van Vliet, Characterizing multiscale mechanical properties of brain tissue using atomic force microscopy, impact indentation, and rheometry, *Journal of Visualized Experiments*, 2016, 115, e54201.

[23] C.A. Tweedie and K.J. Van Vliet, Contact creep compliance of viscoelastic materials via nanoindentation, *Journal of Materials Research*, 2006, 21, 1576-1589.

[24] A.H.W. Nagan and B. Tang, Viscoelastic effects during unloading in depth-sensing indentation, *Journal of Materials Research*, 2002, 17, 2604-2610.

[25] H. Lu, B. Wang, J. Ma, G. Huang, and H. Viswanathan, Measurement of creep compliance of solid polymers by nanoindentation, *Mechanics of Time-Dependent Materials*, 2003, 7, 189-207.

[26] A.C. Fischer-Cripps, A simple phenomenological approach to nanoindentation creep, *Materials Science and Engineering: A*, 2004, 385, 74-82.

[27] M.L. Oyen, Spherical indentation creep following ramp loading, *Journal of Materials Research*, 2005, 20, 2094-2010.

[28] A.S. Mijailovic, B. Qing, D. Fortunato, and K.J. Van Vliet, Characterizing viscoelastic mechanical properties of highly compliant polymers and biological tissues using impact indentation, *Acta Biomaterialia*, 2018, 71, 388-397.

[29] L. Edelsten, J.E. Jeffrey, L.V. Burgin, and R.M. Aspden, Viscoelastic deformation of articular cartilage during impact loading, *Soft Matter*, 2010, 6, 5206-5212.

[30] J.Y. Sun, X. Zhao, W.R.K. Illeperuma, O. Chaudhuri, K.H. Oh, D.J. Mooney, J.J. Vlassak, and Z. Suo, *Nature*, 2012, 489, 133-136.

[31] D.C. Lin, D.I. Shreiber, E.K. Dimitriadis, and F. Horkay, Spherical indentation of soft matter beyond the Hertzian regime: numerical and experimental validation of hyperelastic models, *Biomechanics and Modeling in Mechanobiology*, 2009, 8, 345-358.

[32] E. Herbert, G.M. Pharr, W.C. Oliver, B.N. Lucas, and J.L. Hay, On the measurement of stress-strain curves by spherical indentation, *Thin Solid Films*, 2001, 398-399, 331-335.

[33] J.S. Field and M.V. Swain, Determining mechanical properties of small volumes of material from submicrometer spherical indentations, *Journal of Materials Research*, 1995, 10, 101-112.

[34] F. Schwarzl and A.J. Staverman, Time-temperature dependence of linear viscoelastic behavior, *Journal of Applied Physics*, 1952, 23, 838.

[35] D.B. Haviland, C.A. van Eysden, D. Forchheimer, D. Platz, H.G. Kassa, and Philippe Leclere, Probing viscoelastic response of soft material surfaces at the nanoscale, *Soft Matter*, 2016, 12, 619-624.

[36] T.L. Sun, T. Kurokawa, S. Kuroda, A.B. Ihsan, T. Akasaki, K. Sato, M.A. Haque, T. Nakajima, and J.P. Gong, Physical hydrogels composed of polyampholytes demonstrate high toughness and viscoelasticity, *Nature Materials*, 2013, 12, 932-937.

[37] M. Sakai, Energy principle of the indentation-induced inelastic surface deformation and hardness of brittle materials, *Acta Materialia*, 1993, 41, 1751-1758.

[38] E. Boschung, M. Heuberger, and G. Dietler, Energy dissipation during nanoscale indentation of polymers with an atomic force microscope, *Applied Physics Letters*, 1994, 64, 1794-1796.

[39] E.T. Herruzo, A.P. Perrino, and R. Garcia, Fast nanomechanical spectroscopy of soft matter, *Nature Communications*, 2014, 5, 3126.

[40] P. Attard, Measurement and interpretation of elastic and viscoelastic properties with the atomic force microscope, *Journal of Physics: Condensed Matter*, 2007, 19, 437201.

[41] J. Malzbender and G. de With, Energy dissipation, fracture toughness and the indentation load-displacement curve of coated materials, *Surface and Coatings Technology*, 2000, 135, 60-68.

[42] G.S. Fox-Rabinovich, S.C. Veldhuis, V.N. Scvortsov, L.S. Shuster, G.K. Dosbaeva, and M.S. Migranov, Elastic and plastic work of indentation as a characteristic of wear behavior for cutting tools with nitride PVD coatings, *Thin Solid Films*, 2004, 469, 505-512.

[43] D. Beegan, S. Chowdhury, and M.T. Laugier, Work of indentation methods for determining copper film hardness, *Surface and Coatings Technology*, 2005, 192, 57-63.

[44] F. Alisafaei, C. Han, and S.H.R. Seyed, On the time and indentation depth dependence of hardness, dissipation and stiffness in polydimethylsiloxane, *Polymer Testing*, 2013, 32, 1220-1228.

[45] W.C. Oliver and G.M. Pharr, An improved technique for determining hardness and elastic modulus using load and displacement sensing indentation experiments, *Journal of Materials Research*, 1992, 7, 1564-1583.

[46] I.N. Sneddon, The relation between load and penetration in the axisymmetric boussinesq problem for a punch of arbitrary profile, *International Journal of Engineering Science*, 1965, 3, 47-57.

Chapter 6: Characterization of viscoelastic mechanical properties via impact indentation

6.1 Introduction

The previous chapters introduced and employed impact indentation as a technique to characterize the impact energy dissipation response of brain tissue and potential tissue simulant materials. While we were able to compare and successfully match the impact response of brain tissue with synthetic polymers, we previously could only quantify empirical parameters such as the maximum penetration depth x_{max}, energy dissipation capacity K, and dissipation quality factor Q. However, we could not relate the measured deformation response to more conventional and widely reported mechanical properties of the material such as viscoelastic moduli and relaxation time constants, and thus, we experienced difficulties interpreting impact indentation data in relation to measurements from other techniques like rheology. The implications of being able to quantitatively relate impact indentation to rheological experimental data are two-fold. First, if we can accurately predict the impact response from rheological material properties, it will greatly facilitate the screening of existing gel libraries for tissue simulant material design since vast amounts of rheological data on gels have been reported in the literature. Second, impact indentation possesses unique advantages over conventional characterization methods like rheology that can enable more accurate measurements of viscoelastic mechanical properties, especially for highly compliant materials.

In addition to the design of brain tissue simulant materials, there are several other applications that motivate the need for methods to precisely and accurately characterize brain tissue mechanical properties. For example, measurement of mechanical properties of compliant materials is relevant not only for replacing or mimicking tissues, but also for elucidating the role of material mechanics in disease diagnosis or progression. Several cell types have demonstrated sensitivity to both biochemical and mechanical cues [1-6], and some diseases involving brain tissue, including glioma, multiple sclerosis or autism spectrum disorder, exhibit structural changes within the tissue that may alter local mechanical properties [7-11]. Whether any such mechanical differences can be detected and may modulate biological and behavioral functions (e.g., neuronal connectivity and cognition) remain open and important questions.

Unfortunately, several experimental challenges arise when the material of interest is of such low stiffness, particularly when the material is expected to deform in a rate-dependent or viscoelastic manner. Uniaxial and biaxial tensile experiments are prone to sample damage and experimental artifacts associated with the requirements for sample clamping and uniform cross-sectional geometry [12,13]. Therefore, conventional approaches for characterizing mechanical properties of highly compliant, viscoelastic materials have been relegated chiefly to dynamic frequency sweep tests, creep and stress relaxation tests, commonly using macroscale shear rheology, compressive tests, or indentation-based methods [14,15]. However, one significant limitation of these existing approaches is the requirement of contact detection between the measurement probe and sample surface, prior to the application of the prescribed load or displacement. Accurate contact detection becomes extremely challenging for materials of very low stiffness (less than 10 kPa), due in part to limited signal-to-noise sensitivity of commercial force transducers and to the inertia and finite compliance of the instrument load frame [16-19]. These limitations result frequently in inadvertent "pre-stress" or premature compression of the sample prior to the initiation of the controlled experiment, and can introduce significant experimental variation depending on sample thickness and degree of nonlinear elastic response [11,18,20].

In contrast to shear rheology and conventional indentation, impact indentation does not rely on detecting contact *a priori*. Here, we present a novel analytical method for characterizing viscoelastic moduli and relaxation time constants from impact indentation experiments (Section 6.2). In Section 6.3, we validate our novel approach by utilizing both impact indentation and macroscale shear rheology to measure the properties of PDMS elastomers and demonstrate strong agreement between the two methods. In Section 6.4, we demonstrate our validated method on hydrated, biological soft tissues obtained from porcine brain, murine liver, and murine heart, and report the equilibrium shear moduli, instantaneous shear moduli, and relaxation time constants for each tissue. Finally, in Section 6.5, we highlight the key advantages of impact indentation over conventional techniques and also discuss a few potential challenges of our technique, including ideas for future work.

All of the work presented in this chapter was published in *Acta Biomaterialia* [21]. Aleksandar Mijailovic, also a Ph.D. candidate in the Van Vliet Laboratory for Chemomechanics at MIT, developed the new approach to analyze impact indentation data using linear viscoelastic

theory and contact mechanics, and also wrote MATLAB scripts to facilitate data analysis. The thesis author conducted impact indentation measurements on compliant polymeric gels and porcine brain tissue, and assisted with implementation and validation of the new data analysis method. Impact indentation measurements on murine heart and liver tissue collected previously by Dr. Zeynep Ilke Kalcioglu (Van Vliet group) were also utilized to demonstrate the new approach to extract viscoelastic moduli and time constants, analyzed with the framework below by the thesis author.

6.2 Materials and methods

6.2.1 Theory

Indentation generally includes the controlled deformation of a planar sample surface by a three-dimensional object or probe of known geometry and mechanical properties, such that the probe displacement can be attributed unambiguously to sample deformation and then related directly to mechanical properties of that material through knowledge or measurement of the force and assumptions of specific constitutive laws of the sample material. The specific subset of this deformation of present interest, impact of rigid spheres on a viscoelastic semi-infinite half-space, has been studied previously [22-24]. Our present derivation extends this analysis to the impact of a viscoelastic body by a pendulum with a flat cylindrical punch indenter (Fig. 2-6(A)) under the assumption that wave propagation can be ignored. A torque balance on the pendulum may be rewritten as a force balance between the sum of external forces $F_{ext}(t)$ and the pendulum inertia, pendulum damping, gravity, and the force from Hertzian contact of a flat punch indenter on a viscoelastic half-space [25]:

$$F_{ext}(t) = m_{eff}\frac{d^2u}{dt^2} + b\frac{du}{dt} + k_g u + \frac{4R}{(1-\upsilon)}\int_0^t G(t-t')\frac{du(t')}{dt'}dt' , \qquad (6\text{-}1)$$

where u is the linear displacement of the indenter, m_{eff} is an effective mass related to the moment of inertia of the pendulum, b is intrinsic pendulum damping coefficient, k_g is an equivalent gravitational "stiffness," R is the radius of the indenter, υ is the Poisson's ratio of the sample, and $G(t)$ is the shear relaxation function of the sample. The constants R, m_{eff}, b, and k_g are properties

of the instrumented indenter, and can be determined experimentally (see Appendix G). Elastomers and biological soft tissues are often idealized as incompressible materials, meaning that υ approaches 0.5 and, more importantly, is constant in time. Therefore, if the loading conditions are known, measuring the indenter's displacement enables quantification of the material constitutive law in the form of $G(t)$, as illustrated in Fig. 6-1.

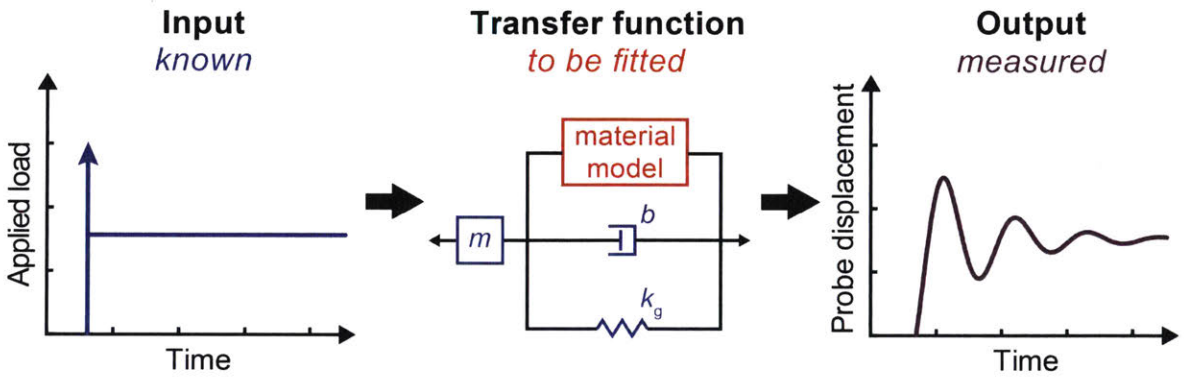

Figure 6-1 Framework for quantifying viscoelastic material properties via impact indentation. The known input and measured output are related by a transfer function defined by the pendulum mass m, damping coefficient b, gravitational stiffness k_g, and a viscoelastic constitutive model that describes the material response. Because m, b, and k_g are calibrated beforehand, the parameters associated with a given material model can be fitted to the displacement response of the sample. From [21].

The external load is approximated as the sum of the inertial impulse from impact [24] and a constant load applied throughout the experiment, as reflects the expected loading history of the instrument used in these impact indentation experiments. With impact at $t = 0$,

$$F_{\text{ext}}(t) = m_{\text{eff}} v_{\text{in}} \delta(t) + F_{\text{el}} H(t), \tag{6-2}$$

where v_{in} is the impact velocity, $\delta(t)$ is the Dirac delta function, F_{el} is the load applied by the electromagnetic coil, and $H(t)$ is the Heaviside step function. The impact event provides an objectively identifiable contact point even in compliant samples, and a sufficiently high prescribed force F_{el} results in maintained contact between the indenting probe and sample surface after the initial impact event or impulse.

In contrast to the direct output obtained from creep, stress relaxation, or rheology experiments, the constitutive behavior $G(t)$ of a material is not obtained from a fit to the raw data such as displacement vs. time. Instead, the form of $G(t)$ is assumed, and the measured displacement response as a function of time is fitted to the solution of Equation 6-1 to obtain the parameters associated with $G(t)$. For instance, in the examples below we assumed the linear viscoelastic Standard Linear Solid (SLS) constitutive model, which is described by the relaxation function as:

$$G(t) = G_\infty + (G_0 - G_\infty)e^{-t/\tau}, \tag{6-3}$$

where G_∞ is the equilibrium shear modulus, G_0 is the instantaneous shear modulus, and τ is the characteristic relaxation time constant.

6.2.2 New impact indentation analysis

In impact indentation, contact detection is not required prior to the application of the prescribed load. However, the point at which contact between the probe and sample occurred needs to be identified during post-processing of the data. The instrumented indenter records the displacement of the probe throughout the impact process. Figure 6-2 illustrates an example of the probe displacement output, along with the corresponding velocity, acceleration, and jerk profiles that can be calculated by taking the first, second, and third derivative of displacement with respect to time, respectively. Jerk, the time derivative of acceleration, will show discontinuities during steps in acceleration or sudden changes in the slope of the acceleration, such as during impact. We defined zero displacement as the position at which the probe made contact with the sample surface at an impact velocity v_{in}. To identify this contact point x_0, we first examined the jerk profile (Fig. 6-2(D)) to identify a sudden change in direction and sharp decrease, as indicated by the red circle. As expected, this point coincided with a noticeable change in slope of the acceleration profile (Fig. 6-2(C)), reflecting that contact in many samples is approximately concurrent with an instance of zero acceleration and maximum velocity. Note that we did not directly assume x_0 to be the point of maximum velocity because of the potential for inherent dissipation by the pendulum. Additionally, the jerk profile appeared smoother when the stiffness of the sample was less than 1 kPa, and thus, the contact point was more difficult to identify

accurately and objectively as polymer or tissue stiffness decreased below this magnitude, for the given instrument design and internal dissipation. Figure 6-3 illustrates an example of the jerk profile obtained for brain tissue at an impact load of 3.5 mN, in which the sudden change in jerk at the point of contact became less obvious but still detectable. Optimizing the manufacturing design of the instrument to decrease the intrinsic damping of the pendulum may lead to increased sensitivity in the contact detection process.

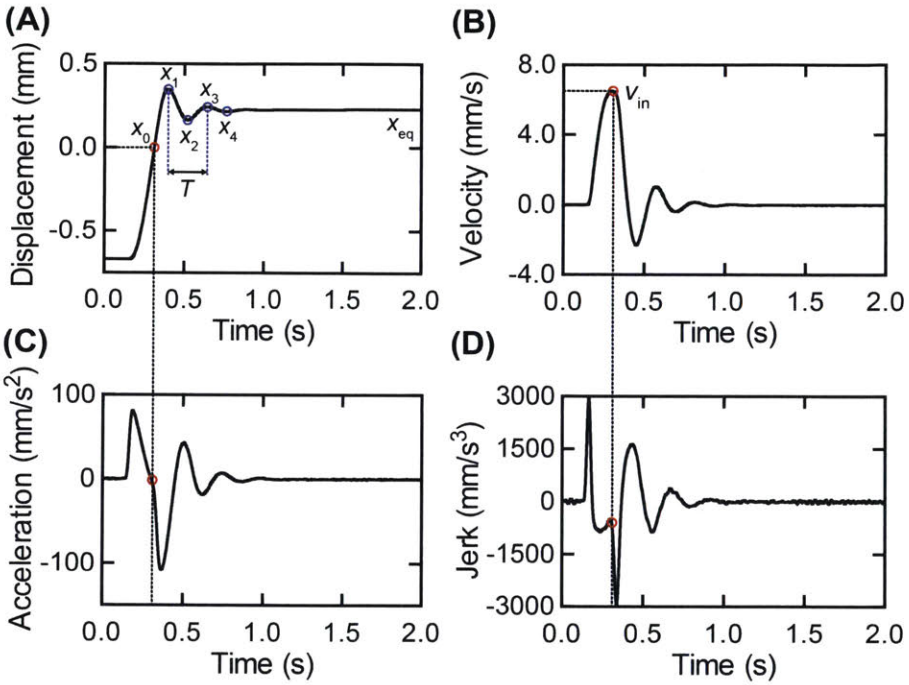

Figure 6-2 (A) Probe displacement is recorded as a function of time during the impact process, and the corresponding (B) velocity, (C) acceleration, and (D) jerk profile can be calculated. The acceleration and jerk profiles are used to determine when contact between the probe and sample occurs, as indicated by the red circles. The blue circles in (A), which correspond to the local maxima and minima of the displacement profile (x_1, x_2, x_3, and x_4), are used to determine the damping ratio and period T of the system. These representative data were obtained from a PDMS gel of 7 kPa. From [21].

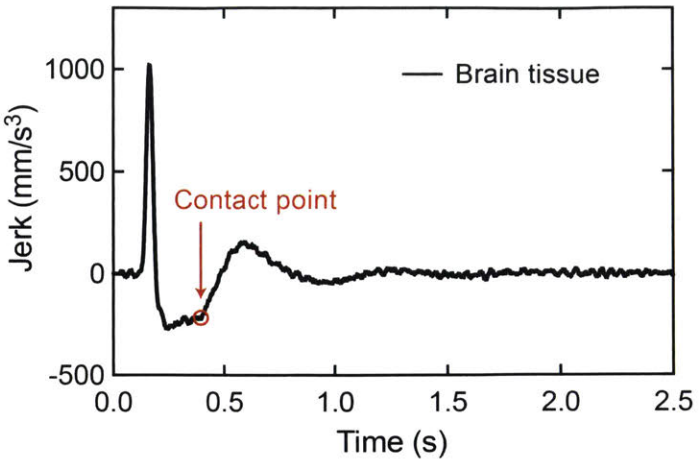

Figure 6-3 Jerk profile used to determine the point of contact between the flat punch probe and porcine brain tissue during an impact process. The red circle indicates when contact occurred, which was selected at the onset of the slight change in the slope of the curve immediately after the trough. From [21].

We obtained the material constants G_∞, G_0, and τ by fitting the solution to Equation 6-1 to the measured displacement as a function of time, examples of which are shown in Fig. 6-4 for a PDMS gel and brain tissue sample. While the form of the solution to Equation 6-1 may be written explicitly, the constants must be calculated by residue theory, and thus there is no closed form solution in terms of the viscoelastic moduli, relaxation time constant, system parameters, loading conditions and initial conditions. For simplicity, we solved Equation 6-1 by performing a numerical inverse Laplace transform of its transfer function:

$$\bar{U}(s) = \frac{\bar{F}(s)}{\bar{P}(s)} = \frac{v_{\text{in}} + \frac{F_{\text{el}}}{m_{\text{eff}} s}}{s^2 + \frac{b}{m_{\text{eff}}} s + \frac{4R}{m_{\text{eff}}(1-\upsilon)}\left(G_\infty + \frac{(G_0 - G_\infty)s}{\left(s + \frac{1}{\tau}\right)}\right) + \frac{k_g}{m_{\text{eff}}}}, \tag{6-4}$$

where s is complex frequency, and $U(s)$, $F(s)$, and $P(s)$ are the Laplace transformed displacement, external load and characteristic polynomial, respectively. The parameters v_{in}, F_{el}, m_{eff}, b, and k_g were known, and the polymers or tissues were assumed to be incompressible (Poisson's ratio $\upsilon = 0.5$), as is commonly assumed for polymers such as PDMS and soft tissues [14,26-28]. We then extracted G_∞, G_0, and τ using a nonlinear curve fitting (MATLAB) of the experimental time-displacement data (Fig. 6-4). We estimated goodness of fit between the

model-predicted and measured displacement vs. time response through calculation of R^2. Although this is an inexact metric of fit quality for nonlinear models [29], it provides a useful first approximation that can be compared across datasets.

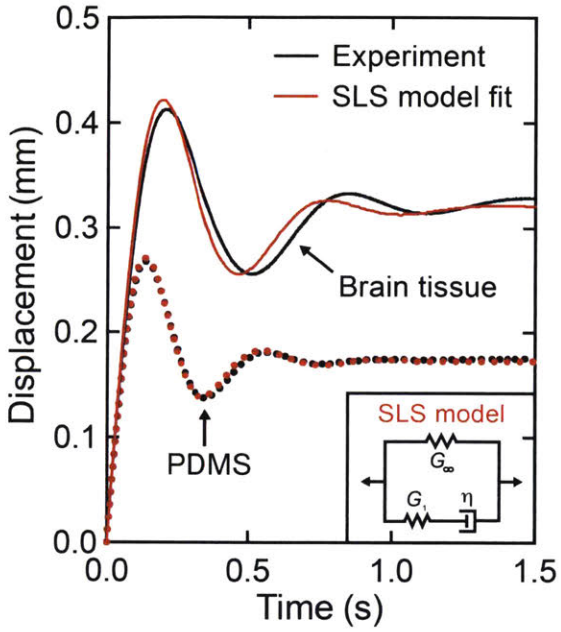

Figure 6-4 Representative experimental data (black) and SLS model fits (red) of the displacement vs. time response obtained from porcine brain tissue (solid curve) and PDMS (dotted curve). Inset: Schematic of the SLS constitutive model for linear viscoelasticity. From [21].

6.2.3 Oscillatory shear rheology

For method validation purposes, we also conducted oscillatory shear rheology experiments at 25°C using a parallel plate rheometer (Anton Paar MCR 501) with a plate diameter of 10 mm to characterize the macroscale viscoelastic mechanical properties of PDMS. We confirmed that frequency sweeps from 0.1 to 100 rad/s at 1% shear strain were in the linear viscoelastic regime using strain sweep experiments. We calculated shear storage moduli G' and loss moduli G'' as a function of frequency via the rheometer vendor software. To compare the impact indentation data to rheological data, we first fitted a Prony series to the measured G' and G'' at different frequencies (see Section 2.3.2.1). We assumed two Maxwell elements because a single time

constant did not produce a good fit. Since we observed a low frequency plateau but did not observe a high frequency plateau, the equilibrium modulus G_∞ was a more robust variable for comparing the two techniques than G_0. Relaxation time constants may not be appropriate to compare because they are limited by the frequency range of the rheology experiment. The time constant with highest weight G_j was used to compare to the time constant obtained from impact indentation.

6.2.4 Materials

We synthesized and used PDMS-based elastomers in validation experiments. CY 52-276 PDMS (Dow Corning®) is a two-component silicone kit, and allowed for easy tunability of elastomer crosslink density and stiffness. Part A contained the prepolymer base, and Part B contained the catalyst. We prepared mixtures of three distinct mass-to-mass ratios of Part A to Part B (1.25:1, 1:1, and 1:1.2), and hereafter refer to these three compositions as PDMS A, B, and C, respectively. After degassing under vacuum to remove air bubbles and pouring into silanized petri dishes, we cured the CY 52-276 samples at 80°C overnight. We then cut samples of cured PDMS, immersed in PBS containing 3% Pluronic® F108, with a surgical punch. Since the mixtures produced highly compliant and adhesive samples, the Pluronic® F108 helped enable clean detachment of the silicone from the Petri dish [30]. The volume of mixture that was prepared controlled the final thickness of the sample. We prepared samples of 2 mm and 6 mm thickness for mechanical characterization via oscillatory shear rheology and impact indentation, respectively.

We harvested whole porcine brains from healthy adult pigs at a local stockyard in Massachusetts. Liver and heart organs were harvested from healthy adult Sprague-Dawley rats obtained from the Division of Comparative Medicine at MIT. All experiments involving tissues followed the University IACUC protocol and the NIH guidelines for animal care. Tissue preparation for mechanical characterization via impact indentation has been detailed previously in Chapter 2. We sliced brain tissue into 6 mm thick sections exhibiting flat and parallel surfaces, and immediately stored samples in Hibernate®-A, a CO_2-independent nutrient medium for adult neural tissue. For both liver and heart, we prepared tissue discs of 8 mm diameter and thickness of 3 to 5 mm using a surgical punch, and stored these discs in Krebs-Henseleit buffer. We conduced mechanical characterization experiments between 3 and 48 hours post mortem, with

samples immersed fully in the corresponding aqueous media. Over this duration, the measured impact response did not vary detectably. To determine whether impact indentation distinguished viscoelastic constants G_∞, G_0, and τ between different tissues, we conducted a series of Mann-Whitney tests for each parameter between each tissue (significance at $p < 0.05$). The Mann-Whitney rank-based test was chosen due to the small number of measurements (n = 4, 8, 12 for liver, heart and brain, respectively).

6.3 Experimental validation on PDMS of different crosslink density

6.3.1 Characterization of G_∞, G_0, and τ

We characterized three PDMS elastomers of varying crosslink density and anticipated stiffness (PDMS A, B, and C, as denoted in order of increasing crosslink density). We fit the impact responses of each PDMS elastomer, assuming an SLS model, to extract G_∞, G_0, and τ. The fits matched well to the experimental data, with R^2 values exceeding 0.95. While we acknowledge that R^2 is an inadequate goodness of fit for nonlinear models [29], it provides a useful first estimate of model agreement across experimental datasets, such as experiments with different loads and materials. The dotted curves in Fig. 6-4 illustrate an SLS model fit for PDMS B, which exhibited an intermediate stiffness. Although we examined each sample under multiple loading conditions, Fig. 6-5 illustrates results acquired at the lowest applied impact velocity. We found G_∞ to span an order of magnitude among these three polymers, whereas G_0 spanned a factor of four and τ was similar among all samples. Specifically, PDMS A exhibited mean G_∞ of 400 Pa, G_0 of 5.5 kPa, and τ of 0.05 s; PDMS B exhibited mean G_∞ of 2.18 kPa, G_0 of 10.425 kPa, and τ of 0.055 s; and PDMS C exhibited mean G_∞ of 4.82 kPa, G_0 of 19.94 kPa, and τ of 0.05 s. As expected, the measured moduli correlated directly with the crosslink density of the PDMS elastomer: moduli increased as crosslink density increased.

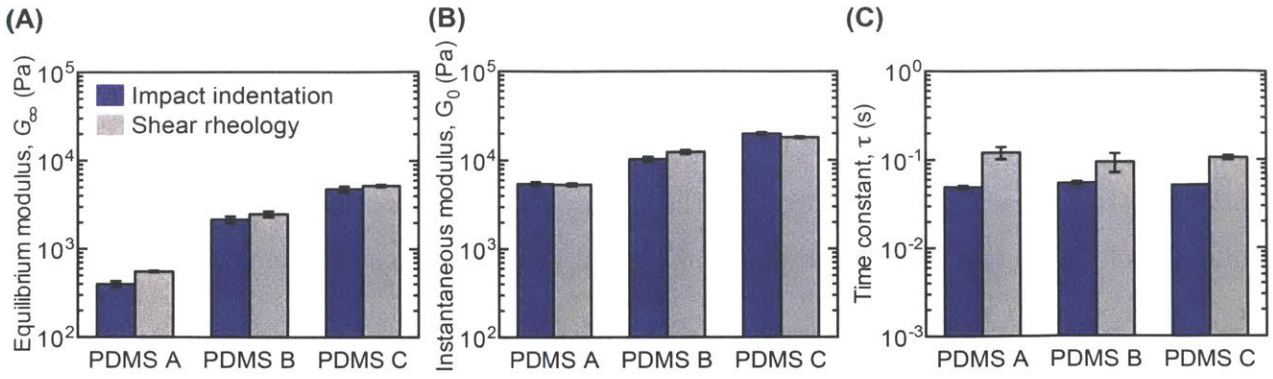

Figure 6-5 Comparison of the (A) equilibrium shear modulus, (B) instantaneous shear modulus, and (C) relaxation time constant calculated by fitting impact indentation data (blue) with an SLS model and fitting oscillatory shear rheology data (gray). Three PDMS elastomers of varying crosslink density were examined. Results are represented as mean ± standard deviation (n = 3 replicate measurements for each experimental technique). From [21].

6.3.2 Comparison to results from oscillatory shear rheology

Figure 6-5 also compares G_∞, G_0, and τ obtained from impact indentation, shown in blue, to those obtained from macroscale shear rheology, shown in gray. The viscoelastic moduli at both very long timescales and very short timescales agreed strongly between the two characterization techniques for all three PDMS samples, as illustrated by Fig. 6-5(A) and Fig. 6-5(B), respectively. Additionally, the characteristic time constants agreed reasonably well between the two methods (Fig. 6-5(C)), though a robust comparison with rheology is difficult because a glassy plateau at high frequencies was not observed in those experiments, and thus, multiple time constants were necessary to fit the shear rheology experimental data. The time constant associated with the largest weight in the Prony series was used for comparison against the time constant measured by impact indentation.

We validated the viscoelastic parameters of engineered, compliant polymers obtained by impact indentation through comparison with oscillatory shear rheology. In all PDMS samples tested, the contact point was identifiable clearly from the acceleration and jerk, and curve fits matched the experimental data well when fitted to only three variables, examples of which are shown in Fig. 6-6. The fits at lower impact loads tended to be stronger, and thus were used to calculate the viscoelastic moduli and relaxation time constants reported in Fig. 6-5. We did not observe an impulse in the acceleration or a discontinuity in the velocity as would be expected

from a rigid body impact, for example. Rather, we observed a clear shift in the acceleration and a discontinuity in the jerk (Fig. 6-2(C and D)), demonstrating the instantaneous response of the impacted material during probe-material contact. For the material surface, the impact corresponds to an instantaneous change in the material surface velocity, assuming that the inertial effects in the material are negligible. Thus, the delta function impulsive "load" in Equation 6-3 may be interpreted physically as an initial condition at $t = 0^+$ in the pendulum-material system, as the material response does not exist prior to impact. The improved contact detection is likely due to instantaneous glassy response of the sample during impact, which is effectively stiffer and therefore more easily measurable than the response in a typical low velocity contact detection procedure.

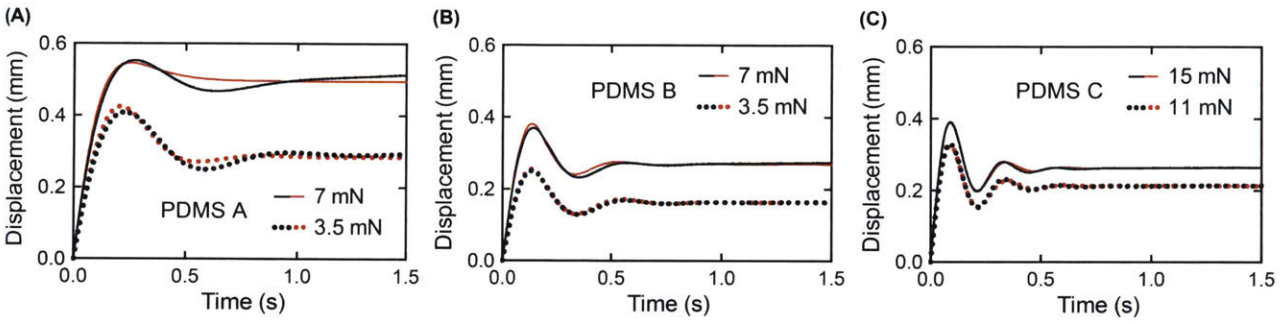

Figure 6-6 Representative examples of the experimental impact response data (black) compared to the SLS model fits (red) for the three PDMS elastomers (A-C). Results at two different impact loads are shown for each sample. The dotted curves correspond to the lower loads used to determine the viscoelastic mechanical properties. The solid curves correspond to the higher loads, which may have led to nonlinear responses. From [21].

Comparison of the measured PDMS viscoelastic properties indeed validated impact indentation against shear rheology. The equilibrium shear modulus measured by impact indentation was in agreement with the fit obtained from macroscale shear rheology experiments (Fig. 6-5(A)). Interestingly, we observed that the computed G_∞ was slightly higher when obtained from macroscale shear rheology compared to that obtained from impact indentation, with the largest difference for the most compliant sample, PDMS A. This comparison is consistent with our hypothesis that impact indentation would quantify a lower G_∞ than rheology, because accurate contact detection afforded by the former approach avoids compressive pre-stress artifacts known to affect rheology and conventional indentation methods [18,31]. While

the instantaneous shear modulus also agreed well between those methods (Fig. 6-5(B)), it is more difficult to definitively compare the magnitudes of G_0 because there existed no observable plateau in the high frequency rheology data that would be assigned unambiguously to G_0. Moreover, comparing time constants between techniques is not meaningful because the entire frequency range is not measured in rheology, and because multiple time constants must be used to obtain a good fit.

6.4 Application to biological soft tissues

An important application of such a validated approach is the mechanical characterization of biological soft tissues. Brain, liver, and heart tissues are relatively compliant as compared to mineralized tissues such as bone, and thus more difficult to mechanically characterize accurately. We characterized mammalian tissues from all three organs via impact indentation to obtain viscoelastic constants. The response predicted by the fitting to Equation 6-1 matched reasonably well to the experimental impact data for these biological samples, with R^2 exceeding 0.9 for all cases. An example demonstrating the quality of fit for brain tissue is shown by the solid curves in Fig. 6-4, and Table 6-1 presents the magnitudes of G_∞, G_0, and τ as determined by an SLS model fit. While the standard deviation of the mean was appreciable among replicate experiments for a given property and tissue source, we attributed this variation chiefly to natural variation among tissue samples (n = 2 to 4 samples per species per tested condition), and also to variation in tissue structure and corresponding mechanical response at distinct locations in the same sample (N = 2 to 4 replicate impact indentation experiments at well-spaced positions in a given sample). Statistical power (see Appendix E) was sufficiently high to confirm statistically significant differences between liver and heart and between brain and heart for G_∞, G_0, and τ (Mann-Whitney U, $p < 0.05$). Liver and brain exhibited significantly different time constants (Mann-Whitney U, $p < 0.05$), but did not exhibit significantly different G_∞ or G_0 (Mann-Whitney U, $p > 0.05$).

Murine heart tissue exhibited the greatest stiffness at short deformation timescales as expressed by the instantaneous shear modulus, with G_0 of ~11 kPa exceeding that of porcine brain (2.4 kPa) and murine liver (2.1 kPa) tissues. Heart tissue also exhibited higher stiffness at longer timescales described by the equilibrium shear modulus, with G_∞ of ~3 kPa exceeding that

of brain (0.1 kPa) and liver (0.2 kPa) tissues by approximately an order of magnitude. Note that because the tissues were sourced from animal species, we do not claim here any inferences from the relative magnitudes attributed to organ tissue type; those differences could be attributed reasonably to a variety of factors including species-dependent or animal age-dependent tissue structure and properties, and systematic comparisons among tissues would consider a single species source. Additionally, we note that the characteristic viscoelastic time constants indicated that liver tissue relaxed noticeably more slowly than the other soft tissues, exhibiting a time constant τ of ~200 ms as compared to ~100 ms for the other two tissues. These comparisons simply illustrate the capacity to obtain three distinct viscoelastic descriptors of soft tissues, with sufficiently high precision and statistical power that one can draw comparisons among hydrated tissue types or testing conditions.

Table 6-1 Viscoelastic mechanical properties of biological soft tissues measured via impact indentation, calculated via Equation 6-1. Data represented as mean ± standard deviation (n = 12, 4, and 8 replicate measurements for brain, liver, and heart tissue, respectively). From [21].

Soft tissue	Equilibrium shear modulus, G_∞ (Pa)	Instantaneous shear modulus, G_0 (Pa)	Time constant, τ (ms)
Brain (Porcine)	125 ± 25	2410 ± 550	115 ± 8
Liver (Murine)	190 ± 97	2075 ± 393	220 ± 17
Heart (Murine)	2885 ± 1505	11035 ± 3266	103 ± 8

To summarize, we demonstrated that impact indentation may be used to measure the viscoelastic mechanical properties of fully immersed and hydrated biological soft tissues, including those obtained from mammalian brain, liver, and heart (Table 6-1).

It is notable that contact was clearly detectable for impact indentation in heart tissue, exhibiting instantaneous changes in slope in acceleration and discontinuities in the jerk profiles that was similar to the PDMS polymers. The contact point was less visually obvious for measurements on brain and liver tissue, but still detectable (Fig. 6-3). In all tissues, the

identifiable contact point likely improved measurement of G_∞. The equilibrium shear modulus is most commonly and straightforwardly measured by other techniques, and therefore it is an appropriate property to assess accuracy of our approach. We found that G_∞ calculated from the impact indentation response was in reasonable agreement with the admittedly wide range of literature reports for all tissues measured herein. For liver and brain tissue, the expected range of G_∞ according to prior reports is on the order of several hundreds of Pa [11,14,16,18,20,32].

For brain tissue specifically, Gefen et al. conducted indentation creep on *ex vivo* porcine brain with a spherical indenter, reporting G_∞ of approximately 450 Pa; this was the same order of magnitude as we determined for this mechanical property, but nearly fourfold higher [33]. Additionally, we had conducted shear rheology previously on the same porcine brain tissue source as those used in our present impact indentation experiments [16] (see Chapter 2). From those shear rheology data, we fitted a Prony series to obtain G_∞ of 208 ± 20 Pa, which was close but higher than our impact indentation measurement of 125 ± 25 Pa. Furthermore, we demonstrated that increasing axial compressive strain increased both G_∞ and G_0 of porcine brain tissue measured by shear rheology, confirming results from previous studies attributed to the pre-strain or pre-stress effect [11,18,31]. This suggests that accurate contact detection via impact indentation resulted in lower magnitude of measured G_∞ by avoiding compressive pre-stress of the tissue. Heart tissue is more structurally anisotropic than these tissues at the length scales considered in this study [34], and we did not design this study to probe mechanical anisotropies in this tissue. As the complex and three-dimensional stress field of indentation does not facilitate direct measurement of anisotropic moduli, we consider the viscoelastic properties reported herein for heart tissue to be order of magnitude estimates that would be refined further through consideration of potential anisotropies.

Along with accurate contact detection, experimental timescales must be sufficiently long to accurately measure G_∞. The porcine brain measurements by Gefen et al. [33] as well as our own rheology experiments were conducted at considerably longer timescales (10s of seconds), yet still measured a stiffer response as compared to impact indentation. These results suggest that our long-timescale stiffness measurements (i.e., G_∞) were not substantially overestimated due to our shorter experimental procedure, at least compared to other potential experimental artifacts. Nevertheless, we note that longer measurements are certainly possible for impact indentation, and may be pursued in future work if necessary for the materials or properties of interest.

In addition to agreement in G_∞, we found that G_0 for porcine brain tissue also agreed well with the range expected in the literature. Chatelin et al. [14] provided a review of available data for brain tissue acquired by various approaches, from which we observed that the magnitude of G' measured by rheology at high frequencies (~100 Hz) was in the range of 500-1000 Pa and not yet plateaued. Our results thus corresponded to prior studies within an order of magnitude. Furthermore, the relaxation time constant we obtained for brain tissue agreed with that reported by Prange et al. [35], in which stress relaxation experiments fitted with two time constants exhibited a dominant time constant at 100 ms (and a secondary time constant of roughly 3 s). Those researchers also reported what was termed a maximum modulus of ~500 Pa, which was significantly less than our measured magnitude of G_0 ~ 2100 Pa. However, the time resolution available to Prange et al. was only on the order of 0.01 s, which is inadequate to measure the true G_0; in contrast, our approach determined G_0 from the natural frequency of the damped oscillation. In previous work by Gefen et al., the authors found a short timescale modulus G_1 of 1200 Pa by fitting a two-branch Prony series to their creep measurements conducted with a spherical indenter [33]. They noted that this G_1 value approaches G_0, but did not reach it due to the inability to achieve a perfect step in load during the experiment, an artifact common to creep compliance and stress relaxation tests. Fitting our rheological measurements on porcine brain [16], we found that $G_0 = 780 \pm 66$ Pa, with measurements up to ~15 Hz. The magnitude of G_0 obtained from rheology was lower than the magnitude obtained from impact indentation, likely because the short-timescale behavior was not sufficiently captured by such rheological measurements. To summarize, we demonstrated that impact indentation may be used to measure the viscoelastic mechanical properties (G_∞, G_0, τ) of fully immersed and hydrated biological soft tissues, including those obtained from mammalian brain, liver, and heart (Table 6-1).

6.5 Discussion

6.5.1 Advantages of impact indentation

Impact indentation provides several advantages over conventional techniques, for which accurate and precise measurements of viscoelastic mechanical properties become increasingly difficult with increasing compliance. One of the most significant challenges for quasistatic indentation

and macroscale oscillatory shear rheology of highly compliant samples is the accurate and objective identification of the contact commencement between the probe and sample. Inaccuracy in contact point identification can lead to overestimates in measured moduli if the polymer or tissue is strain stiffening over that range of actual material deformation [31]. However, impact indentation does not rely on detecting contact *a priori*, but instead determines the point of contact during post-processing of the data through a clear observable change in the acceleration and jerk of the probe (Fig. 6-2), thus providing more accurate contact detection. Shear rheology also requires that a nonzero compressive load be applied to the material prior to data acquisition, to provide sufficient friction between the plate and sample; that requirement can lead to a non-uniform pre-stressed state that may alter the measured shear moduli. Pre-stresses are obviated in impact indentation, as the deformation commences upon impact.

The impact response also improves analysis of short timescale glassy behavior as the natural frequency of the oscillation is directly related to the viscoelastic properties of the material. By contrast, measurement of short timescale glassy behavior of the material may be more difficult in conventional creep compliance and stress relaxation experiments because such experiments cannot achieve sufficiently "instantaneous" steps of applied displacement or load, and the instrument timescale resolution is limited to how quickly these "steps" can be applied. Similarly, rheological experiments cannot reliably access the short timescale behavior of highly compliant samples due to issues with instrument inertia obfuscating the material response signal at high frequencies.

An additional advantage of the present approach, which can be advantageous for materials such as soft tissues that can also exhibit appreciable "stickiness" or adhesion, is the flat punch probe geometry. Adhesion introduces error in instrumented indentation and AFM-enabled indentation (including probe-based creep and stress relaxation experiments) when a spherical indenter is used; the contact area with the sphere varies naturally with indentation depth, and unpredictably so when the extent of probe-material adhesion is not well established [36,37]. In contrast, impact indentation with a flat punch geometry maintains constant contact area between the probe surface and sample surface, minimizing adhesive energy dissipation, provided that slip does not occur at the material surface. Furthermore, because the probe did not retract beyond the original surface plane of the undeformed material during the entire impact process, contact and traction at the probe-material interface were maintained under the impact indentation conditions

reported herein. Thus, artifacts such as tensile loading on the sample when retracting from an adhesive surface and reducing the effective contact were not contributors to the measured response. While the small but finite rotation of the probe may lead to sliding at the surface or misalignment of the probe and surface during impact, these effects are likely negligible as vertical displacements in the present pendulum-based impact experiments are approximately three orders of magnitude smaller than horizontal displacements into the material. Furthermore, as we have demonstrated in Chapter 5, the effects of surface adhesion on the measured impact energy dissipation response is expected to be negligible for the high strain rates (> 1/s) associated with impact indentation.

As in conventional indentation-based techniques, impact indentation also allows for local measurement of viscoelastic properties on the length scale of the probe dimensions. This spatial resolution can provide a significant advantage over macroscale oscillatory shear rheology, dynamic mechanical analysis, and tension tests that only give average properties of the bulk sample, particularly for structurally heterogeneous samples such as biological tissues or composite materials. In this study, we measured properties on the millimeter length scale; in principle, lower length scales may be measured by using a smaller probe. However, a practical limit to this spatial resolution is anticipated because as the probe radius decreases, artifacts due to stress concentrations at the edges of the flat punch will increase in relative contribution to the measured response.

While we have demonstrated this approach specifically for a flat punch probe geometry and an SLS material constitutive model, impact indentation may be generalized readily to other probe geometries and material models. Any linear material model may be used with the solving and fitting methods described herein by replacing the form of the relaxation function $G(t)$. Nonlinear material models may also be used, but in that case, Equation 6-1 becomes nonlinear and may not be solved with Laplace transforms. Spherical probe geometry may also be implemented, again resulting in a nonlinear equation. This invalidates the Laplace transform technique such that the governing differential equation must be solved in the time domain. The spherical probe geometry confers the advantage of avoiding stress concentration at edges, but may be subject to significant adhesive effects due to change in contact area over the course of the data acquisition period. However, as detailed in Chapter 5, we do not expect adhesion to significantly affect the mechanical response measured via impact indentation.

6.5.2 Challenges and future work

While we observed good agreement between the magnitudes of G_∞, G_0, and τ measured by impact indentation and those previously reported in the literature for biological soft tissues, we note that our measured moduli increased with increasing impact velocity and load; equivalently, those measured moduli increased with higher maximum penetration depths and strains. We attribute these trends to nonlinear, strain-stiffening material behavior that would occur at sufficiently high deformation strains and particularly at stress concentrations at the edge of the indenter–material interface. Since our analytical model assumes linear viscoelasticity, it is necessary to determine the linear range for the applied loads and deformations in our experiments. To measure this linear range, we varied the load and impact velocity used. If the measured moduli changed appreciably at increased load or velocity, the deformation was assumed to be nonlinear; if the measured moduli did not change, we concluded that we were measuring the linear range. Figure 6-7 illustrates the effects of load on the measured moduli for the PDMS elastomers and biological soft tissues tested in this study. This approach is analogous to an amplitude strain sweep in rheology, in which changing the maximum strain does not change measured G', G'' in the linear ranges, but changes G', G'' past the linear limit [16,28]. We note that, since flat cylindrical indenters create large stress concentrations at the edge of the interface with the material, it is likely that nonlinear material response occurs in these areas even at smaller deformations. However, at sufficiently low deformations, the nonlinear material deformation should contribute negligibly to the measured force compared to the linear viscoelastic material deformation in the bulk material. In this study, all data presented were measured at the lowest measurable load, and thus were either within or approached the linear approximation.

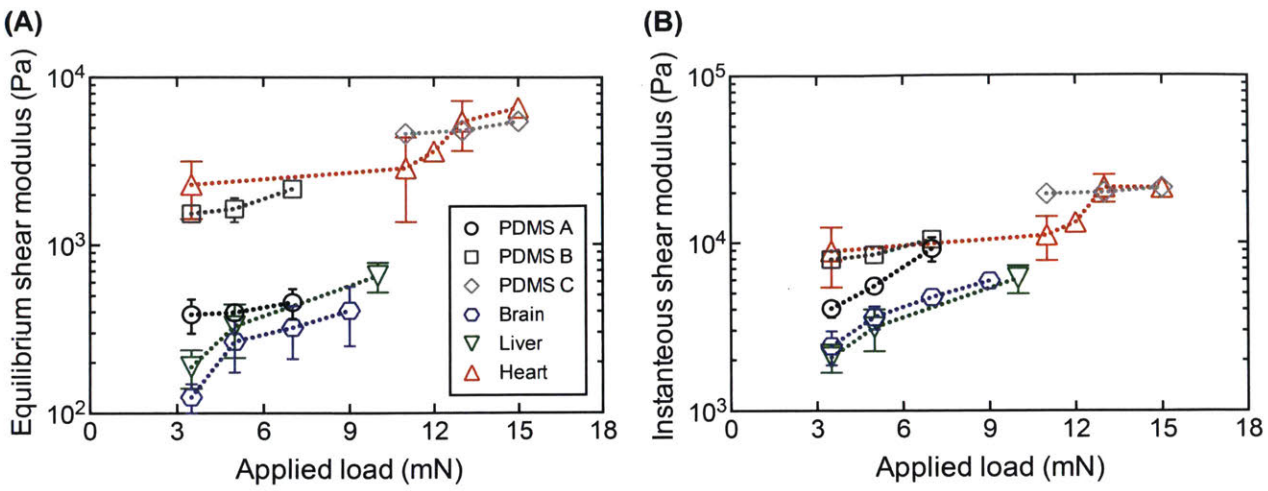

Figure 6-7 Effects of applied impact load on the measured (A) equilibrium shear moduli and (B) instantaneous shear moduli for the three PDMS elastomers and three biological soft tissues. In the linear viscoelastic regime, the moduli will not depend on the applied load or strain. However, the materials tested in this study all exhibit varying degrees of nonlinearity, and thus material characterization should occur at the lowest measurable load in order to approach the linear approximation. From [21].

In addition to material nonlinearity, the intrinsic pendulum parameters m_{eff}, b, and k_{g} may increase measurement error for highly compliant materials if the signal contribution by these parameters to the displacement-time response significantly exceeds the contribution from the material response. These parameters could potentially be optimized for improved instrument design and displacement profile design in future studies. For example, in our measurements for porcine brain tissue, the material "stiffness" term $\frac{4R}{(1-\nu)}G_{\infty}$ was several times smaller than the pendulum parameter k_{g}. As a result, a small error in contact point leads to significant error in measured equilibrium modulus (i.e., k_{g} amplifies the small contact point error). While we maintained the capacity to measure the equilibrium moduli of brain tissue due to accurate contact detection, this issue can also be mitigated by altering the instrument design (e.g., decreasing the pendulum k_{g}) or by simply by increasing the radius of the probe. Similarly, the intrinsic pendulum damping b can be reduced to minimize contributions to the measured dissipative response.

While the pendulum parameters may affect the measurement of G_{∞} significantly depending on the relative viscoelastic properties of the sample, measurement of G_0 should be relatively insensitive to pendulum design for tissues. This robustness is due to the typically small damping

factors (< 0.3), and to the common observation that $G_0 >> G_\infty$ for soft tissues. Under these conditions, the pendulum parameter k_g does not contribute strongly to the measured signal. We also note that we neglected analysis of inertial effects in the impacted materials, because the timescale of deformation was much longer than the time required for stress waves to propagate the thickness of the material [38]. It remains possible that some energy was dissipated through wave propagation, but we have not addressed the extent of this possible error.

While this chapter demonstrates that impact indentation may be used to measure linear viscoelastic mechanical properties of compliant materials including biological tissues, future work is necessary to optimize fully the instrument design, methodology, and modeling of the material behavior. Improved assessment of this approach as compared with other conventional techniques, and across a wider range of polymers, tissues, and testing conditions, will also facilitate robust measurements of accuracy. In the present work, we did not optimize design of the instrument, a pendulum-based indenter, including parameters such as the moment of inertia, damping properties, and gravitational "stiffness" (or m_{eff}, b, and k_g, respectively). Such instrument design optimization would likely improve the accuracy in measuring highly compliant materials (less than 1 kPa), chiefly by increasing the material response signal compared to the intrinsic damping and gravitation effects of the pendulum, as well as by improving the contact detection accuracy.

Additionally, the timescales of our impact indentation experiments were on the order of several seconds, and therefore, we did not consider long-term relaxation. However, straightforward changes to the experimental procedure could improve characterization of long-term viscoelastic behavior. This technique has the capability of extending timescales to thousands of seconds, increasing the frequency window if it is relevant to an application of interest. Therefore, impact indentation has the capacity to measure the same information as a conventional creep experiments at long timescales, but with significantly improved resolution to detect glassy behavior. Future studies should establish the most effective experimental procedure to precisely and accurately calculate viscoelastic moduli and relaxation behavior at all timescales.

Our analysis thus far has been limited to the SLS constitutive model of viscoelastic deformation, but other isotropic, linear viscoelastic constitutive models may be implemented straightforwardly. Other material behavior such as linear poroelastic deformation has been

investigated by indentation [39,40]; extending the present analysis to include such behavior should be feasible in principle, provided that a load-displacement response may be calculated iteratively to fit the experimental data. Under sufficiently large deformation exceeding that reported herein, the assumption of material linearity may not hold for polymers and soft tissues, and nonlinear constitutive behavior should be taken into account [35,41,42]. In general, however, the complex stress and strain fields imposed by indentation present challenges in accurate measurement of nonlinear elastic as well as structurally and mechanically anisotropic materials [43].

6.6 Conclusions

In this chapter, we provided a new analytical model for impact indentation, facilitating measurement of viscoelastic moduli and relaxation time constants of highly compliant polymers and biological soft tissues with shear relaxation moduli as low as hundreds of Pa. This approach confers advantages of millimeter scale resolution, minimal sample preparation, improved contact detection, and minimal artifacts due to probe-sample adhesion. While similar to creep compliance and stress relaxation experiments at long timescales, impact indentation provides the additional capacity to measure the glassy response, and therefore characterizes a more complete viscoelastic response over extended timescales compared to those methods. We also note that impact indentation is generalizable to different material constitutive models and different probe geometries, but that an assumed material model is currently necessary to measure the shear relaxation moduli of the material. These findings motivate future work to apply and extend this approach to a wider range of brain tissues and tissue simulant materials, including for comparisons within tissues and among tissue sources of key viscoelastic properties that may be correlative with tissue structure and injury or disease state.

6.7 References

[1] D.E. Discher, P. Janmey, and Y.L. Wang, Tissue cells feel and respond to the stiffness of their substrate, *Science*, 2005, 310, 1139-1143.

[2] R.G. Wells, The role of matrix stiffness in regulating cell behavior, *Hepatology*, 2008, 47, 1394-1400.

[3] N.D. Leipzig and M.S. Schoichet, The effect of substrate stiffness on adult neural stem cell behavior, *Biomaterials*, 2009, 30, 6867-6878.

[4] Y. Sun, C.S. Chen, and J. Fu, Forcing stem cells to behave: a biophysical perspective of the cellular microenvironment, *Annual Review of Biophysics*, 2012, 41, 519-542.

[5] A.S. Zeiger, B. Hinton, and K.J. Van Vliet, Why the dish makes a difference: quantitative comparison of polystyrene culture surfaces, *Acta Biomaterialia*, 2013, 9, 7354-7361.

[6] A. Jagielska, A.L. Norman, G. Whyte, K.J. Van Vliet, J. Guck, and R.J.M. Franklin, Mechanical environment modulates biological properties of oligodendrocytes progenitor cells, *Stem Cells and Development*, 2012, 21, 2905-2914.

[7] C.F. Lucchinetti, W. Bruck, J.E. Parisi, B. Scheithauer, M. Rodriguez, and H. Lassman, Heterogeneity of multiple sclerosis lesions: implication for the pathogenesis of demyelination, *Annals of Neurology*, 2001, 47, 707-717.

[8] A. Kutzelnigg, C.F. Lucchinetti, C. Stadelmann, W. Bruck, H. Rauschka, M. Bergmann, M. Schmidbauer, J.E. Parisi, and H. Lassman, Cortical demyelination and diffuse white matter injury in multiple sclerosis, *Brain*, 2005, 128, 2705-2712.

[9] P. Curatolo, R. Bombardieri, and S. Jozwiak, Tuberous sclerosis, *Lancet*, 2008, 372, 657-668.

[10] L. Meikle, D.M. Talos, H. Onda, K. Pollizzi, A. Rotenberg, M. Sahin, F.E. Jensen, and D.J. Kwiatkowski, A mouse model of tuberous sclerosis: neuronal loss of Tsc1 causes dysplastic and ectopic neurons, reduced myelination, seizure activity, and limited survival, *Journal of Neuroscience*, 2007, 27, 5546-5558.

[11] K. Pogoda, L. Chin, P.C. Georges, F.J. Byfield, R. Bucki, R. Kim, M. Weaver, R.G. Wells, C. Marcinkiewciz, and P.A. Janmey, Compression stiffening of brain and its effect on mechanosensing by glioma cells, *New Journal of Physics*, 2014, 16, 75002.

[12] K. Miller and K. Chinzei, Mechanical properties of brain tissue in tension, *Journal of Biomechanics*, 2002, 35, 483-490.

[13] X. Nie, B. Song, Y. Ge, W.W. Chen, and T. Weerasooriya, Dynamic tensile testing of soft materials, *Experimental Mechanics*, 2009, 49, 451-458.

[14] S. Chatelin, A. Constantinesco, and R. Willinger, Fifty years of brain tissue mechanical testing: from in vitro to in vivo investigations, *Biorheology*, 2010, 47, 255-276.

[15] B. Rashid, M. Destrade, and M.D. Gilchrist, Mechanical characterization of brain tissue in tension at dynamic strain rates, *Journal of the Mechanical Behavior of Biomedical Materials*, 2014, 33, 43-54.

[16] E.P. Canovic, B. Qing, A.S. Mijailovic, A. Jagielska, M.J. Whitfield, E. Kelly, D. Turner, M. Sahin, and K.J. Van Vliet, Characterizing multiscale mechanical properties of brain tissue using atomic force microscopy, impact indentation, and rheometry, *Journal of Visualized Experiments*, 2016, 115, e54201.

[17] M. Hrapko, J.A. van Dommelen, G.W. Peters, and J.S. Wismans, Characterization of the mechanical behaviour of brain tissue in compression and shear, *Biorheology*, 2008, 45, 663-676.

[18] M. Ayyildiz, S. Cinoglu, and C. Basdogan, Effect of normal compression on the shear modulus of soft tissue in rheological measurements, *Journal of the Mechanical Behavior of Biomedical Materials*, 2015, 49, 235-243.

[19] K. Tan, S. Cheng, L. Juge, and L. Bilston, Characterising soft tissues under large amplitude oscillatory shear and combined loading, *Journal of Biomechanics*, 2017, 46, 1060-1066.

[20] G. Mattei, A. Tirella, G. Gallone, and A. Ahluwalia, Viscoelastic characterisation of pig liver in unconfined compression, *Journal of Biomechanics*, 2014, 47, 2641-2646.

[21] A.S. Mijailovic, B. Qing, D. Fortunato, and K.J. Van Vliet, Characterizing viscoelastic mechanical properties of highly compliant polymers and biological tissues using impact indentation, *Acta Biomaterialia*, 2018, 71, 388-397.

[22] S.C. Hunter, The Hertz problem for a rigid spherical indenter and a viscoelastic half-space. *Journal of the Mechanics and Physics of Solids*, 1960, 8, 219-234.

[23] H.H. Calvit, Numerical solution of the problem of impact of a rigid sphere onto a linear viscoelastic half-space and comparison with experiment, *International Journal of Solids and Structures*, 1967, 8, 951-966.

[24] C.P. Chen and R.S. Lakes, Design of viscoelastic impact absorbers: optimal material properties, *International Journal of Solids and Structures*, 1990, 26, 1313-1328.

[25] L. Cheng, X. Xia, W. Yu, L.E. Scriven, and W.W. Gerberich, Flat-punch indentation of viscoelastic material, *Journal of Polymer Science Part B: Polymer Physics*, 2000, 38, 10-22.

[26] M. Chun, M. Hoon, F. Chiong, and C. Teck, Viscoelastic effects of silicone gels at the micro- and nanoscale, *Procedia IUTAM*, 2015, 12, 20-30.

[27] A. Samadi-dooki, G.Z. Voyiadjis, and R.W. Stout, A combined experimental, modeling, and computational approach to interpret the viscoelastic response of white matter brain tissue during indentation, *Journal of the Mechanical Behavior of Biomedical Materials*, 2018, 77, 24-33.

[28] P.A. Janmey, P.C. Georges, and S. Hvidt, Basic rheology for biologists, *Methods in Cell Biology*, 2007, 83, 3-27.

[29] A. Spiess and N. Neumeyer, An evaluation of R^2 as an inadequate measure for nonlinear models in pharmacological and biochemical research: a Monte Carlo approach, *BMC Pharmacology*, 2010, 10, 1-11.

[30] C.G.P.H. Schroen, M.A.C. Stuart, K.V.D.V. Maarschalk, A. Van Der Padt, and K. Van Riet, Influence of preadsorbed block copolymers on protein adsorption: surface properties, layer thickness, and surface coverage, *Langmuir*, 1995, 11, 3068-3074.

[31] J.D. Kaufman and C.M. Klapperich, Surface detection errors cause overestimation of the modulus in nanoindentation on soft materials, *Journal of the Mechanical Behavior of Biomedical Materials*, 2009, 2, 312-317.

[32] K. Franze, P.A. Janmey, and J. Guck, Mechanics in neuronal development and repair, *Annual Review of Biomedical Engineering*, 2013, 15, 227-251.

[33] A. Gefen and S.S. Margulies, Are in vivo and in situ brain tissues mechanical similar?, *Journal of Biomechanics*, 2004, 37, 1339-1352.

[34] J. Li, X.Y. Luo, and Z.B. Kuang, A nonlinear anisotropic model for porcine aortic heart valves, *Journal of Biomechanics*, 2001, 34, 1279-1289.

[35] M.T. Prange and S.S. Margulies, Regional, directional, and age-dependent properties of the brain undergoing large deformation, *Journal of Biomechanical Engineering*, 2002, 124, 244-252.

[36] D.M. Ebenstein, Nano-JKR force curve method overcomes challenges of surface detection and adhesion for nanoindentation of a compliant polymer in air and water, *Journal of Materials Research*, 2011, 26, 1026-1035.

[37] C. Hui, T. Liu, T. Salez, E. Raphael, and A. Jagota, Indentation of a rigid sphere into an elastic substate with surface tension and adhesion, *Proceedings of the Royal Society A: Mathematical, Physical and Engineering Sciences*, 2015, 471, 20140727.

[38] K.L. Johnson, *Contact Mechanics*, Cambridge University Press, Cambridge, UK, 1985.

[39] L. Han, E.H. Frank, J.J. Greene, H.Y. Lee, H.H.K. Hung, A.J. Grodzinsky, and C. Ortiz, Time-dependent nanomechanics of cartilage, *Biophysical Journal*, 2011, 100, 1846-1854.

[40] Z.I. Kalcioglu, R. Mahmoodian, Y. Hu, Z. Suo, and K.J. Van Vliet, From macro- to microscale poroelastic characterization of polymeric hydrogels via indentation, *Soft Matter*, 2012, 8, 3393-3398.

[41] R.A. Schapery, Nonlinear viscoelastic and viscoplastic constitutive equations based on thermodynamics, *Mechanics of Time-Dependent Material*, 1997, 1, 209-240.

[42] T.P. Prevost, A. Balakrishnan, S. Suresh, and S. Socrate, Biomechanics of brain tissue, *Acta Biomaterialia*, 2011, 7, 83-95.

[43] M.L. Oyen, Nanoindentation of biological and biomimetic materials, *Experimental Techniques*, 2013, 37, 73-87.

Chapter 7: Conclusions

7.1 Thesis summary

This thesis employed various characterization techniques to investigate the mechanical properties of brain tissue at multiple length- and time-scales of deformation. We characterized brain tissues from different animal models to study whether structural and compositional changes can translate to detectable differences in specific mechanical properties. We identified slight variations in impact energy dissipation response among several different mammalian species using impact indentation, suggesting that a highly tunable materials system is required to fully capture the mechanical behavior of specific brain models in response to concentrated impact loading. To achieve enhanced mechanical tunability, we engineered hierarchically structured gels as potential brain tissue simulants. With a simple bilayer composite design, we demonstrated that we could leverage the key properties of each individual layer to independently modulate properties that would otherwise be intrinsically coupled in monolithic systems. Through both experimental approaches and computational modeling, we gained new insights on the mechanisms that govern the extent of deformation and energy dissipation in compliant materials, and ultimately informed the design of a novel polydimethylsiloxane (PDMS)-based system that could be optimized to mechanically mimic porcine brain tissue (the closest representation of human brain that is readily accessible through mammalian animal models) under the loading conditions investigated herein. Finally, we significantly broadened the utility of our impact indentation technique by demonstrating a novel method to extract viscoelastic moduli and relaxation time constants from the measured impact response. Due to the advantages of impact-based approaches, we anticipate that impact indentation will be a valuable tool for characterizing a wide range of viscoelastic soft matter used in diverse biomedical or engineering applications, not limited to brain tissue and brain tissue simulants. Further, we note that the deformation investigated herein is distinct from but related to deformation due to needle or probe insertion into brain tissue during robotic surgical procedures; adaptations of these approaches could also be used to inform improved mechanical design of those systems.

7.2 Contributions

With reference to the concluding sections of Chapters 2 through 6, we list here the key results and scientific questions addressed throughout this thesis.

How do brain tissues from different species respond to concentrated impact loading?

We conducted impact indentation experiments on hydrated brain tissues from three healthy mammalian animal models: adult pig, adult rat, and infant mice [1]. The compliance of brain tissue samples and the maximum measurable depth of the instrumented indenter limited the range of impact velocities that could be tested. Despite impact velocities on the order of mm/s, the corresponding strain energy densities were on the order of 1 kJ/m^3, which approached ballistic strain energy densities, due to the small length scale of the impacting probe. Compared to previous impact indentation studies on other biological soft tissues, we observed that brain tissue was similar to liver tissue in terms of deformation resistance quantified by maximum penetration depth x_{max}, and was significantly more dissipative (at least 20% larger energy dissipation capacity K or 30% smaller dissipation quality factor Q) than either liver or heart tissue. In addition, we identified detectable differences in the magnitude of all three impact response parameters (x_{max}, K, and Q) when comparing brain tissues from different species. These variations in mechanical behavior among species were anticipated, due to species-dependent differences in structure and composition. Of the three species considered herein, porcine brain is most similar to human brain, as both are gyrencephalic and consist of roughly 60% white and 40% gray matter. In contrast, rodent brains are lissencephalic and contain only roughly 10% white matter. Several previous studies reported the stiffness of white matter to be greater and the stress relaxation times to be longer, as compared to gray matter from the same species. Our observations were consistent with those findings, in that porcine brain was more resistant to deformation (i.e., lower x_{max}) and dissipated energy more slowly (i.e., higher Q) than both types of rodent brains.

Do the mechanical properties of brain tissue detectably vary with disease state?

The species-to-species variation in impact response motivated a detailed study to determine whether the structural changes observed in a tuberous sclerosis (TSC) genetic mouse model of autism would translate to detectable differences in mechanical properties [2]. If so, the

mechanical properties of brain tissue could potentially be used as a diagnostic marker to quantify the onset of disease progression. Previous studies found TSC brain tissue to exhibit significantly reduced myelin content and abnormal axon morphology, characteristics that are also associated with brain lesions caused by traumatic injury. However, despite probing the mechanical properties of TSC and control brain tissue with AFM-enabled indentation, impact indentation, and oscillatory shear rheology [3], we found no corresponding changes in the quantified mechanical properties at every length- and time-scale explored. Thus, our hypothesis was not confirmed for this rodent disease model. Stiffness of neuronal axons transfected with *Tsc1* knockout was also unaffected in ways that could be correlated with this mutation, in part because of the experimental design: neurons were modified with plasmid vectors rather than obtained from brains of animals expressing this genetic mutation, and the empty vector control also resulted in mechanical changes in neuron stiffness. Furthermore, through immunohistochemical analysis, we found the expression levels of fibronectin, an extracellular matrix component, in TSC and control brain tissue to be similar, which was consistent with the lack of mechanical differences observed on the tissue and cellular level. This investigation of the mechanical characteristics of brain tissue raised further questions about whether any mechanical differences could be detected in other disease models, or in animal models of traumatic brain injury that also feature abnormal brain tissue structure including lesions.

How does a bilayered composite design improve tunability in tissue simulant candidates?

The key obstacle in developing more accurate brain tissue simulant gels is the inability to independently modulate the material's deformation resistance, which is primarily governed by the elastic properties, and its energy dissipation behavior, which is primarily governed by the viscous properties [4]. To address this challenge, we sought to investigate whether a simple bilayer composite comprised of polydimethylsiloxane (PDMS) layers could provide the necessary tunability to fully match the impact response of brain tissue measured via impact indentation [1]. As in all composites, the goal was to leverage the key properties of different materials to optimize overall performance. We found that varying only the top layer stiffness strongly affected all three impact response metrics (x_{max}, K, and Q), while varying only the top layer thickness slightly affected the energy dissipation metrics (K and Q). Since x_{max} was independent of top layer thickness whereas K and Q were not, we were able to successfully

decouple the deformation resistance from the energy dissipation characteristics of the bilayered composite gel. The extent to which we could decouple x_{max} from K and Q, however, was still bound by the properties of each individual layer. Adjusting the mechanical properties of the bottom layer provides another avenue to increase mechanical tunability, but was not thoroughly studied in this thesis. This simple hierarchical design greatly widens the design space for materials intended to recapitulate the mechanical deformation response of soft tissues. More importantly, both the material design strategy and the mechanical characterization approach can be translated to other applications that require precise, independent modulation of certain mechanical properties.

Can a bilayered composite gel be optimized to match the impact response of porcine brain?

With a better understanding of the additional tunability that the bilayered composite design offers, we established an optimization procedure to fully recapitulate the impact response of adult porcine brain tissue under the range of loading conditions studied herein [1]. The first objective of the optimization process was to identify a composition of CY 52-276 PDMS with mechanical stiffness that resulted in the same deformation resistance as the target tissue. The next objective was to tune the thickness of the CY 52-276 top layer until the bilayered composite exhibited the same energy dissipation metrics as the target tissue, while recognizing that the composite's deformation resistance was independent of top layer thickness. We iteratively identified that a top layer stiffness (i.e., shear elastic modulus G) of 1 kPa and thickness of 0.7 mm reflected the deformation resistance, energy dissipation capacity, and energy dissipation rate of porcine brain tissue over a range of impact velocities, thus achieving our primary design objective of a simple composite that could serve as a mechanical surrogate for brain tissue under concentrated impact loading. Additionally, we demonstrated that neither of the individual components of this bilayer exhibited all of these impact energy dissipation properties, such that the bilayer provided a unique composite response.

How does surface adhesion contribute to mechanical energy dissipation?

To better understand the mechanisms governing the impact response of our bilayered PDMS composite gels, we aimed to elucidate the role of surface adhesion on mechanical energy dissipation. Our experimental approach was to utilize a separate PDMS-based bilayered

composite gel that enabled independent control of the material's surface and bulk properties through modulating the thickness of the top layer [5]. We compared the amount of energy dissipated via surface adhesion and via viscoelastic properties of the bulk material beneath that surface under various loading conditions and strain rates. Impact indentation and quasistatic indentation experiments provided a means to quantify the energy dissipation response of gels at high and low rates of loading, respectively. We found that the relative contributions from surface adhesion and bulk viscoelastic properties to the extent of energy dissipation exhibited an important dependence on strain rate. At strain rates greater than 1/s, viscous dissipation in the bulk material vastly dominated and surface adhesion negligibly contributed to energy dissipation. However, at strain rates less than 0.01/s, increased surface adhesion significantly increased energy dissipation. To validate these experimental results, we developed a finite element model with adhesive contact implemented and examined the effects of independently varying the material's surface properties and probe displacement rate. In summary, our computational parametric analysis also demonstrated that surface adhesion played a diminishing role in energy dissipation as strain rate increased, as compared to bulk viscoelastic contributions, thus strongly supporting our experimental findings. Together, these results suggested that the extreme adhesion exhibited by our PDMS-based brain tissue simulant candidate did not affect the impact energy dissipation response that was measured by impact indentation. In other words, the energy dissipation that we quantified through direct contact was not artefactual due to that contact. Therefore, this dissipation response of the adhesive polymer would be expected to be maintained even if covered with another material such as a simulated skull or protective layer.

Can impact indentation quantify viscoelastic mechanical properties?

Earlier impact indentation studies could only empirically quantify impact response parameters such as x_{max}, K, and Q, which was sufficient for quantitative comparisons between brain tissue and synthetic tissue simulant candidates. However, extension of the impact indentation analysis to enable measurement of viscoelastic mechanical properties would greatly increase the utility of impact indentation as this technique confers unique advantages over conventional characterization techniques for highly compliant materials like brain tissue. These advantages of impact indentation include millimeter scale spatial resolution, minimal sample preparation, improved contact detection, capacity to measure high frequency "instantaneous" response, and

minimal artifacts due to probe-sample adhesion. Thus, we developed a novel analytical method for characterizing viscoelastic moduli and relaxation time constants directly from impact indentation experiments [6]. We successfully validated our new approach by using both impact indentation and oscillatory shear rheology to characterize PDMS elastomers of stiffness ranging from 100s of Pa to nearly 10 kPa. Assuming a linear viscoelastic constitutive model for the material, we found that the viscoelastic moduli and relaxation times obtained from fitting the impact response agreed well with those obtained from fitting the rheological response. Finally, we demonstrated our validated method on hydrated, biological soft tissues obtained from porcine brain, murine liver, and murine heart, and reported the equilibrium shear moduli, instantaneous shear moduli, and relaxation time constants for each tissue.

7.3 Future outlook

This thesis was focused primarily on the development of synthetic materials systems that remain structurally stable in ambient environments and possess the mechanical tunability to accurately mimic the mechanical response of brain tissue under concentrated impact loading. In pursuit of this goal, we designed a silicone-based bilayered composite gel and examined quantitatively how the structure and composition of this composite affected the impact energy dissipation response through impact indentation experiments. While we demonstrated that this bilayered gel could be optimized to fully match brain tissue under the range of impact velocities we investigated (on the order of mm/s to cm/s), we recognize that future studies are needed to appropriately scale up this system for use in tissue simulant applications that represent the human brain under robotic surgery or ballistic impact. For example, in ballistic testing scenarios, the impact velocities of projectiles will be orders of magnitude greater, even if the maximum strain energy density remains similar, and the physical dimensions of the tissue simulant material will also differ. Scaling up a bilayered composite gel to create a more complex shape such as a headform is not straightforward and would require experimental iteration. Thus, an alternative is to use multiscale finite element simulations to determine the optimal layer composition and thickness. Additionally, computational modeling provides an avenue to explore tissue and tissue simulant behavior at higher rates of deformation that are more representative of ballistic conditions. Due to the practical challenges of scaling up a bilayer design, a tissue simulant material that is

homogenous on the macroscale but exhibits hierarchical structure on the micro- to nanoscale will arguably be preferred. In this thesis, we explored one such material system but found that the current designs of protein-based hydrogels produced gels poorly reflected the mechanical behavior of brain tissue. Future work can study other types of polymer composite designs such as silicones loaded with particles. Nonetheless, the findings presented in this thesis identified a new tissue simulant candidate that better approximates the response of brain tissue compared to previous simulants, and will inform the future design of materials with tailored dissipative properties.

Although the last portion of this thesis extended the understanding and analysis of the impact indentation technique to enable direct measurement of viscoelastic moduli and relaxation time constants, several additional advancements to both the instrument design and methodology can be made. The pendulum-based indenter that we used was not initially designed nor optimized for characterization of highly compliant materials (kPa-scale stiffness or less). Pendulum properties, such as the effective mass, damping coefficient, and gravitational stiffness, are all instrument design parameters that can be drastically lowered to effectively amplify the material response signal, which would likely increase the accuracy of contact detection and subsequent measurement of mechanical properties. Another important future consideration is to incorporate imaging options to the impact indentation set up. One key advantage of impact indentation over traditional characterization methods like oscillatory shear rheology is spatial resolution. Impact indentation has the capability of conducting local measurements to probe the heterogeneity of materials like brain tissue. However, the issue with the existing set up is that the multiple objective microscope is incompatible with simultaneous use of the fluid cell, and the fluid cell is necessary for testing of biological tissues in hydrated conditions. A new optics system will need to be designed to facilitate in depth studies of heterogeneous materials. Discussions with Micro Materials Ltd., the manufacturer of the indentation instrument used throughout this thesis, may be required to implement any of the aforementioned changes. See Appendices D and G for other modifications of the instrument that we considered.

In regards to potential improvements to the new methodology that we presented in Chapter 6, the current approach only allows for measurement of the shear relaxation modulus by first assuming a linear viscoelastic material model, such as the standard linear solid (SLS) model. However, a method to explicitly measure the frequency dependent shear storage moduli G' and

shear loss moduli G" will be more useful since the assumed SLS model sometimes may not reflect the material behavior accurately, leading to poor fits to the experimental data. Theoretically, we believe that it is possible to mathematically transform our impact indentation data, which is collected in the time domain, to equivalent data in the frequency domain through either Fourier or Laplace transforms. Curve fitting methods can then be applied to recover G' and G" as a function of frequency. If this approach can be implemented successfully, it will further broaden the utility of our impact indentation technique. After improving the capabilities and accuracy of impact indentation, future studies can focus on reconciling the disparities in reported mechanical properties of brain tissue observed in the literature in addition to exploring other specific animal disease or injury models. We anticipate that impact indentation has the potential to guide the design of brain tissue simulants, and also further elucidate the relationship between brain tissue structure and mechanical properties in the contexts of development, healthy function, and disease progression.

7.7 References

[1] B. Qing and K.J. Van Vliet, Hierarchical design of synthetic gel composites optimized to mimic the impact energy dissipation response of brain tissue, *Molecular Systems Design & Engineering*, 2016, 1, 290-300.

[2] E.P. Canovic, B. Qing, A.S. Mijailovic, A. Jagielska, M.J. Whitfield, E. Kelly, D. Turner, M. Sahin, and K.J. Van Vliet, Characterizing multiscale mechanical properties of brain tissue using atomic force microscopy, impact indentation, and rheometry, *Journal of Visualized Experiments*, 2016, 115, e54201.

[3] B. Qing, E.P. Canovic, A.S. Mijailovic, A. Jagielska, M.J. Whitfield, A.L. Lowe, E. Kelly, D. Turner, M. Sahin, and K.J. Van Vliet, Probing mechanical properties of brain in a tuberous sclerosis model of autism, *Journal of Biomechanical Engineering*, 2018, in review.

[4] R. Mahmoodian, B. Qing, A. Adityan, and K.J. Van Vliet, Multiscale computational design of synthetic gels as simulants of soft-tissue impact response, *Journal of Biomechanics*, in preparation.

[5] B. Qing, L. Cai, K.T. Geiser, S. Lienemann, D.A. Weitz, and K.J. Van Vliet, Decoupling the contributions from surface adhesion and bulk viscoelastic properties to energy dissipation in compliant polymer gels, *Soft Matter*, in preparation.

[6] A.S. Mijailovic, B. Qing, D. Fortunato, and K.J. Van Vliet, Characterizing viscoelastic mechanical properties of highly compliant polymers and biological tissues using impact indentation, *Acta Biomaterialia*, 2018, 71, 388-397.

Appendix A

Brain tissue acquisition protocol

This appendix provides a step-by-step protocol describing the murine brain tissue acquisition procedure prior to mechanical characterization. All experimental studies were approved by the Animal Research Committee of Boston Children's Hospital and comply with the National Institutes of Health Guide for the Care and Use of Laboratory Animals.

1. Prepare a ketamine/xylazine mixture to anesthetize the mice. Combine 5 ml ketamine (500 mg/ml), 1 ml xylazine (20 mg/ml) and 7 ml of 0.9% saline solution.
2. Inject mouse with 7 μl per gram bodyweight of the ketamine/xylazine solution.
3. Once the mouse is fully anesthetized, as demonstrated by a lack of response to toe and tail pinches, euthanize the mouse by decapitation using large dissection scissors.
4. Remove the skull by cutting down the middle using smaller dissection scissors. Starting at the cerebellum, remove pieces of the skull using curved forceps.
5. After removing the skull, extract the brain by using a flat spatula to lift the brain, starting at the cerebellum, and place the brain on a Petri dish. Remove the cerebellum from the brain using a razor blade.
6. If using a whole brain for impact indentation tests on fresh tissue, transfer brain into a round-bottomed tube with CO_2-independent nutrient medium for adult neural tissue on ice. Otherwise proceed to step 6 for slicing procedures.
7. For AFM-enabled indentation experiments, thinly sliced tissue samples (i.e., 350 μm) are preferred. Adjust the vibratome settings to a speed of 0.7 mm/sec, vibration frequency of 70 Hz, and slice thickness of 350 μm.
8. Surround the vibratome dish with ice. Place a dab of superglue onto the vibratome plate and mount brain so that coronal slices can be cut, with the brain oriented to cut through the dorsal side first.

9. Fill the vibratome dish with enough Dulbecco's phosphate-buffered saline (DPBS) to just submerge the brain. Raise the dish on the vibratome so that blade is just submerged in the DPBS.

10. Press start to begin slicing coronal brain sections 350 μm thick.

11. Ensure that each tissue slice has flat and parallel surfaces.

12. Using paintbrushes to avoid damage to the tissue, transfer the brain slices from the vibratome DPBS bath into a round-bottomed tube with CO_2-independent nutrient medium for adult neural tissue on ice and perform measurements on fresh tissue within 48 hr.

Appendix B

Full details of impact indentation setup and experiments

Impact indentation experiments on compliant materials (i.e., kPa-scale stiffness or lower) in fully hydrated conditions require a set of specific adjustments to the default instrument configuration of the Micro Materials Ltd. indenter (NanoTest Vantage) located in the Department of Materials Science and Engineering NanoLab. This appendix provides the full details regarding both the setup and operating procedure. The complete impact indentation procedure can be generally outlined as follows: (1) set up fluid cell; (2) increase the capacitor plate spacing; (3) create new limit stop; (4) depth calibration; (5) set up impact configuration; (6) run impact indentation experiments; (7) standby conditions or shutdown. For any issues or questions, talk to Alan Schwartzman, who is familiar with this setup.

I. Set up and calibrate fluid cell

1) If necessary, first run a load calibration while the NanoTest system is in its normal configuration (this should be repeated every 3 to 4 months).
2) With the Liquid Cell option off, mount the fused quartz sample and tip of interest (unless it is a flat punch; then use a spherical tip).
3) Check that the minus-k table is balanced and a good pendulum test can be obtained.
4) Calibration menu → Liquid Cell → follow computer instructions (summarized below).
   - Make contact → back off in +x by 25 μm → move to a fresh area → Quit.
   - For the Indenter Load (mN) → use default value of 0.05.
   - For the Indenter Type → use "Normal" since there is no lever arm yet.
   - Click Continue → a zero load calibration is performed → the sample then moves towards the tip until the RO is ≈ 0 → obtain a value for Results for the Normal Indenter → click OK.
   - Tip will automatically retract to its original position (≈ 25 μm away from the surface).
5) You are now done with the normal indenter configuration steps.
6) Next, install the lever arm.

- Withdraw the stage in +x direction by at least 5 mm → remove fused quartz sample → move the stage back to the high resolution optics location after making sure that it will not hit any of the objective lenses as it travels back (using the Microscope and Transverse Stage Controller unit).
- Remove the tip.
- Insert the tip into the lever arm.
- Attach the lever arm onto the pendulum as follows:
  i. Loosen the set screw on the pendulum tip mount enough so that the lever arm can slip over the mount → be very careful that the set screw does not fall off.
  ii. Loosen the top set screw on the lever arm.
  iii. Slide the lever arm onto the pendulum tip mount → absolutely no resistance should be felt.
  iv. Tighten both set screws → goal is to have the lever arm parallel to the pendulum as much as possible → to minimize forward tilt, tighten the lever arm set screw first a little bit, then the other set screw, and reiterate.
- Lever arm is now installed.

7) Bring the stage back in front of the NanoTest pendulum after making sure nothing will collide when doing so.
8) Remove the damping plate and put it aside safely → you will not need it anymore.
9) Make sure minus-k table is balanced.
10) Obtain a good pendulum test → the counter-balance weight will need to be moved close to all the way in.
11) Mount the fused quartz sample → move it down in the -z direction to account for the new tip location → make contact → back off in +x by 25 μm → move to a fresh area.
12) Check that minus-k table is still balanced.
13) Calibration menu → Liquid Cell → follow computer instructions (summarized below).
    - Make contact → back off in +x by 25 μm → move to a fresh area (already done).
    - For the Indenter Load (mN) → use default value of 0.05.
    - For the Indenter Type → use "Liquid Cell" since the lever arm is installed.

- Click Continue → same automated process as before → obtain a value for Results for the Liquid Cell Indenter.
- The ratio of the Normal Indenter Result to the Liquid Cell Indenter Result is the Calibration Factor → record it in the logbook → click Save Calibration.

14) The fluid cell calibration is now complete → Calibration Factor should range between 0.6 and 0.8.

15) Confirm that the microscope option is off.

16) Experiment menu → Special Options → Liquid Cell → On → click Update Calibration → click Set Latest Calibration → click Continue → now the green bullet should be lit for "Liquid Cell" in the main window.

17) Liquid cell option is now installed, calibrated, and turned on.

II. Increase the capacitor plates spacing

1) The capacitor plates spacing needs to be increased significantly to enable higher measurable depths, which is necessary for compliant samples.

2) The final goal is to obtain a "Measurable Depth Cal (nm/Volt)" of at least 70,000 → this means a maximum measurable depth of at least 0.5 mm (i.e., the maximum measurable depth is approximately 7 times the measured depth calibration).

3) For large capacitor plates' spacings, the pendulum test will start to look like Fig. B-1, in which the RO curves upward just before contact with the limit stop.

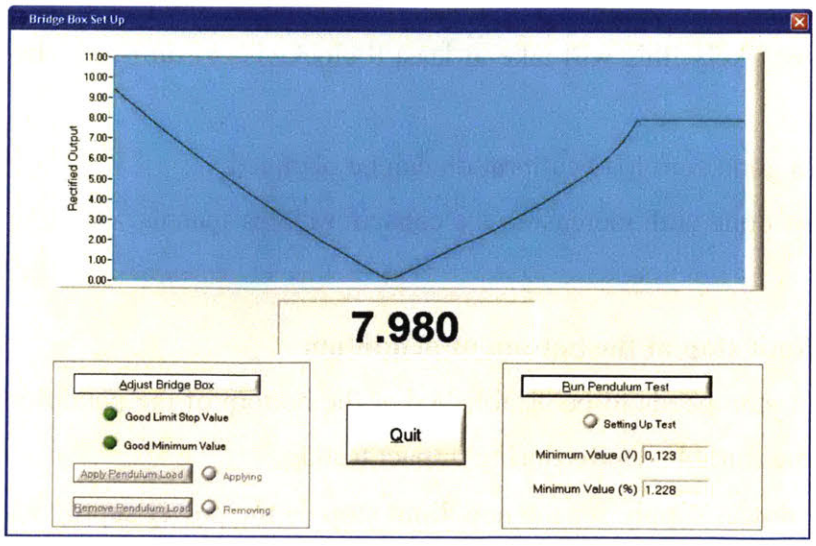

Figure B-1 Example of a good pendulum test after significantly increasing the spacing between the capacitor plates to enable characterization of highly compliant materials.

4) Make changes to some of the machine parameters.
   - Go to System menu → Non Protected Settings → Machine Parameters.
   - Change the Pendulum Test Load Rate (mN/s) from 0.1-0.2 (original value) to 0.5 (new value).
   - Change the Zero Load Rate (mN/s) from 0.01 (original value) to 0.1 (new value).
   - Change the Standby Ramp Offset (V) from 1 (original value) to 3 (new value).
5) Use the small wrench labeled "CAP. PLATE" for the steps below.
6) Make 3 clockwise ¼ turns at a time for the three nuts that control the capacitor plates spacing.
7) After each set of turns → the capacitor plates should still be parallel → also adjust the bridge box and move the counter-balance weight out in order to obtain a good pendulum test.
8) After 6 or 9 ¼ turns, determine the approximate depth calibration as follows:
   - The fused quartz sample should still be mounted.
   - Go to sample stage control window → make contact at a speed of 10 μm/s → keep going in the -x direction until the RO is 4.0 ± 0.1 V → the result is located in the "Approx. Depth Calibration (nm/V)" window.

9) In the end, you want to have an "Approx. Depth Calibration (nm/V)" value of at least 70,000. Most likely, this will take at least 9 clockwise ¼ turns, maybe as much as 15 ¼ turns.

10) Make sure a good zero load calibration can be obtained.

11) You are now done with increasing the capacitor plates spacing.

III. Set up new limit stop at the bottom of pendulum

1) A new limit stop needs to be established at the bottom of the pendulum to further allow for higher measurable depths during impact testing.

2) Plug in the power supply for the new limit stop → the power supply itself will always be on top of the small TV monitor adjacent to the instrument.

3) Connect the switch to the power supply → black goes to black and red to red.

4) Set up the new limit stop at the bottom of the pendulum → see Fig. B-2 below.

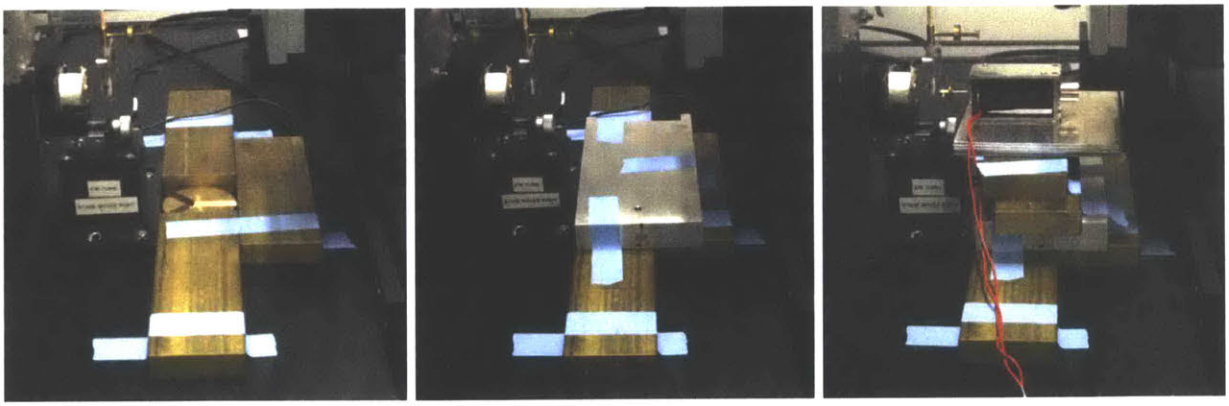

Step 1 Step 2 Step 3

Figure B-2 Setting up the new limit stop at the bottom of the pendulum. See Steps #5-7 below.

5) Place two brass bars on either side of the damping plate stand → place a third brass bar in front of the damping plate stand → tape down all three bars.

6) Use double-sided sticky tape and blue tape to secure the aluminum plate on the brass bars → orient its long side with the y direction → align the -x edge with the brass bars.

7) Position the new bottom limit stop on top of the aluminum plate.

- First, place the bottom limit stop inside the cabinet but not on the aluminum plate → run its two wires through the small hole on the right side of the cabinet → use blue tape to cover the hole to help thermally isolate the cabinet.
- Connect the bottom limit stop wires to the middle screws of the switch→ match the purple and brown colored wires for the bottom limit stop to the switch and the switch to the power supply.
- Make sure the current and voltage knobs on the power supply are at 0.
- Turn on the power supply → increase the voltage to 5 V.
- Turn on the switch → the horizontal piston on the bottom limit stop inside the cabinet should now be sticking outwards.
- Put the new limit stop on top of the aluminum plate but make sure that the horizontal piston does not yet touch the bottom of the pendulum.
- Go to the software → open the bridge box adjustment window → run a pendulum test while the upper limit stop is still the active one → make adjustments to get a good pendulum test if needed → record the final RO value.
- Now move the bottom limit stop towards the pendulum until the horizontal piston sticking out looks like it is just touching the bottom of the pendulum → check the software and make note if the RO voltage has changed → want a slight decrease to indicate that the bottom limit stop is touching the pendulum and pushing the pendulum slightly away from the top limit stop.
- Back off the top limit stop → do 5 full counterclockwise turns.
- Adjust the position of the bottom limit stop to get the original RO value → now carefully tape down the bottom limit stop to the aluminum plate to ensure that it does not move.
- The bottom limit stop is now the active one

8) Readjust the minus-k table.

9) Obtain a good pendulum test.

10) The switch for the bottom limit stop should always be on except during a brief temporary part of the impact indentation experiment, as instructed later on.

IV. Depth calibration

1) The series of steps to perform a depth calibration for this setup is the same as the normal configuration. However, due to the large capacitor plates spacing, it will take much longer, and thus, machine parameters need to be changed to shorten this time.
2) Go to System menu → Non Protected Settings → Machine Parameters → set Dcal Contact Velocity (μm/s) from 0.50 to 1.00 → set Primary Indentation Contact Velocity (μm/s) from 0.20 to 3.00 → set Ultra Low Load Contact Velocity (μm/s) from 0.10 to 1.00 → set Primary Impact Contact Velocity (μm/s) from 0.50 to 3.00.
3) Now do a depth calibration as usual with the fused quartz sample and spherical tip that is already mounted.

V. Set up impact configuration

1) Change the tip, if necessary, to the one of interest without removing the lever arm.
2) Turn on the solenoid's DC power supply → set to 9 V → the maximum accelerating load should be approximately 65 mN.
3) Note that the solenoid's DC power supply's maximum operating voltage is 12 V.
4) Calibrate the swing distance as follows:
   - Use either the fused quartz sample or the outer edge of the fluid cell surface.
   - Go to Experiment menu → select Impact → select Adjust Impulse Displacement → follow the computer instructions (will require positioning the bottom solenoid).

VI. Run impact indentation experiments

1) Due to the new limit stop at the bottom of the pendulum, the procedure for impact tests is slightly altered.
2) First, mount the sample post with the fluid cell bath and attached research sample as follows:
   - Make sure no dripping outside the fluid cell occurs throughout entire process.
   - Have the fluid cell just over the second o-ring → in this fashion, it will be rigidly joined to the sample post and will not wobble → you can adjust to ensure that you

have enough space in the x-direction between the sample and fluid cell edge for the probe to swing.

- Mount the sample post with everything now attached to the stage.
- Using the sample stage control window, position the sample such that the tip in the lever arm is located within the fluid cell (need to move in -z direction, then in -x direction, and finally in +z direction).
- Add fluid in a controlled manner if it is not there already.
- Make contact and back off by ≈ 30 μm.
- You are now ready to run impact indentation experiments.

3) Set up a schedule → select the testing conditions of interest.
4) Run the schedule
5) Keep track in lab notebook of the RO and distance in -x direction traveled as displayed by the software → this will help you troubleshoot any potential issues.
6) The first thing that happens is the sample surface will move in the -x direction in order to make contact with the tip → for highly compliant materials, this contact detection may not be accurate, and thus keeping track of the RO and distance traveled is important.
7) After contact is detected, the pendulum then swings back (pendulum load is removed), and the sample surface continues traveling in the -x direction until it reaches the measurement plane → if the sample surface is very adhesive, the pendulum tip may have trouble swinging back, in which case you need to manually provide a tiny nudge to the pendulum to help it swing back.
8) After the pendulum swings back, turn off the bottom limit stop by flipping the switch→ the piston will retract.
9) The pendulum will swing forward and impact the sample → you will see the displacement vs. time response curve on the computer → the xyz stage window then appears.
10) When the xyz stage window appears, turn on the bottom limit stop switch.
11) If you forget to turn the bottom limit stop back on in time, use a tip box to gently push the pendulum back → while the pendulum is pushed back → turn the limit stop switch on → then let the pendulum come back to the limit stop piston slowly.

12) Extract impact indentation data when experiments are complete for subsequent analysis via MATLAB (see Appendix H).

VII. Standby conditions or shutdown

1) If more experiments are to be done for another day, turn off the bottom limit stop switch after first carefully pushing the pendulum back with a tip box.
2) Lower the limit stop's power supply voltage to 0 → turn off power supply.
3) Move the bottom solenoid back to its standby position → lower the solenoid's power supply voltage to 0 → turn off power supply.
4) To recreate the setup next time you use it:
   - Reactivate the bottom limit stop → use a tip box to gently push the pendulum back → while the pendulum is pushed back → turn the limit stop switch on → then let the pendulum come back to the limit stop piston slowly.
   - With the tip outside the fluid cell bath, adjust the bridge box if necessary to obtain a good pendulum test.
   - Redo the depth calibration if it has been weeks since your last set of tests.
   - Mount your new sample onto the sample post and slide the fluid cell over it.
   - Redo the swing distance calibration → use either the outer surface of the fluid cell or a fused quartz sample.
   - Lower the tip into the fluid cell bath and make contact → back off by ≈ 30 μm.
   - You are now ready to run more impact indentation experiments.
5) To shutdown the impact indentation setup, follow these instructions:
   - Turn off the bottom limit stop switch → lower voltage to 0 → turn off its power supply.
   - Move the bottom solenoid back to its standby position → lower the solenoid's power supply voltage to 0 → turn off power supply.
   - Dismantle the support structure for the bottom limit stop switch → make sure to recover the small side port with blue tape to help the cabinet reach thermal steady state in the future.

- Dismantle the liquid cell setup → it is fine to remove the lever arm with the tip still attached and then remove the tip.
- Turn off the liquid cell software option.
- Return all machine system parameters back to the default values (see above).
- Return the upper limit stop to its normal position → wind the counter-balance weight all the way in → now the upper part of the pendulum falls towards the loading magnet → also the capacitor plates are not touching → wind the limit stop micrometer in (turn clockwise) until it pushes the pendulum vertical, as determined by the right angle square → wind the counter-balance all the way out or close to all the way out.
- Decrease the capacitor plates spacing → aim for an approximate depth calibration factor between (5000 and 6000 nm/V) → intermittently balance the bridge box and counter-balance weight → as you get close to the final configuration, the adjustments become smaller.
- Put the damping plate back on.
- Balance the minus-k table.
- Establish a good pendulum test → reiterate any of the above steps if necessary.

Appendix C

Strain energy density calculations

Impact indentation experiments with the current setup were limited to impact velocities on the order of mm/s to cm/s (well below that of ballistic conditions) for materials with similar compliance to brain tissue. However, the resulting strain energy densities were on the order of kJ/m^3, which did approach ballistic conditions, due to the small length scales of the experiments. Strain energy densities u can be calculated as impact energy E_{imp} normalized by the geometric contact volume V of the probe at the maximum penetration depth x_{max} as shown in Equation C-1. Thus, u will depend on parameters such as the radius R of the impacting probe, impact velocity v_{in}, pendulum effective mass m, and material's resistance to deformation.

$$u = \frac{E_{imp}}{V} = \frac{\frac{1}{2}mv_{in}^2}{V}, \tag{C-1}$$

In the case of a spherical probe, V is defined as follows:

$$V_{sphere} = \frac{2\pi R^3\left(1-\cos\left(arcsin\left(\frac{a}{R}\right)\right)\right)-\pi a^2(R-x_{max})}{3}, \tag{C-2}$$

where contact radius a at x_{max} is calculated as $2\pi R x_{max} - \pi x_{max}^2$. In contrast, for a cylindrical flat punch probe, a does not change as a function of indentation depth, and is only dependent on probe radius. Thus, V for a flat punch probe geometry is quantified using Equation C-3:

$$V_{flat\ punch} = \pi R^2 x_{max}, \tag{C-2}$$

An example of calculating the strain energy density from impact indentation data collected on porcine brain tissue is demonstrated here. The probe was a flat punch of 1 mm radius. At the highest applied impact velocity of 5.5 mm/s, the maximum depth of penetration was measured to be 0.7 mm. The effective mass of the pendulum was calibrated previously to be 0.171 kg. Using Equations C-1 and C-3:

$$u = \frac{E_{imp}}{V} = \frac{\frac{1}{2}mv_{in}^2}{\pi R^2 x_{max}} = \frac{\frac{1}{2}(0.171)(0.0055)^2}{\pi(0.001)^2(0.0007)} = 1176\,\frac{\mathrm{J}}{\mathrm{m}^3}$$

Appendix D

Impact indentation with temperature control

Viscoelastic materials such as polymers and biological tissues exhibit both rate-dependent and temperature-dependent mechanical behavior. Previously, the impact indentation with the fluid cell setup was confined to characterization only at room temperature. The instrument capabilities have since been extended to enable impact experiments on fully hydrated samples at slightly elevated and constant temperatures (i.e., 37°C or physiological temperature), and this appendix summarizes the changes that were implemented. A new aluminum sample post, along with a compatible fluid cell, was developed and built in the MIT Central Machine Shop. Temperature control was implemented through resistive heating of this new sample post coupled to a PID (proportional-integral-derivative) controller. A plastic spacer was also designed such that it could screw into the plate holder to prevent direct contact between the plate holder and sample post. A photo of these new components that enable temperature control is shown in Fig. D-1.

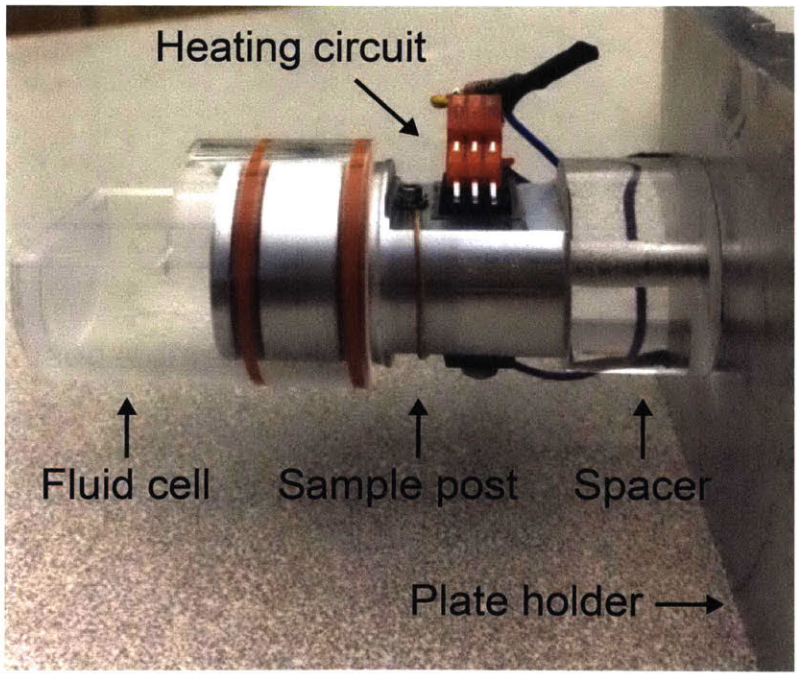

Figure D-1 New components designed to facilitate impact indentation experiments on fully hydrated biological tissues or polymer gels at elevated temperatures. The sample will be adhered to the free surface of the heated sample post.

To operate the temperature controller adjacent to the instrument, the following settings need to be used and can be adjusted through the menu options: Configure OUT1 ⇒ PROP: 020.0 ⇒ RSET: 0010 ⇒ RATE: 001.0 ⇒ OUT LO: 35% ⇒ OUT HI: 99% ⇒ dPNG: 0004. For more details regarding the circuit setup that drives the resistive heating or if any issues related to the temperature control occur, consult Mr. David Bono, the lab manager for the Undergraduate Teaching Lab in the Department of Materials Science and Engineering, who helped assemble this new setup. Because our design controls the temperature of the sample post, rather than the fluid immersing the sample, there may be a small temperature gradient between the sample post and the sample surface. Control studies were conducted on a polydimethylsiloxane (PDMS) gel immersed in phosphate buffered saline (PBS) to measure the temperature of the sample post, which was set to 37°C, and of the PBS using two thermocouples. The temperatures were recorded for over two hours, as shown by Fig. D-2. Initially, it takes approximately 10 to 15 minutes for the temperature to stabilize at the set value, but the temperature will remain steady for the remainder of the experiment. Additionally, the temperature gradient between the sample post and the sample surface was determined to be approximately 2°C.

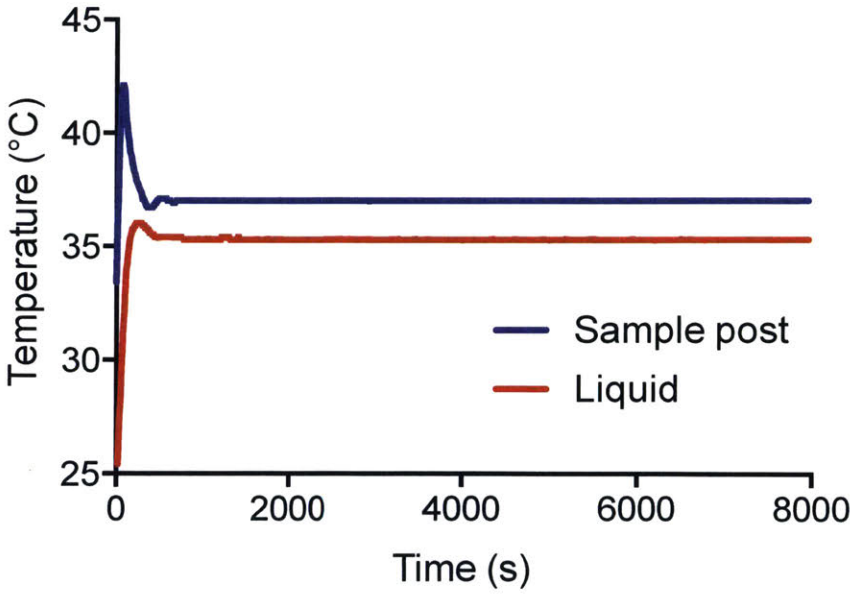

Figure D-2 Temperature of the sample post and liquid recorded over time. The setpoint temperature of the sample post was 37°C. After a brief stabilization period, the temperatures remain steady for over two hours, and a small temperature gradient between the sample post and liquid is observed.

Appendix E

Statistical analysis methods

This appendix provides details on the statistical analysis methods that were used to conclude whether the mechanical properties of certain brain tissues differed significantly from that of other brain tissues with distinct structural and compositional features.

Chapter 2 explored how mammalian brain tissue from various animal models responded to concentrated impact loading using impact indentation. The measured impact response, in terms of three metrics (maximum penetration depth x_{max}, energy dissipation capacity K, and dissipation quality factor Q), was compared among three different species (mouse, rat, and pig). To determine if there was detectable species-to-species variation, we conducted an ordinary one-way analysis of variance (ANOVA) to test the null hypothesis that the means of these three species were statistically equal. A one-way ANOVA is largely based on computing the F-statistic, which compares variance between groups to variance within a group for a single factor. Multiple sets of ANOVA were conducted for each impact response parameter at each applied impact velocity in the GraphPad Prism software, which was also used to generate the plots in this thesis. A statistically significant distinction was identified among the three species for x_{max}, K, and Q (p-values < 0.001) at each impact velocity. In addition to using p-values to determine statistical significance, we also examined the effect size as an alternative approach to make pairwise comparisons between different species. Effect size quantifies the magnitude or size of the difference between groups. While p-values provide a statistical significance, effect sizes provide a substantive significance. Here, we demonstrate an example of the types of conclusions that can be drawn from t-tests and calculating effect size.

The following K data sets were obtained at an impact velocity of ~ 4 mm/s:
Pig group: [0.879, 0.882, 0.889, 0.905, 0.883, 0.901, 0.901, 0.896, 0.890, 0.894, 0.888, 0.889]
Mouse group: [0.935, 0.918, 0.920, 0.960, 0.943, 0.956, 0.908, 0.942, 0.949, 0.970, 0.959, 0.943, 0.921, 0.914, 0.934, 0.907, 0.944, 0.905]

The mean, standard deviation, and standard error for the pig group are 0.891, 0.008, and 0.002, respectively. In comparison, the mean, standard deviation, and standard error for the mouse group are 0.935, 0.020, and 0.005, respectively.

For a two-tailed *t*-test of unequal variances:

1) Take the absolute difference in means between the two groups: 0.044
2) The standard error for *t*-test when variances are not necessarily equal:

$$\sqrt{\frac{StDev(pig)^2}{n(pig)} + \frac{StDev(mouse)^2}{n(mouse)}} = \sqrt{\frac{0.008^2}{12} + \frac{0.02^2}{18}} = 0.0036$$

3) The *t* statistic is 0.044/0.0036 = 13.368
4) The degrees of freedom is calculated as:

$$\left(\frac{StDev(pig)^2}{n(pig)} + \frac{StDev(mouse)^2}{n(mouse)}\right)^2 / \left(\frac{\left(\frac{StDev(pig)^2}{n(pig)}\right)^2}{(n(pig)-1)} + \frac{\left(\frac{StDev(mouse)^2}{n(mouse)}\right)^2}{(n(mouse)-1)}\right) = 34.113$$

5) Use the Excel function TDIST(13.368, 34.113, 2) to obtain p-value = 4.283e-15

Since this p-value << 0.05, the conclusion is that *K* of pig is statistically different than that of mouse.

Now looking at effect size, or the magnitude of difference between groups:

1) Ratio of means (mouse:pig) = 0.935/0.891 = 1.049
2) The standard error is calculated as:

$$\frac{Mean(mouse)}{Mean(pig)}\sqrt{\left(\frac{SEM(pig)}{Mean(pig)}\right)^2 + \left(\frac{SEM(mouse)}{Mean(mouse)}\right)^2} = 1.049\sqrt{\left(\frac{0.002}{0.891}\right)^2 + \left(\frac{0.005}{0.935}\right)^2} = 0.006$$

3) Use the Excel function TINV(1-0.95, n(pig) + n(mouse) – 2) to calculate *t* dist of 2.048
4) The 95% upper confidence interval is 1.049 + (0.006)(2.048) = 1.061
5) The 95% lower confidence interval is 1.049 - (0.006)(2.048) = 1.037

Thus, the conclusion from this analysis is that *K* of mouse is larger than that of pig by 4.9% with a 95% confidence interval of this difference ranging from 3.7% to 6.1%.

In Chapter 3 and Chapter 6, the moduli of different types of tissue were compared. Data were obtained from AFM-enabled indentation, impact indentation, and oscillatory shear rheology experiments, and were analyzed under different assumptions and idealizations to obtain either elastic or viscoelastic moduli. In both of those studies, a series of Mann-Whitney tests were conducted in MATLAB for each measured parameter to determine whether the mechanical properties of one group of tissue differed statistically from that of another group. Significance thresholds of either 0.01 or 0.05 were selected. This statistical analysis method was chosen primarily due to the low number of measurements in certain cases (e.g., number of tuberous sclerosis (TSC) mouse brains characterized was < 5). The Mann-Whitney rank-based test is a nonparametric test applied to independent samples and does not require the assumption of normal distributions. Additionally, the Mann-Whitney test is considered more conservative than Student's *t*-tests.

Appendix F

Computational design of gels as tissue simulant materials

The experimental work on hierarchical composite gels as potential candidates for brain tissue simulants presented in Chapter 4 was predicated on finite element simulations conducted previously by Dr. Roza Mahmoodian (Van Vliet group). Dr. Mahmoodian's simulations predicted that a simple bilayer design could enable simultaneous capturing of deformation resistance and energy dissipation metrics of biological soft tissues. The thesis author then piloted experiments to validate portions of the model predictions and demonstrated that a bilayered silicone-based gel could be tuned to match the full impact response of murine heart tissue via impact indentation. This appendix contains the full details of these computational studies and preliminary validation studies in the form of a manuscript in preparation.

Multiscale Computational Design of Synthetic Gels as Simulants of Soft-Tissue Impact Response

Roza Mahmoodian[1], Bo Qing[2], Aarthy Adityan[1], and Krystyn J. Van Vliet[1,2]*

[1]*Department of Materials Science and Engineering, Massachusetts Institute of Technology, Cambridge, MA 02139 USA*
[2]*Department of Biological Engineering, Massachusetts Institute of Technology, Cambridge, MA 02139 USA*

*Corresponding author:
Email: krystyn@mit.edu
Address: 77 Massachusetts Avenue, Room 8-237, Cambridge MA 02139 USA
Phone: 617- 253-3315
Fax: 617-253-8745

Keywords: finite element analysis, multiscale analysis, soft tissue simulants, impact indentation, rheology, energy dissipation

Abstract
The response of both synthetic polymers and biological soft-tissues to abrupt mechanical loading (impact) is complex. Materials that can replicate the impact response of soft tissues, and also remain structurally stable under non-physiological conditions, are required as test media to optimize both tissue protective strategies and robotic surgery methods. Organogel libraries comprising poly(dimethylsiloxane) or PDMS-based networks and solvents are potential candidates with demonstrated stiffness in the range of soft tissue stiffness from organs such as heart and liver. However, monolithic gels from these libraries have not yet accurately replicated both the impact energy dissipation capacity and penetration depths of these tissues. Here, we describe a multi-scale computational model of impact loading, and experimentally validate this model against impact responses obtained for PDMS-based gels of uniform composition. We then use that model to design simple bilayered gel systems that could replicate the penetration depth x_{max} and the impact energy dissipation capacity K of soft tissues from heart, liver, and brain. We demonstrate that a simple bilayer can decouple these impact response parameters, and also experimentally replicate the impact response of heart tissues with reasonable fidelity. These validated computational predictions suggest a wider design space for soft-tissue simulant materials, including composite design of existing gel libraries.

Introduction

The high incidence of impact injuries resulting from civilian first-responders and military conflict, transportation system collisions, sports, and falls has prompted increased demand for tissue simulant materials. Such materials, as mechanical mimics of tissue response, are not intended for regenerative medicine or tissue engineering. Instead, these materials are required as test media to aid in understanding damage extent under a range of traumatic impact scenarios, and in evaluation of new protective garments or equipment designs.

Tissues comprising abdominal organs are examples of soft condensed matter, due to the low elastic moduli and high water content of such so-called "soft tissues." Owing to the inherent complexities of tissue microstructure (e.g., striation of heart tissue indicated in Fig. 1a), soft tissues exhibit complex mechanical behavior including fluid/solid interactions, load-displacement hysteresis, loading rate-dependence, and residual stresses. Robust tissue simulants face the dual challenges of replicating this complex biomechanical response while also exhibiting environmental stability, cost effectiveness, processing ease, and tunability to reflect a wide range of soft tissue types. Polymer-based gels are attractive candidates that include a solvent and solid network (Fig. 1), and thus offer some modulation of the mechanical response. Indeed, significant progress has been made in the experimental iteration and development of such options (Stammen et al. 2001; Juliano et al. 2006; Lenhart et al. 2006; Moy et al. 2006; Seitz et al. 2009; Gong 2010; Kalcioglu et al. 2011; Mrozek et al. 2011; Mrozek et al. 2012; Kalcioglu et al. 2013). However, the discovery process by which such gels are synthesized – and tested recursively to compare and ultimately match the relevant mechanical response of interest against that of a target biological tissue – is inefficient. Complementary computational analyses can improve this efficiency by elucidating correlations among composition, microstructure, constituent mechanical properties, and geometry of these gels and tissues that can be difficult to realize experimentally.

Blunt injury is caused by energy transfer to the body by an impacting object that concentrates a large force to the head, chest, or abdomen (Viano et al. 2000). The maximum depth of impactor penetration and energy dissipation capacity are thus pertinent metrics for design of tissue simulant materials. Kalcioglu and Mrozek et al. have previously characterized the mechanical impact response of gels that were considered as possible tissue simulant candidates, and comprised chemically crosslinked poly(dimethylsiloxane) (PDMS) networks loaded with a non-reactive PDMS solvent (Kalcioglu, Mrozek et al. 2013). By experimentally analyzing a large library of candidate gels under a range of loading conditions and rates, they showed that impact energy dissipation capacity and penetration depth could be varied by altering the network structure of the solid network, as well as the molecular weight and relative volume of solvents within the gel. However, that study was one of several illustrating that many experimental iterations are required to effectively vary these design metrics to match the impact response of a specific tissue target (Kalcioglu, Qu et al. 2011; Kalcioglu, Mrozek et al. 2013; Juliano et al. 2006; Pervin et al. 2011). Further, it is a common finding that, for a given class of polymers, it is not possible to effectively decouple the depth of penetration from the extent of mechanical damping; this renders such polymers poor candidates for tissue types that exhibit both low stiffness and high energy dissipation capacity, as is common of soft tissues such as those from organs including heart, liver (Kalcioglu, Qu et al. 2011), and brain.

To that end, we constructed a multiscale finite element model and validated our ability to effectively simulate polymer gels at the constituent level, specifically under concentrated loading applied in impact indentation experiments. Next, inspired by the structural hierarchy of biological tissues (Fig. 1a), we sought to determine the capacity of a bilayered composite, with each layer exhibiting different dissipative and deformational properties, to decouple energy dissipation response metrics and to match the response of specific biological tissues. These layered materials would comprise computational representations of the PDMS-based gels (Fig. 1b), as an example of an existing gel library that is amenable to further tuning. This simple composite afforded at least the potential to better replicate the energy dissipation response of soft tissues, by varying either the mechanical characteristics of and/or thickness of each layer. Indeed, we found that it is possible to fully decouple the impact penetration resistance (quantified by penetration depth x_{max}) and energy dissipation capacity K in this manner, without adding significant structural/synthesis complexity as is crucial for practical implementation. This approach identified new gel multilayer designs, derived from a single library of gels, that successfully replicated the simulated K and $x_{\max}$ for tissues from heart, liver, and brain. Further, we experimentally validated this approach through facile synthesis and demonstration of a bilayer that replicated the impact response that we measured for murine heart tissue.

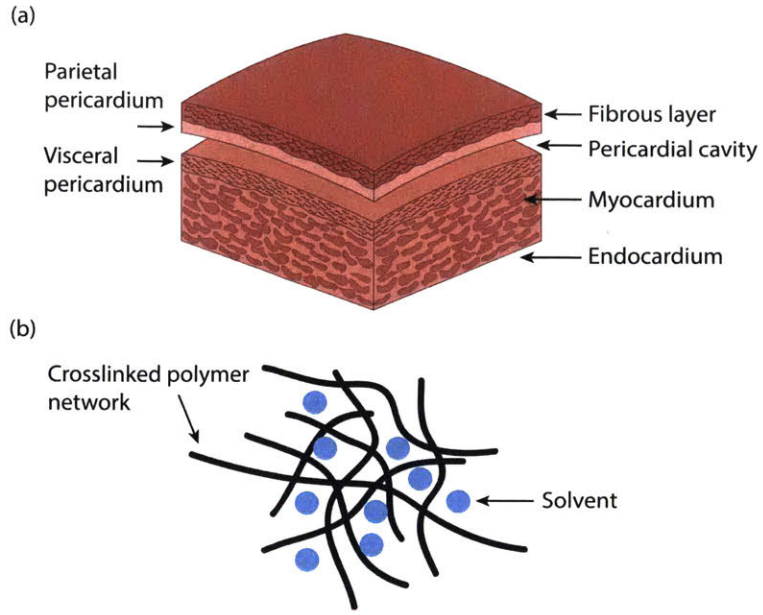

Figure 1. Schematic of (a) heart tissue, illustrating a layered multi-component structure, with layers of ~10s-100s μm in thickness [adapted from Ref. XXX]; and (b) a polymer gel consisting of a crosslinked polymer swollen by solvent. By varying the solid polymer network composition and solvent parameters, gel mechanical properties can be tuned over a range comparable to tissue stiffness, as described previously (Kalcioglu, Mrozek et al. 2013). Such gels are spatially uniform in composition at the μm-scale.

Materials and Methods

Materials and instrumented impact indentation: Experimental impact indentation data for tissues and gels used to validate the present computational model were reported previously (Kalcioglu, Mrozek et al. 2013). Briefly, the gels comprised a chemically crosslinked vinyl-terminated PDMS network (with a precursor chain length of 117 kg/mol) loaded with a non-reactive theta solvent (methyl-terminated PDMS) (Mrozek, Cole et al. 2011). The molar ratio of silane to vinyl functional groups (the degree of network crosslinking) varied from 4:1 to 2:1. Solvent loading varied from 10 vol% to 80 vol%, and solvent molecular weights (MW) were 1.1, 139, and 308 kg/mol (Mrozek, Cole et al. 2011; Kalcioglu, Mrozek et al. 2013). Heart and liver organs were harvested from adult rats. Tissue discs of 8 mm in diameter and 3-5 mm in thickness were excised for impact indentation experiments, and remained hydrated in Krebs-Hensleit buffer throughout experiments (Kalcioglu, Mrozek et al. 2013).

Impact indentation was conducted on all gels and tissues with a stainless steel flat punch of $R = 1$ mm at 25°C using a commercially available pendulum-based instrumented indenter (Micro Materials Ltd., UK), with methods and analyses described (Constantinidies et al. 2008; Constantinides et al. 2009; Kalcioglu, Qu et al. 2011). Tissue data used for comparison with the multilayered structures designed below corresponded to an impact velocity of 0.7 cm/s; gel data used for model validation were those obtained at impact velocities of 0.7, 1.1, 1.4 and 1.7 cm/s (Kalcioglu, Mrozek et al. 2013). Due to the relatively small probe contact area and volume, these

impact velocities correspond to strain energy densities of 6-18 kJ/m^3, which are comparable to that of other macroscale impact testing methods such as pneumatic gun and falling weight tests (Snedker et al. 2005).

Gel solvent extraction: To obtain rheological properties of the PDMS gels in the absence of solvent (i.e., of the solid network), solvent-swollen gel samples were immersed in 250 mL of toluene and the toluene was replaced every 4 days for 8 weeks. Extraction was monitored by measuring the recovered solvent isolated from the toluene via rotary evaporator (RE300, Yamato Scientific America, Inc., Santa Clara, CA). After extraction, the toluene was replaced with a 50/50 v/v toluene/isopropanol solution for 24 h, followed by a 25/75 v/v toluene/isopropanol solution for 24 h, and 100% isopropanol for 24 h to deswell the gel samples. The gels were then dried in air for 72 h. After complete drying the samples were massed to determine the extent of extraction (Mrozek, Cole et al. 2011).

Rheology: Frequency-dependent storage and loss moduli (G' and G'', respectively) of solvents were acquired at 5% shear strain over a frequency range of 0.1-100 Hz. Solvent-extracted gels and Sylgard PDMS were tested under oscillatory shear in parallel plate geometry at 1% shear strain over 0.01-10 Hz. These parameters corresponded to the linear viscoelastic regime of the solvent or the solvent-extracted networks at room temperature, using a MCR 501 rheometer (Anton Paar, Austria). Sample thickness was determined by plate gap height at which contact force was detected.

Characterization of organogel and solvent G(t): Solvents and solvent-extracted gels were each represented as linear viscoelastic materials in a finite element (FE) model. Most FE packages require input descriptions of linear viscoelasticity by specifying the shear relaxation modulus $G_R(t)$ through a Prony series:

$$G_R(t) = G_0\left[1 - \sum_{i=1}^{N} g_i\left(1 - e^{-t/\tau_i}\right)\right] \qquad \text{Eqn. 1}$$

where $G_0=G_R(0)$, τ_i and g_i are the instantaneous shear moduli, relaxation times and the corresponding series weights, respectively. Rheological data were therefore converted to a Prony series by extracting G_0, and g_i at pre-selected τ_i via curve fitting of the following implicit equations to the experimental loss and storage moduli, using a constrained nonlinear least squares optimization scheme in MATLAB (The MathWorks, Inc., Natick, MA)

$$G'(\omega) = G_0\left[1 - \sum_{i=1}^{N} g_i\right] + G_0\sum_{i=1}^{N}\frac{g_i\tau_i^2\omega^2}{1+\tau_i^2\omega^2} \qquad \text{Eqn. 2a}$$

$$G''(\omega) = G_0\sum_{i=1}^{N}\frac{g_i\tau_i\omega}{1+\tau_i^2\omega^2} \qquad \text{Eqn. 2b}$$

where ω is the testing frequency. The residual to be minimized is represented by:

$$E = \sum_{i=1}^{M} \left[\left(\frac{G'_{exp}(\omega_i)}{G'_{fit}(\omega_i)} - 1 \right)^2 + \left(\frac{G''_{exp}(\omega_i)}{G''_{fit}(\omega_i)} - 1 \right)^2 \right] \quad \text{Eqn. 3}$$

where M is the total number of data points, and G'_{exp}, G''_{exp}, G'_{fit} and G''_{fit} are the experimental and fitted values (from Eqns. 2a,b) of storage and loss moduli, respectively.

The physical constraints imposed in the fitting procedure were $g_i > 0$ and $\sum_{i=1}^{N} g_i < 1$, since $G_\infty = G_0(1 - \sum_{i=1}^{N} g_i)$ must be positive. The appropriate number of terms was chosen by obtaining the best fit at different values of N (series length), and selecting the total number of terms that yielded the lowest residual (Fig. 2). The above parameters were then estimated for that particular N for each material. Prony series for human brain tissue were obtained by digitizing and curve fitting to the dynamic frequency data reported by Nicolle et al. (Nicolle et al. 2005); remaining tissues and samples used experimental data reported by Kalcioglu et al. (Kalcioglu, Mrozek et al. 2013).

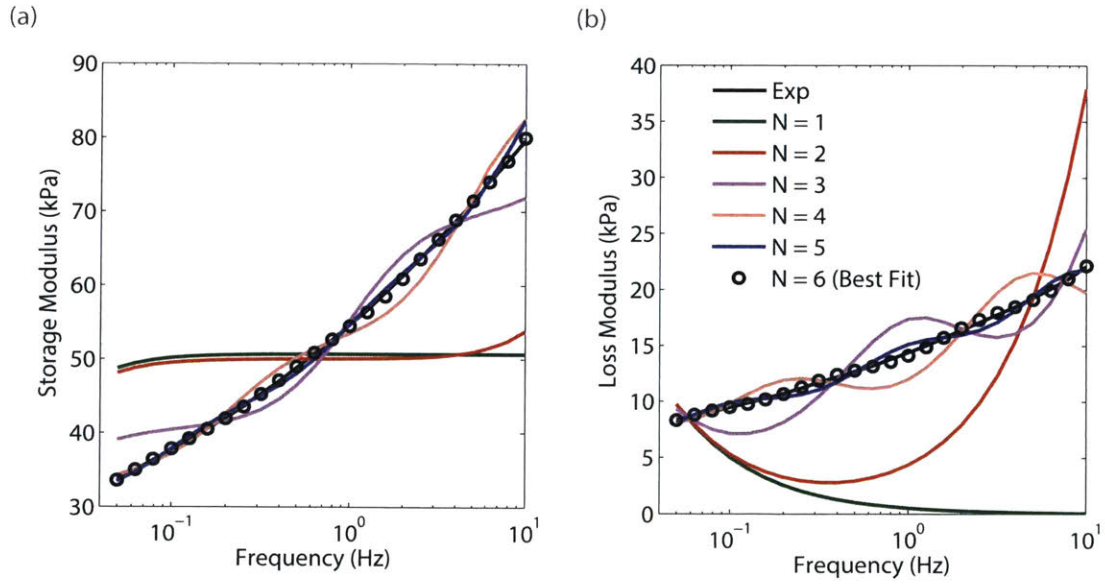

Figure 2. Simultaneous curve fitting to shear storage (a) and shear loss (b) moduli subject to a positivity constraint on shear modulus at infinite times, G_∞. The appropriate number of Prony series terms N was chosen by increasing it from a starting value of 1, and obtaining the best fit each time until no significant improvement was observed in the quality of fit, at which point the number of terms was chosen as the optimum series length. These data illustrate Prony series optimization for one specific PDMS-based gel considered.

Synthesis and Experimental Characterization of Layered Composites: Different variations of the bilayered composite gels were synthesized to compare calculated impact parameters with those of heart tissue. The bottom layer for all composites was comprised of the same viscoelastic PDMS organogel of 60 vol% 1.1 kg/mol solvent with 2.25:1 silane:vinyl stoichiometry. Sylgard® 184 from Dow Corning was used to represent the linear elastic top layer. The stiffness of Sylgard PDMS can be tuned by varying the weight ratio of pre-polymer base to curing agent. Additionally, its thickness can be controlled through the volume of the mixture that is prepared. The samples were cured at 80°C overnight.

Oxygen plasma treatment of the two layers enabled strong bonding at the PDMS bilayer interface. Surface oxidation has been shown previously to create covalent siloxane bonds from exposed silanol groups at the surface of PDMS layers (Eddings et al. 2008). After exposure to oxygen plasma (30 W, 30 sec), the two layers were pressed together immediately. Impact response of the bilayered composite gels was quantified using impact indentation as described above. Due to the adhesive nature of compliant PDMS, the gels were immersed in an aqueous solution containing 3% Pluronic® F108 during impact characterization (Kalcioglu, Mrozek et al. 2013).

Finite Element Simulations: An axisymmetric finite element model consisting of four-noded quadrilateral elements (CAX4) was constructed in Abaqus/Standard 6.10-1 (Dassault Systemes Simulia Corp., Providence, RI) to approximate experimental loading and geometry. The flat indenter (R = 1 mm) was modeled as rigid with frictionless contact with the material surface. The bottom of the sample was constrained against translation in the y and z directions, and impact loading proceeded along the y direction (Fig. 3a).

To incorporate the gel network and solvent phases separately, Abaqus was linked with DIGIMAT (e-Xstream Engineering, Luxembourg) to enable multiscale analysis. The solvent loading and properties of the dried, solvent-extracted gel and of the solvent were entered individually. In this scheme, Abaqus calls DIGIMAT at every time increment and for every integration point; DIGIMAT then conducts mean-field homogenization to compute volume averages of the stress and strain fields. The updated composite stiffness is then communicated to Abaqus (Fig. 4a).

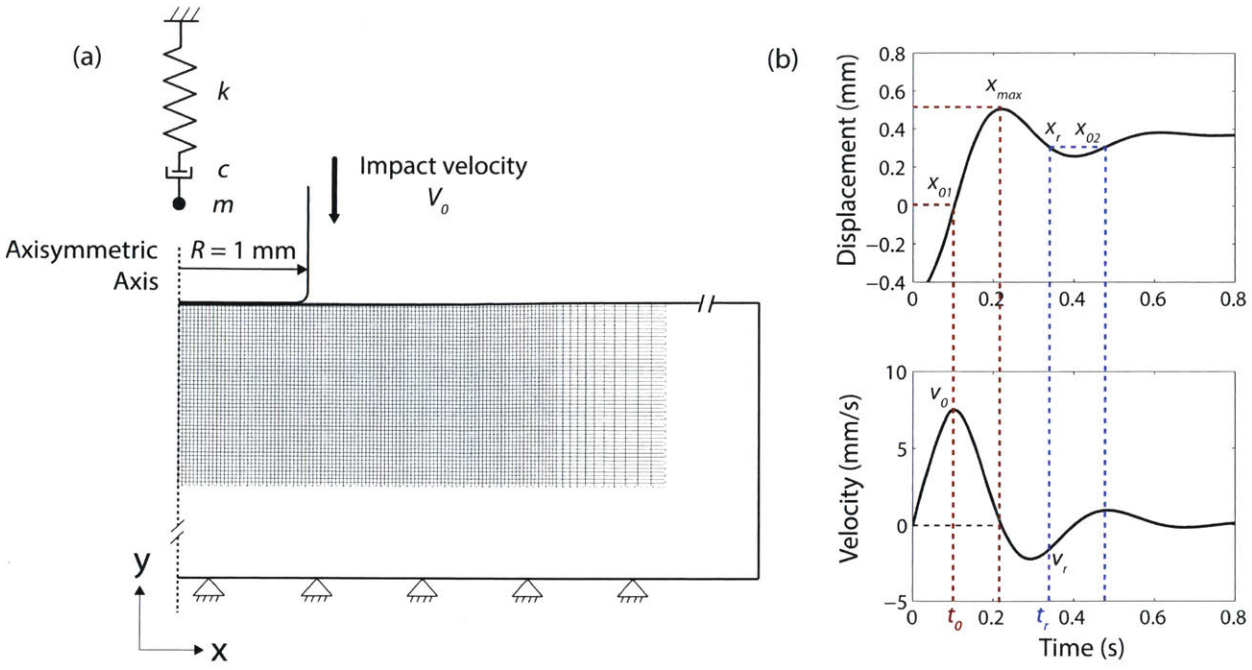

Figure 3. (a) Axisymmetric finite element model with a flat circular indenter of radius R=1 mm. The spring (k=10 N/m^2), dashpot (c=0.96 Ns/m) and mass (0.215 kg) elements are introduced to account for the pendulum-based indenter in the experiments, and are attached to the reference point of the rigid body, i.e., the indenter. (b) Velocity is calculated as the first time derivative of the indenter oscillatory displacement history. The maximum velocity V_0 before contact defines the contact point x_{01}. The position of the relaxed sample surface following the first impact is denoted by x_r and is taken to be equivalent to x_{02} (surface position at second impact). Rebound velocity V_r is then defined as the velocity at position x_r. The maximum penetration depth (in the first impact cycle) is x_{max} - x_{01}. Energy dissipation capacity K is calculated as the energy dissipated by the sample normalized by the sum of the dissipated and recovered sample energies over the t_0 - t_r period.

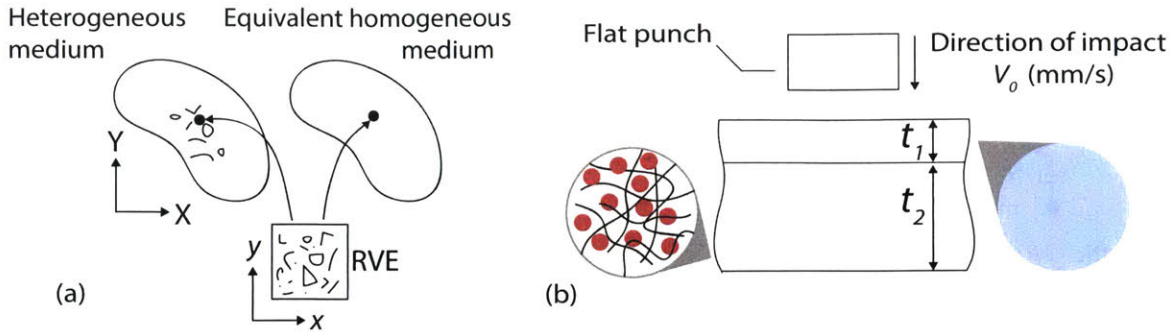

Figure 4. (a) Schematic of micro-macro (two-scale approach). At the microscopic scale, the medium is heterogeneous including the polymeric solid network and polymeric solvent; at the macroscale, this representative volume element (RVE) can be considered as an equivalent homogeneous medium. [Adapted from (Nemat-Nasser et al. 1993).] DIGIMAT applies mean-field homogenization to compute estimates of the volume averages of the stress and strain fields. (b) A viscoelastic gel represented by this equivalent homogeneous medium (here, of thickness t_2) is combined with a layer of a linear elastic material (here, of thickness t_1), to investigate the collective and independent effects on total energy dissipation. The thickness and relative position of each layer (top or bottom) were varied independently.

For a given set of input conditions (material constitutive responses, boundary and loading conditions), the indenter displacement x was output as a function of time. Impact resistance and energy dissipation capacity were computed from data obtained in the form of indenter displacement history as in Fig. 3b, from which the velocity profile was calculated (Kalcioglu, Mrozek et al. 2013). Maximum penetration depth x_{max} was calculated as the sample deformation at the time where the indenter came to a rest (zero velocity in Fig. 3b) in the first impact event; high impact resistance thus corresponds to low values of x_{max}. Energy dissipation capacity K was calculated as the energy dissipated by the sample E_d^s normalized by the sum of dissipated and recovered sample energies $(E_d^s + E_r^s)$ via the relevant velocities in the first impact event:

$$K = \frac{E_d^s}{E_d^s + E_r^s} = \frac{E_d^s}{E_t^{system} - E_r^p + E_d^p} \qquad \text{Eqn. 4}$$

The total energy of the system E_t^{system} was defined with respect to the impact velocity as

$$E_t^{system} = \frac{1}{2} m V_0^2 \qquad \text{Eqn. 5a}$$

The energy recovered by the pendulum E_r^p was calculated as

$$E_r^p = \frac{1}{2} k_p \left(x_{\max} - x_r \right)^2 \qquad \text{Eqn. 5b}$$

and the energy dissipated by the pendulum was calculated as

$$E_d^p = \int_{x_0}^{x_{max}} b_p \frac{\partial x}{\partial t} dx + \int_{x_{max}}^{x_r} b_p \frac{\partial x}{\partial t} dx \qquad \text{Eqn. 5c}$$

where k_p is the rotational stiffness of the pendulum and b_p is the pendulum damping coefficient. This calculation approach of energy dissipation parameters corresponded to that described previously for experimental analyses [e.g., see SI of (Kalcioglu, Mrozek et al. 2013)].

We evaluated our ability to effectively model polymer gels at the constituent level, for the purpose of studying their response under concentrated loading at relevant impact velocities. The indentation model was first calibrated to account for the effective mass, spring and damping coefficients of the pendulum-based indenter (Constantinides et al. 2008; Constantinides, Tweedie et al. 2009). Next, simulations were compared against results of impact indentation experiments conducted on select PDMS gels exhibiting a range of crosslinking extent, solvent loading, and solvent molecular weights. Energy dissipation capacity K and maximum penetration depth x_{max} from the coupled Abaqus/DIGIMAT analyses were compared with the same parameters determined from experiments.

Combination of a Non-Dissipative and Dissipative Material as Layers: To introduce a means to decouple the energy dissipation capacity and impact resistance metrics, we investigated the effect of combining a highly dissipative and non-dissipative material in a bilayered form (Fig. 4b). Two systems were studied: (1) a topmost, layer of varied thickness t_1 and varied Young's modulus E, above a bottom layer of varied thickness t_2, described by a fixed set of linear viscoelastic Prony series material parameters (corresponding to one of the present gels with 2:1 silane:vinyl stoichiometry loaded at 60 vol% with solvent MW of 1.1 kg/mol, hereafter referred to as gel A); and (2) similar to the previous system, but with the order of materials reversed along the direction of impact, such that the linear viscoelastic layer was topmost. We investigated the effect of variation of elastic layer stiffness, thickness ratios of layers, and the ordering of layers with respect to the direction of impact (Fig. 4b). Nodes at the layer interface were tied in all directions (no slip between layers). Frictionless contact was assumed between the indenter and the sample surface as before.

Results

Model Validation

Our multiscale computational model of impact response for linear viscoelastic gels was validated by comparing its predictions against impact indentation experiments. Modeling of PDMS gels by separately characterizing the solvent and solvent-extracted (dry) gel phases using a coupled Abaqus/DIGIMAT analysis provided close agreement between the measured and simulated displacement and velocity profiles, and of the calculated design metrics K and x_{max}. Figure 5 illustrates an example of these responses for a PDMS gel with a 4:1 silane:vinyl stoichiometry loaded at 50 vol% with the 1.1 kg/mol methyl-terminated PDMS solvent.

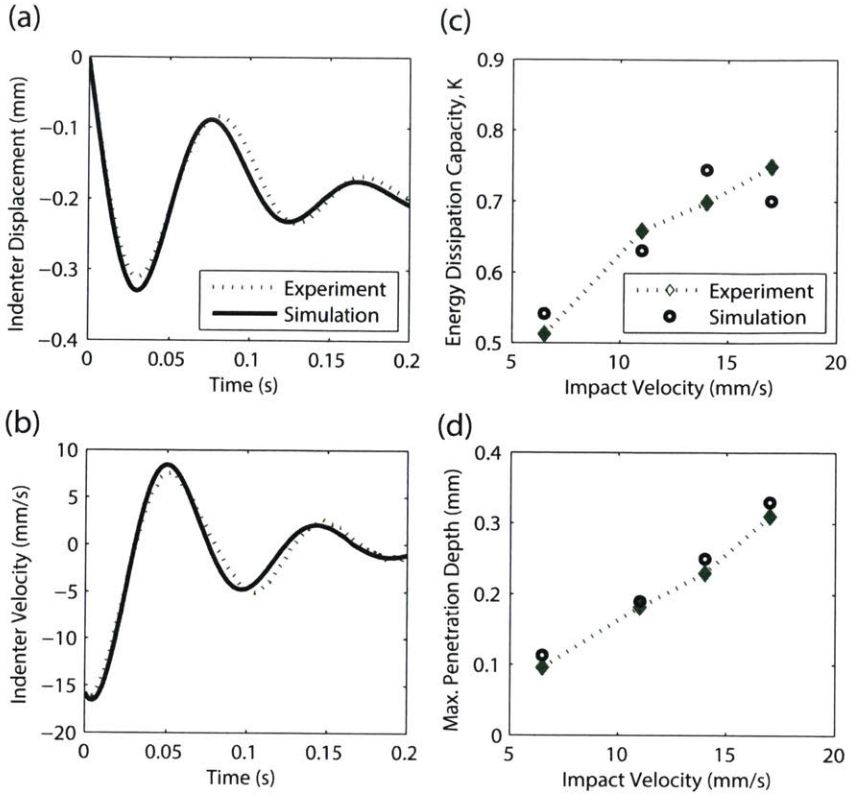

Figure 5. Displacement (a) and velocity (b) profiles of a PDMS-based gel comprising 50 vol% of 1.1 kg/mol PDMS solvent with a 4:1 silane:vinyl stoichiometry. Experiment (green) and simulation (black) shown at an impact velocity of 17 mm/s, illustrating capability of the finite element model to reproduce experimental results. The experimental energy dissipation capacity K (c) and maximum penetration depth x_{max} (d) were predicted successfully using the finite element model at different impact velocities. Error bars indicating standard deviation for experimental values at each impact velocity render hollow diamonds to appear solid.

Layered composite of non-dissipative and dissipative materials: As none of the individual PDMS-based gels considered well-matched both K and x_{max} of three specific tissues of interest (from heart, liver, and brain), we next used this validated model to identify potential layered composite designs that would achieve this goal. Noting that the energy dissipation capacity and impact resistance are highly coupled within any given gel (see Fig. X or SI), we created layered composites that included a linear elastic (non-dissipative) layer described by a Young's elastic modulus and Poisson's ratio, as well as a linear viscoleastic (dissipative) layer described by the Prony series of a given gel. These layers were of defined thickness t_i and relative position with respect to the impact loading site (see Methods and Fig. 4).

As a preliminary assessment of the dependence of K and x_{max} on layer thickness t_i for different linear elastic layer stiffness E, simulation results were obtained and graphed (Figs. 6-7) for Young's moduli spanning a range below and above those typical of these PDMS gels (~10s kPa); viscoelastic properties of PDMS gel A were assumed and described by the appropriate Prony series. A Poisson's ratio of 0.49 was considered for both the PDMS gel (instead of 0.5

(Mark 2009)) and the arbitrary linear elastic layer. Density of PDMS was defined as 970 kg/m^3 (Mark 2009). Next, we tested the ability of these systems to match simultaneously both K and x_{max} of a certain target tissue – specifically, murine heart and liver and human brain tissues as examples. A recursive method was pursued to determine a combination of elastic layer thickness and stiffness that provided magnitudes of K and x_{max} matching those of heart, liver, or brain. Those energy dissipation parameters are represented as horizontal, dashed lines in Figs. 6, 7, and are taken from (Kalcioglu, Mrozek et al. 2013) for heart and liver; and on our impact simulation predictions based on data provided in (Nicolle et al. 2005) for brain. First, t_i at which the K and x_{max} values obtained at a specific stiffness matched those of the target tissues were calculated by finding the point of intersection of each curve with the horizontal line corresponding with the target metric value, giving the layer thickness t_1 for each stiffness and each tissue (Figs. 6c, 7c). Interpolated t_1 vs. stiffness points were added for K and x_{max} (green and black curves in Figs. 6c, 7c), and the point at which these two curves met (not necessarily a simulation data point) for each tissue represented the unique combination of thickness and stiffness that was expected to provide a match to both K and x_{max} of that tissue. This combination was then used as a starting point to determine the next Young's modulus and investigate if further tuning of E and t_1 could achieve a better match of both K and x_{max} for that tissue.

Figure 6 displays energy dissipation capacities and maximum penetration depths of a composite that includes the linear elastic layer of thickness t_1 above a viscoelastic material of t_2 (Fig. 6b, inset). Each line color in these graphs represents a specific design, corresponding to distinct elastic moduli for the top layer; the linear viscoelastic layer properties remain constant and are described by the Prony series of PDMS gel A. The horizontal lines represent K (Fig. 6a) and x_{max} (Fig. 6b) for tissues from murine heart and liver (from experiments) and human brain (from simulations). As the linear elastic layer thickness increased, K decreased from nearly unity to zero; this is the limit when the sample is entirely linear elastic and thus dissipating no mechanical energy (Fig. 6a). Although K decreased slightly with increasing elastic layer stiffness, K was not strongly dependent on variations in E within the relevant range of stiffness relevant to the tissue responses. (Note that data corresponding to E greater than 30 kPa were omitted for clarity in Fig. 6c.) In contrast, x_{max} spanned a wider magnitude range and varied nonlinearly with elastic layer thickness (Fig. 6b). This behavior was more pronounced at higher elastic moduli and lower layer thicknesses ($t_1/t_2<0.4$). Figure 6b shows that these trends in x_{max} saturated as the top layer thickness increased, while the sharp decline in x_{max} was more pronounced at low elastic layer thickness. This finding provides a straightforward means to independently tune these two energy dissipation parameters, since it is chiefly x_{max} that drives the choice of the most fitting combinations of elastic layer thickness and stiffness to match the impact response of a particular target tissue.

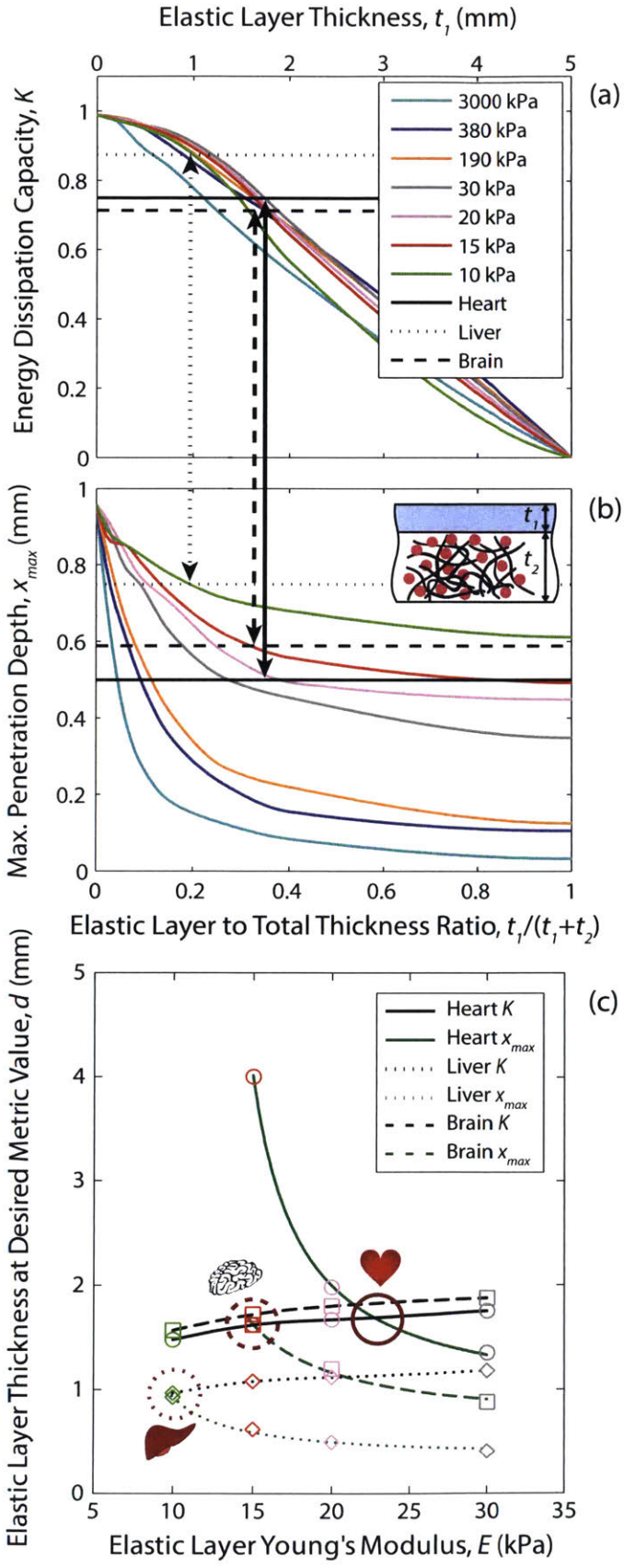

Figure 6. Energy dissipation capacity (a), maximum penetration depth (b), and elastic layer thickness required to meet tissue energy dissipation characteristics d as explained in the text (c) for a layered system consisting of gel A below a linear elastic layer with varying thickness t_1 and stiffness E. Points are simulation data, and lines are interpolated values. With changing the elastic modulus of top layer (0.01-3 MPa), K remains relatively unchanged while great variation is observed in penetration depths allowing for decoupling of these two metrics. Based on K and x_{max}, layered polymer candidates for matching heart, liver and brain tissues are obtained at t_1~1.8 mm/E~25 kPa (solid arrow and circle), t_1~1 mm/E=10 kPa (dotted arrow and circle), and t_1~1.6 mm/E=15 kPa (dashed arrow and circle) combinations, respectively. In (a) and (b), K and x_{max} of tissues are shown by horizontal lines to allow visualization of points at which these values are produced by layered structures.

In Figure 6c, the vertical axis represents d, the top layer thickness at which a certain target metric value is expected to be met, given a particular stiffness for this layer as indicated on the x-axis. In other words, d gives the elastic layer thickness to achieve points of intersection of K and x_{max} curves with the horizontal lines in Figures 6a and 6b. Black and green lines indicate d as a function of E for K and x_{max}, respectively; different line styles represent different target tissues. After an initial database of K and x_{max} for various thickness and stiffness combinations was constructed (Figures 6a-b), the thickness and stiffness at the point of intersection of black and green lines in Figure 6c was either chosen as the final layer design that was predicted to mimic the target tissue best, or was input for further simulations to refine predictions.

According to these results and based on averaged tissue K and x_{max} values, the layered structure comprising the PDMS-based gel A beneath an elastic layer thickness t_1~1.8 mm and elastic layer stiffness E~25 kPa (solid arrows in Figures 6 a-b; gray circles in Figure 6c) is expected to recapitulate the energy dissipation metrics of heart tissue. For the liver tissue, the design with an elastic top layer of t_1~1 mm and E=10 kPa (dotted arrows in Figures 6 a-b; green diamonds in Figure 6c) is the proposed simulant candidate. The candidate for metrics obtained for tissues simulants of human brain is that comprising an elastic top layer of thickness t_1~1.6 mm and stiffness E=15 kPa (dashed arrow in Figures 6 a-b; ~red squares in Figure 6c). Considering that the experimental values are not exact due to errors, more combinations can be viable matches.

Figure 7 shows similar output for the layered material system comprising a linear elastic material topped with a linear viscoelastic material described by the properties of PDMS-based gel A. This arrangement offered less flexibility and tunability of energy dissipation characteristics, as compared to the previous design of a PDMS gel of thickness t_1 above by a linear elastic layer of Young's modulus E_2. In Figure 7a, as the underlying elastic layer's stiffness increased, a particular energy dissipation capacity value was matched at lower gel-layer thickness. In other words, the points of intersection of colored curves with the target horizontal lines moved in the descending direction of the x-axis, while this trend was reversed for penetration depths. Increasing stiffness values drives K and x_{max} curves in opposite directions as a function of layer thickness. Further, reducing elastic layer stiffness below a certain limit (e.g., red curves in Figures 7a-b) results in the points of intersection with K and x_{max} "passing" each other. This means that for the range of the target values considered herein (K and x_{max} of heart, liver, and brain), there is an intermediate range of elastic layer Young's moduli that provides an agreement with both x_{max} and K for a specific elastic layer thickness. Tissue simulant candidates for heart and brain tissues using this viscoelastic gel-topped design were t_1/E_2 ~ 0.5 mm/20 kPa and 0.5 mm/12 kPa, respectively. For the combinations studied here with the viscoelastic gel on top, none provided a match to the x_{max} and K of liver tissue. However, if the dotted curves in Figure 7c were extrapolated, a potential intersection point could be at t_1/E_2 ~ 1.2 mm/5 kPa.

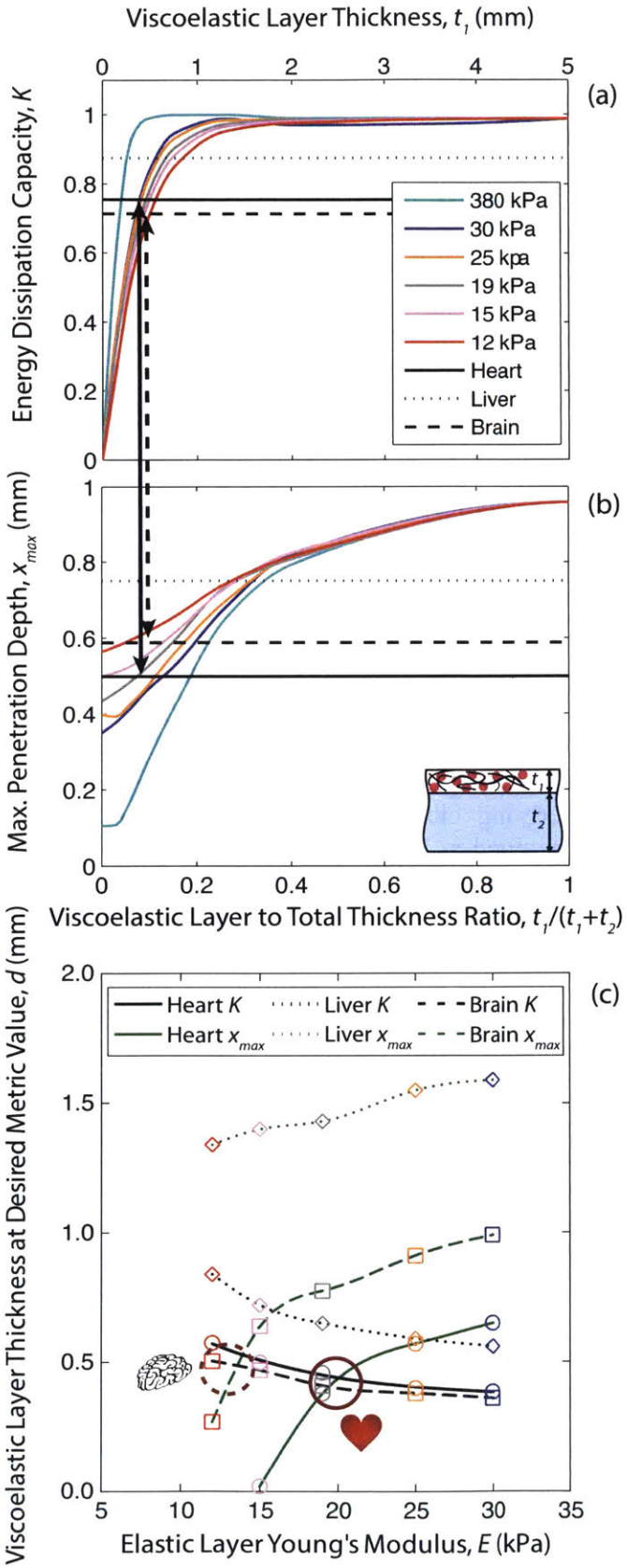

Figure 7. Energy dissipation capacity (a), maximum penetration depth (b), and gel A layer thickness to achieve targeted dissipation metrics d, as explained in text (c), for a layered system consisting of gel A with varying thickness t_1 positioned above a linear elastic layer with varying stiffness and thickness, E and t_2 respectively. With changing the elastic modulus of the bottom elastic layer (0.012-38 MPa), K remains relatively unchanged while some variation is observed in penetration depths allowing for decoupling of these two metrics. Based on K and x_{max}, candidates for matching heart and brain tissues are t_1~0.5 mm/E~20 kPa (solid arrow and circle) and t_1~0.5 mm/E~12 kPa (dashed arrow and circle) respectively. In parts a and b, K and x_{max} of tissues are shown by horizontal lines to allow visualization of points at which these values are produced by layered structures – not to be confused with dependence on layer thicknesses.

Figure 7 shows similar output for the layered material system comprising a linear elastic material topped with a linear viscoelastic material described by the properties of PDMS-based gel A. This arrangement offered less flexibility and tunability of energy dissipation characteristics, as compared to the previous design of a PDMS gel of thickness t_1 above by a linear elastic layer of Young's modulus E_2. In Figure 7a, as the underlying elastic layer's stiffness increased, a particular energy dissipation capacity value was matched at lower gel-layer thickness. In other words, the points of intersection of colored curves with the target horizontal lines moved in the descending direction of the x-axis, while this trend was reversed for penetration depths. Increasing stiffness values drives K and x_{max} curves in opposite directions as a function of layer thickness. Further, reducing elastic layer stiffness below a certain limit (e.g., red curves in Figures 7a-b) results in the points of intersection with K and x_{max} "passing" each other. This means that for the range of the target values considered herein (K and x_{max} of heart, liver, and brain), there is an intermediate range of elastic layer Young's moduli that provides an agreement with both x_{max} and K for a specific elastic layer thickness. Tissue simulant candidates for heart and brain tissues using this viscoelastic gel-topped design were $t_1/E_2 \sim 0.5$ mm/20 kPa and 0.5 mm/12 kPa, respectively. For the combinations studied here with the viscoelastic gel on top, none provided a match to the x_{max} and K of liver tissue. However, if the dotted curves in Figure 7c were extrapolated, a potential intersection point could be at $t_1/E_2 \sim 1.2$ mm/5 kPa.

In both multilayer designs (represented in Figure 6 for the elastic layer on top, and Figure 7 for the viscoelastic gel A on top), the energy dissipation capacity parameter remained very close to that of gel A as long as about 20% of the total thickness comprised gel A. However, the changes in maximum penetration depths depended noticeably on whether the linear elastic or viscoelastic layer was uppermost. Since the viscoelastic material mainly controls the energy dissipation, the addition of a non-dissipative layer is expected to chiefly modulate the maximum penetration depths. This effect was stronger when the linear elastic layer was positioned above the viscoelastic layer with respect to the loading direction, due to having a more direct impact as a result of its proximity to the indenter. Variation in the stiffness of this layer therefore caused larger changes in maximum penetration depths.

In the reversed scenario when the viscoelastic layer was atop the elastic layer, there was a thickness ratio threshold ($t_1/t_2 \sim 0.2$) beyond which the viscoelastic layer thickness had negligible effects on energy dissipation capacities (Figure 7a). Simultaneously with the viscoelastic layer effects on K vanishing, the effect of the elastic layer on x_{max} became less prominent due to the increasing distance from the indenter (Figure 7b). Thus, in contrast to the previous system, the impact of the linear elastic layer vanished rapidly with increasing the viscoelastic layer thickness towards this threshold, providing less tunability than the former.

Experimental Validation of Bilayer Design: To validate the computational predictions, we synthesized and characterized several bilayered PDMS composites. From Figure 6, the simulations estimated that a composite with $t_1 = 1.8$ mm and $E = 25$ kPa would provide a match to heart tissue for both K and x_{max}. Using a mixture of 50:1 Sylgard® 184 (polymer base to curing agent), we were able to generate top PDMS layers with a stiffness of 25 kPa but at different thicknesses. Impact indentation responses were quantified for these bilayered composites at an impact velocity of approximately 0.7 cm/s. As shown in Figure 8, the viscoelastic PDMS organogel by itself fails to mimic either K or x_{max} of heart tissue. However, the addition of the 25

kPa Sylgard PDMS layer modulates both the penetration resistance and energy dissipation characteristics of the overall composite. The composite with a thicker top layer (Bilayer 2) resulted in a lower K and x_{max} value, as predicted by the simulations, and was the only gel that matched heart tissue for both metrics. This result is a promising validation of the overall approach, demonstrating that computational modeling can be a powerful tool to guide the design of mechanical simulant gels for various biological soft tissues.

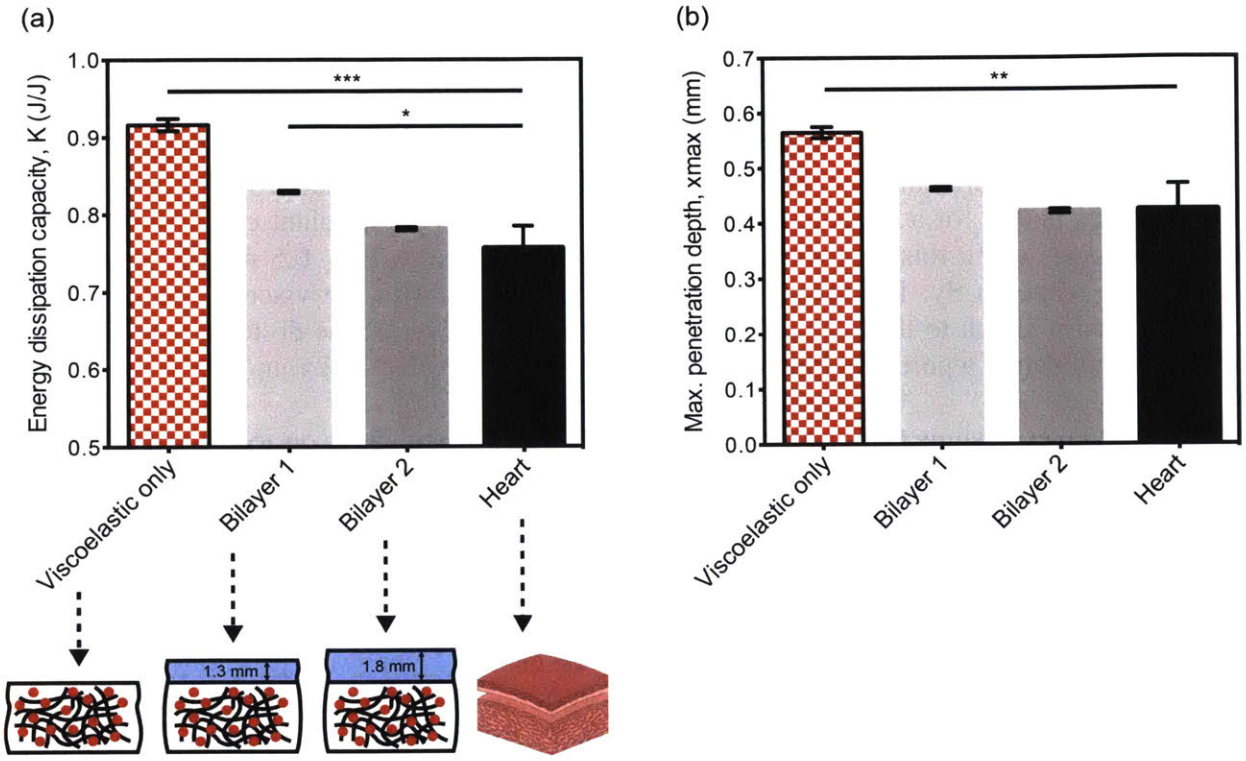

Figure 8. Validation of optimized impact response for PDMS bilayered composites intended to experimentally match heart tissue in terms of (a) energy dissipation capacity and (b) maximum penetration depth. Bilayer 1 was comprised of Sylgard PDMS with t_1 = 1.3 mm and E = 25 kPa atop a viscoelastic PDMS organogel of 60 vol% 1.1 kg/mol solvent with 2.25:1 silane:vinyl stoichiometry. Bilayer 2 was comprised of a 1.8 mm thick top layer with all other parameters the same as in Bilayer 1. The impact response of the viscoelastic PDMS organogel alone was also quantified. As the model predicted, bilayer 2 was the only gel well-matched to heart tissue for both K and x_{max}. The data correspond to an impact velocity of 0.7 cm/s (same as in simulations) and are represented as mean ± standard deviation.

Discussion

One key challenge encountered in previous experimental design of tissue simulant gels (e.g., Kalcioglu, Mrozek et al. 2013) was to independently tune distinct metrics of energy dissipation capacity and impact resistance in such gels to recapitulate the impact responses of biological tissues. Here, we explored alternative and yet tractable approaches for the design of these materials that could enable such decoupling. To that end, we constructed a multiscale

computational model that utilized a coupling between Abaqus/Standard and DIGIMAT and examined impact energy dissipation characteristics of mono-/bi-layered compliant materials. The model predictions of impact indentation test agreed favorably with the experimental data for the monolayered viscoelastic PDMS gels previously studied (Kalcioglu, Mrozek et al. 2013). The model was then used to produce higher fidelity designs for simultaneous capturing of energy dissipation and impact resistance metrics via a layered arrangement that took advantage of already available and easily synthesized materials with different dissipative characteristics as a means for decoupling the two design metrics. It must be noted that the interaction between the crosslinked network chains and the solvents was not taken into account, despite which a close agreement was obtained between simulations and experiments within the range of strain rates explored herein.

This approach enabled control over tissue simulant material design at two scales: at the component level (solvent and crosslinked polymer chains) for each individual gel, and at the layer level. In addition, the order in which the layers were arranged affected the composite, as expected. This dependence provided a simple additional tool to modulate the impact behavior of these structures. The advantage of the present design is that it can achieve a target performance with great flexibility and tunability, by combining the deformation and energy dissipation mechanisms characteristic of each involved component without the need for synthesizing new gels. The viscoelastic behavior of the two phases of each materials and/or each of the layers can be chosen to be dominant at multiple time scales to tailor the macroscopic viscoelastic behaviors. The present framework provides guidelines for engineering and tailoring the mechanical behavior and energy dissipation of materials for a wide range of applications including tissue simulants for large-scale simulations of soft tissue response under impact. In particular, it allowed for a straightforward implementation of presently available PDMS gels with existing linear elastic materials that can be easily made. The obtained results are encouraging and demonstrate promising prospects for viable soft-tissue simulant materials, and provide fine tunability beyond the levels attainable via experimental approaches alone.

Acknowledgements
We acknowledge Dr. Joseph L. Lenhart and Dr. Randy A. Mrozek at the U.S. Army Research Laboratory for providing the gel material, information on the procedure to extract the solvent from these materials, and rheology data of solvents used in synthesis of gels. We also thank Dr. Zeynep I. Kalcioglu for providing impact indentation data for gels and tissues. This research was supported by the U.S. Army through the Institute for Soldier Nanotechnologies (ISN), under Contract W911NF-07-D-0004.

References
Constantinides, G., C. A. Tweedie, et al. (2008). "Quantifying deformation and energy dissipation of polymeric surfaces under localized impact." Materials Science and Engineering A 489(1-2): 403-412.

Constantinides, G., C. A. Tweedie, et al. (2009). "Quantitative impact testing of energy dissipation at surfaces." Experimental Mechanics 49(4): 511-522.

Eddings, M. A., M. A. Johnson, et al. (2008). "Determining the optimal PDMS-PDMS bonding technique for microfluidic devices." Journal of Micromechanics and Microengineering 18(6): 067001.

Gong, J. P. (2010). "Why are double network hydrogels so tough?" Soft Matter 6(12): 2583-2590.

Juliano, T. F., A. M. Foster, et al. (2006). "Multiscale Mechanical Characterization of Biomimetic Physically Associating Gels." J. Mater. Res. 21(8): 2084-2092.

Kalcioglu, Z. I., R. A. Mrozek, et al. (2013). "Tunable mechanical behavior of synthetic organogels as biofidelic tissue simulants." Journal of Biomechanics http://dx.doi.org/10.1016/j.jbiomech.2013.03.011i.

Kalcioglu, Z. I., M. Qu, et al. (2011). "Dynamic impact indentation of hydrated biological tissues and tissue surrogate gels." Phil. Mag. 91: 1339–1355.

Lenhart, J. and P. Cole (2006). "Adhesion properties of lightly crosslinkedsolvent-swollen polymer gels." Journal of Adhesion 82: 945–971.

Mark, J. E. (2009). Polymer data handbook. New York, Oxford Univ. Press.

Moy, P., T. Weerasooriya, et al. (2006). Dynamic Response of an Alternative Tissue Simulant, Physically Associating Gels (PAG). Proc. 2006 SEM Annu. Conf. Exp. Mech., St. Louis, Missouri.

Mrozek, R. A., P. J. Cole, et al. (2011). "Influence of solvent size on the mechanical properties and rheology of polydimethylsiloxane-based polymeric gels." Polymer 52: 3422-3430

Mrozek, R. A., D. B. Knorr, et al. (2012). "Impact of precursor size on the chain structure and mechanical properties of solvent swollen epoxy gels." Soft Matter 8(43): 11185-11192.

Nemat-Nasser, S. and M. Hori (1993). Micromechanics: Overall Properties of Heterogeneous Materials. Amsterdam; New York, North-Holland.

Nicolle, S., M. Lounis, et al. (2005). "Shear linear behavior of brain tissue over a large frequency range." Biorheology 42: 209-223.

Pervin, F. and W. W. Chen (2011). "Mechanically similar gel simulants for brain tissues." Dynamic Behavior of Materials, Volume 1 pp. 9-13, Springer New York.

Seitz, M. E., D. Martina, et al. (2009). "Fracture and large strain behavior of self-assembled triblock copolymer gels." Soft Matter 5(2): 447-456.

Snedker, J., M. Barbezat, et al. (2005). "Strain energy density as a rupture criterion for the kidney: impact tests on porcine organs, finite element simulation, and a baseline comparison between human and porcine tissues." Journal of Biomechanics 38: 993-1001.

Stammen, J. A., S. Williams, et al. (2001). "Mechanical properties of a novel PVA hydrogel in shear and unconfined compression." Biomaterials 22(8): 799–806.

Viano, D. C. and A. I. King (2000). Biomechanics of chest and abdomen impact. The biomedical engineering handbook. J. D. Bronzino. Boca Raton, CRC Press. 2.

Appendix G

Calibration of pendulum parameters

To analyze impact indentation data using the methods presented in Chapter 2 and Chapter 6, we needed to use information related to the intrinsic properties of the pendulum. The effective mass m, damping coefficient b, and gravitational stiffness k_g of the pendulum are the key parameters that can be determined beforehand through calibrations. This appendix describes the procedure that we used to calculate m, b, and k_g.

There are several approaches to determine these pendulum parameters. The general principle of the approach that we employed is as follows:

1) Let the pendulum freely swing in the absence of any loads to obtain the free oscillation period and the natural damping factor → note that these two parameters are related directly to m, b, and k_g. More details on how to achieve a free damped oscillation are provided at the end of this appendix.
2) Determine m:
    - Conduct an impact against a leaf spring inserted between the pendulum and opposing sample holder, as shown in Fig. G-1.

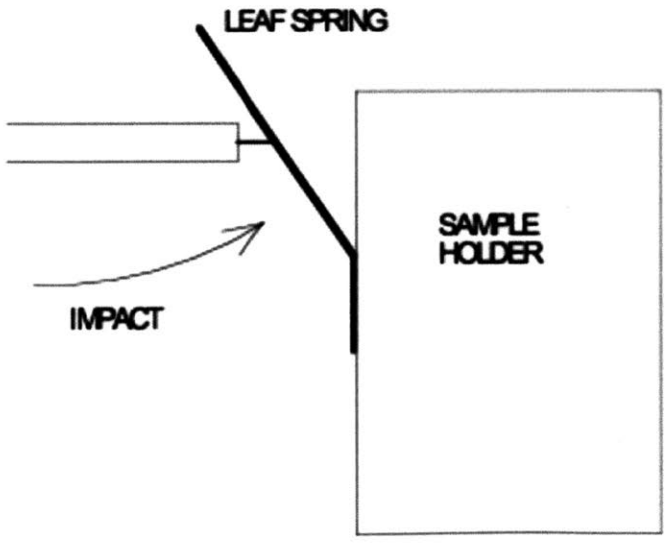

Figure G-1 Impact against a leaf spring with known stiffness to determine pendulum parameters.

- Measure the leaf spring stiffness through simple force-displacement tests and fitting the slope of the line.
- The effective mass of the pendulum m can be calculated using the pendulum resonant frequency during the impact and the leaf spring stiffness.

3) Now that m is known, b and k_g can be calculated using the free oscillation period and the natural damping factor (obtained from the logarithmic decrement) that was previously determined in Step 1.
4) For reference, our most recent round of calibrations found m, b, and k_g to be 0.26 kg, 0.57 Ns/m, and 9.62 N/m, respectively.

For standard impact tests with the pendulum-based instrumented indenter (Micro Materials Ltd., NanoTest Vantage), the accelerating or impact load is continuously applied throughout the entire experiment such that the pendulum cannot swing freely in this configuration. To enable a free damped oscillation of the pendulum, changes to the instrument software were implemented with the help of Dr. Stephen Goodes from Micro Materials Ltd. Essentially, an extra step was added to the standard impact procedure, which is outlined as follows (new step bolded):

1) Place the sample in position.
2) Energize the lower solenoid to hold the pendulum and probe away from the sample.
3) Set the acceleration (impulse) load by applying correct current through the pendulum coil.
4) De-energize the lower solenoid to release the pendulum and start collecting the depth vs. time data.
5) **Reduce the accelerating load (and pendulum zero load) to zero by reducing the current through the pendulum coil to zero before the probe impacts the sample surface.**

Now, when defining a new schedule in the software, it will prompt you to either keep or remove the accelerating load. However, one important consideration is that without this accelerating load (and pendulum zero load), the default equilibrium position of the pendulum does not correspond to the perfectly vertical position or the position of the sample surface. Instead, the pendulum at equilibrium will be swung all the way back towards the lower solenoid and away from the sample surface. Therefore, to achieve contact with the sample or a simple free oscillation, the

equilibrium position will need to be adjusted by moving the counter-balance weight inwards iteratively. During the process of moving the counter-balance weight, one can visually check the new equilibrium position by going to the bridge box adjustment window and selecting remove pendulum load. Continue moving the counter-balance weight until the desired equilibrium position is reached. These new modifications to the standard impact experiments are illustrated in Fig. G-2, along with preliminary tests at four different impulse loads (5 mN, 10 mN, 15 mN, and 45 mN). The equilibrium position of the pendulum once all external loads were removed for these experiments was set to be right at the surface of the sample, as indicated by the final depths of approximately 0 in Fig. G-2(B). We observed that the input impulse load did not affect the resulting displacement response, which demonstrated that impacts under this configuration were driven solely by gravity.

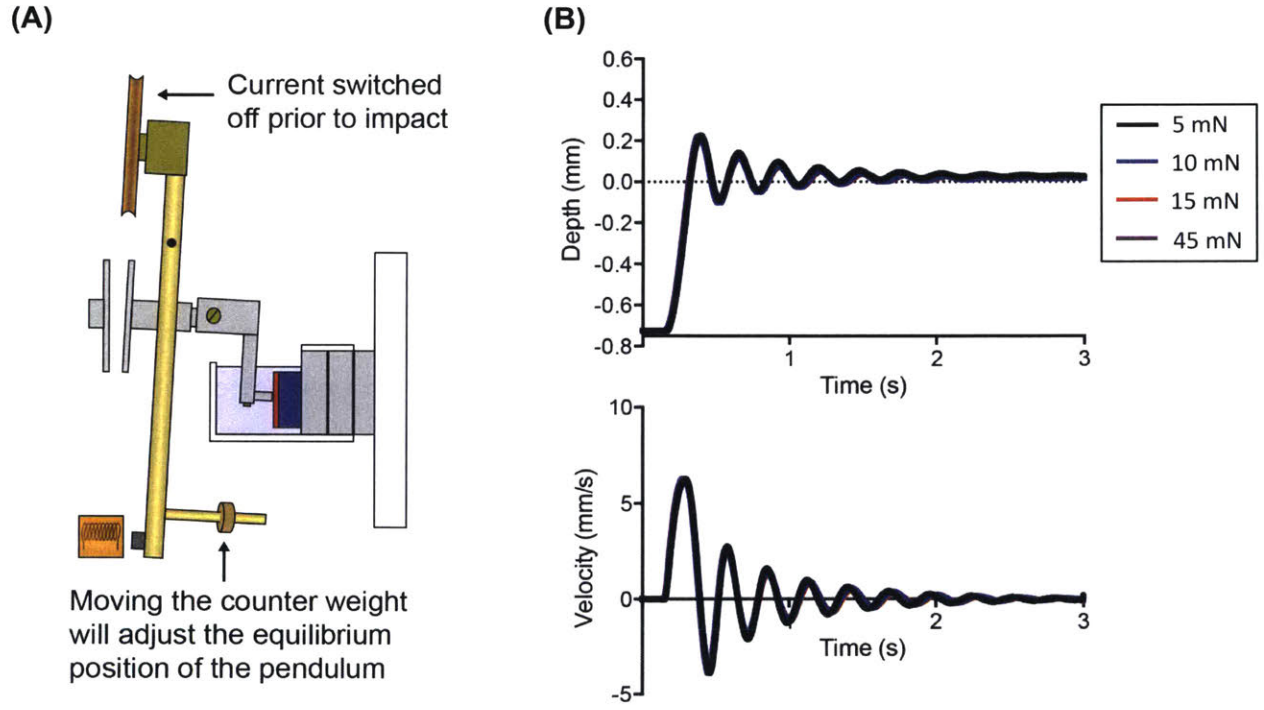

Figure G-2 (A) Schematic illustrating the modifications that were implemented to the impact indentation setup. Switching off the coil current removes the accelerating load prior to contact with the sample. Position of the counter-balance weight consequently needs to be adjusted. (B) Preliminary impact experiments were conducted at four distinct impulse loads. However, the input impulse load did not affect the measured displacement response due to removal of the accelerating load.

Appendix H

MATLAB codes for indentation analysis

This appendix contains the MATLAB codes that were used to analyze the displacement vs. time data (from impact indentation) and the load-depth hysteresis data (from quasistatic indentation). Brief annotations are provided throughout the codes.

I. Impact indentation analysis

ImpactAnalysisBQ.m (calculates x_{max} and K from measured displacement profile)

```
clear;
close all;
mass=0.171;          % effective mass of pendulum in kg
kp = 3;              % stiffness of pendulum in N/m
c = 0.6;             % damping coefficient of pendulum in Ns/m
Radius=1*10^-3;      % radius of flat punch probe in m

[savefile, savepath] = uiputfile('output.dat', 'Save file name');
loadpath = uigetdir('', 'Choose folder containing data');
cd(savepath);
fid = fopen(savefile,'w');
fprintf(fid, 'filename\t xo \t xmax \t xr \t vin \t vout \t K \t ErP \t EdP
\t e\n');

A = ls('*.txt');
A = char(strread(A,'%s'));
filecount = 1;

while(filecount <= size((A),1))
    %% load raw data
    input_sheet = A(filecount,:);

    curve = load(A(filecount,:));

    time = smooth(curve(:,1),25);   % time in s
    % zero the depth and change units to m
    depth = (smooth(curve(:,2),25) - curve(1,2))/10^9;
    % make velocity vector same size as time vector
    vel = smooth([0; diff(depth)./diff(time)],25);
    % smooth acceleration vector
    accel = smooth([diff(vel)./diff(time); 0],25);

    % cut second half of all curves
    time2 = time(1:length(time)/2);
    depth2 = depth(1:length(depth)/2);
    vel2 = vel(1:length(vel)/2);
    accel2 = accel(1:length(accel)/2);
```

```
%% calculate max velocity, which is not necessarily impact velocity
[v_max,v_max_ind] = max(vel2);


%% manually find contact point and impact velocity
figure
plot(time2,accel2,'r-')
% find where acceleration drops suddenly at ~0 by hand
[t_in,a_in] = ginput();   % window with cursor will pop up

[a_max,a_max_ind] = max(accel2);      % find index of max acceleration
n = 1;                                % set counter
% make new acceleration curve after the max point
for i = a_max_ind:length(accel2)
    accel3(n) = accel2(i);
    n = n + 1;
end

% get index of manually selected acceleration
for a_in_ind = 1:length(accel3)
    if accel3(a_in_ind) < a_in
        break
    end
end
in_ind = a_in_ind + a_max_ind - 1;    % index of impact

v_in = vel2(in_ind);                  % define impact velocity
x_0 = depth2(in_ind);                 % define contact point


%% calculate max penetration depth
n = 1;
% make new velocity curve after impact velocity
for i = in_ind:length(vel2)
    vel3(n) = vel2(i);
    n = n + 1;
end

% get index of x_max (where velocity falls to zero)
for xmax_ind = 1:length(vel3)
    if vel3(xmax_ind) < 0
        break
    end
end
x_max_ind = xmax_ind + in_ind - 1;
% define x_max with respect to contact point
x_max = depth2(x_max_ind) - x_0;


%% calculate rebound velocity and corresponding position x_r
% make new velocity curve to find second peak
vel4 = vel2(x_max_ind:length(vel2));
% find index of second peak
[v_max2,vmax2_ind] = max(vel4);
% adjust index to correct value
v_max2_ind = vmax2_ind + x_max_ind - 1;
```

```
x_02 = depth2(v_max2_ind);      % define x_02


n = 1;
% make new depth curve for values between x_max and x_02
for i = x_max_ind:v_max2_ind
    depth3(n) = depth2(i);
    n = n + 1;
end

for xr_ind = 1:length(depth3)          % get index of x_r
    if depth3(xr_ind) < x_02
        break
    end
end
x_r_ind = xr_ind + x_max_ind - 1;
x_r = depth2(x_r_ind) - x_0;    % define x_r with respect to contact point
v_out = vel2(x_r_ind);          % define v_out
v_out = -v_out;


%% calculate energy dissipated by pendulum EdP
n = 1;
for i = in_ind - 1:x_r_ind
   dampingforce(n) = c * vel2(i);      % calculate from x_0 to x_r
   n = n + 1;
end

m = 1;
for i = in_ind:x_r_ind + 1             % get the depths from x_0 to x_r
   depthdamping(m) = depth2(i) - x_0;
   m = m + 1;
end

r = length(depthdamping);

for i = 1:r - 1
   energy(i) = dampingforce(i) * (depthdamping(i+1)-depthdamping(i));
end

EdP = sum(energy);


%% calculate energy recovered by pendulum ErP
ErP = 0.5 * kp * (x_max - x_r)^2;


%% calculate K as described in Kalciolgu et al. 2011
K = (0.5*mass*(v_in^2-v_out^2)-EdP)/((0.5*mass*v_in^2)-ErP-EdP);


%% calculate v_out/v_in
e = v_out/v_in;
```

```
    %% print values, clear variables, read next file
    count = fprintf(fid, '%s\t', input_sheet);
    count = fprintf(fid,'%f\t', x_0);
    count = fprintf(fid, '%f\t', x_max);
    count = fprintf(fid, '%f\t', x_r);
    count = fprintf(fid, '%f\t', v_in);
    count = fprintf(fid, '%f\t', v_out);
    count = fprintf(fid, '%f\t', K);
    count = fprintf(fid, '%f\t',ErP);
    count = fprintf(fid, '%f\t',EdP);
    count = fprintf(fid, '%f\n',e);

    filecount = filecount + 1;      % increment index to read next file

    close all                       % close all figures
    clear curve
    clear time
    clear depth
    clear vel
    clear accel
    clear time2
    clear depth2
    clear vel2
    clear accel2
    clear t_in
    clear a_in
    clear a_max
    clear a_max_ind
    clear accel3
    clear a_in_ind
    clear in_ind
    clear v_in
    clear x_0
    clear vel3
    clear xmax_ind
    clear x_max_ind
    clear x_max
    clear vel4
    clear v_max2
    clear vmax2_ind
    clear v_max2_ind
    clear x_02
    clear depth3
    clear xr_ind
    clear x_r_ind
    clear x_r
    clear v_out
    clear dampingforce
    clear depthdamping
    clear r
    clear energy
    clear EdP
    clear ErP
    clear K
    clear e

end
cd(savepath);
```

multiRun.m (calculates Q from measured displacement profile)

```
clear;
close all;
m=0.171;          % effective mass of pendulum in kg

[savefile, savepath] = uiputfile('output.dat', 'Save file name');
loadpath = uigetdir('', 'Choose folder containing data');
fcnpath = uigetdir('', 'Choose folder containing functions');
cd(savepath);
fid = fopen(savefile,'w');
fprintf(fid, 'filename\t hContact \t Xmax \t vMax \t tau \t gHalf \t Ho \t
tRet \t nCyc \t gT \t b \t w \t tanD \t QtanD \t Qwo \t nPrd \t bp \t delQ
\n');

cd(loadpath);
A = ls('*.txt');
A = char(strread(A,'%s'));
filecount = 1;


while(filecount <= size((A),1))
   cd(loadpath);
   input_sheet = A(filecount,:);

   curve = load(A(filecount,:));
   cd(fcnpath);

[hContact,Xmax,vMax,tau,gHalf,Ho,tRet,nCyc,gT,b,w,tanD,QtanD,Qwo,nPrd,bp,delQ
] = impactMulti(curve); % function impactMulti is defined below

   count=fprintf(fid, '%s\t', input_sheet);
   count=fprintf(fid,'%f\t', hContact);
   count=fprintf(fid, '%f\t', Xmax);
   count=fprintf(fid, '%f\t', vMax);
   count=fprintf(fid, '%f\t', tau);
   count=fprintf(fid, '%f\t', gHalf);
   count=fprintf(fid, '%f\t', Ho);
   count=fprintf(fid, '%f\t', tRet);
   count=fprintf(fid, '%f\t', nCyc);
   count=fprintf(fid, '%f\t', gT);
   count=fprintf(fid, '%f\t', b);
   count=fprintf(fid, '%f\t', w);
   count=fprintf(fid, '%f\t', tanD);
   count=fprintf(fid, '%f\t', QtanD);
   count=fprintf(fid, '%f\t', Qwo);
   count=fprintf(fid, '%f\t', nPrd);
   count=fprintf(fid, '%f\t', bp);
   count=fprintf(fid, '%f\n', delQ);

   %Increment index to read next file
   filecount = filecount + 1;

end

cd(savepath);
```

impactMulti.m (function called in multiRun.m)

```
function
[hContact,Xmax,vMax,tau,gHalf,Ho,tRet,nCyc,gT,b,w,tanD,QtanD,Qwo,nPrd,bp,delQ
] = impactMulti(u)

% one with the velocity intersections and the rerun capability

% parameters for loop
rerun = 1;          % starts at 1 to run the loop at least once
rangeRatio = .5;    % where should the first peak be located
peakRatio = 0.01;   % percentage you care about
timeRatio = .5;     % percentage you care about
smoothFactor = 30;  % how much should the derivative be smoothed?

while rerun == 1
    close all
    %1. This section just loads the data
    t = u(:,1); %time data
    d = u(:,2); %displacement data

    %2. This section finds the first max and min used to define the scales
    % first peak has to be in first half of data
    [firstPeak,indPeak] = max(d(1:round(length(d)*rangeRatio)));

    indPeak = indPeak(1);      % index of first max
    tPeak = t(indPeak);        % time of first max

    % only use this data to search because all extrema will be in it
    dUse = d(indPeak-1:end);
    tUse = t(indPeak-1:end);  % time to search in

    [firstValley,indValley] = min(dUse);  % find the fist min
    indValley = indValley(1);             % index of first min
    tValley = tUse(indValley);            % time of first min

    %3. This section define the scales
    % how close in amplitude maxs and mins are before no longer considered?
    peakScale = peakRatio*(firstPeak-firstValley);

    % used as thresh in findZeroCross to group close intersections
    timeScale = timeRatio*(tValley - tPeak);

    %4. This section actually finds the extrema
    derD = diff(dUse)./diff(tUse);          % take the derivative

    derDsmooth = smooth(derD,smoothFactor); % smooth the derivative
    tDer = tUse(1:end-1);                   % dervative time

    % find zero crossing of derivative (function findZeroCross defined below)
    [indIntF,tExtrema] = findZeroCross(tDer,derDsmooth,timeScale);

    extrema = dUse(indIntF);                % actual extrema

    % sorts into maxs and mins (function sortExtrema defined below)
    [tMaxs,maxs,tMins,mins] = sortExtrema(tExtrema,extrema,peakScale);
```

```
hF = mean([maxs(end), mins(end)]);

%6. This section fits the exponential
maxsSH = maxs - hF;              % shifts the maxs down by hContact
% shifts the maxs so the first max is on the y axis
tMaxsSH = tMaxs - tMaxs(1);

% cfit = fit(tMaxsSH',maxsSH','exponential');
maxsSHLog = log(maxsSH);

p = polyfit(tMaxsSH,maxsSHLog,1);      % fits straight line to log of data
params = [p(1) exp(p(2))];             % gamma/2 = gHalf, Ho

%7. This section displays the fit
dUseSH = dUse - hF;
tUseSH = tUse - tPeak;

fitCurve = params(2)*exp(params(1)*tUseSH);

plot(tUseSH,dUseSH,tUseSH,fitCurve,tMaxsSH,maxsSH,'go')
xlim([0 tUseSH(end)])

%8. This section calculates the parameters
dHC = d(1:indPeak);         % define the section that should be searched
tHC = t(1:indPeak);
derDHC = diff(dHC)./diff(tHC);
[maxHC,indHC] = max(derDHC);
hContact = dHC(indHC);      % this is the displacment of the surface
vMax = maxHC;               % this is the maximum velocity
Xmax=firstPeak-hContact;    % this is the max depth

tau = mean(diff(tMaxsSH)); % average time between peaks (average period)

gHalf = abs(params(1));  % magnitude of decay constant of exponential fit

Ho = params(2);           % amplitude constant of exponential fit

% time for exponential fit to decay 1/e*first Max
tRet = (-1/gHalf)*log((((1/exp(1))*maxsSH(1))/Ho));

% number of cycles to 1/e*first Max
nCyc = tRet/tau;

gT = 2*gHalf; % gamma

mass = 0.171; % [Kg]
b = mass*gT;

w = (2*pi)/tau; % frequency

tanD = 1/(pi*nCyc);

QtanD = 1/tanD;

wo = 161.625; % frequency
```

```
    Qwo = wo/gT;

    % number of periods
    nPrd = Qwo/pi; % number of periods should be close to cycle number

    bs = 0.604255; % [Ns/m]
    bp = gT*mass-bs;

    gammaS = bs/mass; % [s^-1]
    delQ = wo*((1/gT)-(1/gammaS));

    %9. This section runs the dialog box and message box
    % message box to show the data
    hBox = msgbox({['hContact = ' num2str(hContact)],
        ['Xmax = ' num2str(Xmax)],
        ['vMax = ' num2str(vMax)],
        ['tau = ' num2str(tau)],
        ['gHalf = ' num2str(gHalf)],
        ['Ho = ' num2str(Ho)],
        ['tRet = ' num2str(tRet)],
        ['nCyc = ' num2str(nCyc)],
        ['gT = ' num2str(gT)],
        ['b = ' num2str(b)],
        ['w = ' num2str(w)],
        ['tanD = ' num2str(tanD)],
        ['QtanD = ' num2str(QtanD)],
        ['Qwo = ' num2str(Qwo)],
        ['nPrd = ' num2str(nPrd)],
        ['bp = ' num2str(bp)],
        ['delQ = ' num2str(delQ)]},'Values','replace');
    set(hBox,'Position',[50 50 125.2500 198.7500])

    %dialog box for any changes
    prompt={'hello Rerun? 1 for yes, 0 for No', 'rangeRatio', 'peakRatio',
'timeRatio', 'smoothFactor'};
    defans={'0', '.5', '0.01', '.5','30'};
    fields = {'rerun','rangeRatio','peakRatio', 'timeRatio', 'smoothFactor'};
    info = inputdlg(prompt, 'Make Choices', 1, defans);

    if ~isempty(info)              % see if user hit cancel
        info = cell2struct(info,fields);
        rerun = str2num(info.rerun);                % convert string to number
        rangeRatio = str2num(info.rangeRatio);      % convert string to number
        peakRatio = str2num(info.peakRatio);        % convert string to number
        timeRatio = str2num(info.timeRatio);        % convert string to number
        smoothFactor = str2num(info.smoothFactor); % convert string to number
    end

end
```

findZeroCross.m (function called in impactMulti.m)

```
function [indIntF,tInt] = findZeroCross(t,d,thresh)

ind0 = find(d==0);
S1 = d(1:end-1).*d(2:end);
ind1 = find( S1 < 0 );
ind = sort([ind0; ind1]);
tIntPre = t(ind);

% ICs
tInt = [tIntPre(1)];
indInt = [1];

for i = 2:length(tIntPre)

    if tIntPre(i) - tInt(end) >= thresh
        tInt = [tInt tIntPre(i)];
        indInt = [indInt i];
    end

end

indIntF = ind(indInt);
```

sortExtrema.m (function called in impactMulti.m)

```
function [tMaxs,maxs,tMins,mins] = sortExtrema(tExtrema,extrema,peakScale)

maxs = [];
tMaxs = [];
mins = [];
tMins = [];

i = 1;

while extrema(2*i-1) - extrema(2*i) >= peakScale

        maxs = [maxs extrema(2*i-1)];
        mins = [mins extrema(2*i)];
        tMaxs = [tMaxs tExtrema(2*i-1)];
        tMins = [tMins tExtrema(2*i)];
        i = i + 1;

        if i > floor(length(extrema)/2)
            break
        end

end
```

II. Quasistatic indentation analysis

CalculateHysteresis.m (analyzes load-depth response from quasistatic adhesion experiments)

```
clear;
close all;

LD = csvread('filename');
depth = LD(:,1);
load = LD(:,2);

%% Find indices at which loading ends and at which force reaches 0 (unloading
ends)

% ind1 is index at which loading curve ends
for ind1 = 1:length(depth)

    if depth(ind1) > depth(ind1+1)
        break
    end

end

if depth(ind1) < depth(ind1+1)
    ind1 = ind1 + 1;
end

% ind2 is index immediately before unloading force reaches 0
for ind2 = ind1:length(load)

    if load(ind2) < 0
        break
    end

end
ind2 = ind2 - 1;

%% Caculate areas under loading and unloading curve using trapezoidal
numerical integration

% area1 is area under loading curve
area1 = trapz(depth(1:ind1),load(1:ind1));
% area2 is area under unloading curve
area2 = trapz(depth(ind1:ind2),load(ind1:ind2));
% area3 is area below x-axis of unloading curve
area3 = trapz(depth(ind2+1:length(depth)),load(ind2+1:length(load)));

dis_work_ind = area1 + area2;       % dissipated work of indentation
dis_work_ratio = dis_work_ind/area1;% normalized to total work of indentation
```